“Dynamics of topological defects in freely floating smectic liquid crystal films and bubbles”

Thesis

for the degree of

doctor rerum naturalium (Dr. rer. nat.)

approved by the Faculty of Natural Sciences of Otto von Guericke University Magdeburg

by M.SC. Amine Missaoui

born on 29/12/1993 in Sbiba (Tunisia)

Examiner: Prof. Dr. Ralf Stannarius
Dr. Ingo Dierking
Dr. Teresa Lopez-Leon

submitted on: 22/02/2021 defended on: 22/03/2021

« There are only two ways to live your life.
One is as though nothing is a miracle.
The other is as though everything is a miracle.»

Albert Einstein

General introduction

The aim of this thesis is to study the dynamics of topological defects in liquid crystals (LC). Among the wide range of possible choices, we are interested in the thermotropic smectic-C (*SmC*) liquid crystalline phase. The unique property of this LC phase allows to form freely suspended films, that are supported on a holder and bounded by a meniscus Harth et al. [2011]; Loudet et al. [2011], and freely floating bubbles Harth et al. [2019]; May et al. [2012]. The studies in these suspended systems are on the one hand less influenced by the boundary conditions that exist in the case of the LC cells and on the other hand easier to interpret thanks to the two-dimensional geometry of these films and bubbles. The aim of my PhD consists in exploiting the properties of *SmC* freely suspended films and bubbles for the study of the dynamics of topological defects.

Studying topological defects is important. They have a significant influence on the macroscopic properties of materials such as mechanical or electrical properties. For these latter ones one main example is the vortex of superconducting materials. In many applications defects are absolutely necessary, for example the topological networks for liquid crystal displays (LCDs) Kim and Serra [2020]. Their dynamic properties share many universal features. LC topological defects for example are useful for laboratory exploration of the dynamics of cosmologically relevant defects Chuang et al. [1991]. As a result LC topological defects have been studied a lot already : In the literature, the "textures" of topological defects have been described in several phases of liquid crystals Dierking [2003] and numerous theoretical models have been developed to describe their interactions Dafermos and Constantine [1970]; Kiyoshi et al. [1997]; Svenšek and Zumer [2003]. On the other hand, numerous works have been performed in order to investigate experimentally the dynamics of topological defects in liquid crystals. Most of them have been carried out in enclosed cells where the liquid crystal is encapsulated between two plates, or in spherical shells where the liquid crystal is in the form of a droplet Blanc et al. [2005]; Dierking et al. [2005]; Kiyoshi et al. [1997]; Lopez-Leon et al. [2012]; Noh et al. [2020]; Pargellis et al. [1994]. These types of methods can lead to results that are not always easy to interpret because of the three-dimensionality of the geometric problem on the one hand and the influence of the cell boundaries and of the shell geometry on the other hand. It is in this perspective that it is interesting to investigate the dynamics of topological defects in freely suspended films that represent ideal systems where we can get rid of the limitations imposed in the case of cell's ex-

periments. Results obtained from 2D LC systems could be generalized to several other systems that develop topological defects, for example thin magnetic films Hertel and Schneider [2006]; Rissanen and Laurson [2016]; Wachowiak et al. [2002].

During this thesis, we focus on three main topics with flat and curved freely suspended smectic films. In the first part, I focus on the dynamics of ± 1 disclinations in freely suspended *SmC* flat films of thickness of the order of $1 \mu m$. From optical observations, we study the annihilation processes of the defect pairs, and then identify the main parameters involved in the defect dynamics. Since recent theoretical models have been developed to describe the influence of the defect orientation on their dynamics Tang and Selinger [2017], our experimental investigations can serve as a basis for discussing the theoretical models. Finally we ask the question in the third chapter, if only the properties of the defects themselves control their dynamics features or if there are some other parameters that should be taken into account as suggested by the simulations by Svenšek and Zumer [2003]?

The second part of the thesis concerns curved smectic films in the form of freely floating smectic bubbles, identical to soap bubbles but with a *SmC* membrane. These structure represent exciting frame for investigation of topological defect dynamics and thin fluid film behavior due to the absence of meniscus and therefore of material reservoirs. Since Harth et al. [2019]; May et al. [2012] have pointed out that intern smectic structure plays an important role in the relaxation dynamics of smectic bubbles, we investigate the dynamics of the so-called smectic islands created in the *SmC* film during the relaxation of the freely floating bubble. What is the effect of the dislocation lines around these islands on their dynamics? How do these islands behave under compression stress? In order to help us to answer these questions, we have chosen to carry out our experiments in micro-gravity conditions created during parabolic flights. Micro-gravity conditions facilitate the optical observation of free-floating smectic bubbles, which is not easy to achieve under the Earth's gravity conditions where bubbles are influenced by the gravity force.

Keywords:

liquid crystals, smectic phase, freely suspended film, topological defects, dislocations, disclinations, backflow, freely floating bubbles, islands, wrinkles.

0.1 References

Blanc, C., Svensek, D., Zumer, S., and Nobili, M. (2005). Dynamics of nematic liquid crystal disclinations: The role of the backflow. *Physical Review Letters*, 95:097802. vii

Chuang, I., Durrer, R., Turok, N., and Yureke, B. (1991). Cosmology in the laboratory: Defect dynamics in liquid crystals. *Science*, 251(4999):1336–1342. vii

Dafermos and Constantine, M. (1970). Disclinations in liquid crystals. *The Quarterly Journal of Mechanics and Applied Mathematics*, 23(2):49–64. vii

Dierking, I. (2003). *Textures of Liquid Crystals*. John Wiley and Sons. vii

Dierking, I., Marshall, O., Wright, J., and Bulleid, N. (2005). Annihilation dynamics of umbilical defects in nematic liquid crystals under applied electric fields. *Phys. Rev. E*, 71:061709. vii

Harth, K., Schulz, B., Bahr, C., and Stannarius, R. (2011). Atomic force microscopy of menisci of free-standing smectic films. *Soft Matter*, 7:7103–7111. vii

Harth, K., Trittel, T., May, K., and Stannarius, R. (2019). Dynamic wrinkling of freely floating smectic films. *Soft Matter*, 15:6769–6778. vii, viii

Hertel, R. and Schneider, C. M. (2006). Exchange explosions: Magnetization dynamics during vortex-antivortex annihilation. *Phys. Rev. Lett.*, 97:177202. viii

Kim, M. and Serra, F. (2020). Topological defect arrays in nematic liquid crystals assisted by polymeric pillar arrays: Effect of the geometry of pillars. *Crystals*, 10:314. vii

Kiyoshi, M., Yasuyuki, K., Kohzo, I., and Reinosuke, H. (1997). Dynamics of annihilation process of disclination pairs in nematic liquid crystals. *Molecular Crystals and Liquid Crystals Science and Technology*, 302(1):345–355. vii

Lopez-Leon, T., Bates, M. A., and Fernandez-Nieves, A. (2012). Defect coalescence in spherical nematic shells. *Phys. Rev. E*, 86:030702. vii

Loudet, J. C., Dolganov, P. V., Patrício, P., Saadaoui, H., and Cluzeau, P. (2011). Undulation instabilities in the meniscus of smectic membranes. *Phys. Rev. Lett.*, 106:117802. vii

May, K., Harth, K., Trittel, T., and Stannarius, R. (2012). Dynamics of freely floating smectic bubbles. *EPL Europhysics Letters*, 100(1):16003. vii, viii

Noh, J., Wang, Y., Liang, H.-L., Jampani, V. S. R., Majumdar, A., and Lagerwall, J. P. F. (2020). Dynamic tuning of the director field in liquid crystal shells using block copolymers. *Phys. Rev. Research*, 2:033160. vii

Pargellis, A. N., Green, S., and Yurke, B. (1994). Planar xy-model dynamics in a nematic liquid crystal system. *Phys. Rev. E*, 49:4250–4257. vii

Rissanen, I. and Laurson, L. (2016). Coarsening dynamics of topological defects in thin permalloy films. *Phys. Rev. B*, 94:144428. viii

Svenšek, D. and Zumer, S. (2003). Hydrodynamics of pair-annihilating disclinations in smc films. *Phys. Rev. Lett.*, 90:155–501. vii, viii

Tang, X. and Selinger, J. V. (2017). Orientation of topological defects in 2d nematic liquid crystals. *Soft Matter*, 13:5481–5490. viii

Wachowiak, A., Wiebe, J., Bode, M., Pietzsch, O., Morgenstern, M., and Wiesendanger, R. (2002). Direct observation of internal spin structure of magnetic vortex cores. *Science*, 298(5593):577–580. viii

Table of contents

List of figures

List of Tables

Chapter 1

Introduction

> *" Liquid crystals stand between the isotropic liquid phase and the strongly organized solid state. Life stands between complete disorder, which is death and complete rigidity, which is death again "*
>
> Dikran Dervichian

Contents

1.1 Introduction to Liquid Crystals Mesophases

To write this introduction many sources were available, we were inspired by two fundamental books for the study of liquid crystals which are the first edition of "The Physics of Liquid Crystals." of De Gennes [1969] and the two volumes of Oswald and Pieranski [2006].

1.1.1 History of mesophases

In 1888, an Austrian scientist, Friedrich Reinitzer was experimenting with a cholesterol type material compound. He was trying to accurately determine the physical properties of the substance, like its melting point [1] and the correct empirical formula [2]. Reinitzer noticed that the cholesterol compound had two melting points! This was very unusual. He sent the sample to Otto Lehmann, a German physicist who was an expert in crystal optics for further investigation. Lehmann discovered that the substance was birefringent Lehmann [1889]. He called it "flowing crystal" because it combined both properties of a liquid and a solid. At that time, this idea was very bold! All scientists believed that there was only three states of matter and only one melting point (For example, water has a melting point of 0^o C, where it changes from a solid to a liquid state, and a boiling point of 100^o C, where it changes from a liquid to a gas state.). The idea for a new phase was not easily accepted by the scientific community until the early 1900's, where scientists established conclusively that "liquid crystals" exist and correspond to a specific physical state Friedel [1922]. Today, liquid crystals are very common. We exploit their properties for many new advances. For example, the vast majority of electronic devices have liquid crystal displays (LCs) Mosley [1993].

The basic composition of the liquid crystals consist of organic molecules, but inorganic materials are also known to present mesophases Liang-shi et al. [2002]. The liquid crystals are usually divided into thermotropic and lyotropic materials. The lyotropic substances exhibit mesophases by changing the molecule concentration in solvent Collings and Goodby [2017], while the thermotropic substances exhibit different mesophases through temperature changes Vertogen and Jeu [2012]. The main differ-

---

[1] The melting point of a substance is the exact temperature at which a substance changes states from solid to liquid and melts.

[2] A substance's chemical description that tells you how many of each type of atom is an a substance. For example, the empirical formula for water is H_20.

ence between the mesophases is the molecules orientation and organization. When the temperature increases, the liquid crystal will change state progressing from solid to liquid.

Today, many different type of mesophases have been discovered. In Fig. 1.1, we show the arrangement of three mesophases, where molecules are represented as rods because they have similar elongated shape in particular in the LC that we study. First there is the nematic phase, where molecules are distributed without order of position but remain on average roughly parallel to each other. Second, there are the liquid crystal smectic phases, somewhere in between the solid and nematic states, where molecules form well-defined layers. Usually, the nematic phase is obtained at higher temperature.

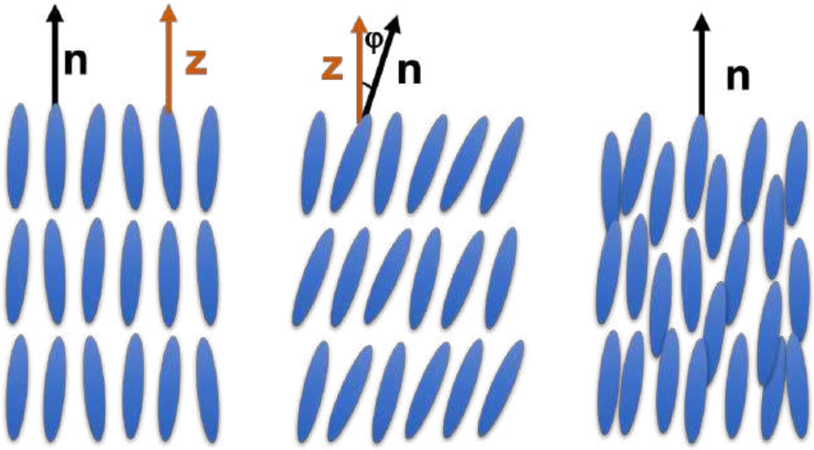

(a) SmA (b) SmC (c) Nematic

Figure 1.1 – The arrangement of molecules in the (a) *SmA*, (b) *SmC* and (c) Nematic mesophases made of rod-like molecules.

1.1.2 Nematic liquid crystals

Rotational symmetry breaking creates the nematic liquid crystal state in which molecules are aligned along a common axis. The direction of preferred orientation of the molecules in the neighborhood of any point is represented by a dimensionless, nonpolar unit vector $\vec{n}$ (here $\vec{n}$ and -$\vec{n}$ are equivalent) called the *n-director* (Fig .1.1c), whose orientation can change smoothly and slowly from point to point (except at singularities discussed in the next paragraph). From a microscopic point of view, the phase order is characterized by the order parameters, s, which can be calculated from the distribution function of the orientation of the molecules in relation to the *director*:

$$s = \frac{1}{2}\langle(3cos^2\beta - 1)\rangle, \tag{1.1}$$

β is the average tilt angle of the molecules with respect to the *director* (Fig .1.1c). This orientation gives the liquid crystal birefringence property. A nematic liquid crystal can be uniaxial medium with the optical axis along the *n-director* or, a biaxial medium. A nematic liquid crystal alters the polarization of light passing through it. When it is placed between crossed polarizing filters, light may get through because the nematic material changes the polarization of the light if the *n-director* is not aligned with either of the polarizing filters and if light is not propagating along the optic axis.

1.1.3 Smectic liquid crystals

As temperature decreases, matter in general varies from profoundly disarranged states with continuous symmetries toward ordered states. In general there are three independent directions for translational symmetry. When this symmetry is broken along only one direction, a new liquid crystal phase is obtained: the smectic phase (Fig. 1.1a and Fig. 1.1b). From a structural point of view, all smectics are stratified structures with a well-defined interlayer spacing. Molecules in most smectic phases are mobile in two directions and can rotate along one axis. The interlayer interaction is weaker than the lateral forces between molecules, which leads to layers able to slide over one another. This results in a system presenting higher viscosity than nematics. There are several types of smectic phases, giving rise to different macroscopic "textures", readily recognized by optical observation Dierking [2003]. The smectic phases differ from each other in the existing order inside the layer. In this section, we will discuss briefly the *smectic-A (SmA)* and the *smectic-C (SmC)* phases properties.

A closer look to the molecules arrangement in the *SmA* phase is shown in Fig. 1.1a. The average orientation axis of the rod-like molecules is parallel to the layer normal, which corresponds to the *n-director* orientation. In each layer, the center of gravity shows no long-range order. We can consider each layer as a two-dimensional liquid. This property will be important for the following. Optically, the *SmA* phase is a uniaxial system, the optical axis is normal to the layer plane and the directions *z* and *-z* are equivalent.

When the temperature decreases, the *SmA* phase may transform into a phase with an even lower symmetry. This corresponds to the appearance of tilting of molecules relative to the layer normal. This new phase is called the *SmC* phase (Fig. 1.1b). The average molecule orientation is tilted regarding the layer normal and the angle of tilt is defined as ϕ. The *c-director* is the projection of the *n-director* in the *xy* layer plane, as shown in Fig. 1.2, with θ the angle between the *x-axis* and the *c-director*. Unlike the apolar nematic *n-director*, the polar *c-director* is a true vector, thus $\vec{c}$ is not equivalent to -$\vec{c}$. The difference can be observed from the Fig. 1.2 where the angle $\theta_{\vec{c}} = \theta_{-\vec{c}} + \pi$. This characteristic property of the *SmC* phase also has an impact at the optical level as we will see later.

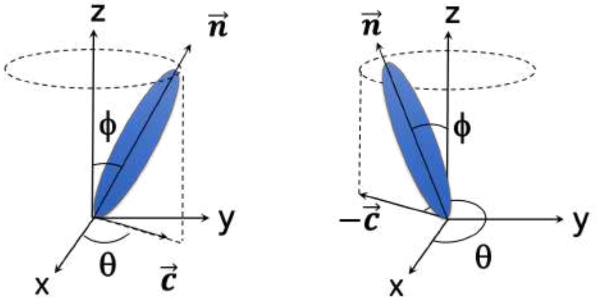

Figure 1.2 – The *SmC* director. The projection of molecules onto the layer plane (xy) allows the construction of the *c-director*. Unlike the nematic director $\vec{n}$, $\vec{c}$ is not equivalent to $-\vec{c}$.

1.1.4 Freely suspended films made with smectic LCs

The group of smectic liquid crystals possess a unique property which makes them very interesting. Thermotropic and lyotropic mesophases are able to form thin freely suspended films. Reports in the literature about nematic freely suspended films show that they are not stable Iglesias et al. [2011]. A very well known example of membranes equivalent to freely suspended smectic films that we are familiarized with is the soap films Friedel [1922]. A soap film consists of a layer of water encapsulated between two layers of soap molecules. The hydrophilic heads of the soap molecules point toward the water while the hydrophobic tails point toward the air. However, the water in the middle layer evaporates and becomes thinner and thinner. This explains why soap films are not stable and only last a few minutes. Thanks to their high boiling point and the low vapor pressure, freely suspended films made of smectic liquid crystal can remain for months without evaporating or breaking.

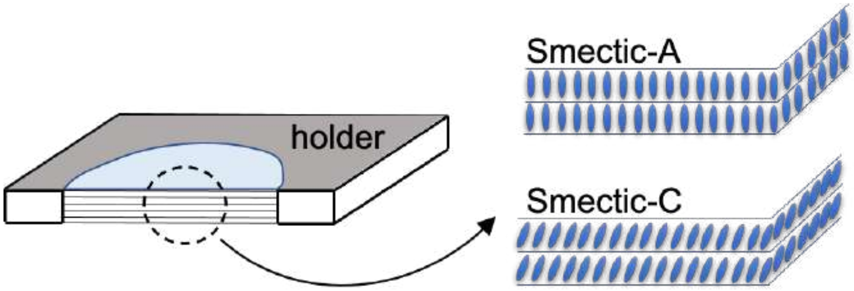

Figure 1.3 – The structure of *SmA* and *SmC* freely suspended films. The membranes are spanned on a metallic holder (frame).

1.1.4.1 *SmA* freely suspended films

A freely suspended *SmA* film is formed by a stack of identical smectic layers with molecules pointing in parallel to the layer normal as shown in Fig. 1.3. These films are characterized by the dominance of surface properties in their mechanical behavior. They represent homogeneous, stratified structures with well defined thickness associated with a discrete number of layers, which can be as small as a single molecular mono-layer ($\approx 3-4$ nm thick) and as big as thousands of layers (some μm) Kraus et al. [1997]. Such film can be treated as two-dimensional liquid with a quasi-2D flow, they have a large surface-to-volume ratio.

1.1.4.2 *SmC* freely suspended films

A freely suspended *SmC* film is analogous to the previously discussed *SmA* film except that the molecules are on average tilted by an angle ϕ with respect to the layers (Fig. 1.3). Within these layers, the molecules behave in a liquid-like manner. They can rotate around the vertical axis to the layers while keeping the same tilt, which correspond to the local variation of the *c-director* orientation which cost energy. On the other hand, compression or expansion of the smectic layers may occur, for example due to thermal fluctuation Mach et al. [1997]; Tweet et al. [1990]; Young et al. [1978]. In this case, an increase or decrease of the tilt of the molecules may take place. As a result, the optical observations reflect the local average tilt in the film, as we will show later.

The *c-director*, which is the projection of the *n-director* into the layer plane, forms a two-dimensional nematic-like field in the film plane. Thus, *SmC* films are generally treated as 2D polar nematics. Quantitatively, this consideration is appropriate as long as the *director* variations along the film normal are small, which is fulfilled in micrometer or sub-micrometer thin *SmC* films. Moreover, the textures observed in *SmC* films are analogous to those of nematic liquid crystals but in 2D, as we will show afterwards.

1.1.4.3 Structure of the meniscus

A freely suspended film cannot exist spontaneously. It needs to be prepared, through the stretching of the smectic liquid crystal material above a solid frame. Fig. 1.3 shows the structure of a freely suspended smectic film stretched on a circular metallic holder. It has been also shown that they can be successfully stretched on a fractal-shaped[3] frame Even et al. [1999] as well as with isospectral polygonal[4] frames of DeTurck Even and Pieranski [1999].

Freely suspended films are bounded by a thick region called the "meniscus", which connect the film to the solid holder. Fig. 1.4 illustrates a typical aspect of the meniscus geometry for a film of thickness h. The shape and extent of the meniscus depend, in general on the geometry of the holder, the LC material, and the conditions under which the film was drawn Geminard et al. [1997]; Loudet et al. [2011]. The smectic film can not be seen as independent of the meniscus. This latter acts as a reservoir of material for the film, so that exchanges of molecules occurs when required Pieranski et al. [1993].

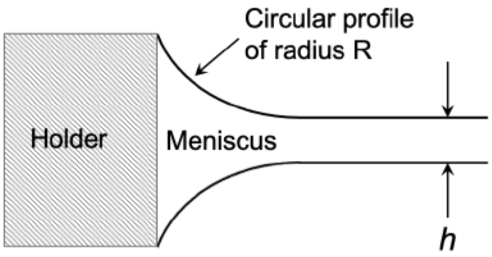

Figure 1.4 – Meniscus profile of radius R connecting the freely suspended film, of thickness h, to the holder.

In mechanical equilibrium, an isotropic liquid in contact with the air must present the same pressure as the air on its flat interface Rowlinson and Widom [1984]. This is not necessarily true in case of freely suspended smectic films. Because of their specific geometry, the curvature of the interface with the air varies discontinuously when it passes from the meniscus to the film (Fig. 1.4) Geminard et al. [1997]. This discontinuity

---

[3] Irregular geometries permit to describe many irregular systems in a well-defined geometrical framework.

[4] Irregular special geometry built with seven identical triangles.

creates a pressure difference between the flat surface of the film and the air ($\Delta P = P_{air} - P_{smectic}$), which can only be balanced by compressing the layers in the film. Mach et al. [1997] showed that the magnitude of the total compression was found to be as large as 3 Å for 3 layers film. By applying Laplace law for an ordinary fluid, ΔP is given by Pieranski et al. [1993]

$$\Delta P = \frac{\gamma}{R} \tag{1.2}$$

where γ is the specific surface free energy of the smectic-air interface. In mechanical equilibrium, the pressure is the same in the film and in the meniscus ($\Delta P = Constant$). This leads to a meniscus profile that should be circular of radius R. This result is different from a horizontal water layer that wets a vertical wall, where the meniscus has an exponential profile, as experimentally observed by Geminard et al. [1997]. The measured pressure difference was usually about 10–100 Pa, while the smectic-air surface tension was found to be close to 25.10^{-3}N/cm Geminard et al. [1997]. As a conclusion, the planar film can exist outside the meniscus because the elasticity and compressibility of the smectic layers compensate the pressure difference ΔP.

The thermodynamic state of the meniscus has an importance in determining the mechanical properties of the film Kraus et al. [1997]. The execution and interpretation of many hydrodynamic experiments are complicated because of the presence of this thick region. For example, thermally driven convection in smectic films in vacuum was reported to be driven exclusively by thermal gradients in the meniscus, which mask the intrinsic thermocapillary effects in the films Godfrey and Winkle [1996]. It has been also shown that the presence of the meniscus influences most of the motion, evolution and dynamic of inclusions in the film Dolganov et al. [2020].

On the other hand, freely suspended films are the thinnest known stable structures of any fluid phase preparation. They have the largest surface-to-volume ratio which can lead them to be considered as two-dimensional fluid systems. In contrast with soap films, thermotropic smectic films appear to be very robust. We can, for example manipulate them with a glass wire, create mechanical deformations, change their structure by changing the surrounding temperature or humidity and even introduce inclusions for an in situ dynamical study Bohley and Stannarius [2007]; Conradi et al. [2006]. Another additional value of these membranes is the free boundaries at the two interfaces: they are freely suspended in the air. Hence, surface ordering effects and phase transitions can be accurately studied Bahr [1994]. Sirota et al. [1987] have shown that the two-dimensional geometry of the freely suspended films shifts the temperature of the phase transition and even suppress some phases.

Freely suspended smectic films do not only represent systems where we can study phase transition or thin fluid film surfaces. We show in the following parts that topological defects exist in such fluid membranes, where investigations on their coarsening dynamics are of a high interest.

1.2 Defects and Textures in Liquid Crystals

1.2.1 Introduction

In recent years scientists and engineers have become interested in liquid crystals because of their attractive properties such as excellent optical anisotropy. Their unusual physical properties have made them exciting materials for more fundamental research in relation with topological defects. The study of defects also, is an important subject in material science, since defects play an important role in determining the relationship between structure and properties of materials. Topological defects created by symmetry-breaking phase transitions have received considerable attention in particle physics, condensed matter physics and even cosmology. Liquid crystal defects are remarkably useful for laboratory exploration of the dynamics of cosmologically relevant defects Chuang et al. [1991a]. The observation of the topological point defects coarsening in LC systems allows for the direct study of "scaling solutions", providing models for the evolution of monopoles, multipoles, and textures. Liquid crystals are one of the most valuable systems for studying the coarsening dynamics of topological defects, because different kinds of defects can be created and controlled through symmetry-breaking phase transitions. In addition, LC defects observation can be particularly simple, since optical microscopes allow for direct studies Dierking [2003].

The presence of topological defects can be important also for several applications. For example, in thermotropic liquid crystals, they can be used in high strength fibers Picken et al. [2011], field-active displays Tsukada [2000] and wave-guide modulators Walker et al. [1996]. Hence, understanding and controlling the defect textures becomes required.

1.2.2 Elastic deformations and free energy density

1.2.2.1 The nematic phase

Under small deformations, a nematic liquid crystal acts like an orientationally elastic medium, where the three principal types of distortions are the splay, twist and bend as shown by Fig. 1.5. The corresponding elastic constants (or Frank constants) are k_S, k_T and k_B, respectively.

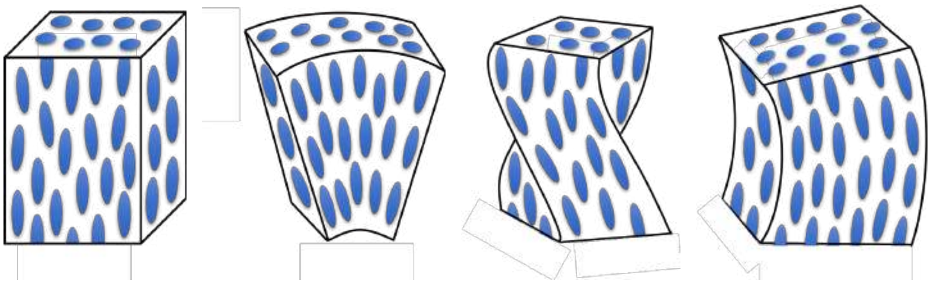
(a) Equilibrium (b) Splay (c) Twist (d) Bend

Figure 1.5 – The principal types of deformations in a nematic liquid crystal.

When the nematic director orientation is almost unchanged locally, the distortional free energy f per unit of volume, may be expanded in powers of the director $\vec{n}$ Frank [1958]:

$$f = \frac{1}{2}[k_S(\bigtriangledown \cdot \vec{n})^2 + k_T(\vec{n} \cdot \bigtriangledown \times \vec{n})^2 + k_B(\vec{n} \times \bigtriangledown \times \vec{n})^2] \tag{1.3}$$

For typical nematics, the Frank elastic constants are approximately 10^{-6} dyn (10^{-11} J/m). The bend and splay constants are usually approximately equal, while the twist constant is significantly lower. It should also be noted that the values of these elastic constants decrease rather strongly when temperature increases, to finally become zero in the high temperature isotropic state.

Two-dimensional nematics

In the case of a nematic liquid crystal with two-dimensional geometry, a planar structure with $\vec{n}$ lying in the xy plane is assumed. The components of $\vec{n}$ are ($\cos\theta$, $\sin\theta$, 0), where θ is the angle between $\vec{n}$ and the *x-axis* (see Fig. 1.1b). A number of the elastic deformations are not allowed and the 3D expression can be simplified. Thus the free energy density (Eq. 1.3) reduces to

$$\begin{aligned} f &= \frac{k_S}{2}(\bigtriangledown \cdot \vec{n})^2 + \frac{k_B}{2}(\bigtriangledown \times \vec{n})^2 \\ &= \frac{k_S}{2}\left(-\sin\theta\frac{\partial\theta}{\partial x} + \cos\theta\frac{\partial\theta}{\partial y}\right)^2 + \frac{k_B}{2}\left(\sin\theta\frac{\partial\theta}{\partial y} + \cos\theta\frac{\partial\theta}{\partial x}\right)^2 \end{aligned} \tag{1.4}$$

With the assumption of equal elastic constants associated with a medium considered as elastically isotropic, $k_S = k_B = k$, Eq. 1.4 is simplified as following

$$\begin{aligned} f &= \frac{k}{2}\left[\left(\frac{\partial\theta}{\partial x}\right)^2 + \left(\frac{\partial\theta}{\partial y}\right)^2\right] \\ &= \frac{k}{2}(\nabla\theta)^2 \end{aligned} \tag{1.5}$$

Thanks to the above simplification, the minimum of the free energy is given by solving the Laplace equation $\Delta\theta = 0$.

1.2.2.2 Two-dimensional *SmC*

SmC liquid crystals possess a stratified structure where the molecules are tilted with respect to the layer normal. Similar to the nematic phase where the *n-director* is used to describe the average molecule orientation, the unit vector $\vec{c}$ is used to describe the molecular orientation. The main elastic deformations in *SmC* correspond to the layer displacement along the normal and the angular distortion of the *c-director* in the layer plane (see Fig. 1.2). A complete theory for the description of incompressible *SmC* phases has been introduced many years ago Leslie et al. [1991]. In thin planar *SmC* films with straight and fixed layers, the director deformations normal to the film plane can be disregarded. Taking into account the molecules tilt, the projection of the director $\vec{n} = (n_x, n_y, n_z)$ onto the smectic layer plane is $\vec{n}_0 = (n_x, n_y, 0)$, considered as the 2D order parameter. The unit vector along the direction of $\vec{n}_0$ is usually referred to as *c-director*. Thus, free energy expansion of the film can be written as Harth et al. [2011]; Svenšek and Zumer [2003]

$$f = A|\vec{n}_0|^2 + C|\vec{n}_0|^4 + k_S(\nabla \cdot \vec{n}_0)^2 + \left[k_T(\vec{n} - \vec{n}_0)^2 + k_B\vec{n}_0^2\right](\nabla \times \vec{n}_0)^2, \tag{1.6}$$

The Landau parameters $A < 0$ and $C > 0$ set the equilibrium length of $\vec{n}_0$ and the equilibrium tilt angle $\phi = \arcsin\sqrt{-A/(2C)}$ respective to the layer normal. Their magnitude describes the resistance against changes of the tilt angle. The elastic constant

k_S, k_T and k_B correspond to respectively the splay, twist and bend elastic constants for the *n-director*. At non-zero tilt, the *c-director*, $\vec{c}$, can be defined as $\vec{c} = \vec{n}_0 / n_0$ Harth et al. [2011].

Taking in account the two-dimensional geometry of thin *SmC* films, only splay and bend deformations of $\vec{c}$ are possible, the twist deformation can be neglected. The elastic deformations K_S and K_B of the *c-director* can be obtained from those of the nematic *n-director* and the tilt angle ϕ as Harth et al. [2011]

$$\begin{aligned} K_S &= k_S \sin^2(\phi) \\ K_B &= k_T \sin^2(\phi) \cos^2(\phi) + k_B \sin^4(\phi) \end{aligned} \tag{1.7}$$

Thus, the free energy density for thin *SmC* films in term of the director $\vec{c} = (\cos\theta, \sin\theta, 0)$ reduces to Harth et al. [2011]:

$$\begin{aligned} f &= \frac{K_S}{2}(\nabla \cdot \vec{c})^2 + \frac{K_B}{2}(\nabla \times \vec{c})^2 \\ &= \frac{K_S}{2}\left(-\sin\theta \frac{\partial\theta}{\partial x} + \cos\theta \frac{\partial\theta}{\partial y}\right)^2 + \frac{K_B}{2}\left(\sin\theta \frac{\partial\theta}{\partial y} + \cos\theta \frac{\partial\theta}{\partial x}\right)^2 \end{aligned} \tag{1.8}$$

$\theta(\vec{r})$ is the disorientation of the *c-director* with respect to a fixed *OX-axis* (Fig. 1.1b). Similar to the nematic case, when we use the one-constant approximation, $K_S = K_B = K$ the free energy density can be expressed in a form similar to the one of Eq. 1.5.

To conclude, the free energy density equations, that describe a deformed specimen relative to the undeformed one, were introduced for nematic and smectic phases for both bulk and 2D geometry. When the deformations are too strong, topological defects always appear. It is thus important to investigate the defect formation in smectic liquid crystals.

1.2.3 Topological defects in nematic and smectic liquid crystals

If a liquid crystal is deposited on a surface, molecules fall at random positions and orientations, especially if the surface is not treated for specific LC orientations. In bulk, molecules are free to move as in a liquid, but they tend to remain oriented parallel to the *director* which can be determined by the surfaces thus possibly leading to the formation of "defects" in the LC bulk. Topological defects are surfaces in which the order parameter vanishes. They form specific "textures", which can be easily observed by the means of optical polarized microscopy Dierking [2003].

This introductory section presents a systematic account of the structures, energies and interactions of defects in the nematic and *SmC* phase of liquid crystals. Relevant experimental observations will be described in the next chapter.

1.2.3.1 Disclinations

Disclinations are singular lines along the *z-axis*, normal to the layers for the smectics, in which rotational symmetry is broken. They can be found in both nematic and smectic phases. In the smectic phase, they present an additional layer constraint: they are lines around which the layers will rotate. In the following part, we introduce the structure and energy of these topological defects.

Nematic phase

There are several techniques that allow one to create disclinations in nematics. A well known method consists in a rapid phase transition from the isotropic to the nematic phase, which could be achieved by temperature quench or application of a quick reduction of pressure Chuang et al. [1991a,b]. Randomly oriented patterns of disclination are created after the disorder–order transition. When observed under polarized optical microscope, nematic films possess a unique texture, called the schlieren[5] texture, shown in Fig. 1.6, where the white circle points out the presence of a disclination.

In order to describe the director field around a single disclination point, one considers a planar geometry with the *n-director* into the xy plane, i.e. $\vec{n}$ is independent of the normal to the film z, $n_x = \cos\theta$, $n_y = \sin\theta$, $n_z = 0$. Eq. 1.5 reduces to

$$\nabla^2\theta = 0 \tag{1.9}$$

A first solution for Eq. 1.9 is of the form $\theta = 0$. This type of solution is of no interest. The second interesting solution, which is independent of $r = \sqrt{(x^2+y^2)}$ is of type:

$$\theta(\vec{r}) = S\phi(\vec{r}) + \theta_0 \tag{1.10}$$

Where $\phi(\vec{r}) = \tan^{-1}(y/x)$ and θ_0 is the constant that defines the defect phase. Geometrically, θ_0 describes a global rotation of the *director* about the *OX-axis* passing through the right side of the defect core.

---

[5] The texture is called a schlieren texture after the German word for streak; Schliere.

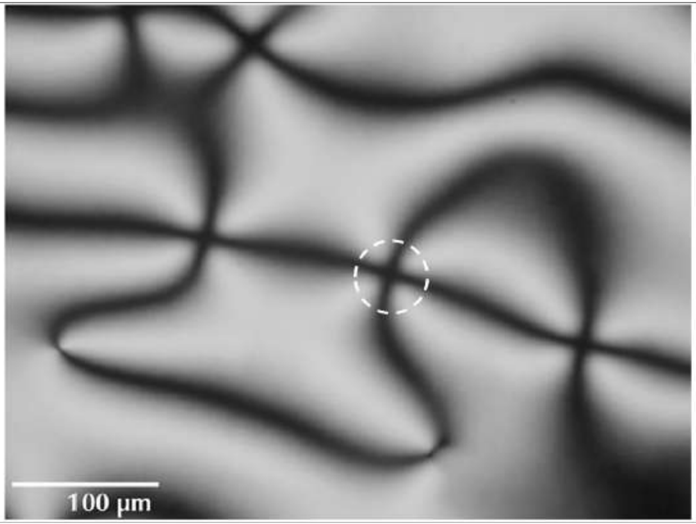

Figure 1.6 – An example of the characteristic schlieren texture of nematic liquid crystals observed by the mean of polarizing microscope between crossed polarizers. The white circle points out one singular point. Reproduced from Publication Lagerwall and Scalia [2012]. Copyright (2012), with permission from Elsevier.

$$S = \pm\tfrac{1}{2}, \pm 1, \pm\tfrac{3}{2}, \ldots \text{ with } 0 < \theta_0 < \pi.$$

S is known as the topological charge (or strength) of the disclination. $\theta(\vec{r})$ describes the *director* orientation at a distance $\vec{r}$ from a disclination point of a topological charge S and phase θ_0. Fig. 1.7 shows the *director* field configuration in the vicinity of disclinations of various strengths as given by Eq. 1.10. The black dot at the center indicates the defect core (the point where the *director* is not defined anymore) with a radius r_c.

The energy per film thickness of an isolated defect in a circular film of radius R is given by the following equation

$$E = \int f dxdy = E_c + \pi k S^2 \ln(R/r_c) \tag{1.11}$$

Where k is the elastic constant and E_c is the core energy which is not known.

The second term in Eq. 1.11 is proportional to S^2, which implies that defects of strength $|S| > 1/2$ are unstable and should dissociate into $|S| = 1/2$ defects. If one considers an infinitely extended film ($R \to \infty$), an isolated disclination should have an infinite energy ($E \to \infty$). Such a situation does not exist in reality. Therefore, defects exist in pairs of opposite charge.

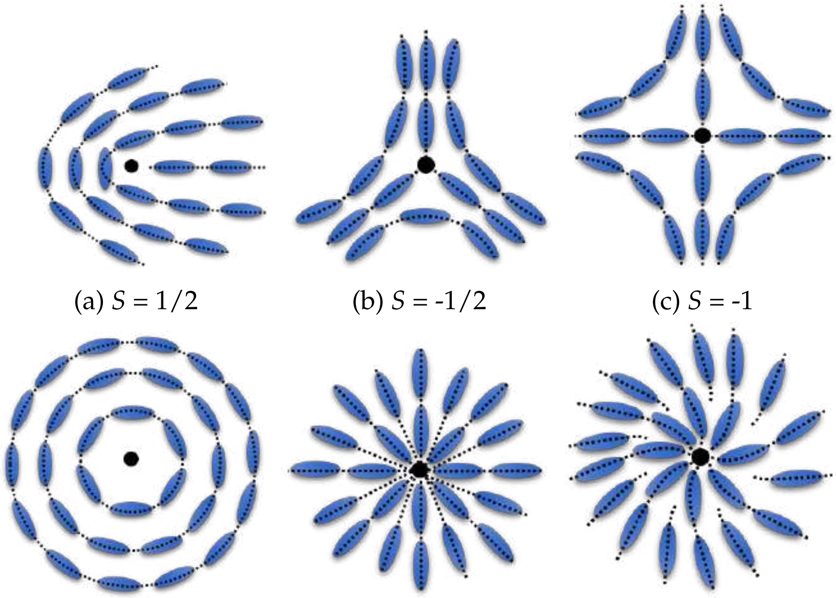

(a) $S = 1/2$ (b) $S = -1/2$ (c) $S = -1$

(d) $S = 1, \theta_0 = \pi/2$ (e) $S = 1, \theta_0 = 0$ (f) $S = 1, \theta_0 = \pi/4$

Figure 1.7 – *Director* field around disclinations of various strengths.

SmC phase

In the *SmC* phase, the *c-director* characterizes the local orientation of the optical anisotropy in the film plane. The spatially uniform alignment of the *c-director* is the undistorted state, any splay or bend deformations of this vector costs energy. Therefore, defects in the *SmC* phase are disclinations in the *c-director* field with the topological charge designated by how much the *director* changes in a counter-clockwise circle around the defect.

In the one-constant approximation, $K_S = K_B = K$, the *SmC* free energy density has the same form as in the nematic case, Eq. 1.5. Unlike the nematic *n-director*, the *c-director* is polar, so that only defects of integral strength can occur ($S = \pm 1, \pm 2, ...$) in *SmC* films.

Fig. 1.8 shows the structure of point disclinations of unit strength with different configurations. Due to the polarity of the *c-director*, the S = +1 disclination with radial configuration can now present two independent solutions, Fig. 1.8a and Fig. 1.8b. Moreover, S = -1 no longer displays a fourfold symmetry (Fig. 1.8e).

1.2.3.2 Dislocations

Beside disclinations that can occur in a nematic or a smectic liquid crystal, another type of topological defects can be observed in stratified phases, i.e. in smectics. A

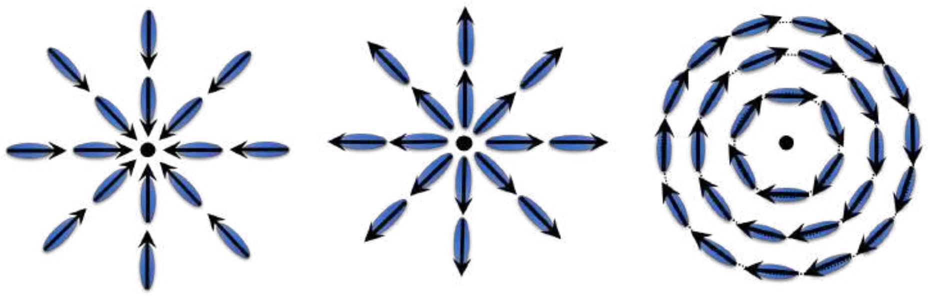

(a) Radial inward S = 1, $\theta_0 = \pi$ or $-\pi$ (b) Radial outward S = 1, θ_0 = 0 (c) Tangential S = 1, θ_0 = $-\pi/2$

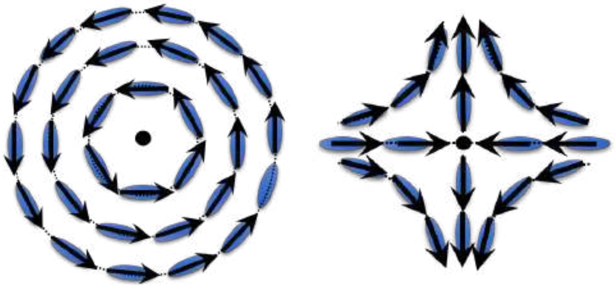

(d) Tangential S = 1, $\theta_0 = \pi/2$ (e) S = -1, $\theta_0 = \pi$ or $-\pi$

Figure 1.8 – S = 1 wedge disclination with a radial configuration: (a) sink (inward) , (b) source (outward) and tangential configuration: (c) vortex (clockwise), (d) anti-vortex (counterclockwise). (e) S = - 1 hyperbolic disclination.

dislocation is a defect line with the annihilation of parallel (screw) or perpendicular (edge) smectic layers at the defect (Fig. 1.9). This topological defect is characterized by a Burgers vector $\vec{b} = Md\vec{z}$, where M is the number of involved layers and d is the thickness of one layer. The Burgers vector is parallel to screw dislocations and perpendicular to edge ones. Therefore, the energy per line unit of a wedge dislocation is written as Oswald and Pieranski [2006]

$$E_{\text{wedge}} = (KB)^{1/2} \frac{b^2}{4\pi r_c} + E_c \tag{1.12}$$

Where B is the elastic constant corresponding to the layer compression or dilatation distortion. r_c is the core radius, which is of the order of one layer thickness. The core energy is assumed to be $E_c \approx 2\gamma_c r_c$, with γ_c is the cutoff energy that is negligible at the *nematic-SmA* phase transition. Thus, E_{wedge} can be simplified as

$$E_{\text{wedge}} = \left(\frac{2B\lambda\gamma_c}{\pi}\right)^{1/2} \vec{b} = \left(\frac{2}{\pi}\right)^{1/2} B^{1/4} K^{1/4} \gamma_c^{1/2} \vec{b} \tag{1.13}$$

Where λ is the penetration length as shown on Fig. 1.10. The energy of a single edge dislocation is independent of the sample size and proportional to the Burgers vector $\vec{b}$.

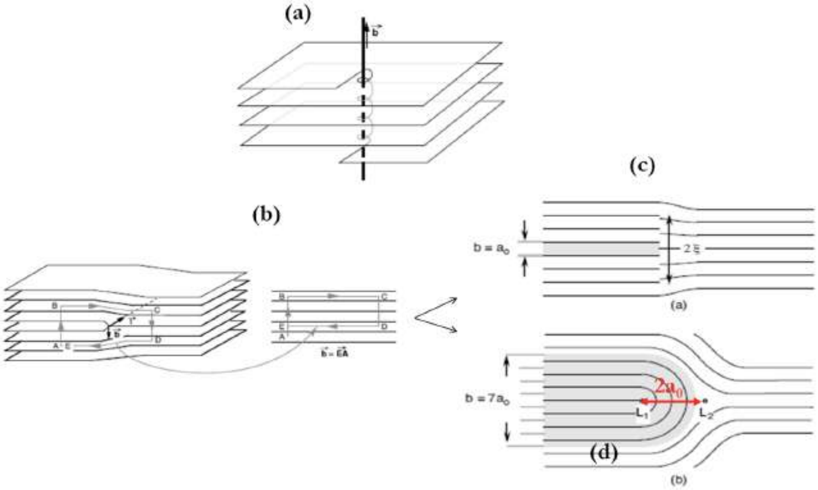

Figure 1.9 – (a) Screw dislocation. (b) Edge dislocation. (c) Small edge dislocation with annihilation of a layer (sliding perpendicular to the layers). (d) Giant edge dislocation associated with two lines of inclinations. Figure reprinted from Oswald and Pieranski [2006].

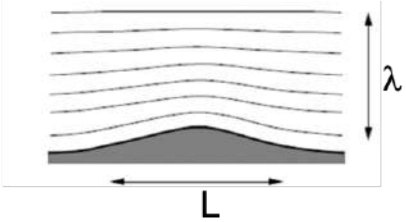

Figure 1.10 – The penetration length λ in smectic films. Figure reprinted from Oswald and Pieranski [2006].

Dislocations in freely suspended smectic films

In freely suspended films, the layers are perfectly parallel to the free surfaces and when the number of layers is different in two parts of the same film, a step is formed in between (Fig. 1.11). A violent compressing or stretching can create holes or islands (region of lower or larger thickness than the background film) when drawing a freely suspended smectic film (Fig. 1.11). The step around such regions is associated with an edge dislocation. In general, we do not see the dislocation lines directly with a reflective microscope, as their size is well below the resolution limit. What we see is the boundary between two regions of different thicknesses, therefore of different reflectivity and contrast.

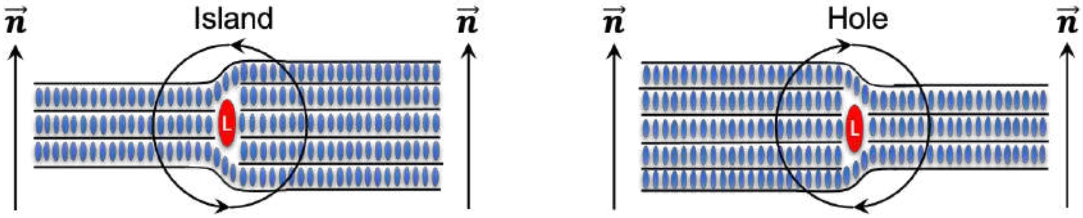

Figure 1.11 – Cross section of an edge dislocation of unit strength in freely suspended smectic films. Thick (thin) region is bounded by an edge dislocation loop (in red) providing a line tension.

Fig. 1.12 displays an example of a smectic island observed in optical polarized microscope. The line tension of the dislocation loop, which is the one-dimensional analog of surface tension, is responsible for the island's circular shape. Lejcek and Oswald [1991] have expressed the line tension of a dislocation in a freely suspended film as following

$$E_{\text{disloc}} = E_{\text{wedge}} + \delta E_s \tag{1.14}$$

Were E_{wedge} is the bulk term, given by Eq. 1.13. The second term is the surface correction for interactions with the freely suspended film free surfaces Oswald and Pieranski [2006]

$$\delta E_s = \frac{B^{1/2}\gamma^{1/2}b^2}{4\sqrt{\pi d(M+1/2)}} \tag{1.15}$$

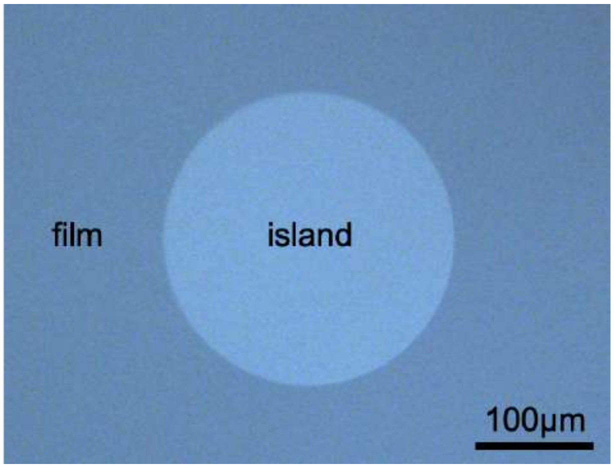

Figure 1.12 – Thicker circular domain (island) in a freely suspended *SmC* liquid crystal. The reflection colors arise from the interference of the light reflected from the top and bottom surfaces. The island is bounded by an edge dislocation loop providing a line tension responsible for the circular shape of islands.

Several methods have been developed to measure the line tension of a dislocations in freely suspended smectic films. Geminard et al. [1997] determined the critical radius, r_{crit}, a radius for which islands and holes grow or shrink according to their initial radius after nucleation. The critical radius of nucleation of a dislocation loop, r_c, is linked to the dislocation line tension by

$$r_{crit} = \frac{E_{disloc}}{\vec{b}\Delta P} \tag{1.16}$$

Were ΔP is the pressure difference between the air and the smectic (Eq. 1.2). The critical radius was determined by successive steps via the nucleation of different-sized loop. A drawback of this technique is that it is only compatible with thick films where the dislocations line tension is independent of the thickness.

Géminard et al. [1998] reported another method inspired by sessile drop method used to measure the surface tension of a liquid Kwak et al. [2018]. The technique is based on the nucleation of different dislocation loop in a vertical film. The measurement of the shape anisotropy of the island when it is in contact with the top edge of the frame are linked directly to the line tension. This method has been very useful because it allowed to measure the dislocation line tension whatever the film thickness (Fig. 1.13).

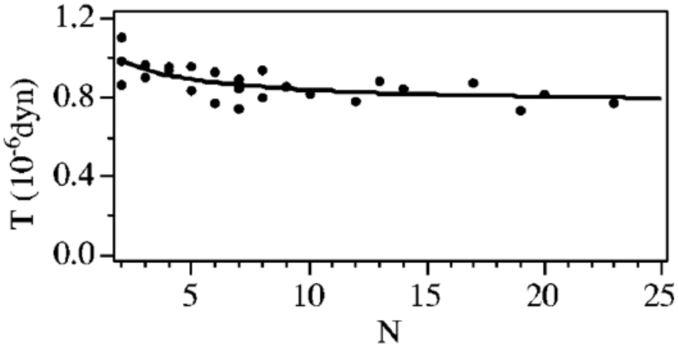

Figure 1.13 – Line tension as a function of the layers number N. Reprinted from Géminard et al. [1998]. Copyright (1998) by The American Physical Society.

1.3 Dynamics of Topological Defects in Liquid Crystals

1.3.1 Interaction between point disclinations

The presence of topological defects increases the energy of the liquid crystal film. In order to minimize the elastic distortion and to satisfy the zero total charge law, defects of opposite topological charge attract each other. Thus, a scenario of primary interest is the annihilation of the disclination pair.

Models for defect interactions were developed for nematic liquid crystals in the one-constant elastic theory Dafermos and Constantine [1970]; Minoura et al. [1997]. The simplest model assumes that the defects pass through quasi-equilibrium states, where the *director* field is taken as the linear superposition of the single defect equilibrium solutions of the *director* field (Eq. 1.10) Dafermos and Constantine [1970]. In a 2D planar nematic as the one shown in section.1.2.3, for two defects of topological charges S_1, S_2 and phases θ_1, θ_2, Eq. 1.10 implies that at positions $\vec{R_1} = (x_1, y_1)$ and $\vec{R_2} = (x_2, y_2)$, the *director* configuration around the pair is given by

$$\theta(\vec{r}) = S_1 \arctan\left(\frac{y-y_1}{x-x_1}\right) + S_2 \arctan\left(\frac{y-y_2}{x-x_2}\right) + \theta_\infty \tag{1.17}$$

θ is defined with respect to the *OX-axis* that joins the two defects. This solution is sketched in Fig. 1.14, for $S_1 = +1$ (left), $S_2 = -1$ (right) and $\theta_\infty = -\frac{\pi}{2}$ (the *c-director* angle at infinity).

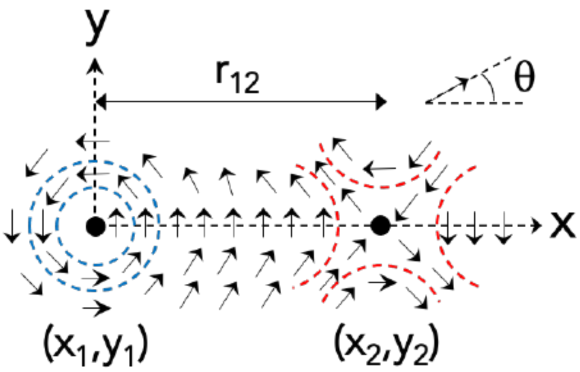

Figure 1.14 – Point defects with topological charges +1 (left) and −1 (right). θ is the *c-director* angle with respect the *OX-axis*, r_{12} is the defect separation distance.

The models assume that during their mutual interaction, the defects pass through quasi-equilibrium solutions of the type sketched in Fig. 1.14. This type of solution describes all defect pairs with "matched" orientations respective to each other. Geometrically, this implies that the *c-director* along the line connecting the two cores has a constant orientation. Thus, the defect pairs are expected to move towards or away from each other on straight paths along the *OX-axis* because any displacement far from this axis induces extra elastic deformation of the *director* field.

As shown in Eq. 1.11, the energy per film thickness for a pair of disclinations separated by a distance r_{12} is Dafermos and Constantine [1970]

$$E = \pi k(S_1 + S_2)^2 \ln(R/r_c) - 2\pi k S_1 S_2 \ln(r_{12}/2r_c) \tag{1.18}$$

If $S_1 = -S_2$, the first term in the energy equation is null. Only the second term remains, which is independent of R. The force between two disclination points, acting along the separation vector $\vec{r}_{12}$ is analogous to the force between two infinite line charges separated by r_{12}

$$F_{elastic} = 2\pi k S_1 S_2 / r_{12} \tag{1.19}$$

This force is inversely proportional to the separating distance r_{12}. Accordingly, disclinations of like signs repel and those of opposite signs attract each others on straight paths.

The defects motion is limited by the viscosity of the film, or the dissipation associated with *director* reorientation, and by the viscosity of the surrounding medium, which exerts a drag force on the defects during their motion. In the absence of material flow, this specific force (per film thickness) on a defect of topological strength S moving with velocity v in a film is Imura and Okano [1973]

$$F_{drag} = \pi \gamma_1 S^2 v \ln(L/r_c) \tag{1.20}$$

γ_1 is the rotational viscosity, v is the defect velocity and L is a characteristic system size. The issue with this equation is its logarithmic divergence with L, which requires the setting of a long-distance cut-off. Ryskin and Kremenetsky [1991] improved the previous equation for a defect moving in a finite liquid crystal film

$$F_{drag} = \pi \gamma_1 S^2 v \ln(3.6/E_r) \tag{1.21}$$

γ_1 is the rotational viscosity of the *c-director*, $E_r = \frac{\gamma_1 v r_c}{K}$ is the Ericksen number. Since the disclinations are immaterial objects, material transport is not included in this estimate. Hence, the shear viscosity is not included in the drag force equation.

Defects are expected to move with a velocity determined by the balance of the elastic forces that arise from the elastic deformation (Eq. 1.18) and counteracting viscous forces caused by *director* reorientation and possible coupling to material flow (Eq. 1.21)

$$v = \pm \frac{K}{\gamma_1 \ln(3.6/E_r) r_{12}} = \pm \frac{D_1}{r_{12}} \tag{1.22}$$

D_1 contains the elastic constant K and depends on the velocity of the defect via the Ericksen number. In approximation, it is considered as a diffusion coefficient. According to Eq. 1.22, two defects of opposite topological charges approach each other with a velocity inversely proportional to the separating distance r_{12}. Taking the derivative of $\dot{r}_{12} = 2v$, one determines the evolution of r_{12} with time as following

$$r_{12} = \sqrt{4 D_1 t} \tag{1.23}$$

Hence, during the annihilation of the defect pair, the separation distance r_{12} is expected to follow a square root of time dependence.

1.3.2 Dynamics of disclinations in nematic LCs

Pargellis et al. [1994] improved the quenching technique previously used to form random disclinations using by a well-defined homeotropic anchoring of the nematic *director*. The phase transition (T_c) was achieved by cooling one plate sandwiching the

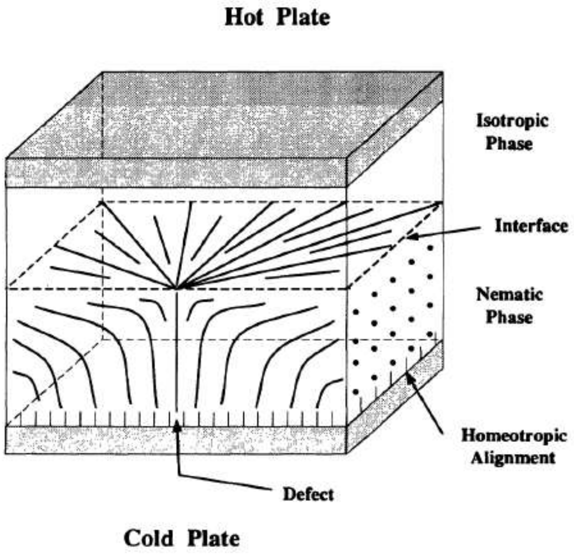

Figure 1.15 – Nematic *director* configuration showing an integer disclination in the middle plane between the cell plates. Reprinted from Pargellis et al. [1994]. Copyright (1994) by The American Physical Society.

nematic film below T_c and heating the other above T_c. Under these conditions, integer-strength disclinations are formed in the middle of the sample between the cell plates, i.e. at the nematic-isotropic interface (Fig. 1.15).

Minoura et al. [1997] studied the dynamics of pairs of disclinations with a strength of $S = \pm 1$ in a thermally quenched nematic liquid crystal. The effects of an electric field were also investigated. The author revealed the existence of time regimes in the annihilation process. When the separation distance between defects is large, r_{12} decreases linearly with time (Fig. 1.16). As the disclinations become too close, r_{12} decreases as a function of the square root of time. These results are in clear contrast with the usual square root of the time dependency predicted for the dynamics of long-distance as well as short-distance dislocations (Eq. 1.23). Pargellis et al. [1992] has interpreted these results by introducing the "ordering field" which causes a strain field between pairs of defects.

The authors also showed that the annihilation process becomes faster when an electric field is applied to the sample. The rate of annihilation was found to be proportional to the intensity of the applied field, the higher the electric field applied, the faster the annihilation process (Fig. 1.16). This result can be explained by the fact that the electric field changes the orientation of the director to a homogeneous state. This compresses the elastic deformations created by the presence of the defects, which accelerates their annihilation.

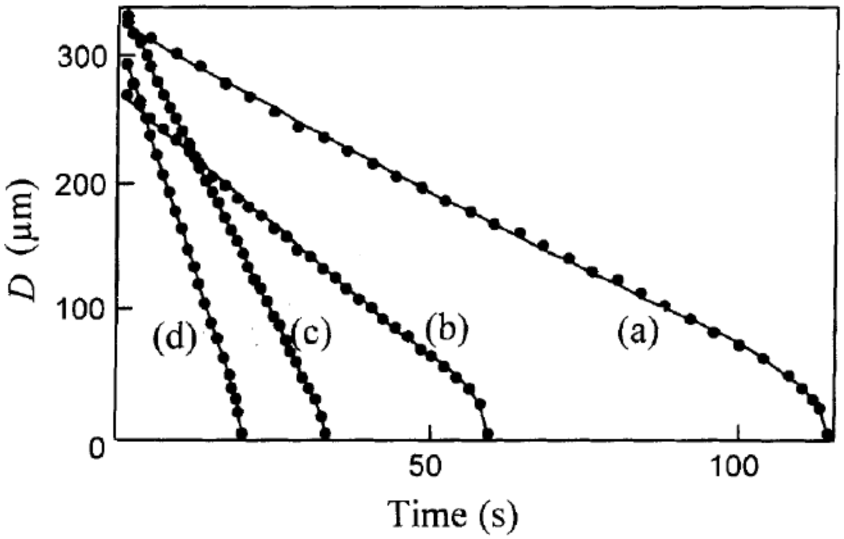

Figure 1.16 – The time dependence of the separation distance r_{12} with and without an applied electric field. (a) 0 kV/m, (b) 2 kV/m, (c) 6 kV/m and (d) 10 kV/m. Reprinted from Minoura et al. [1997]. Copyright (1997) by the Taylor & Francis.

More recently, Blanc et al. [2005] measured the annihilation of disclination pairs with topological charges $S = \pm 1/2$ induced by an electric field applied to the nematic cell. The author reported that during the annihilation process, the positive defects systematically move twice as fast as the negative ones (Fig. 1.17). This effect was attributed to the hydrodynamic flow in the nematic cell. When the defects move in a liquid medium (LC), the coupling between the rotation of the *director* and the velocity field, the so-called backflow, causes the symmetry to break.

However, research on the dynamics of disclination pairs in nematics has proven to be complicated to carry out. The influence of the boundaries of the thin cells encapsulating the nematic material in a two-dimensional system on the one hand and the three-dimensional nature of the deformations for the thick cells on the other hand play a crucial role on the dynamics of the disclinations Blanc et al. [2005]; Minoura et al. [1997]; Pargellis et al. [1992, 1994]. The hydrodynamic drag forces opposing the attraction between the defects proved to be related to the flow fields, which also complicates the system. Thanks to the 2D freely suspended *SmC* films geometry, analogous to 2D polar nematics, the dynamics of disclination points can be reduced to a two-dimensional problem without boundary effects, simplifying theoretical description and modeling.

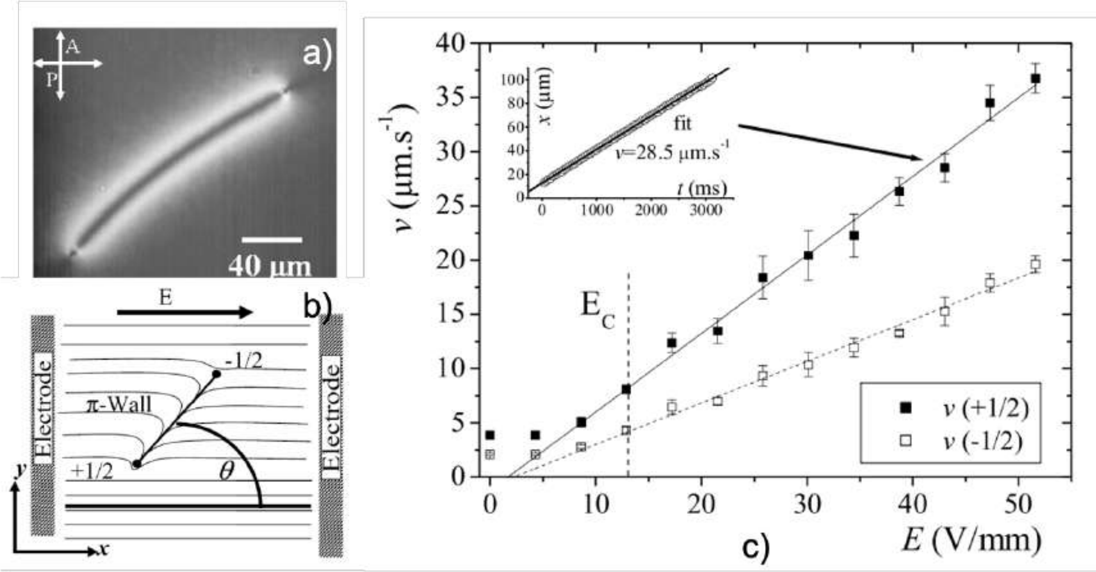

Figure 1.17 – (a) A pair of $\pm 1/2$ disclination pair in nematic cell separated by a π wall. (b) The nematic *director* field between the two plates. (c) The velocities of the defects depending on the electric field. The inset shows distance vs time for a $+1/2$. Reprinted from Blanc et al. [2005]. Copyright (2005) by The American Physical Society.

1.3.3 Dynamics of topological defects in freely suspended *SmC* films

Studies on topological defects in nematic liquid crystals are not easy to interpret because of the three-dimensionality of the geometric problem and the influence of the cell boundaries. Since nematic films are not stable enough, they cannot form freely suspended 2D films. However, stable thin films of *SmA* or tilted *SmC* phases can be prepared. The latter can be treated as an equivalent of a 2D polar nematic. The simplicity of optical observations is another additional value of this thin-film geometry. When *SmC* freely suspended films are observed using a polarized optical microscopy, the characteristic optical textures reflect the local *c-direction* orientations, where the type of defect and position can be easily determined.

During our study, we focus on freely suspended *SmC* films in order to study a variety of dynamics and properties of topological defects in reduced dimensionality.

1.4.2.1 Dynamics of disclinations

Disclinations are defect lines perpendicular to the normal layers, but since freely suspended *SmC* films can be considered as 2D nematics, the disclinations can be treated as defect points. Numerical models for pair annihilation have been extended from nematics to *SmC* films Svenšek and Zumer [2003]. The models predict an asymmetry in the defect motion. The positive disclination is predicted to move faster than the negative one due to the effects of viscous flow fields and elastic anisotropy. On the other hand, it has also been shown that the annihilation process is expected to be faster than that predicted by the classical model Svenšek and Zumer [2003]. In order to verify these predictions, experiments on the dynamics of topological defects in freely suspended *SmC* films are required.

Topological defects can exist when the deformations of the *c-director* are very strong. Clark et al. [2017]; Radzihovsky et al. [2017] reported that when a smectic film is suddenly disturbed, i.e. by a sudden air flow causing complex shear flow patterns in the film plane, topological defects may form. Disclination points have also been created in very thick freely suspended *SmC* films ($10-40\ \mu$m) at the phase transition from *SmA* to *SmC* Pargellis et al. [1992]. This technique used to generate disclinations is quite complicated due to the difficulties in avoiding spatial temperature inhomogeneities during phase transition, which can induce Marangoni flow effects, and advection phenomena Trittel et al. [2019].

An example of the annihilation of a pair of dislocations of opposite charges $S = \pm 1$ is shown in Fig. 1.18a. The texture observed between the pairs of defect was of an unusual appearance compared to those found by other authors Minoura et al. [1997]. The *c-director* distortions were located in narrow walls. The authors reported that arrays of layer dislocations that exist in such thick films acted as an external electric field. They tend to compress the distortion connecting the defects to a narrow wall, thus reducing wall length and energy, which changes the defect dynamics qualitatively. They showed that the separation r_{12} between the defects scale linearly with time at long distance and decreases as the square root of time at small separation (Fig. 1.18b). Although these results are in agreement with the results reported for the nematics Minoura et al. [1997], they are still in clear contrast with the classical model which predicts a dependence of the square root of time on the separation distance at long distance as well as at short distance (see section.1.3.1).

Muzny [1994] and Wachs [2014] have studied the dynamics of oppositely charged, $S = \pm 1$ disclinations in thin freely suspended *SmC* films. The defects were induced by the mechanical deformation of the film by air pumping. The quick depression induces a transition to the *SmA* phase and relaxation to the *SmC* phase creates disclinations.

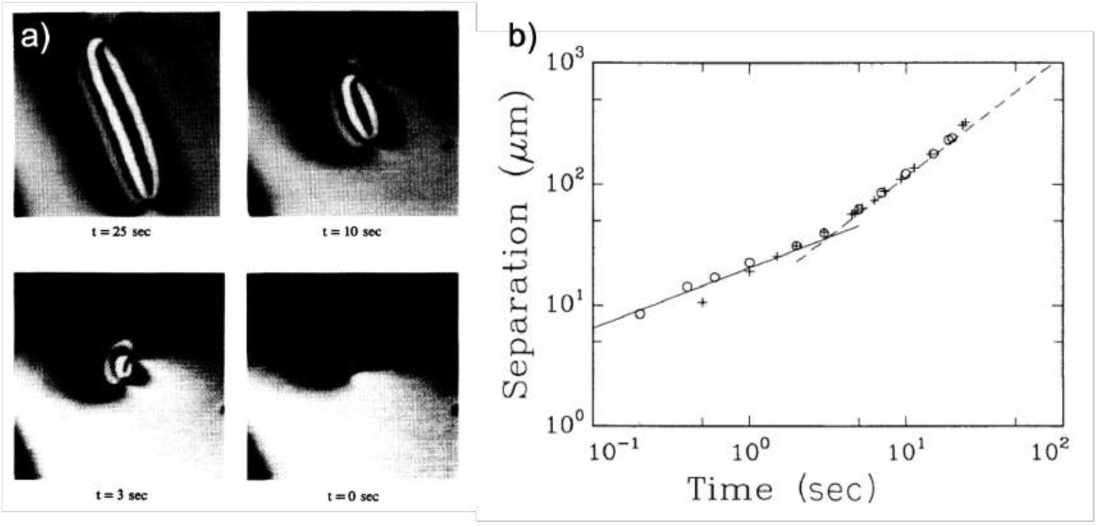

Figure 1.18 – (a) Coalescing ±1 disclination pair created at the SmA-SmC phase transition in freely suspended film. (b) Separating distance between the defects as a function of time, presented in the log-log scale. Reprinted from Pargellis et al. [1992]. Copyright (1992) by The American Physical Society.

The number of defects produced was found to be proportional to the volume of air pumped and the speed at which the film is released. Muzny and Clark [1992]; Wachs [2014] reported that the separation distance r_{12} as a function of time fit well to classical model for some pairs of defects (Fig. 1.19a) but for other pairs, they deviated from the predictions at small separation distances (Fig. 1.19b).

Such an experiment is delicate because the film could break if the initial deformation is too high, whereas a too small deformation does not induce any defect. In addition, the speed of the defects remains unchecked due to the observed drift motion of the disclinations in the film, which may be caused by external airflow perturbations.

More recently, Stannarius and Harth [2016] have developed a technique to capture high-strength disclinations in localized traps in *SmC* freely suspended films. The stripe textures shown in Fig. 1.20 are carrying +1 disclinations at their tips (white dots). These positive defects are found to repel each other until they reach the meniscus, which is in agreement with the expected force between two singularities of same sign (Eq. 1.18). The trajectories of the inclinations were used to determine the interaction potentials. It was shown that the displacement scales with square root of time. On the other hand, the experimental results reveal some limitations with respect to classical defect interaction models. Some disclinations were found to move more slowly than others. The authors attributed this discrepancy to differences in defect interaction forces. The inter-

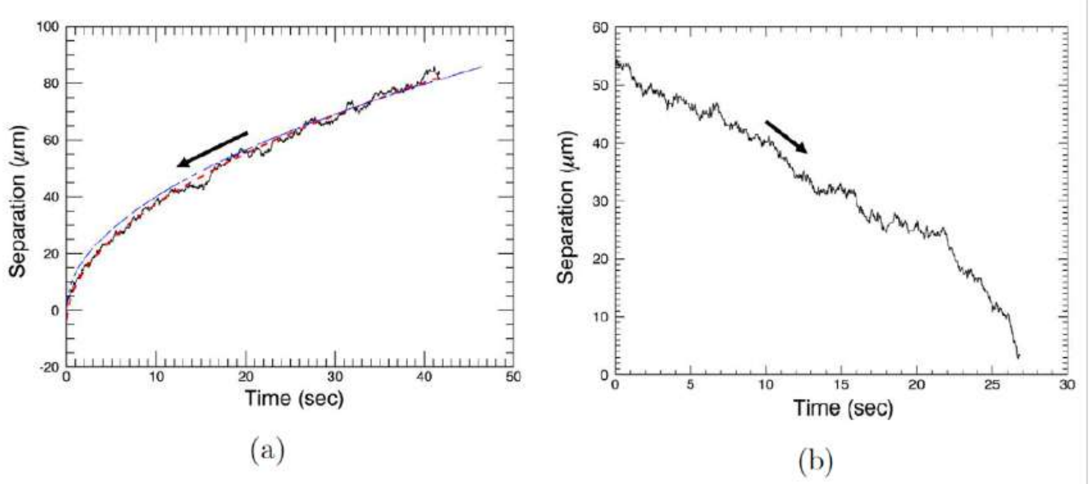

Figure 1.19 – Separation distance r_{12} as a function of time for different set of disclination pairs. Reproduced from Wachs [2014].

action equation (Eq. 1.19) must therefore be corrected.

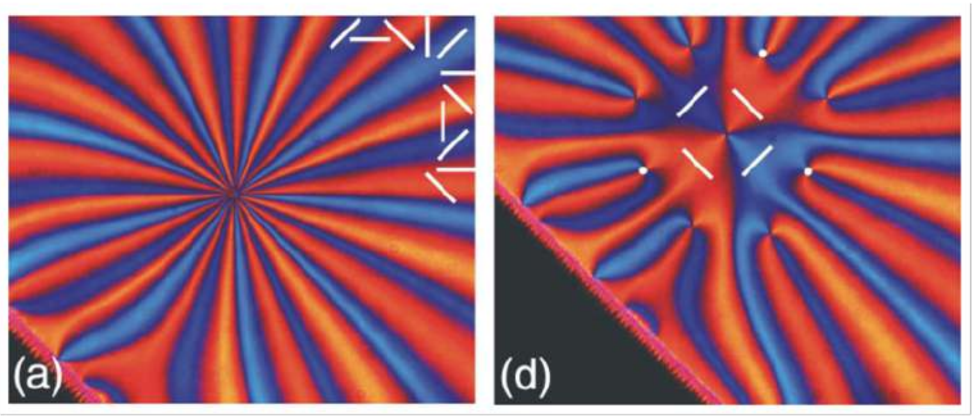

Figure 1.20 – (a) Nine trapped defects in freely suspended *SmC* film. (b) The same region of the film observed 5 s later. The white line indicates the *c-director* orientation, while the white dot shows some selected defect positions. Reprinted from Stannarius and Harth [2016]. Copyright (2016) by The American Physical Society.

In conclusion, the process of annihilation of pairs of topological defects has not been studied so far in freely suspended *SmC* films. All the work cited above shows a limitation of the classical model which is sometimes related to the geometry of the system where the defects are created. Several properties predicted by the classical models are still not verified in thin freely suspended *SmC* films, for example the velocity and trajectories of the defects on the one hand and the square root of time law on the other hand.

1.4.2.2 Dynamics of dislocations

Holes and islands are bounded by dislocation loops connecting them to the background film. These topological defects are responsible for the growth or shrinkage of these structures. Their dynamics has been investigated by Oswald and Pieranski [2006] in *SmA* films, where they showed that it depends on several factors. The variation of the free energy during the motion of a dislocation, of a Burgers vector $\vec{b}$ and a radius r, nucleated in a film of N layers is given by Oswald and Pieranski [2006]

$$\Delta F = -\pi r^2 b \frac{\gamma}{R} + \pi r^2 (f(Nd - b) - f(Nd)) + 2\pi r E_{disloc}. \tag{1.24}$$

The first term gives the global variation of the surface energy of the system. γ is given by Eq. 1.2, where the pressure difference ΔP tends to enlarge the dislocation size. The second term corresponds to the variation of the energy of the film by considering the interaction between the free surfaces (islands and film). The last term corresponds to the line energy of the dislocation, where E_{disloc} is the line tension, which tends to reduce its size.

Oswald and Pieranski [2006] have determined the equation for predicting the growth dynamics of a dislocation loop in a smectic film with a critical nucleation radius, r_c, as the following

$$\frac{dr}{dt} = m\Delta P \left(1 - \frac{r_c}{r}\right), \tag{1.25}$$

where m is the mobility of the dislocation in an infinite environment determined by the shear viscosity μ parallel to layers and the permeability λ_p of layers by $m \approx \sqrt{\lambda_p / \mu}$.

The evolution of the radius *r(t)* of the dislocation loop can be given by the first integral of Eq. 1.25 as Oswald and Pieranski [2006]

$$r - r_i + r_c \ln \left|\frac{r - r_c}{r_i - r_c}\right| = m\Delta P\, t, \tag{1.26}$$

where r_i is the initial radius of the dislocation.

Oswald and Pieranski [2006] experimentally studied the dynamics of dislocation loops around holes in freely suspended *SmA* films. Fig. 1.21 shows that below the critical radius r_c, the dislocation loop shrinks and the hole disappears. When the initial hole radius is larger than r_c, the latter grows to reach the meniscus, which induces an overall change in film thickness by one layer or more.

Unlike the smectic holes which can grow or shrink depending on their initial radius, smectic islands can only shrink. This can also be deduced from the Eq. 1.16, where for

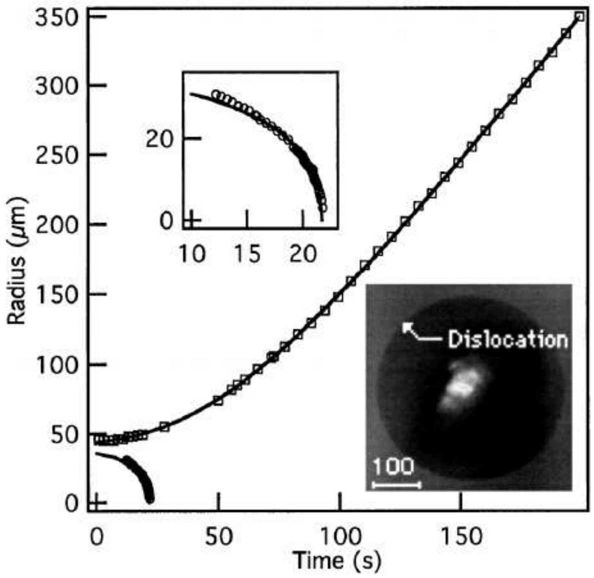

Figure 1.21 – Experimental determination of the radius of the dislocation loop of the smectic hole. Solid curves are fitting of the experimental data by the theoretical prediction (Eq. 1.25). Reprinted from Oswald and Pieranski [2006].

an island, the surface energy ($b\Delta P$) increases and the dislocation loop tends to shrink because its growth is always energetically unfavorable. Experimental studies have been carried out on the dynamics of islands in freely suspended *SmA* films (8CB). Dolganov et al. [2017] showed that the dislocation dynamics leads to the collapse of islands. It has been reported that for a film of homogeneous thickness, the thick islands (of large Burgers vector $\vec{b}$) shrink more slowly than the thin ones.

The author also reported that islands can interact with each other. A remarkable change in the disclinations dynamics behavior was observed when two islands are adjacent to each other. The material from the thin island is found to be displaced to the thick one. When the smallest island totally collapses, the thick one starts to decrease by transferring the material to the meniscus.

To conclude, the presence of islands and holes disturbs the mechanical equilibrium between the freely suspended smectic film and the meniscus. They create a flow of material from the film to the meniscus. Their dynamics is well described by theoretical models Oswald and Pieranski [2006].

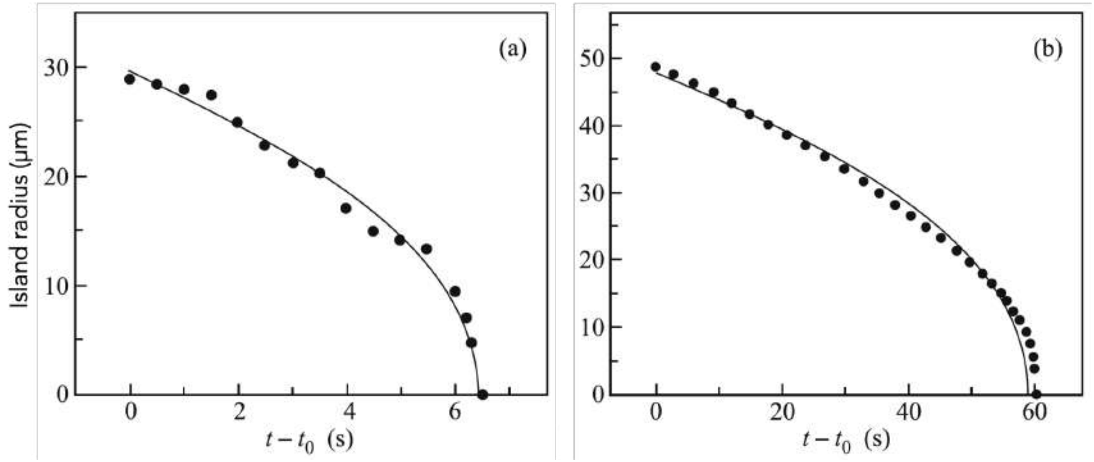

Figure 1.22 – Experimental determination of the dislocation loop radius. Islands with a thickness of (a) 7 and (b) 8 smectic layers. Reproduced from Publication Dolganov et al. [2017]. Copyright (2017), with permission from Springer Nature.

1.3.4 Summary

Topological defects occur in a wide variety of physical systems. Many features of defect dynamic properties are universal. In LCs, they can be observed in facile polarizing microscopy experiments, with comparably simple equipment. Nevertheless, experiments with liquid crystals in sandwich cells are not easy to interpret because of the three-dimensionality of the geometric problem. Defects, even if they are well-localized in the cell mid-plane, usually extend from one glass plate to the other Pargellis et al. [1994]. Interactions with boundaries, such as pinning, and a preferential alignment or 3D *director* field distortions near the cell walls have to be taken into account.

The elementary process of pair annihilations of topological oppositely-charged defects allows one to construct scaling solutions for more complex defect patterns Chuang et al. [1991a]. Even though not all results obtained from 2D LC systems can be generalized to 3D geometries, the obvious value of such studies is twofold: Several other systems that develop topological defects, e.g., thin magnetic films, are also 2D, and the scaling of pair annihilation dynamics is independent of the dimensionality of the problem Hertel and Schneider [2006]; Rissanen and Laurson [2016]; Wachowiak et al. [2002]. We have thus decided to concentrate on *SmC* freely suspended films to study the dynamics of topological defects.

In *SmC* freely suspended films, the dynamics of dislocation loops is well described by the models developed so far Oswald and Pieranski [2006]. Even though, the model for the dynamics of defect points has been developed through a continuum theory Oseen [1933], little has been done to experimentally examine the dynamics and structure of point defects and their mutual interactions in *SmC* freely standing films Muzny [1994]; Muzny and Clark [1992]; Stannarius and Harth [2016]; Wachs [2014], have performed measurements suggesting that still some discrepancy could be identified with the classical models Muzny and Clark [1992]; Stannarius and Harth [2016]; Wachs [2014]. Moreover, some hydro-dynamical predictions still need to be confirmed in order test the theoretical models and their predictions Harald [1988]; Radzihovsky [2015]; Svenšek and Zumer [2003].

In the second chapter, we review the interactions and dynamics of topological defects in liquid crystals in quasi-two-dimensional geometries. We will show that well-defined and isolated defect pairs can be created using simple mechanical techniques. We investigated their dynamics and we compared it to existing theories. In addition to the experimental characterization, an analytical and numerical description was developed. Finally, we will propose new corrections to the classical models, which have been neglected in the previous studies.

Even though models for the hydrodynamics of topological defects in LC have been developed for a few years Svenšek and Zumer [2003], few experiments have been carried out to test the effects of backflow, with non in freely suspended smectic film. In the third chapter, we focus on the annihilation of opposite-charged disclinations in freely suspended smectic films with a full backflow coupling study.

1.4 Liquid Crystals in Micro-Gravity

1.4.1 Introduction to micro-gravity

Gravity is the force that governs movement all through the universe. It holds us to the ground, and it keeps the moon in orbit around Earth and Earth in orbit around the sun. It is an attractive force, which is always present between two objects that have a mass.

However, we can make conditions in which we don't encounter the impacts of gravity. A first way to "get rid" of gravity is: "free fall"! Objects in a state of "free fall" are said to be weightless. For scientific experiments, a variety of facilities to create micro-gravity conditions exists (Fig. 1.23). The drop tower is a huge tower, some 150 m high. The experiments are dropped from the upper end of an enclosed metal tube of 3 m diameter. The experiment, and everything inside it, is in "micro-gravity" as it falls for around four seconds until it hits a bed of foam flakes. The experiment thus needs to endure such accidents. Another famous way to get rid of gravity is the use of aircraft flying in parabolic arcs allowing to create micro-gravity conditions for tests and simulations that last 20-25 seconds. During the parabola, people and objects inside the airplane are in "free fall". This technique will be discussed in details in the next section. A third way to achieve "free fall" is to place the experiment into orbit such as in International Space Station (ISS). In this way, an object in "free fall" circling the Earth at the perfect speed (27850 km/h) and height can seem weightless. This is the situation with the ISS. It is the largest manufactured object that revolves around the Earth. The ISS represents a unique testing ground for life and matter sciences in micro-gravity but is also a platform for observing Earth and universe.

In our research, we use micro-gravity for the study of fluid dynamic behavior in reduced dimensionality, and for the exploration of fundamental non-equilibrium fluid interfacial phenomena. Spherical freely suspended smectic liquid crystal bubbles can be made with a very small ratios of film area to perimeter, yielding systems in which coupling to bulk fluid is extremely weak or nonexistent. In my PhD, I have performed experiments utilizing micro-gravity conditions achieved by parabolic flights.

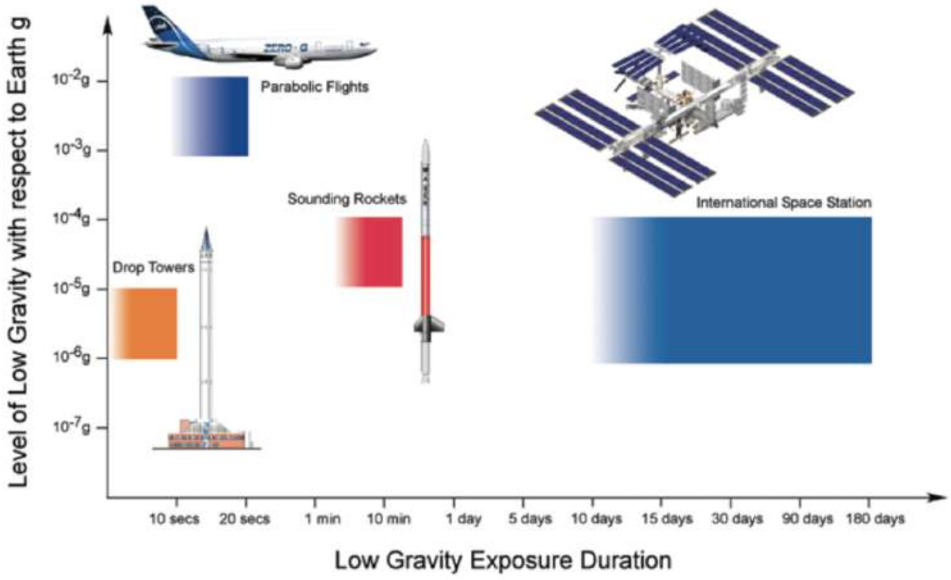

Figure 1.23 – Low gravity magnitude and duration for the four low gravity platforms. Image reproduced from The European Space Agency (ESA) website.

1.4.2 Parabolic flight

Parabolic flights have been successfully used to improve knowledge of aeronautical medicine, to study the effects of weightlessness in preparation for the first human explorations of space, to train astronauts, and provide a weightless platform for the scientific community. The use and development of this type of flight has been closely linked to space exploration. The beginning of the parabolic flight goes back to 1950, when two scientists, Fritz Haber and Heinz Haber, publish a theory to reproduce weightlessness conditions on board of an aircraft whose trajectory describes a parabola Haber and Haber [1950]. It took only one year then to start experimental tests. Nowadays, many organizations like NOVESPACE are operating their own airplane for public parabolic flights.

A parabola is a trajectory that allows to subject an object to weightlessness. This is the principle of sounding rockets and parabolic flights. With this particular trajectory (Fig. 1.24), all objects and persons present in the plane will be in a weightless state. Lift is the aerodynamic force of air on the wings and fuselage of the aircraft that maintains the aircraft in flight. This force is partially reversed by tilting the aircraft at a certain angle of flight. The drag is also an aerodynamic force that cannot be undone but will be compensated by the thrust of the aircraft's engines. The specific flight operations cancel all the forces due to the friction of the air on the aircraft which is then subjected only to gravity and will therefore be weightless. From a stabilized horizontal flight altitude of 6100 m, one of the pilots gradually increases the aircraft's bank to an angle of 50° attitude. During this phase, the apparent weight of the aircraft and its occupants is 1.8 times higher than normal weight: a vertical load factor of 1.8 g applies. The crew then carries out an injection : the aircraft is flown in such a way as to follow a trajectory describing approximately a parabola and the engine power is reduced. The vertical load factor of the aircraft is decreased from 1.8 g to 0 g. This load factor change is not instantaneous and lasts less than 5 seconds. This input resource phase takes approximately 24 seconds. The aircraft is in the micro-gravity phase for approximately 22 seconds. An exit phase at 1.8 g, symmetrical to the entry phase, is then performed on the descending part of the parabola to bring the aircraft back into stabilized horizontal flight for about 20 seconds. The experimenters then have about 1 minute and 40 seconds minimum before the next parabola. During a parabolic operation, the residual gravity level for any object attached to the aircraft structure normally varies between $\pm 2.10^{-2}$ g on the Z (vertical) axis, and between $\pm 10^{-2}$ g on the X (longitudinal) and Y (transverse) axes of the aircraft. Standard parabolic flight campaigns include 3 flights of 31 parabolas over 3 days. The duration of such flight is three to five hours maximum. The 31 parabolas are divided into 6 sets. The duration between sets of parabola varies between 5 and 8 minutes, allowing experimenters to modify and adjust their experiments.

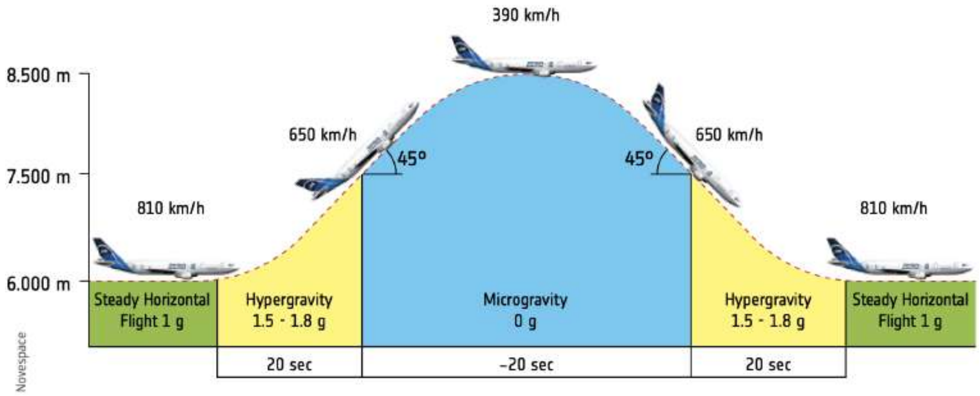

Figure 1.24 – Parabolic flight manoeuvre profile. Image reproduced from The European Space Agency (ESA) website.

During our participation at the CNES parabolic flight campaign (PFC) VP153 and VP154, the flights operations were carried out with an aircraft called the NoveSpace

A310 ZERO-G.

1.4.3 Freely suspended smectic films in micro-gravity

The vast majority of experiments in freely suspended smectic films have historically been performed with films with planar geometry using planar supports resulting in thin freely suspended films bound by a meniscus, connecting the film with the holder. The meniscus can exchange material with the film, for instance, for islands and holes generation or shrinkage. This exchange as we will show later has a considerable impact on the film and islands dynamics, it impacts the movement and advancement of inclusion in the meager films, influencing their structure and development. There have been numerous experiment to minimize the impacts of the meniscus or even to get rid of it Stannarius and Cramer [1998]Harth et al. [2019]. One example is to limit the length of the film boundaries by blowing the films in a circular shape, either supported on an in inflation tube or floating freely. In this non-planar geometry, any inclusion in the film, especially in the *SmA* and *SmC* phases, will be susceptible to sedimentation affected by gravity attraction. Only micro-gravity conditions avoid sedimentation and improve the long-term investigation of the generation or motion of smectic bubbles.

The smectic film is surrounded by air or some other fluid, motion in the film plane couples strongly to the environment. Due to the momentum exchange between the film and the embedding fluid, the flow in the film displays features of both 3D and 2D hydrodynamics. Thus, a smectic film surrounded by a 3D viscous medium, and containing inclusions such as islands or particles, represents an opportunity to explore hydrodynamics in restricted geometries. Several researchers have developed a variety of micro-gravity applications of thin liquid crystal films to study fluid structure and hydrodynamic problems in 2D and quasi-2D systems Dähmlow et al. [2018]; Harth et al. [2019]; Klopp et al. [2019]; May et al. [2012]; Stannarius et al. [2019]; Trittel et al. [2019]. Freely suspended smectic films in micro-gravity (Fig. 1.25) help for the study of fluid dynamic and thermodynamic behavior in reduced dimensionality, and for the exploration of fundamental non-equilibrium fluid interfacial phenomena Clark et al. [2017].

Another motivation to avoid gravity is to improve the investigation of films under non-isothermal conditions. Within the sight of gravity, temperature gradient will fundamentally prompt lightness driven air convection Stannarius et al. [2019]. Since the

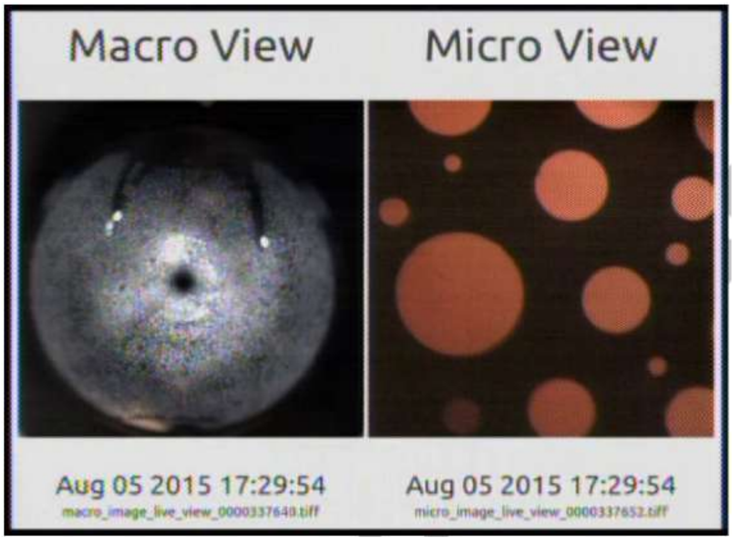

Figure 1.25 – Typical macro- and micro-views of the smectic bubble experiment showing smectic islands on a thin background film. Reprinted from Publication Clark et al. [2017]. Copyright (2017), with permission from Elsevier.

films are so thin, airflow will promptly advect the film material. Accordingly, any flow in a uniformly thin smectic film is basically confined to the layer plane Picano et al. [2000]Oswald and Pieranski [2006] Basic pumping of the film chamber does not solve this issue, in light of the fact the film establishes thermal equilibrium with the environment by irradiation losses, independent of the nearby warm limit conditions forced by the experimenter.

In my PhD, I have performed experiments to study fluid dynamics behavior in freely floating *SmC* bubbles. Under normal gravity conditions, the bubbles leave the field of view of the optical microscope rather fast as they are attracted by gravitational forces. Experiments were thus carried out in micro-gravity condition during CNES parabolic flights campaign at NOVESPACE (Bordeaux, France).

1.5 Structure of the manuscript

During this thesis, we focus on three main topics with flat and curved freely suspended smectic films. Investigations of these field will allow us to learn about defect pattern formation, their dynamics, hydrodynamics and behavior of the so-called smectic island during the relaxation of smectic bubbles. Even though, the three topics are based on the use of smectic liquid crystals, the results may be generalized for many other different fields. I have thus tried in the following to allow for possible separate reading of the three parts of the manuscript.

Dynamics of topological defect in freely suspended smectic films

Freely suspended smectic films represent a stable peculiar form of anisotropic fluids. Even though, the properties of such 2D structure has been widely investigated, studies on the dynamics of disclinations in freely suspended film received less intention also because formation of isolated pairs of point like defect in such film geometry remained challenging. In the second chapter, I report an experiment and theoretical study of the dynamics of topological defects in freely suspended *SmC* films.

Hydrodynamics of topological defect in freely suspended smectic films

A peculiarity of the liquid crystal is the hydrodynamics coupling of a nonuniform *director* reorientation to material flow. Therefore, the disclination motion is affected by such phenomenon. During the third chapter, we will focus on the hydrodynamics of opposite-charged disclination pairs in freely suspended *SmC* films.

Dynamics of smectic islands in freely floating smectic bubbles

Similar to freely suspended smectic films, freely floating smectic bubbles represent an exciting frame for investigation of topological defect dynamics and thin fluid film behavior. While smectic bubbles are drawn in a similar way than soap membranes, their hydrodynamics is quite different. The properties of the internal smectic structure play an important role Harth et al. [2019] in the relaxation dynamics of smectic membrane. In the last chapter, we investigate the behavior of smectic islands created in bubbles during the shape relaxation from strongly distorted non-equilibrium shapes to the spherical equilibrium. We demonstrate that at extreme condition, smectic material behave similarly to thin elastic sheet.

1.6 References

Bahr, C. (1994). Influence of conditionality and surface ordering oh phase transition: studies of freely-suspended liquid-crystals films. *International Journal of Modern Physics B*, 08(22):3051–3082. 8

Blanc, C., Svensek, D., Zumer, S., and Nobili, M. (2005). Dynamics of nematic liquid crystal disclinations: The role of the backflow. *Physical Review Letters*, 95:097802. 24, 25

Bohley, C. and Stannarius, R. (2007). Colloidal inclusions in smectic films with spontaneous bend. *The European Physical Journal. E*, 23(1):25—30. 8

Chuang, I., Durrer, R., Turok, N., and Yureke, B. (1991a). Cosmology in the laboratory: Defect dynamics in liquid crystals. *Science*, 251(4999):1336–1342. 9, 13, 31

Chuang, I., Turok, N., and Yurke, B. (1991b). Late-time coarsening dynamics in a nematic liquid crystal. *Phys. Rev. Lett.*, 66:2472–2475. 13

Clark, N. A., Eremin, A., Glaser, M. A., Hall, N., Harth, K., Klopp, C., Maclennan, J. E., Park, C. S., Stannarius, R., Tin, P., Thurmes, W. N., and Trittel, T. (2017). Realization of hydrodynamic experiments on quasi-2d liquid crystal films in microgravity. *Advances in Space Research*, 60(3):737 – 751. 26, 36, 37

Collings, P. J. and Goodby, J. W. (2017). *Introduction to liquid crystals: chemistry and physics*. Taylor and Francis. 2

Conradi, M., Ziherl, P., Sarlah, A., and Musevic, I. (2006). Colloids on free-standing smectic films. *The European Physical Journal. E, Soft Matter*, 20:231–6. 8

Dafermos and Constantine, M. (1970). Disclinations in liquid crystals. *The Quarterly Journal of Mechanics and Applied Mathematics*, 23(2):49–64. 20, 21

De Gennes, P. G. (1969). Conjectures sur l'état smectique. *J. Phys. Colloques*, 30(C4):C4–65–C4–7. 2

Dierking, I. (2003). *Textures of Liquid Crystals*. John Wiley and Sons. 4, 9, 12

Dolganov, P., Kats, E., and Dolganov, V. (2017). Collapse of islands in freely suspended smectic nanofilms. *JETP Letters*, 106:229–233. 30, 31

Dolganov, P. V., Shuravin, N. S., Dolganov, V. K., and Kats, E. I. (2020). Dynamics of island-meniscus coalescence in free-standing smectic films. *Soft Matter*, 16:8506–8511. 8

Dähmlow, P., Trittel, T., May, K., Harth, K., and Stannarius, R. (2018). Surface reduction of freely floating smectic bubbles. *Liquid Crystals*, 45(7):993–1003. 36

Even, C. and Pieranski, P. (1999). On "hearing the shape of drums": An experimental study using vibrating smectic films. *Europhysics Lett.*, 47(5):531–537. 7

Even, C., Russ, S., Repain, V., Pieranski, P., and Sapoval, B. (1999). Localizations in fractal drums: An experimental study. *Phys. Rev. Lett.*, 83:726–729. 7

Frank, F. C. (1958). I. liquid crystals. on the theory of liquid crystals. *Discuss. Faraday Soc.*, 25:19–28. 10

Friedel, G. (1922). Les états mésomorphes de la matière. *Annales de Physique*, 9(18):273–474. 2, 5

Geminard, J.-C., Holyst, R., and Oswald, P. (1997). Meniscus and dislocations in free-standing films of smectic-a liquid crystals. *Physical Review Letters*, 78:1924–1927. 7, 8, 19

Géminard, J.-C., Laroche, C., and Oswald, P. (1998). Edge dislocation in a vertical smectic-*a* film: Line tension versus film thickness and burgers vector. *Phys. Rev. E*, 58:5923–5925. 19, 20

Godfrey, M. I. and Winkle, D. H. V. (1996). Surface-tension-gradient-induced flow in freely suspended liquid crystalline films. *Phys. Rev. E*, 54:3752–3764. 8

Haber, F. and Haber, H. (1950). Possible methods of producing the gravity-free state for medical research. *Journal of Aviation Medicine*, 21(5):395–400. 34

Harald, P. (1988). Dynamics of a disclination point in smectic-c and -c liquid-crystal films. *Phys. Rev. A*, 37:3986–3992. 32

Harth, K., Eremin, A., and Stannarius, R. (2011). Vortex flow in free-standing smectic c films driven by elastic distortions. *Soft Matter*, 7:2858–2868. 11, 12

Harth, K., Trittel, T., May, K., and Stannarius, R. (2019). Dynamic wrinkling of freely floating smectic films. *Soft Matter*, 15:6769–6778. 36, 39

Hertel, R. and Schneider, C. M. (2006). Exchange explosions: Magnetization dynamics during vortex-antivortex annihilation. *Phys. Rev. Lett.*, 97:177202. 31

Iglesias, W., Choi, J., Mann, E. K., and Jakli, A. (2011). Freely suspended nematic films. page J9.005. 5

Imura, H. and Okano, K. (1973). Friction coefficient for a moving disinclination in a nematic liquid crystal. *Physics Letters A*, 42(6):403 – 404. 22

Klopp, C., Trittel, T., Eremin, A., Harth, K., Stannarius, R., Park, C. S., Maclennan, J. E., and Clark, N. A. (2019). Structure and dynamics of a two-dimensional colloid of liquid droplets. *Soft Matter*, 15:8156–8163. 36

Kraus, I., Bahr, C., and Pieranski, P. (1997). Mechanical properties of freely suspended smectic films. *J. Phys. II France*, 7(11):1617–1634. 6, 8

Kwak, W., Park, J. K., Yoon, J., Lee, S., and Hwang, W. (2018). Measurement of surface tension by sessile drop tensiometer with superoleophobic surface. *Applied Physics Letters*, 112(12):121602. 19

Lagerwall, J. and Scalia, G. (2012). A new era for liquid crystal research: Applications of liquid crystals in soft matter nano-, bio- and microtechnology. *Current Applied Physics*, 12:1387–1412. 14

Lehmann, O. (1889). Über fliessende krystalle. *Zeitschrift für Physikalische Chemie*, 4U(1):462–472. 2

Lejcek, L. and Oswald, P. (1991). Influence of surface tension on the stability of edge dislocations in smectic a liquid crystals. *J. Phys. II France*, 1(8):931–937. 18

Leslie, F. M., Stewart, I. W., and Nakagawa, M. (1991). A continuum theory for smectic c liquid crystals. *Molecular Crystals and Liquid Crystals*, 198(1):443–454. 11

Liang-shi, L., Joost, W., Liberato, M., and Paul, A. A. (2002). Semiconductor nanorod liquid crystals. *Nano Letters*, 2(6):557–560. 2

Loudet, J. C., Dolganov, P. V., Patrício, P., Saadaoui, H., and Cluzeau, P. (2011). Undulation instabilities in the meniscus of smectic membranes. *Phys. Rev. Lett.*, 106:117802. 7

Mach, P., Johnson, P. M., Wedell, E. D., Lintgen, F., and Huang, C. C. (1997). Layer compression in free-standing liquid-crystal films. *Europhys. Lett.*, 40(4):399–404. 6, 8

May, K., Harth, K., Trittel, T., and Stannarius, R. (2012). Dynamics of freely floating smectic bubbles. *EPL Europhysics Letters*, 100(1):16003. 36

Minoura, K., Kimura, Y., Ito, K., and Hayakawa, R. (1997). Dynamics of annihilation process of disclination pairs in nematic liquid crystals. *Molecular Crystals and Liquid Crystals Science and Technology. Section A. Molecular Crystals and Liquid Crystals*, 302(1):345–355. 20, 23, 24, 26

Mosley, A. (1993). Liquid crystal displays an overview. *Displays*, 14(2):67 – 73. 2

Muzny, C. (1994). Phd thesis. *University of Colorado at Boulder*. 26, 32

Muzny, D. C. and Clark, A. N. (1992). Direct observation of the brownian motion of a liquid-crystal topological defect. *Phys. Rev. Lett.*, 68:804–807. 27, 32

Oseen, C. W. (1933). The theory of liquid crystals. *Trans. Faraday Soc.*, 29:883–899. 32

Oswald, P. and Pieranski, P. (2006). *Smectic and columnar liquid crystals: Concepts and physical properties illustrated by experiments*. 2, 17, 18, 19, 29, 30, 31, 37

Pargellis, A. N., Finn, P., Goodby, J. W., Panizza, P., Yurke, B., and Cladis, P. E. (1992). Defect dynamics and coarsening dynamics in smectic-c films. *Phys. Rev. A*, 46:7765–7776. 23, 24, 26, 27

Pargellis, A. N., Green, S., and Yurke, B. (1994). Planar xy-model dynamics in a nematic liquid crystal system. *Phys. Rev. E*, 49:4250–4257. 22, 23, 24, 31

Picano, F., Hołyst, R., and Oswald, P. (2000). Coupling between meniscus and smectic-a films: Circular and catenoid profiles, induced stress, and dislocation dynamics. *Phys. Rev. E*, 62:3747–3757. 37

Picken, S. J., Sikkema, D., Boerstoel, H., Dingemans, T., and Zwaag, S. (2011). Liquid crystal main-chain polymers for high-performance fibre applications. *Liquid Crystals*, 38:1591–1605. 9

Pieranski, P., Beliard, L., Tournellec, J. P., Leoncini, X., Furtlehner, C., Dumoulin, H., Riou, E., Jouvin, B. B., Fenerol, J.-P., Palaric, P., Heuving, J., Cartier, B., and Kraus, I. (1993). Liquid crystals. *Physica A.*, 36(194):364–389. 7, 8

Radzihovsky, L. (2015). Anomalous energetics and dynamics of moving vortices. *Phys. Rev. Lett.*, 115:247–801. 32

Radzihovsky, S. P., Cranfill, C., Nguyen, Z., Park, C. S., Maclennan, J. E., Glaser, M. A., and Clark, N. A. (2017). Two-dimensional island emulsions in ultrathin freely-suspended smectic liquid crystal films. *Soft Matter*, 13:6314–6321. 26

Rissanen, I. and Laurson, L. (2016). Coarsening dynamics of topological defects in thin permalloy films. *Phys. Rev. B*, 94:144428. 31

Rowlinson, J. S. and Widom, B. (1984). Molecular theory of capillarity. *Clarendon Press, Oxford, 1982*, 88(6):586–586. 7

Ryskin, G. and Kremenetsky, M. (1991). Drag force on a line defect moving through an otherwise undisturbed field: Disclination line in a nematic liquid crystal. *Phys. Rev. Lett.*, 67:1574–1577. 22

Sirota, E. B., Pershan, P. S., Sorensen, L. B., and Collett, J. (1987). X-ray and optical studies of the thickness dependence of the phase diagram of liquid-crystal films. *Phys. Rev. A*, 36:2890–2901. 8

Stannarius, R. and Cramer, C. (1998). Self-supporting bubbles of thermotropic smectic liquid crystals. *Europhysics Letters*, 42(1):43–48. 36

Stannarius, R. and Harth, K. (2016). Defect interactions in anisotropic two-dimensional fluids. *Phys. Rev. Lett.*, 117:157801. 27, 28, 32

Stannarius, R., Trittel, T., Klopp, C., Eremin, A., Harth, K., Clark, N. A., Park, C. S., and Maclennan, J. E. (2019). Freely suspended smectic films with in-plane temperature gradients. *New Journal of Physics*, 21(6):063–033. 36

Svenšek, D. and Zumer, S. (2003). Hydrodynamics of pair-annihilating disclinations in smc films. *Phys. Rev. Lett.*, 90:155–501. 11, 26, 32

Trittel, T., Harth, K., Klopp, C., and Stannarius, R. (2019). Marangoni flow in freely suspended liquid films. *Phys. Rev. Lett.*, 122:234–501. 26, 36

Tsukada, T. (2000). *Active-Matrix Liquid-Crystal Displays*. Springer Berlin Heidelberg, Berlin, Heidelberg. 9

Tweet, D., Hołyst, R., Swanson, B., Stragier, H., and Sorensen, L. (1990). X-ray determination of the molecular tilt and layer fluctuation profiles of freely suspended liquid-crystal films. *Physical Review Letters*, 65:2157–2160. 6

Vertogen, G. and Jeu, W. H. D. (2012). *Thermotropic Liquid Crystals, Fundamentals*, volume 45. Springer Science and Business Media. 2

Wachowiak, A., Wiebe, J., Bode, M., Pietzsch, O., Morgenstern, M., and Wiesendanger, R. (2002). Direct observation of internal spin structure of magnetic vortex cores. *Science*, 298(5593):577–580. 31

Wachs, K. (2014). Dynamics of smectic-c point disclinations in freely-suspended liquid crystal films, bachelor thesis. *University of Colorado at Boulder*. 26, 27, 28, 32

Walker, D. B., Glytsis, E. N., and Gaylord, T. K. (1996). Ferroelectric liquid-crystal waveguide modulation based on a switchableuniaxial–uniaxial interface. *Appl. Opt.*, 35(16):3016–3030. 9

Young, C. Y., Pindak, R., Clark, N. A., and Meyer, R. B. (1978). Light-scattering study of two-dimensional molecular-orientation fluctuations in a freely suspended ferroelectric liquid-crystal film. *Phys. Rev. Lett.*, 40:773–776. 6

Chapter 2

Dynamics of Topological Defects in Freely Suspended Smectic Films

> *"(1) Recite in the name of your Lord who created (2) Created man from a clinging substance (3) Recite, and your Lord is the most Generous (4) Who taught by the pen (5) Taught man that which he knew not."*
>
> Quran - Al-Alaq

Contents

In this chapter, before describing and discussing the results, I describe the apparatus and techniques used to study the dynamics and interactions between topological defects in freely suspended *SmC* films. The chapter begins with a general introduction on disclinations in liquid crystals. Then, I present the LC material used in the experiments and the process used to draw the films and generate defect pairs. This is followed by a description of how to determine the film thickness. Later, I show the microscopic technique of depolarized reflected light that is used to visualize the *c-director*. Finally, I discuss the results on the dynamics of the defect pairs.

2.1 Introduction

Topological defects have been the subject of interdisciplinary physical research since they play an important role in determining the relationship between structure and properties of materials Jonathan [2016]. They occur in a wide variety of physical systems, for example, in soft matter Brugués et al. [2008]; Guimarães et al. [2013]; Muševič et al. [2006]; Muševič [2019]; Poulin et al. [1997]; Poulin and Weitz [1998]; Tkalec et al. [2011], quantum systems Polkovnikov et al. [2011]; Robert [2003]; Weiler et al. [2008], thin magnetic films Hertel and Schneider [2006]; Rissanen and Laurson [2016]; Wachowiak et al. [2002], super-fluid liquids Bäuerle et al. [1996]; Ruutu et al. [1996], and even cosmology Chuang et al. [1991]; Zurek [1996]. Often, complex defect patterns are generated after symmetry-breaking phase transitions. Their coarsening dynamics can be essential for the establishment of the new, ordered state.

Studies on the dynamics of topological defects in the nematic phase are complicated for several geometrical reasons that we have mentioned in the first Chapter, e.g. the influence of the cell boundaries and the 3D flow field. This also includes the complication of studying the dynamics of defects with integer topological charge. The presence of a +1 disclination is energetically unfavorable, hence it is splits into pairs of defects of strength $\pm 1/2$. On the other hand, the polar *c-director* in freely suspended SmC films can only form defects of integer strengths. It shares this characteristic with all other systems where vector field vortices are relevant (e.g., Hertel and Schneider [2006]; Wachowiak et al. [2002]).

In this study, we explore the dynamics of a pair of defects having the lowest possible integer topological charges in freely suspended *SmC* films, i.e., ± 1, during their mutual attraction and annihilation.

2.2 Experimental Setup

2.2.1 Stretching of smectic films

In order to form a freely suspended smectic film, the following procedure is used: first, two metal blades are brought into contact and then brushed with a small amount of thermotropic smectic material. Then the mobile slide is slowly moved. A freely suspended film is formed in the gap between the two slides. When this latter is stable, it is optically detected by a finite reflectivity. This method, inspired by the work of Oswald and Pieranski [2006], has the advantage that the width of the film, *W*, can be easily changed by simply opening or closing the mobile part. In order to achieve a controllable film thickness, a mechanically stable moving slide is required to ensure that the displacement is as smooth as possible. Indeed, as we will see in the next section, a change in the pulling speed can generate spontaneous thinning of the film or even break it. This requirement for mechanical stability during the film pulling process is satisfied in our system, in which the fixed parts are beveled at 45°, so as to form rails on which the mobile parts, themselves beveled in the same way, can slide in order to have notches suitable for mounting on the rails.

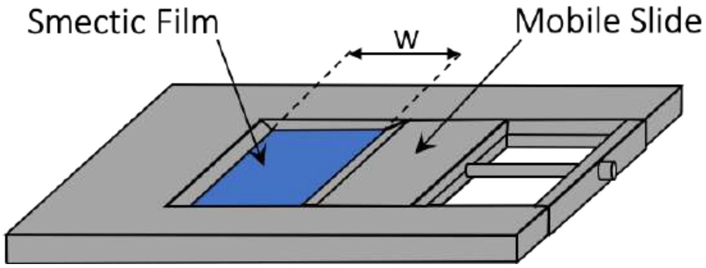

Figure 2.1 – Freely suspended smectic film formed between two mobile slides.

2.2.2 Liquid crystal material and microscope

We report observations in freely suspended films of a mixture of equal amounts of 5-n- octyle-2-[4-(n-hexyloxy)phenyl]pyrimidine and 5-n-decyl-2-[4-(n-octyloxy) phenyl] pyrimidine synthesized by SYNTHON Chemicals (Fig. 2.2). The room temperature

SmC phase is followed upon heating by SmA phase (T_{CA} = 52°C) and nematic phase (T_{AN} = 68°C) before the isotropic phase is reached (T_{NI} = 72°C). Films are drawn and observed at room temperature by means of polarized light microscopy in reflected light (Fig. 2.3). Their width can be manipulated by moving the mobile slide (Fig. 2.1); thereby, the film area can be rapidly changed. To avoid external disturbances that may affect the films, such as vibrations and air circulation, they are kept inside a closed box during the experiments.

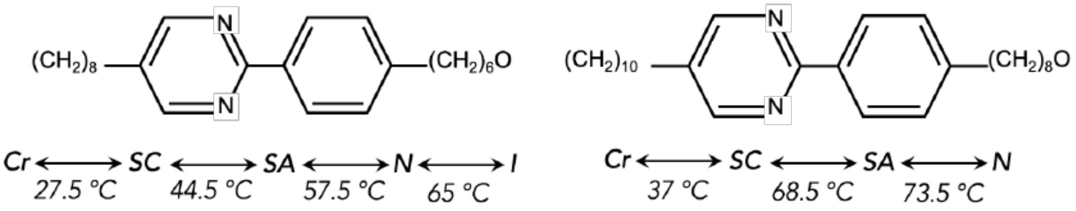

(a) (b)

Figure 2.2 – Characteristic proprieties of the two liquid crystal components (a) ST00552 and (b) ST00557. The diagram gives the phase transition temperature.

The film holder is mounted on the rotary stage of a Leica microscope. A Canon EOS 600D camera is mounted on the output port at the top of the microscope, which is equipped with different magnifications. Two frame rates were used to record the data of the experiments: either 30 frames per second (fps) at 1920 × 1080 pixels or 50 fps at 1280 × 720 pixels.

2.2.3 The film thickness measurements

Observations under the reflected light microscopy show that the final thickness of freely suspended *SmC* films is strongly dependent on what happens at the beginning of the stretching process (Fig. 2.4). When we start to open slowly the gap between the two slides, an initial germ[1] of the film appears. This small area is connected to the metallic frame through the meniscus (see section.1.1.4). If the stretching speed is slow and constant, the film thickness remains unchanged. However, in most cases, the speed is not strictly uniform, and thinner holes appear and extend along the film surface. This is why beautiful reflection colors appear (Fig. 2.4). They can be explained by the interference of the light reflected from the top and the bottom surface of the film.

---

1. A small region with a circular shape and a uniform thickness *h* that can goes from a few layers to several hundred.

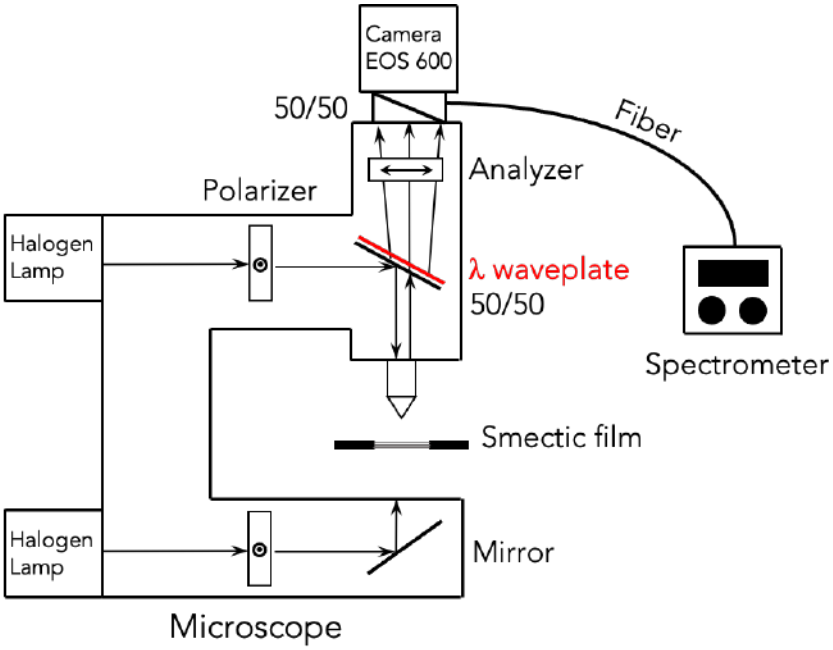

Figure 2.3 – The experimental setup showing the reflection microscopy for observing smectic freely suspended films. The film holder is mounted on a rotary stage.

Regions of different colors are separated by steps. Each step is a change of the thickness of the film by one or more layers.

The Michel Levy chart is used to estimate the film thickness with an accuracy of about 10 nm. However, the steps move towards the meniscus and the film tends to be homogeneous over time (see section.1.3.3). The final thickness of the film is that of the thinnest hole. The duration of the holes growth process depends on the thickness of the film, it can take hours for thin films and even days for very thick films. The film will be stable after this process and can remain for months if it is kept away from external disturbances such as air circulation or vibrations.

Quantitatively, the local film thickness is determined from the reflectivity $R(\lambda)$ in monochromatic light of wavelength λ. A photo-spectrometer is mounted on the output port on top of the microscope and connected to the computer (Fig. 2.3). We start by measuring the reflectivity spectrum of the monochromatic lamp as a function of wavelength using a mirror placed on the rotary table of the microscope. Then the film is illuminated in reflection mode and the reflected light spectrum is recorded. The local thickness of the film can be determined from the reflectivity $R(\lambda)$ using the equation

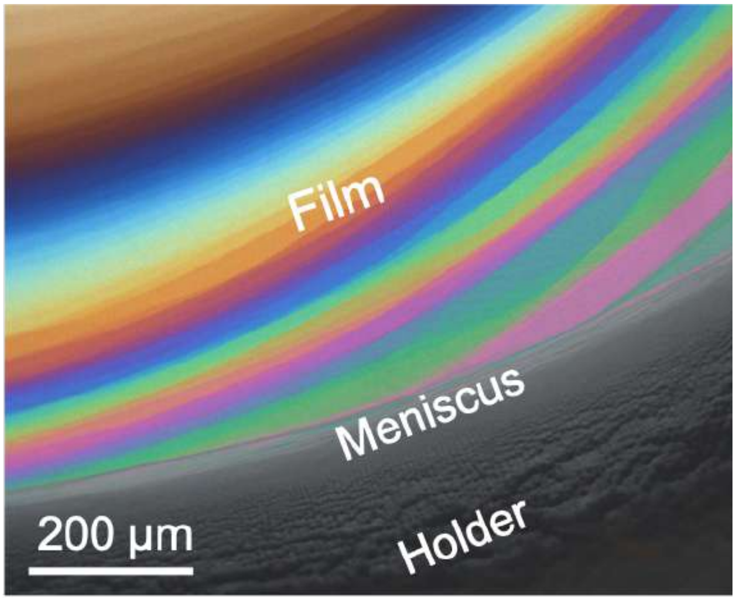

Figure 2.4 – Freely suspended *SmC* film observed under reflective microscope at room temperature. The colors reveal the difference of thickness between the film regions.

Rosenblatt and Amer [1980]:

$$R = \frac{2r^2(1 - cos2\delta)}{1 - 2r^2cos2\delta + r^4}, \tag{2.1}$$

r = (1-n)/(1+n) is a reflection coefficient related to the effective refractive index n. δ is the retardance which is equal to $\delta = 2\pi nMd/\lambda$ with M the layer number and d the layer thickness. In a *SmA* film, the refractive index n is equal to the ordinary refractive index, n_o. On the other hand, due to the molecules tilt, in a *SmC* film, the refractive index depends on the *c-director* orientation with respect to the polarization plane. It can vary between n_o and

$$n_{eff}^{max} = \frac{n_e n_0}{\sqrt{n_e^2 cos^2\theta + n_o^2 sin^2\theta}}, \tag{2.2}$$

n_e is the extraordinary refractive index. However, the exact effective refractive indices in the *SmC* phase of the materials we used is unknown. We assume an approximate refractive index $n_{eff} = 1.5$. We used a Matlab program [2] for the calculation of the final film thickness. In our experiments, the film thicknesses are of the order of 1μm, which corresponds to $M \approx 300 \sim 400$ layers.

---

[2] We thank Professor Eremin for the development of the Matlab code which allows us to estimate the thickness of freely suspended films.

2.2.4 C-director visualization and defect generation

In smectic liquid crystals, the index of refraction along the molecular long axis, n_e, is larger than the index in the perpendicular direction, n_o. The light intensity after going through a polarizer, the smectic film, and another crossed analyzer, relies upon the direction of the local molecules.

In a *SmA* freely suspended film, the *n-director* and the normally incident light beam are parallel. Hence, the films appear in dark. Whereas in a *SmC* film, the *n-director* is tilted with respect to the light beam. Thus, dark and bright regions appear depending on the local *c-director* orientation. The transmitted intensity reach the maximum when the *c-director* is aligned diagonal to the polarizers, and a minimum when it is aligned parallel to the polarizer or analyzer (See Fig. 2.5). However, the *c-director* can have an orientation either of 45° or 135° in bright regions. In most experiments, this ambiguity can be resolved by using a diagonally inserted proper phase plate (523 nm). When it is used, the local phase lag in the phase plate will be either additive or subtractive with respect to that of the film. Thus, different interference colors arise from regions with 45° or 135° orientations of the *c-director*. If the extraordinary component of the wave plate and the *c-director* are parallel, the total path difference is decreased, and the interference color goes downscale, perhaps to blue. If the ordinary component is perpendicular to the *c-director*, the interference color goes up to yellow. We show in Fig. 2.5 the *c-director* and the optical appearance when the film is observed between crossed polarizers and a diagonally inserted phase plate.

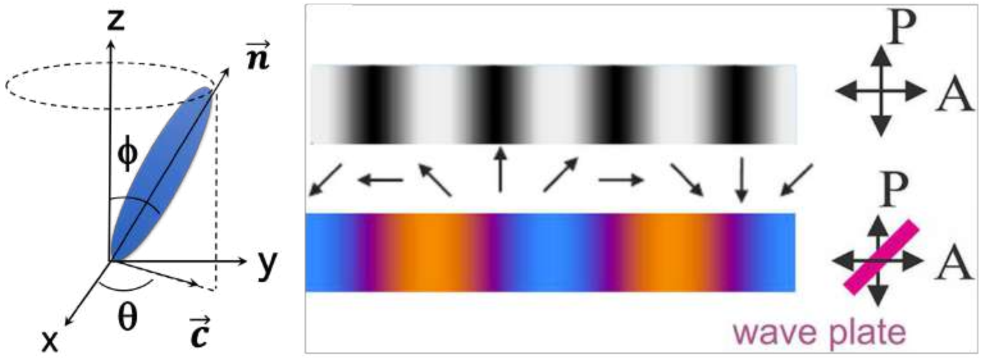

Figure 2.5 – C-director and optical appearance when the planar film is observed with crossed polarizers (top) and with crossed polarizers and diagonally inserted phase plate (bottom). The arrows give the $\vec{c}$ orientation. Figure reproduced from Harth and Stannarius [2020] Front. Phys. (2020), with authors permission.

Far from external disturbances (e.g. airflow), the *c-director* of *SmC* films tends to be uniform in order to reduce splay and bend deformations. However, if the film is disturbed, defects may be generated. In our experiment, disclinations are created in a homogeneous film by touching its surface with a hair-tip. At the point of contact with the circumference of the fiber, the film can enforce a preferential tangential anchoring of the *c-director*, i.e., a +1 defect. Consequently, a compensating nearby -1 defect is created to satisfy the net zero total charge as discussed in the first Chapter (See section.1.2.3). When the fiber is removed from the film surface, an isolated pair of ± 1 defects remains.

Fig. 2.6 shows the typical textures of a ± 1 topological defects pair observed between crossed polarizers with a diagonally inserted phase plate. The initial separation distance of the defects, r_{12}, is about 200 μm. At first glance, it seems difficult to differentiate between the two defects because they share the same four-branches structure. In fact, we can distinguish between the $+1$ and -1 defects by simply rotating the film with respect to the polarizers (and the phase plate). The positive defect possess a tangential configuration which is invariant to rotations (See Fig. 1.8c and Fig. 1.8d). Thus, the rotation of the film does not imply the rotation of the *c-director* with respect to the polarizers. Therefore, the colored branches around the $+1$ do not rotate during sample rotation. On the other hand, looking at the configuration of the *c-director* around the negative defect (Fig. 1.8e), we notice that the rotation of the film implies the rotation of the *c-director* with respect to the polarizers. Thus, the branches around the -1 defect rotate as we rotate the film. One should mention that we cannot make the difference between the clockwise/counterclockwise tangential and in/out-ward radial configurations of the +1 defect (See Fig. 1.8). However, these configurations could be distinguished by tilting the film with respect to the incident light beam along the axis 45° or 135° towards the polarizers. This tilt of the film will induce either an increase or decrease of the effective tilt of the *n-director* with respect to the incidence direction. Thus, regions with increased effective tilt appear brighter and those with decreased one appear darker.

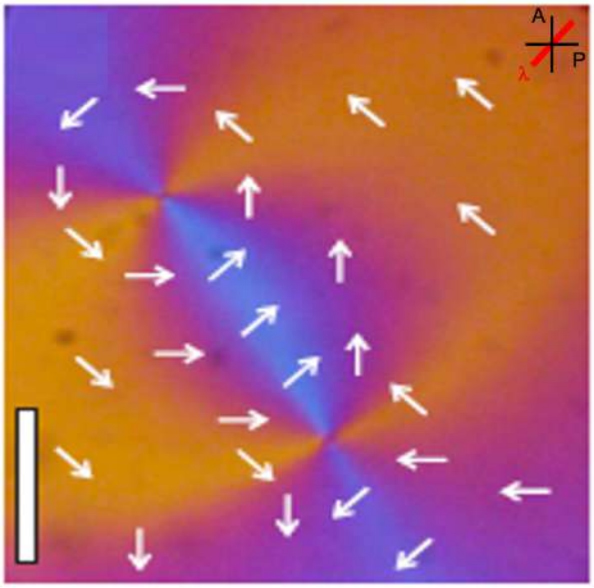

Figure 2.6 – Defect pair on the way to annihilation. White arrows sketch the *c-director* configuration. The $+1$ defect (top) and the -1 defect (bottom) about 21 seconds before the annihilation time. The white bar is 50 μm. Experimental data carried out by Peter Salamon. Reprinted from Missaoui et al. [2020]. Copyright (2020) by The American Physical Society.

2.3 Pair Annihilation Models

2.3.1 Effects of mutual ± 1 defect orientations

Models for defects annihilation consider the one-constant approximation ($K_S = K_B = K$). This condition may be so far used in our experiments as for our material $K_S \approx 2.2\ K_B$, except in the very vicinity of the +1 defect. At equilibrium, when K_B is lower than K_S, the positive defect chooses the configuration with lower energy which corresponds to pure bend. Thus, it adopts the tangential orientation (See Fig. 1.8). The *c-director* is pinned near the core and the phase of the defect $\theta_1 = \pm\pi/2$. It was reported that even a small difference between K_S and K_B may be sufficient to fix the defect phase Stannarius and Harth [2016]. During our study, we choose to set $\theta_1 = +\pi/2$ as shown in Fig. 2.7a. However, for $\theta_1 = -\pi/2$, all conclusions would be the same except that one has to change the sign of the *c-director*. It is wort noting that the situation of a fixed $\theta_1 = \pm\pi/2$ is quite common, not only for smectic films, but in particular in systems where the divergence of the vector field is suppressed or inhibited (vortex flow of an incompressible liquid or splay of a magnetic or electric polarization). The -1 defect is less affected by elastic anisotropy, the director field is only slightly modified by respective values of K_S and K_B, and the phase θ_2 only rotates the defect (See Fig. 2.7).

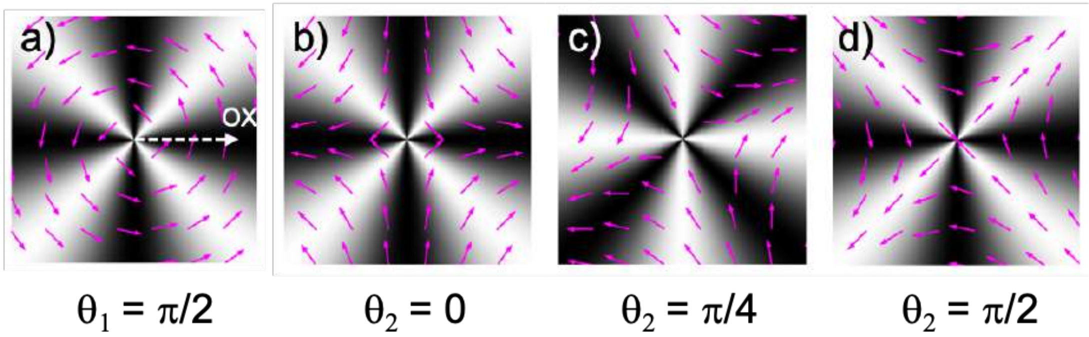

Figure 2.7 – Sketch of +1 and -1 defects for different orientations (phases $\theta_{1,2}$).

2.3.1.1 Mismatch Angle $\delta\theta$

We have shown in the first Chapter that the quasi-equilibrium states that describe the *director* field around an oppositely charged $S_{1,2}$ defect pair have the form of Eq. 1.17. This type of solution is sketched in Fig. 2.8a for the case of $S_{1,2} = \pm 1$ with the phases $\theta_1 = +\pi/2$ and $\theta_2 = -\pi/2$ respectively. Note that the phases θ_1 and θ_2 describe the angle of the *c-director* near the right side of the defect core and about the *OX-axis* connecting the defects. For the example shown in Fig. 2.8a, the orientation of the *c-director* near the right side of the core of the +1 (-1) and about the *OX-axis* connecting the defects is equal to $+\pi/2$ $(-\pi/2)$, as shown by the green arrows. Hence, $\theta_1 = +\pi/2 = -\theta_2$. The description of quasi-equilibrium states is appropriate only in the case of pairs of defects whose phases match, $\theta_2 = \theta_1 + \pi$, i.e. the *c-director* along a straight line connecting the defects is constant (see section.1.3.1). However, the situation of a non-constant *c-director* along the direction connecting the two defects may occur. This can occur, for example, when one or both of the defects rotate or change their spatial position. Fig. 2.8b and Fig. 2.8c show two examples of a ±1 defect pair where the position of the negative defects is no longer along the *OX-axis* which is now defined as the initial axis joining the two defects at the beginning. Even though the conjugated defects possess $\theta_1 = +\pi/2 = -\theta_2$, the *c-director* orientations along the pair connecting line are not constant anymore. The mismatch between the orientations of the *c-director* near the cores with respect to the pair joining line (shown in orange arrows), defined by the term "mismatch angle", $\delta\theta$, in the following, is respectively equal to $\pi/2$ and $\pi/3$ for Fig. 2.8b and Fig. 2.8c.

The spatial position and the phase of the defects are very important to determine the mismatch angle. One defines the angle φ_D as the angle between the defects connecting vector $\vec{r}_{12}$ and the *OX-axis*. In the two examples shown in Fig. 2.8b and Fig. 2.8c, φ_D is respectively equal to $\pi/4$ and $\pi/6$. It is clear that the mismatch angle $\delta\theta$ and φ_D are not independent. In the examples shown in Fig. 2.8 the mismatch angle is exactly $2\varphi_D$.

The defects cannot annihilate without reducing the mismatch, which is possible either by changing the phase of the -1 defect, i.e., simply rotating in the 2D space or by changing the spatial coordination of the two defects. This will have consequences on their trajectories, which will no longer be straight. Such a situation is called; mismatched defects pair.

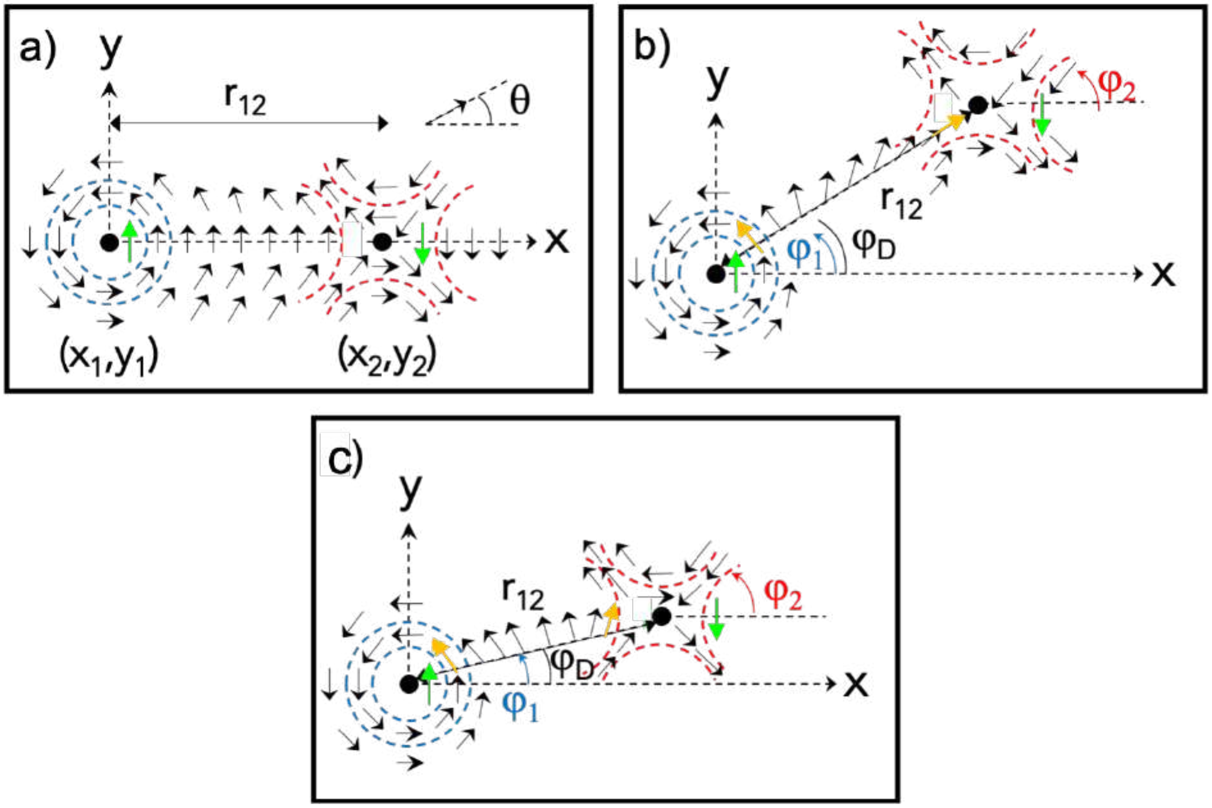

Figure 2.8 – (a) Point defects with topological charges +1 (left) and -1 (right) in match, $\theta_1 = \pi/2 = -\theta_2$; θ is constant along the line joining the defect pair (dashed line). (b) Defect pair in mismatch, $\theta_1 = \pi/2 = -\theta_2$. $\varphi_{1,2}$ are the angles of the relative positions $\vec{r} - \vec{r}_{12}$ with the *OX-axis*. $\varphi_D = \pi/4$ define the orientation of the pair, given by angle between the defect interconnection vector $\vec{r}_{12}$ and the *OX-axis*. (c) $\theta_1 = \pi/2 = -\theta_2$ and $\varphi_D = \pi/6$.

Recently, Vromans and Giomi [2016] discussed the effects of mutual defect orientation mismatch in the nematic phase. They revealed that the interaction between half integer defects was affected qualitatively by their generic orientation. New trajectories were found for an annihilating pair, where the motion of the disclinations is no longer along the interconnecting line $\vec{r}_{12}$. Later, Tang and Selinger [2017] generalized the theory of mutual defect orientations to an arbitrary defect strengths in the *SmC* phase. They defined a tensors of rank $n \mid 1 - S \mid$ to describe the orientation of defects of topological charge S. Thus, the +1 defect was considered as a scalar and the -1 as a tensor of rank 2. During their study, the authors derived an explicit expression under the one-constant approximation ($K_S = K_B = K$), that describes the director field around ±1 defect pairs and takes into account their mutual orientation mismatch, $\delta\theta$ as

$$\theta(\vec{r}) = \arctan\left(\frac{y-y_1}{x-x_1}\right) - \arctan\left(\frac{y-y_2}{x-x_2}\right) + \frac{\delta\theta}{2}\left[1 + \frac{\ln(|\vec{r}-\vec{R}_1|) - \ln(|\vec{r}-\vec{R}_2|)}{\ln(r_{12}) - \ln(r_c)}\right] + \theta_0, \tag{2.3}$$

Where

$$\begin{aligned} \delta\theta &= \theta_2 - \theta_1 - 2\ \arctan\left(\frac{y_1-y_2}{x_1-x_2}\right) \\ \theta_0 &= \theta_1 + \arctan\left(\frac{y_1-y_2}{x_1-x_2}\right) \end{aligned} \tag{2.4}$$

One recognizes from Eq. 2.3 the solution for pairs mutually matching (Eq. 1.17) in the two first terms with θ_0. The third term with the parameter $\delta\theta/2$ is a solution of the Laplace equation with fixed boundary conditions $\theta = 0$ at the core of the $+1$ disclination and $\theta = \delta\theta$ at the core of the -1 disclination. This term favors the orientational alignment between the pair toward the optimal orientation $\delta\theta = 0$.

We use Tang and Selinger [2017] concept to discuss effects of defect orientations on interactions of conjugated pairs $S_{1,2} = \pm 1$. In the previous equations, it is very important to choose the correct quadrants of the arctan functions. In order to avoid any ambiguities that may occur because of the choice of the right quadrant, one added $-\pi$ and $+\pi$ in the definitions of $\delta\theta$ and θ_0 respectively Missaoui et al. [2020]

$$\begin{aligned} \delta\theta &= \theta_2 - \theta_1 - 2\varphi_D - \pi, \\ \theta_0 &= \theta_1 + \varphi_D + \pi \end{aligned} \tag{2.5}$$

In Eq. 2.3, the *c-director* field far from the two defects ($r \to \infty$) approaches the uniform value $\theta_\infty = \delta\theta/2 + \theta_0$, i.e.,

$$\theta_\infty = \frac{\theta_1 + \theta_2 + \pi}{2}. \tag{2.6}$$

θ_∞ depends on the phases of the two defects, which are in general not constant during their mutual approach and annihilation. We can consider for example the variation of θ_2 when the -1 defect rotates to reduce the mismatch angle during the annihilation. However in experiments, the far director field is usually fixed and independent of the defect configurations, e.g., the positions and orientations. Therefore, it is useful for an interpretation of the equilibrium configurations to consider them with respect to the far *c-director* orientation. For such a purpose, we rotate the coordinate system such that the infinitely far *c-director* is along *OX-axis*, $\theta'_\infty = 0$. The equilibrium solutions are therefore given by

$$\begin{aligned}\varphi'_D &= \varphi_D - \theta_\infty = -\pi - \theta_1 - \frac{\delta\theta}{2}\\ \theta'_1 &= \theta_1 - \theta_\infty = \theta_1\\ \theta'_2 &= \theta_2 - \theta_\infty = -\theta_1 - \pi\end{aligned} \tag{2.7}$$

One can quickly check that the mismatch equation remains unchanged, $\delta\theta' = \delta\theta$ and the phase of the positive defect is preserved, $\theta'_1 = \theta_1$. Another important point is that φ'_D and $\delta\theta$ are not independent of each other at equilibrium (see Eq. 2.7). We have shown that the defects need to match ($\delta\theta = 0$) in order that the annihilation can occur. This is fulfilled when $\varphi'_D = -3\pi/2$. However, if the last condition is not fulfilled, the -1 defect has to change its spatial position during the annihilation in order that φ'_D tends to $-3\pi/2$. The -1 defect always chooses an equilibrium mismatch angle that can be provided by its position, and vice versa, in a given external *c-director* field, corresponding to the energetic minimum. This aspect was not noticed by Tang and Selinger [2017] where the effects of the director field at infinity were ignored.

2.3.2.1 Misalignment angle $\delta\phi$

We have mentioned that the pairs can annihilate only when their phases match ($\delta\theta = 0$). Yet, when $\delta\theta \neq 0$, the mismatched ±1 pair either has to move to an appropriate angle φ'_D in order to minimize the mismatch or the -1 defect has to rotate by θ_2, or both. However, after the annihilation of a matched pair ($\delta\theta = 0$) with a *c-director* orientation on the connecting axis at both sides of the pair differs from the boundary condition $\theta'_\infty = 0$, the *c-director* field would be defect free but distorted at the annihilation site. Thus, the pair would have to rotate locally to avoid such deformation after the annihilation. We define the misalignment angle $\delta\phi$ such that it reaches zero when the defect orientations match ($\delta\theta = 0$) as

$$\delta\phi = \varphi'_D + \pi + \theta_1. \tag{2.8}$$

This is a reasonable choice, as $\theta_1 + (\varphi'_D + \pi)$ is exactly the *c-director* angle near the +1 core on the side opposing the conjugate defect. The pair is considered aligned when the misalignment angle $\delta\phi$ equals θ'_∞.

Solutions for the *c-director* field around a ±1 defect pair for three randomly chosen $\delta\phi$ and $\delta\theta$ are shown in Fig. 2.9. In the middle, a mutually matching $\delta\theta = 0$, aligned $\delta\phi = 0$ pair is shown. In the left and right figures, we have arbitrarily chosen $\delta\theta = \pi/2$, $\theta_1 = \pi/2$, $\delta\phi = -\pi/4$ and $\delta\theta = -\pi/2$, $\theta_1 = \pi/2$, $\delta\phi = \pi/4$ respectively. In general, other orientations may be conceived as well. In particular, for *SmC* films with $K_S < K_B$, one could have the situation $\theta_1 = 0$ or $\theta_1 = \pi$. Following the model reported by Tang and Selinger [2017], if $\delta\theta = 0$, the misalignment φ'_D is equal to -$3\pi/2$. We obtain a relationship between $\delta\theta$ and $\delta\phi$ as

$$\delta\theta = -2\delta\phi. \tag{2.9}$$

Finally, Tang and Selinger [2017] derived a new equation for the elastic free energy for a film of thickness h associated with the distorted configurations of a defect pair

$$E = 2\pi Khln\left(\frac{r_{12}}{2r_c}\right) + \frac{\pi Kh\delta\theta^2}{2}\frac{ln(r_{12}/(2r_c))}{[ln(r_{12}/r_c)]^2}. \tag{2.10}$$

The first term represents the common elastic energy for matching defects with topological charges S=±1 that we have introduced in the first Chapter via Eq. 1.18. The second term takes into account the mismatch contribution, which favors orientational alignment between the defects toward the optimal orientation. The free energy is thus associated to an aligning torque Harth and Stannarius [2020]

$$T = -\frac{\partial E}{\partial(\delta\theta)} = -\frac{\pi Kh}{\ln(r_{12}/r_c)}\delta\theta. \tag{2.11}$$

The torque decreases as $\pi Kh/ln(r_{12}/r_c)$ when the defect separation is much greater than the core radius.

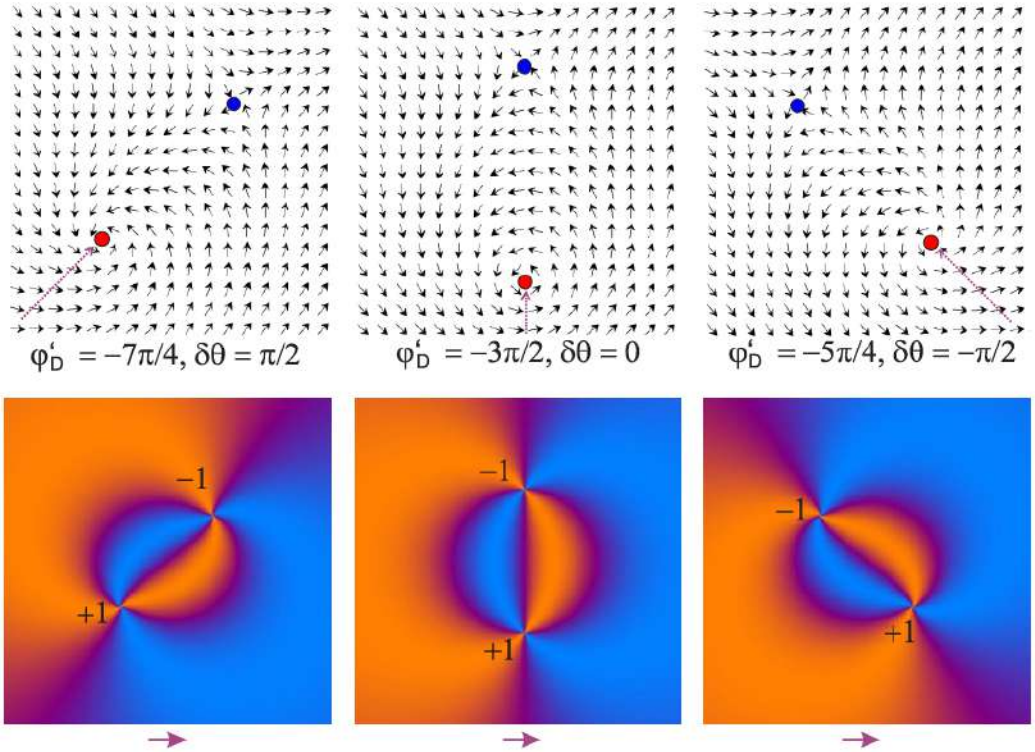

Figure 2.9 – Equilibrium *c-director* orientations around defect pairs with strengths ±1, calculated with Eq. 2.3 for fixed defect positions. $\delta\phi = (-\pi/4, 0, \pi/4)$ from left to right. The defect cores are marked by circles (red for +1, blue for -1). The top row shows the *c-director* fields, with orientation $\theta_\infty = 0$ (magenta arrows) in infinity. The bottom row sketches the corresponding optical images with crossed polarizers and diagonally inserted wave plate. Dotted arrows: see text. Reprinted from Missaoui et al. [2020]. Copyright (2020) by The American Physical Society.

2.3.2 Summary

The classical models describe the motion of the defect pairs by a quasi-equilibrium configurations. However, the orientation of the defects was not discussed at all. The recent studies by Tang and Selinger [2017], pointed out the important effects of this phenomena. Therefore, a new description of the defect dynamics phenomenon was introduced, allowing the derivation of new analytical equations. The classical theories remain valid for the special case of aligned, matching pairs.

We have further modified the model by Tang and Selinger [2017] through a coordinate transformation, allowing for a quantitative comparison of experimental results with the recent analytical equations. We demonstrate in the next section the importance of the two orientation parameters, i.e. the phase mismatch $\delta\theta$ of the pair and the misalignment $\delta\phi$, on the defect dynamics.

2.4 Pair Annihilation Experiments

Here, we are interested in disclinations with the lowest possible topological charges, $S = \pm 1$. We analyzed data from 24 experiments of isolated defect pairs. The positions of the defects were easily detected in the microscopic images. Therefore, we have developed a Matlab program to determine their positions with an accuracy of approximately 1 μm. The *c-director* orientation can be retrieved from the texture colors as discussed previously (Fig. 2.5); the accuracy is of about 10°. The relation between $\vec{c}$ and optical texture is indicated in Fig. 2.6. We cannot determine the sign of $\vec{c}$ with our observations, and thus we choose a given sense of direction and used this assignment consistently for all experiments. This has no consequences for the evaluation of the data; the equations are independent of the sign of the tilt azimuth. It is possible that all arrows in the images actually represent $-\vec{c}$.

The experimental data for the mismatch angle, $\delta\theta$, are obtained by determining the mismatch between the orientations of the *c-director* near the defects core on the side facing the conjugated defect. The orientations can be retrieved from the texture colors in Fig. 2.5 (See section.2.2.4). We used a Matlab code that allows to extract the local orientation with an accuracy of about 10°.

The experimental data for $\delta\phi$ are determined *a posteriori* from the video images after the annihilation of the defect pairs.

On Fig. 2.10, I selected two examples of defect pairs during their mutual annihilation. Fig. 2.10a shows two defects whose phase matches ($\delta\theta = 0$), defined in the following as "aligned pair”. One notice that the color remains the same along the joining line, a characteristic of constant *c-director* orientation. Fig. 2.10b shows an example of a "misaligned pair", where $\delta\theta \neq 0$. The color changes along the connecting line, indicating a non-constant *c-director*. In the next section, I discuss first the aligned pairs then I discuss the mismatched pair situation.

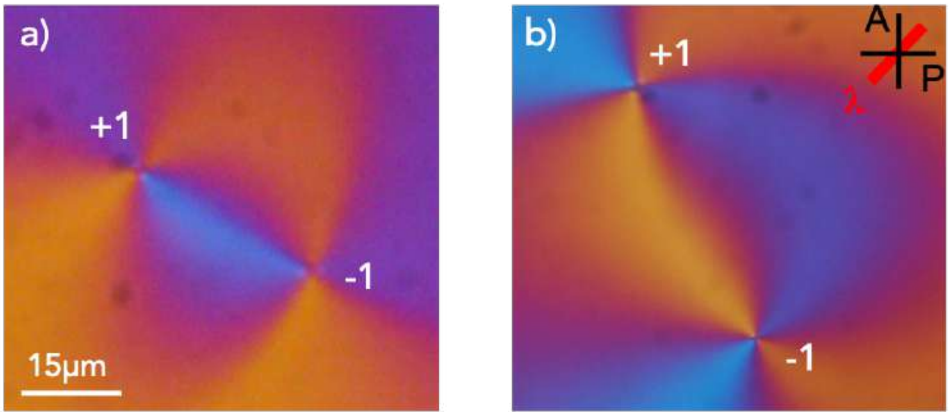

Figure 2.10 – Point defects with topological charges $+1$ (left) and -1 (right) during annihilation. (a) Aligned pair. (b) Misaligned pair. Experimental data carried out by Peter Salamon.

2.4.1 Aligned defect pairs

As discussed previously in section 2.3.1, an aligned defect pair is composed of defects whose phase matches (Fig. 2.8a). The *c-director* along a straight line connecting the pair has a constant orientation. Figure 2.11 shows an initially matching ($\delta\theta \approx 0$) and aligned ($\delta\phi \approx 0$) defect pair. Such conditions (within approximately 10° accuracy) were achieved coincidentally in five experiments over 24. Eq. 2.7 predicts that when the orientations of the defects match ($\delta\theta = 0$), the misalignment of $\vec{r}_{12}$ with respect to the far *c-director* should be $\varphi'_D = -\pi - \theta_1 = -3\pi/2$. This agrees with our observations. Immediately before annihilation, we found $\varphi'_D = -\pi - \theta_1 = -3\pi/2$ and $\delta\phi = 0$ in all experiments except one.

Fig. 2.11 shows the *c-director* orientation in the vicinity of the defects pair (see white arrows). The director field was extracted from the microscope images (See section.2.2.4). For a pair of aligned ±1 defects, the *c-director* field seems to be in agreement with Eq. 1.17 of a solution drawn in Fig. 2.8a. The angle θ of the *c-director* remains constant along the straight line connecting the two defects during the annihilation.

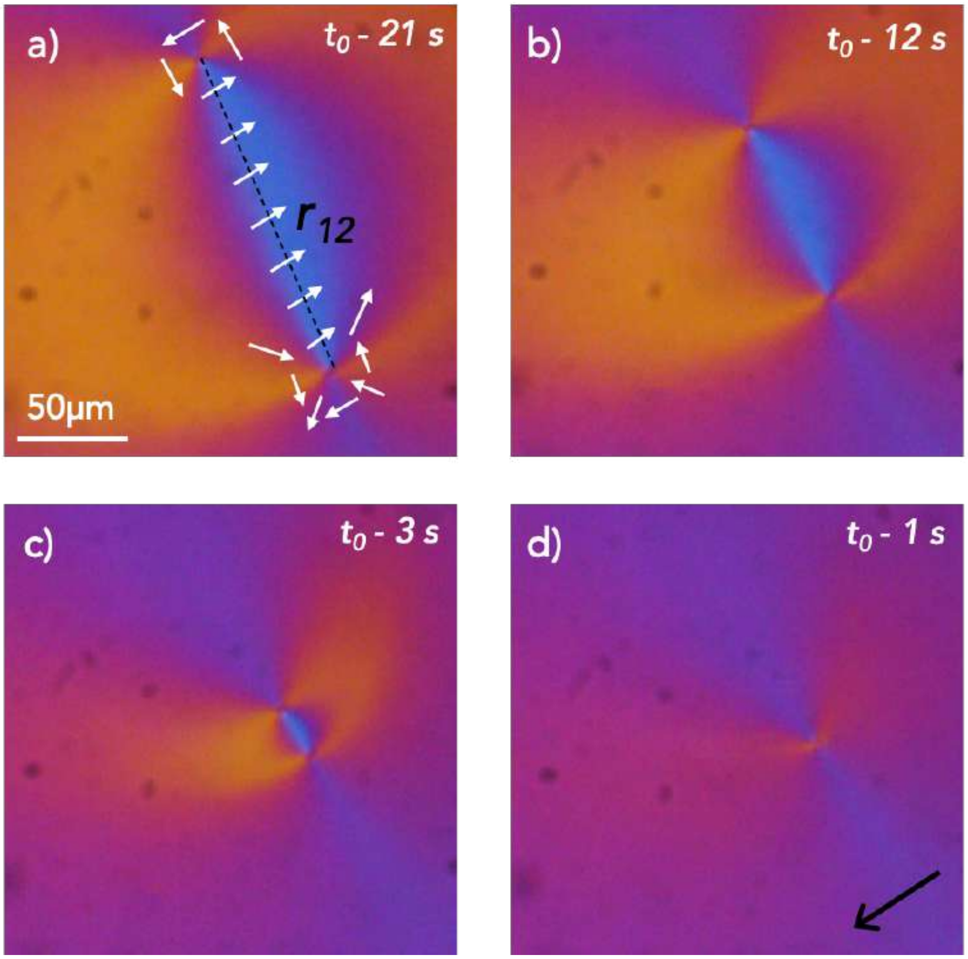

Figure 2.11 – Matched ($\delta\theta$) and aligned ($\delta\phi$) defect pair on the way to annihilation. The upper defect is the -1 and bottom one is the +1. The white arrows indicate the local *c-director* orientation. The separation distance r_{12} is shown by the dashed black line. t_0 is the annihilation time. The black arrow shows the far *director* orientation, θ'_∞. Experimental data carried out by Peter Salamon. Reproduced from Missaoui et al. [2020]. Copyright (2020) by The American Physical Society.

As they are easily identified in the optical microscope images, we succeeded to extract the trajectories of the disclination pairs by tracking their instant positions from the data videos. Fig. 2.12a shows an example of the trajectory of a pair of aligned defects. In agreement with the models, when the relation $\delta\theta = \delta\phi = 0$ is fulfilled, $\delta\theta$ and $\delta\phi$ remain constants and the defects follow straight paths. We measured the separation distance r_{12} of the defects as a function of time. The results are shown in Fig. 2.12b and Fig. 2.13. We found that for an aligned defect pair, the separation distance follows the square root of time dependence predicted by the theoretical model for large distances as well as for short distances (see section.1.3.1).

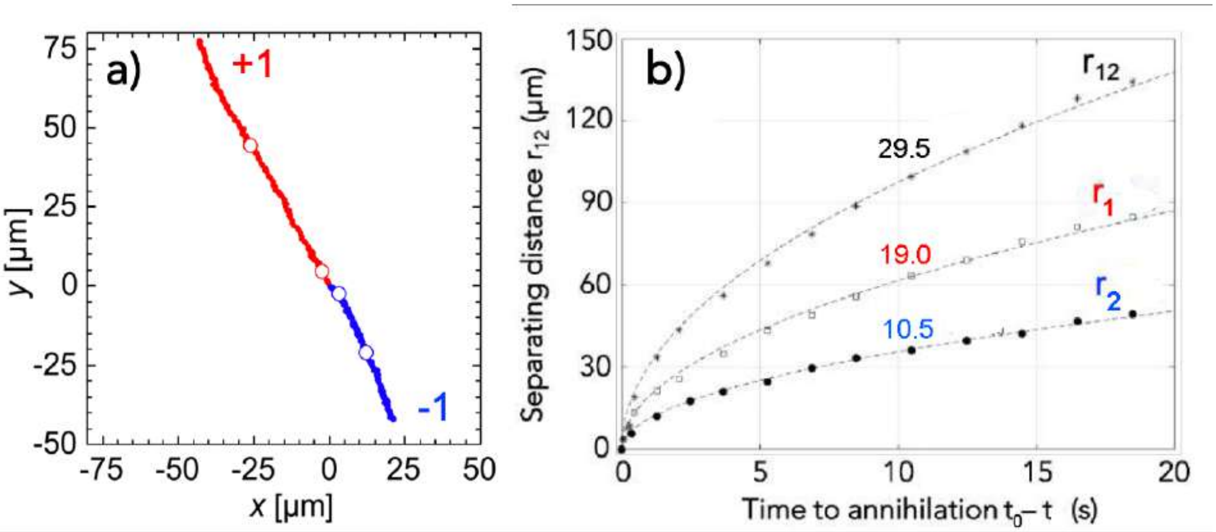

Figure 2.12 – (a) Trajectory of a defect pair on the way to annihilation. In red (blue) shows the trajectory of the +1 (-1) respectively. The meeting point is at (0,0). The black arrow shows the far *director* field orientation, θ'_∞. Reproduced Figure from Missaoui et al. [2020]. Copyright (2020) by The American Physical Society. (b) Distances of two matching defects with respect to the annihilation point. The graphs show the defect separation r_{12} and the distances r_1 of the +1 defect and r_2 of the -1 defect from the point where they finally meet and annihilate. The dashed lines are square-root fits $r = D\sqrt{t}$, and the numbers give D in units of $\mu\text{ms}^{-1/2}$.

We have noticed from the trajectories data that the pairs move at different velocities, where the positive defect is systematically faster than the negative one. As a result, the pairs do not meet at half way but closer to the initial position of the -1 defect. This result is in contrast with the classical model which predicts a symmetry of the speed of the two defects (see section.1.3.1). However, this phenomenon of broken symmetry has been previously described by a numerical model in two-dimensional nematics by Dierking et al. [2012]; Tóth et al. [2002]. Blanc et al. [2005] later confirmed these results through an experimental study in the nematic phase, where a +1/2 defect was found to move faster than the -1/2 to the annihilation point. Svenšek and Zumer [2003] generalized the numerical model for *SmC* freely suspended films. In all these works, the defect asymmetric velocity was attributed mainly to the hydrodynamic flow-coupling of a nonuniform director reorientation to material flow (see next chapter).

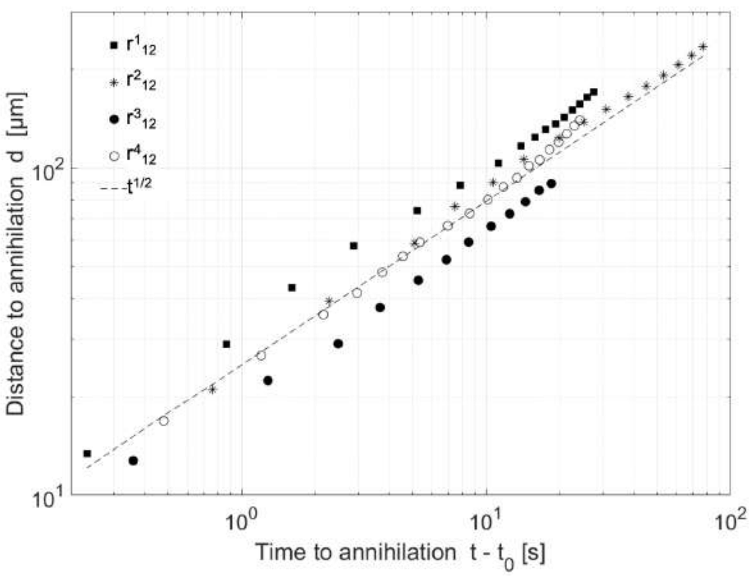

Figure 2.13 – Separation distance for four examples of aligned pairs, presented in log-log scale. The dashed line is for $t^{1/2}$.

2.4.2 Misaligned defect pairs

In this part, we discuss the case of mismatched defect pairs, previously defined by a mismatch $\delta\theta$ and a misalignment $\delta\phi$. From 24 experiments, 19 randomly produced defect pairs with either positive or negative misalignment $\delta\phi$. The initial alignment angle could not be controlled; it is determined *a posteriori* from the video images. Figures 2.14a and 2.14b show typical examples with initially negative $\delta\phi$ and positive $\delta\theta$. The *c-director* changes along the defect connection line. As a result, the trajectories are no longer straight. Fig. 2.14c shows a typical example of the trajectory for a defect pair of initially positive $\delta\theta$ and negative $\delta\phi$. This new type of trajectory has a curved shape, called the "*S-shaped*" in the following. The case of initially negative $\delta\theta$ and positive $\delta\phi$ produces the opposite curvature regarding to the "*S-shaped*". As shown in Fig. 2.14d and Fig. 2.14f, the texture forms a "*mirrored-S-shaped*" trajectory with respect to Fig. 2.14a and Fig. 2.14b.

The positive defect is still faster than the negative one. The misaligned pairs share this behavior with the aligned pairs. As we have mentioned, this phenomena will be analyzed in the third chapter.

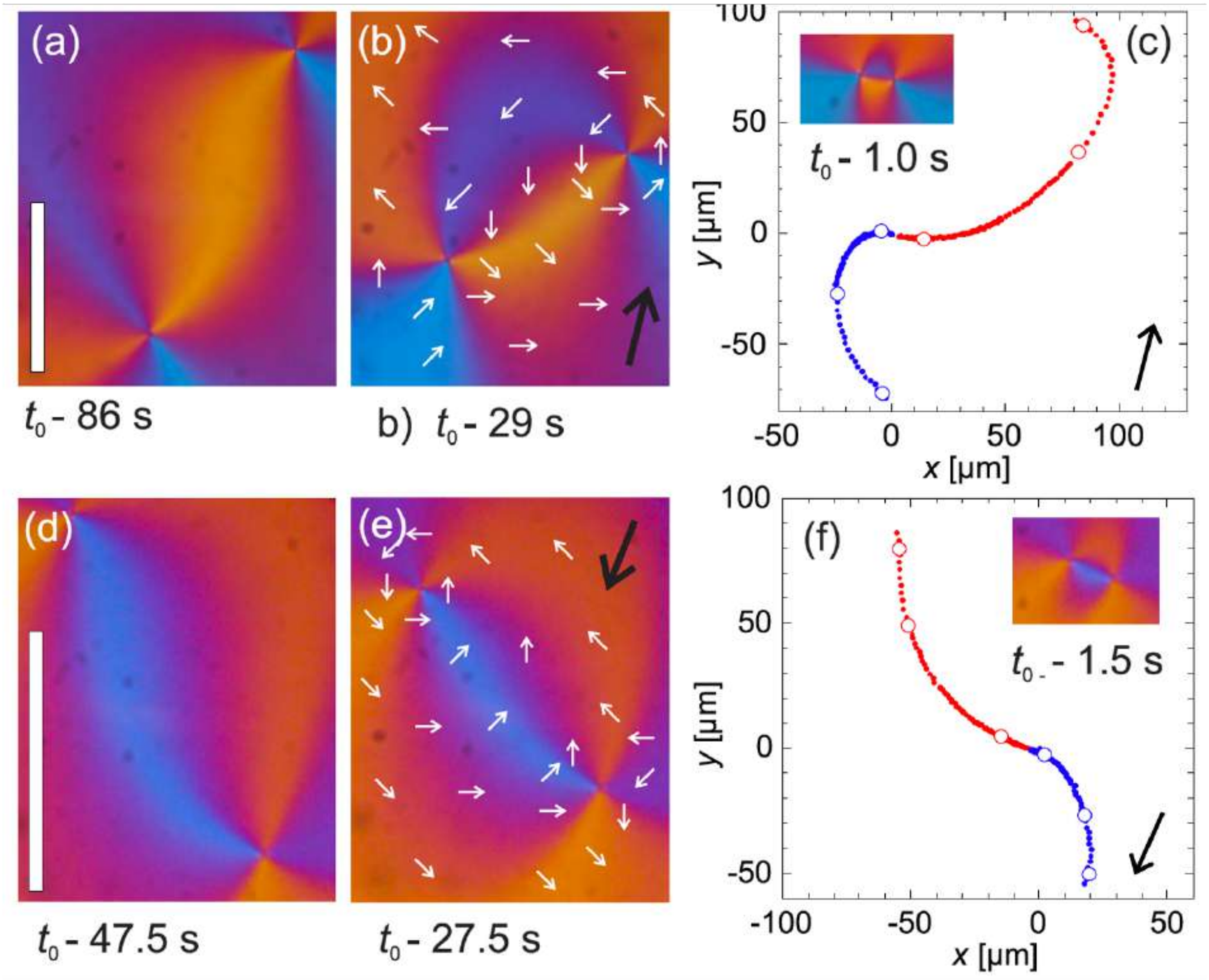

Figure 2.14 – (a),(b) Mismatched (initial $\delta\theta \approx 65°$) and misaligned (initial $\delta\phi \approx -36°$) defect pair on the way to annihilation. White arrows sketch the c-director. The +1 defect (top) is ≈ 1.8 times faster than the -1 defect. The black arrow indicates the outer director field. (c) Trajectories respective to the annihilation point. Circles mark the defect positions in frames (a)–(c). (d),(e) Mismatched (initial $\delta\theta \approx -50°$) and misaligned (initial $\delta\phi \approx 79°$) pair. (f) Trajectories, circles mark the defect positions in frames (d)–(f). The velocity ratio is ≈ 1.7. The white bars represent 100 μm. Experimental data carried out by Peter Salamon. Reprinted from Missaoui et al. [2020]. Copyright (2020) by The American Physical Society.

2.4.2.1 Correlation between $\delta\theta$ and $\delta\phi$

The relaxation on curved trajectories shown in Fig. 2.14, at first glance looks very similar to the numerical simulations in Tang and Selinger [2017] and Vromans and Giomi [2016]. They indeed appear to be primarily caused by the torque of the external director on the topological dipole. One can consider this as an analog, with some peculiarities, of an electrical dipole in a uniform external field. The electrical dipole tends to align parallel to the external field to minimize its energy. Likewise, the conjugated topological defect pair can optimize its elastic energy, no matter the mismatch angle is, by choosing a proper orientation φ'_D respective to the uniform far *c-director*. If one defines the "topological dipole", for instance, as a unit vector $\vec{p} = \vec{r_{12}}/|r_{12}|$ pointing from the +1 to the -1 defect, the energetic minimum is defined at the angles φ'_D that minimize the elastic distortion as low as possible. In our experiment, where $\theta_1 = \pi/2$, the topological dipole aims to align with an angle $\varphi'_D = -\pi - \theta_1 - \delta\theta/2 = (-\pi - \delta\theta)/2$ (See Eq. 2.7) respective to the far *c-director* in order to minimize the elastic distortion caused by the misalignment of the pair.

The measurements of $\delta\phi$ are shown in Fig. 2.15. The relaxation of $\delta\phi$ follows a similar square-root of time dependence as the defect separation r_{12}. This produces the observed curved trajectories as seen in Fig. 2.11. The origin of this dependence with time is no yet clear.

Immediately before the annihilation, both defects orientations should match, $\delta\theta \to 0$, and become aligned, $\delta\phi \to 0$. This should hold for all defect pairs independent of the initial angles to allow for an undistorted film after annihilation. The insets in Fig. 2.14c and Fig. 2.14f show that the pairs become almost matched ($\delta\theta \approx 0$) about 1 *s* before the annihilation time (t_0). The far director field orientation is indicated by the black arrows in the two plots. It is obvious that the corresponding misalignment of $\vec{r}_{12}$ with respect to the far *c-director* orientation $\varphi'_D \approx \pm\pi/2$, at the annihilation time, which is in agreement with the expected final values for this angle. All initial combinations of $\delta\theta$ and $\delta\phi$ are shown in Fig. 2.15a. A correlation is obviously irrespective of the deviations that are most probably caused by global distortions of the film orientation when the defects are created. By inserting the expression for φ'_D (See Eq. 2.7) into Eq. 2.8, one obtains the relation $\delta\theta = -2\delta\phi$ (Eq. 2.9) in the quasi-equilibrium states (elastic energy minima at fixed defect positions), which is in clear contrast to the experimental results that lead to a relationship definitely closer to $\delta\theta = -\delta\phi$.

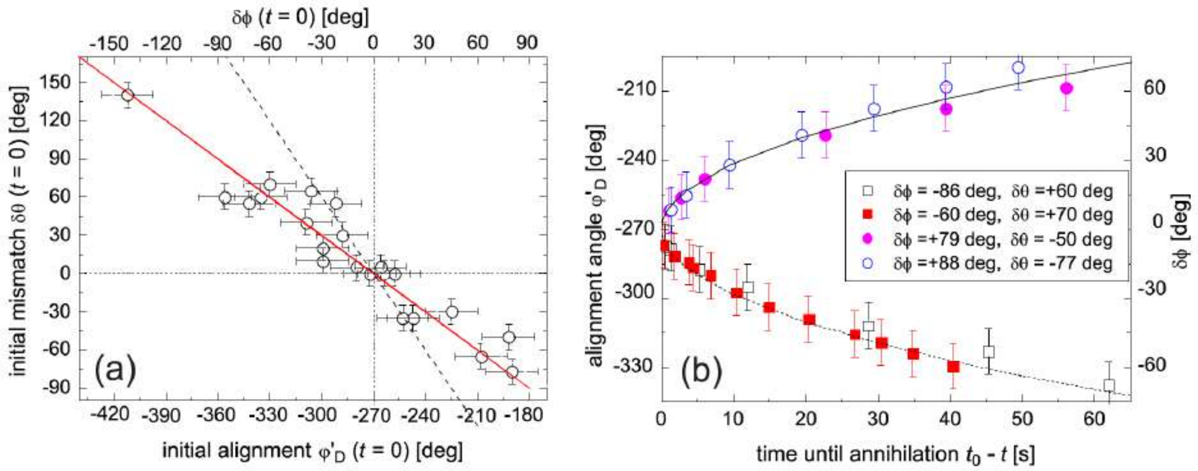

Figure 2.15 – (a) Mismatch $\delta\theta$ vs alignment φ'_D; the solid line represents $\delta\theta$ = -$\delta\phi$. Even though individual experiments deviate by up to 20°, it is obvious that the two angles are correlated. Eq. 2.8 predicts a linear dependence with slope -2 (dashed line) for the quasi-equilibrium configurations. (b) Time dependence of the pair alignment angle φ'_D for four selected defects. The solid and dashed lines represent $\delta\phi = \pm 9^\circ \sqrt{t_0 - t}/\sqrt{s}$. Reprinted from Missaoui et al. [2020]. Copyright (2020) by The American Physical Society.

The preparation technique produces random alignment angles φ'_D, but it seems unlikely that touching the films creates correlated combinations of $\delta\theta$ and $\delta\phi$. The initial angles $\delta\theta$ and φ'_D in Fig. 2.14 and Fig. 2.15 were taken with a short delay after the microscope was focused onto the film surface in the spot where the defects appeared. This took a few seconds, differing between individual runs. Thus, they do not reflect the true initial values after defect pair creation. Initial fast reorientation of the *c-director* field are not accessible. We conclude that the defects rearrange within this short period of time after creation, irrespective of the initial conditions, into an orientation that fulfills the condition $\delta\theta = -\delta\phi$ at least approximately. It is reasonable to assume that the rotation of the -1 defect in place can proceed much faster than a spatial displacement of the same defect on a circle around the opponent. Fig. 2.16 shows four typical experiments, two with *S-shaped* and two with *mirrored-S-shaped* trajectories. The two angles $\delta\phi$ and $\delta\theta$ remain strongly correlated, roughly proportional to each other, although there is a slight tendency of $\delta\theta$ to relax faster than $\delta\phi$. The reason why there is a factor of nearly 2 between the calculated equilibrium states Tang and Selinger [2017] and the experimental observation is not clear.

With respect to the model by Tang and Selinger [2017], our hypothesis is that the equilibrium configurations for $K_S = K_B$ could be not appropriate quantitative descrip-

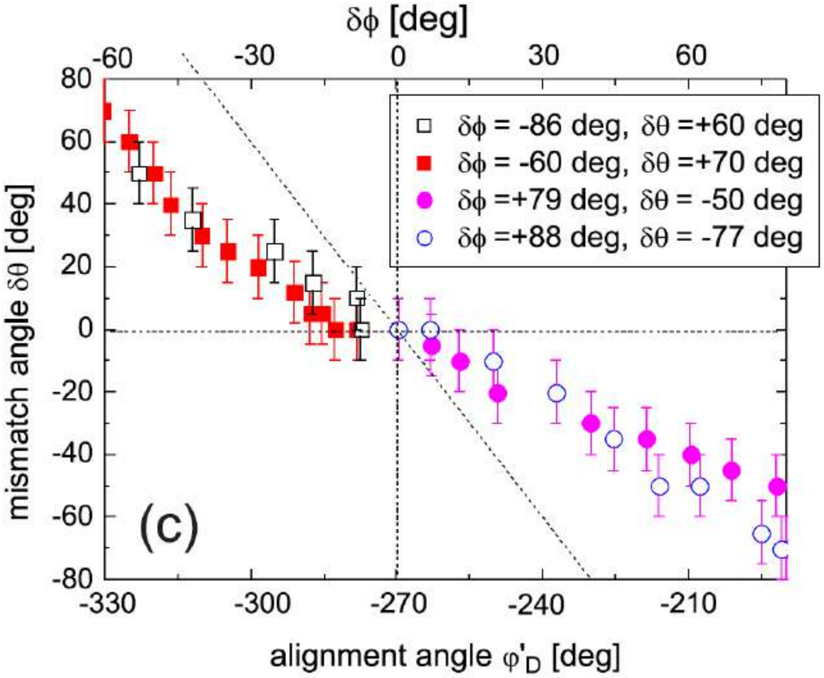

Figure 2.16 – Mismatch angles vs alignment angles during the approach of exemplary defect pairs with *S-shaped* and *mirrored-S-shaped* trajectories. The dashed line represents Eq. 2.8. The values of $\delta\phi$ and $\delta\theta$ shown in the box are the initial values. Reprinted from Missaoui et al. [2020]. Copyright (2020) by The American Physical Society.

tions of the states that the annihilating defect pair passes on its approach. Moreover, the torque predicted from the quasi-equilibrium configurations is probably causing an initial reorientation of the -1 defect, which is too fast to be observed in our experiment. The relation $\delta\theta = -\delta\phi$ observed in our study is presumably a balance between the torque exerted by the +1 opponent and the torque exerted by the far *c-director* field. The latter is obviously not modeled by Tang and Selinger [2017] in a way that is appropriate to describe our experiment with fixed boundary conditions.

We conclude that: first, the system establishes certain combinations of $\delta\theta$ and $\delta\phi$ spontaneously, irrespective of the details of the defect creation, and second, either the experimental system does not develop through quasi-equilibrium states on the way to annihilation, or the equilibrium states are different from those predicted from one-constant elastic theory possibly because the far *c-director* configuration was not taken into account by the theoretical models. In the next section, I discuss briefly a qualitative estimation of the effects of elastic anisotropy, $K_s \neq K_B$ on the equilibrium alignment.

2.4.2.2 Distribution of splay and bend contribution

We will focus here on whether the deviation of the measured $\delta\phi$ ($\delta\theta$) from the theory can be attributed to the elastic anisotropy present in the experiment, but neglected in the analytical model. The splay and bend contributions to the elastic deformations of the *c-director* are not uniformly distributed around the defect pair as we have discussed in section.2.3.1. In fact, in the very vicinity of the +1, since K_S is larger than K_B, bend is the predominant situation, all +1 defects adopt tangential orientation ($\theta_1 = \pm\pi/2$) in equilibrium. However, in the case $K_S \neq K_B$, the equilibrium configurations are no longer computable from solutions of the Laplace equation. Analytical solutions are only available for very special geometries.

In the present problem of the defect pair, the nonlinear differential equation describing the equilibrium has to be solved numerically. The numerical calculation of the exact energies of the equilibrium solutions in that case is not straightforward because the energy density becomes very large near the defect cores. We can, however, estimate the influence of an elastic energy by considering the distribution of splay and bend in the *c-director* field. Figure 2.17 shows three situations where a ±1 defect pair is aligned (center) and misaligned by a positive or negative $\delta\phi$ (left and right, respectively). The logarithm of the local elastic energy densities of the splay (green) and bend (purple) terms was calculated and color coded.

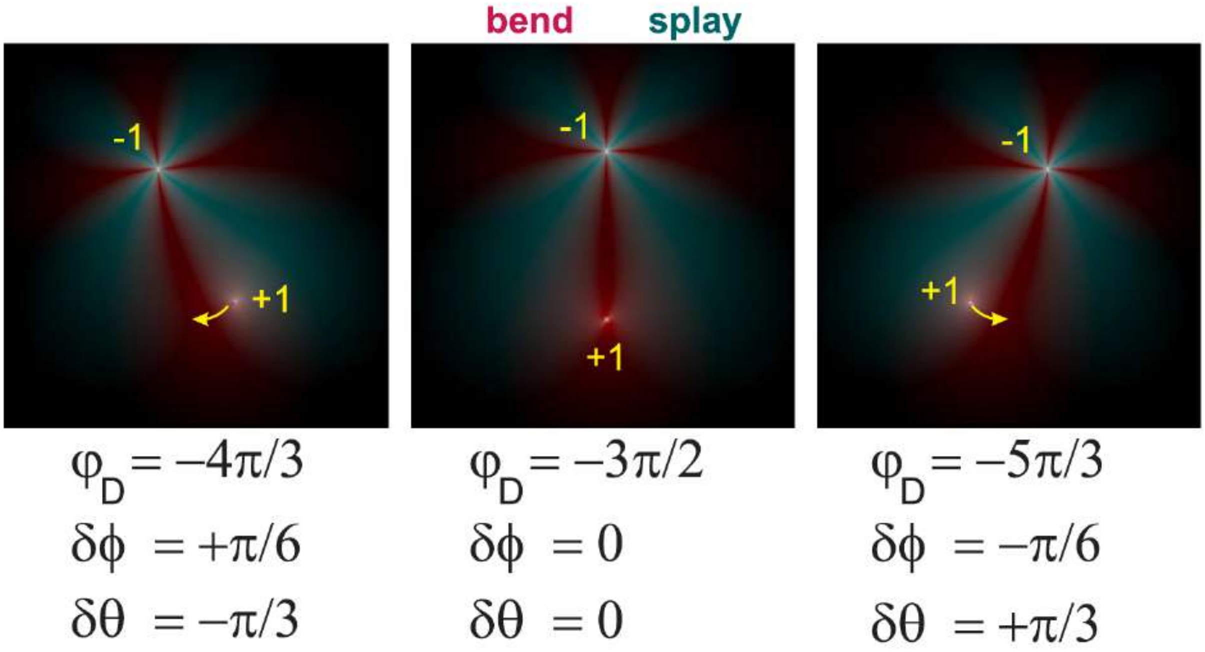

Figure 2.17 – Distribution of splay (green) and bend (purple) regions in the xy plane in the vicinity of a defect pair with different alignment angles φ'_D in the equilibrium director configurations calculated with Eq. 2.3. The color saturation reflects the logarithm of the splay and bend energy, respectively. In the case of $K_S > K_B$ it is expected that the splayed (green) regions spread out, while the bent (purple) regions contract. This suggests that the +1 defect is relocated closer to the -$3\pi/2$ alignment respective to the -1 defect (yellow arrows) in both misaligned geometries, increasing the discrepancy to the experimentally observed $\delta\phi \approx -\delta\theta$. Reprinted from Missaoui et al. [2020]. Copyright (2020) by The American Physical Society.

In our experiment, $K_S = 2.2\ K_B$ Missaoui et al. [2020], the system will tend to compress bent regions in favor of expanding splay regions (compared to the one-constant solutions). One may expect that in Fig. 2.17 the bent *c-director* region (purple) below the -1 defect will contract, and the splayed (green) regions at both sides of this region will expand. In a simplistic interpretation, this means that in the left image, where $\delta\phi$ is positive, the +1 defect will be relocated clockwise around the -1 defect, reducing φ'_D and $\delta\phi$. In the right image, the +1 defect relocates counterclockwise, thus increasing $\delta\phi$. This effect is opposite to the observation in the experiment where we find $|\delta\phi|$ larger than the value $|\delta\theta|/2$ predicted in the one-constant model.

One may conclude from these considerations that the elastic anisotropy may have an influence on the relation between misalignment and mismatch. However, it seems that it is not the primary cause of the observed differences between experiment and the model given by Eq. 2.3 since the elastic anisotropy effects would apparently increase the discrepancy. An accurate computation of the actual equilibrium configurations at $K_S \neq K_B$ will be needed to verify this relation observed quantitatively. This consequently suggests that the most important parameter ignored in the previously developed model by Tang and Selinger [2017] may be the influence of the far field *c-director*.

Recently Tang and Selinger [2020] extended their previous theories Tang and Selinger [2017] to ±1 defects in a 2D *SmC* liquid crystal film by taking into account the effects of the elastic anisotropy. The authors reported that unequal elastic constant significantly changes the annihilation trajectories even for pairs without initial misalignment. *S-shaped* trajectories, similar to the ones observed during our study were reported. The reason behind this phenomena is attributed to the special features of the +1 defect. It was shown that a pure splay or bend +1 defect tends to move into a region with the corresponding deformations with a speed mainly dependent on the elastic constants. However, the speed of the negative defect depends on the average of both constant as this defect contains both deformation in the vicinity of the core. As a result, the velocity of the defects is different, where the +1 is found to move faster then the -1 to the annihilation point as shown in Fig. 2.18. This latter result will be consequently discussed in the third Chapter related to the difference in the velocities of both defects.

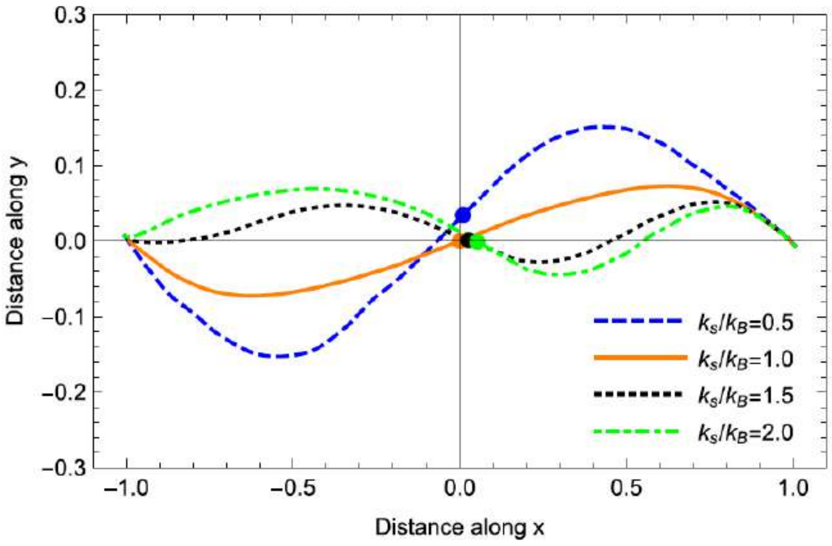

Figure 2.18 – *S-shaped* trajectories for annihilating ±1 defect pairs. Different elastic constant have been used The backflow effects are neglected and the defects are considered aligned with the far *c-director* field. Reprinted from Tang and Selinger [2020]. Copyright (2020) by The American Physical Society.

2.4.2.3 Measurements of the separation distance r_{12}

We remind that the distance r_{12} is defined in the classical model as the distance separating the two defects considered along the connecting line. The model predicts that r_{12} must follow a square root of time dependence (see Eq. 1.15). The measurements of r_{12} in the case of misaligned defects show that this latter deviates from the expected dependency, as shown in Fig. 2.19. This deviation can be attributed to the neglect of the effects of defects orientation in the classical model on the one hand, and to the considerations of equal elastic constants on the other hand.

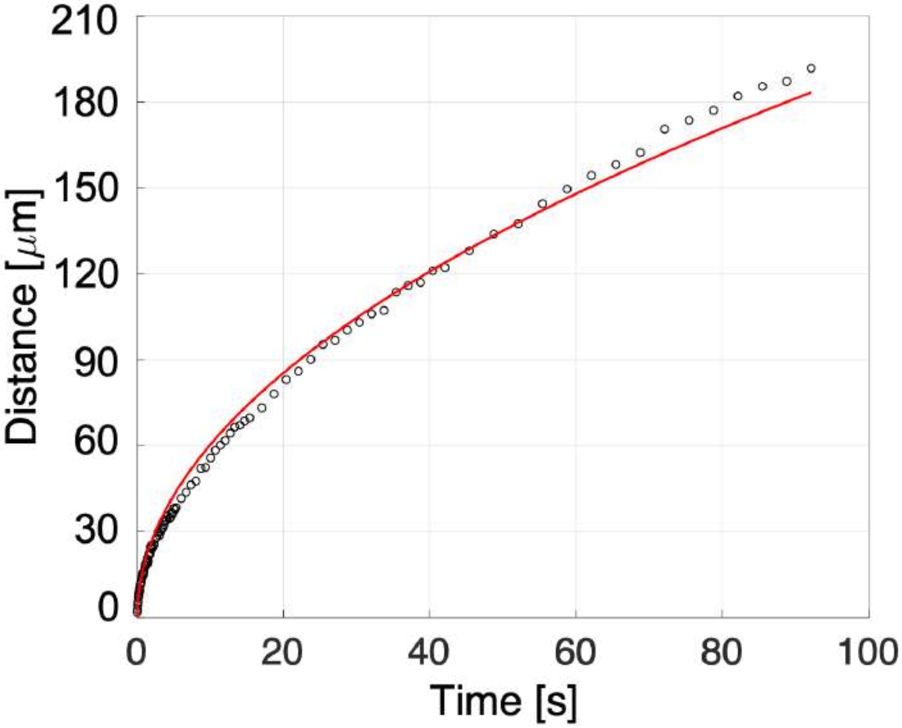

Figure 2.19 – Measurements of the separation distance r_{12}. $t = 0\ s$ is the annihilation time. The red line is a square root of time fit.

An explanation might be given basing on the elastic and drag forces (see Eq. 1.18 and Eq. 1.21). These forces are considered to be acting along the defects connecting line. However, when we consider the orientation of the defects, it is more appropriate to consider the forces pointing along the instant defects orientation, which changes during the annihilation of the pair. Thus, one defines the new separation distance between the pairs by r'_{12}, which is the distance measured along the curved trajectory (See Fig. 2.20a). This new parameter is measured *a posteriori* in the experiments from the trajectories of the defect pairs (See Fig. 2.20).

Fig. 2.20b shows the measurements of the separation distance between the defect pairs, basing on the new definition, for three defect pairs. We found that r'_{12} varies as a function of the square root of time.

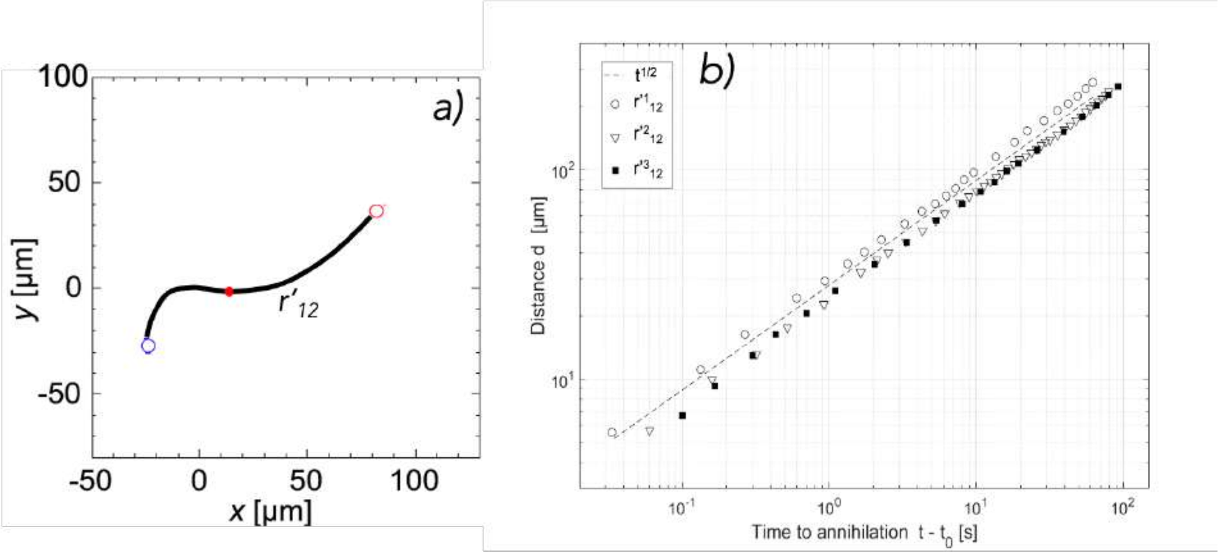

Figure 2.20 – (a) Trajectory of a misaligned pair and the new definition of the separation distance r'_{12} along the defect path. The red point in the trajectory path is the annihilation point. (b) Measurements of r'_{12} for three randomly chosen pairs. The dashed line is for $t^{1/2}$.

2.4.3 Summary

We have shown that the results of aligned ±1 defect pairs are in a good agreement with the classical model introduced in the first Chapter. They annihilate in a straight path, while the separation distance r_{12} follow the square root of time dependence. Nevertheless, the majority of the defect pairs in our study are misaligned. We have shown that such misaligned pairs deviate from the classical model. Their trajectories are not straight and they annihilate along an *S-shape* or *mirrored-S-shaped* path. Such a result was not predicted by classical models because the defect orientation was neglected. If we define the new separation distance between the misaligned pair as the distance along their path, the separation distance r'_{12} appears in a good agreement with the square root of time dependence.

An improved version based on the classical model and taking into account the effects of the mutual defects orientation has been reported by Tang and Selinger [2017].

The authors showed that the defects orientation induces curved trajectories similar to the ones that we have observed in the experiments. They have shown that the mismatch angle between the defect pair, $\delta\theta$, which is geometrically the difference of orientation of the *c-director* near the cores and along the pair joining line, is the key parameter behind the curved trajectories. However, the authors neglected the effects of the far director field, which is fixed in the experiments.

After we applied the coordinate transformation in order to fix the far *c-director*, we ended up with an equation that links the two orientation parameters: the phase mismatch angle $\delta\theta$ of the pair and their misalignment $\delta\phi$ relative to the far *c-director* given in Eq. 2.9. In our experiments, we demonstrate that the interrelation of the two orientation parameters is different than the predicted dependency. We found the relation $\delta\theta \approx -\delta\phi$ instead of $\delta\theta = -2\delta\phi$. The mismatch between Tang and Selinger [2017] model and the experimental results can be attributed to the balance between the torque exerted by the +1 and the torque exerted by the far *c-director* field which is neglected in their model. We have also shown that the unequal elastic constant cannot be the primary cause of the reported difference between the experiments and Tang and Selinger [2017] model.

2.5 Finite Element Method

In this section, I model quasi-equilibrium static state solutions of the ± 1 defect pairs in two-dimensional geometry. One uses the commercial software *COMSOL Multiphysics* in order to perform numerical calculations using the finite element method. The simulation code was developed by Kirsten Harth from the University of Magdeburg (OvGU). The calculations allow for a direct measurement of the interaction energy of the two defects in a rectangular geometry. We check the variation of the interaction energy as a function of: the separation distance between the defects pair r_{12}, the defect mismatch $\delta\theta$ and the misalignment $\delta\phi$. We have used the one-constant approximation $K_S = K_B = K = 10^{-11} J/m$. The material flow was not simulated. The defect positions are fixed and their velocities are set to zero.

2.5.1 Principles

The geometry of the calculation is defined as the following: The freely suspended smectic film is assigned to a 2D square and the defect cores are assigned to two circles extracted from the square at positions (x_1,y_1) and (x_2,y_2). Fixed boundary conditions are imposed at the circles circumference in order to reconstruct the appropriate *n-director* configuration the describes the ±1 defects. The two components of the *director* $\vec{n} = (n_x, n_y, 0)$ at the circles circumference are used in Dirichlet[3] boundary conditions as

$$\begin{aligned} n_x &= \sqrt{-A/C}(\cos(S_i(\arctan(y - y_i/x - x_i) + \theta_i))) \\ n_y &= \sqrt{-A/C}(\sin(S_i(\arctan(y - y_i/x - x_i) + \theta_i))) \end{aligned} \tag{2.12}$$

The Landau parameters $A < 0$ and $C > 0$ set the equilibrium length of $\vec{n}$ in the *xy-plane*. We set A = -1.8 and C = 7.2 . The defects phases are defined by θ_i.

Fig. 2.21 shows the solutions for a +1 tangential defect with the phase $\theta_1 = -\pi/2$ (Fig. 2.21a) and twofold -1 defect with $\theta_2 = \pi/2$ (Fig. 2.21b). Such defect configuration is equivalent to the ±1 pairs that we have studied in the previous sections.

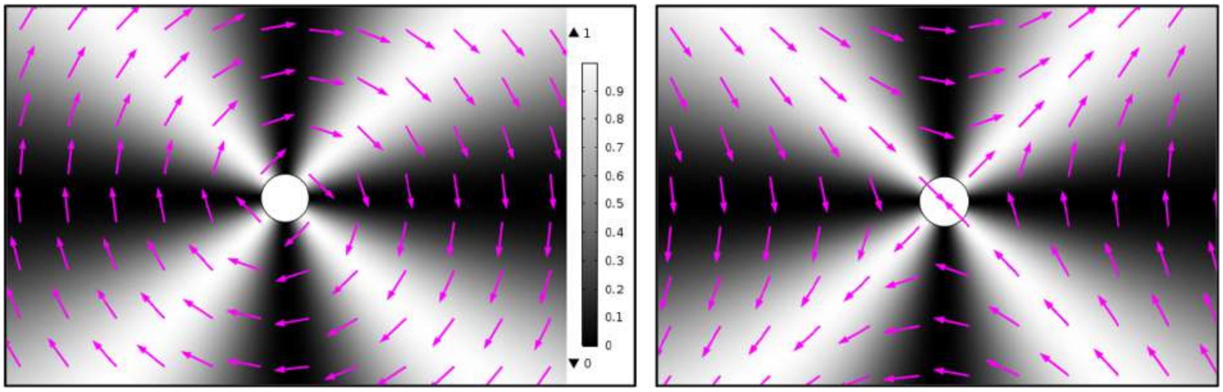

Figure 2.21 – (a) Tangential +1 defect with $\theta_1 = -\pi/2$. (b) Twofold -1 defect with $\theta_2 = \pi/2$. The pink arrows indicate the *director* orientation.

The calculation method consists in subdividing the large square into smaller parts called finite elements. It is achieved by a particular space discretization in the space dimensions, which is implemented by the construction of a "mesh" of the object: the numerical domain for the solution, which has a finite number of points. Fig. 2.22

---

[3] A type of boundary conditions that impose the value that the solution function needs to take along the domain

shows the discretization of the film geometry into fine mesh. In the very vicinity of the defects, a very fine mesh is used in order optimize the calculations.

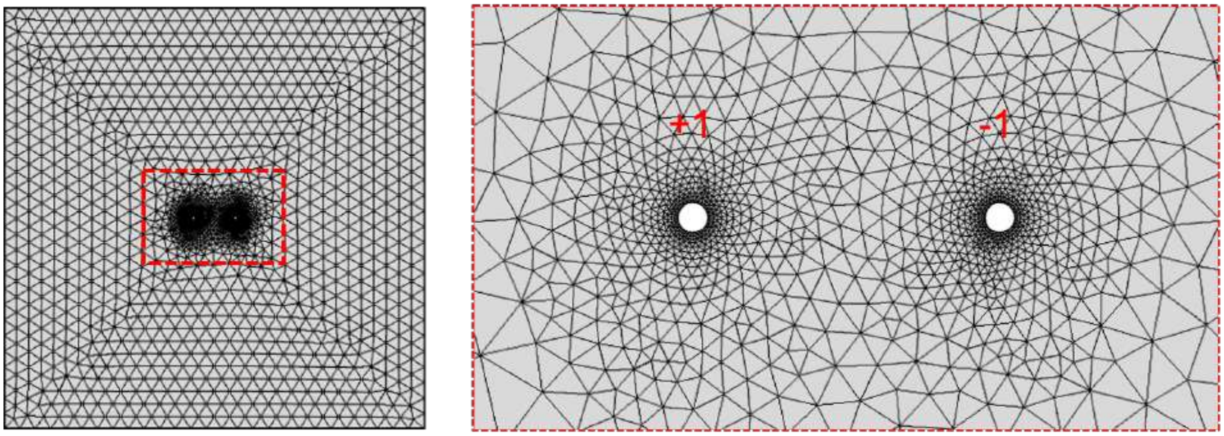

Figure 2.22 – (a) The mesh distribution showing the space dimension discretization into finite elements. (b) Zoom on the region around the defects pair showing finer mesh distribution.

Fig. 2.23 shows an example of simulated defect pair with a topological charges ±1. The square has a dimension of 5 mm $*$ 5 mm and the defect core has a radius of $r_c = 1$ nm. The defects phase were fixed to $\theta_1 = -\pi/2 = -\theta_2$, in order to have defect pairs whose phases match $\delta\theta = 0$. The *director* orientation is indicated by the pink arrows. In agreement with an aligned defect pair, θ appears constant along the connecting line $\vec{r}_{12}$. The boundary conditions at the film edges are not imposed, i.e., "free boundaries". Thus, the far *director* orientation is free to rotate depending on the defects phase. As a consequence, the calculations produce pairs with the minimum possible distortion, because for a matched defect. The misalignment fulfills $\delta\phi = 0$.

2.5.2 Energy calculation

During the following sections we will focus on the evaluation of the pair interaction energy, F, in function of the separation distance, r_{12} and the defects orientational properties, $\delta\theta, \delta\phi$. The interaction energy can be measured by integrating the free energy density f in the one-constant approximation through the film geometry

$$F = \int \frac{K}{2}\left(\left(\frac{\partial n}{\partial x}\right)^2 + \left(\frac{\partial n}{\partial y}\right)^2\right) dxdy. \tag{2.13}$$

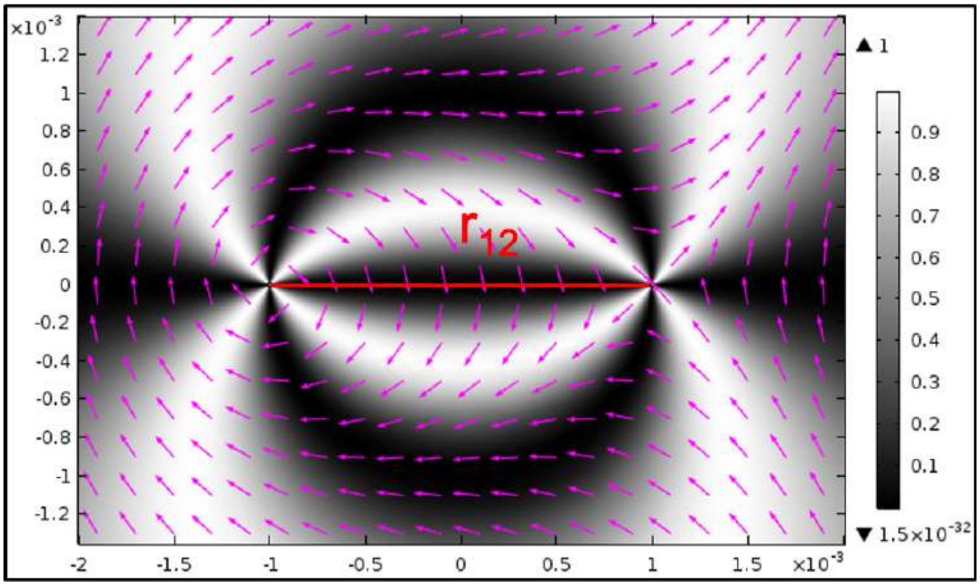

Figure 2.23 – Zoom on a tangential +1 ($\theta_1 = -\pi/2$) and twofold -1 ($\theta_2 = +\pi/2$) defects pair. The full calculation box dimension is 5 mm $*$ 5 mm. The defects core radius $r_c = 1$ nm. The arrows describe the local *director* field orientation. The separation distance r_{12} is equal to 2 mm .

2.5.2.1 The energy measurements as a function of separation distance r_{12}

The interaction energy for a defect pair with opposite topological charges $S_{1,2} = \pm 1$ is expected to be logarithmic dependent on the separation distance r_{12}

$$F = 2\pi K h \ln\left(\frac{r_{12}}{2r_c}\right). \tag{2.14}$$

Fig. 2.24 shows the measurements of the interaction energy for several separation distances between two aligned defect pairs ($\delta\theta = 0$). The data are presented in the semi-log scale and fitted with a linear fit (dashed line). In agreement with Eq. 2.14, the energy is perfectly logarithmic dependent on the separation distance r_{12}.

2.5.2.2 The energy dependence of the mismatch $\delta\theta$

We have shown in the first Chapter that Tang and Selinger [2017] corrected the classical model for the defects interaction in order to consider the mutual defects orientations. In Eq. 1.18, the first term corresponds to the interaction energy given by the model for an aligned and matched defects pair. The additional term is the new contribution, which takes into account the defects mismatch $\delta\theta$.

$$F = 2\pi K h S^2 \ln\left(\frac{r_{12}}{2r_c}\right) + \delta\theta^2 \frac{\pi K h}{2} \frac{\ln(r_{12}/(2r_c))}{[\ln(r_{12}/r_c)]^2}. \tag{2.15}$$

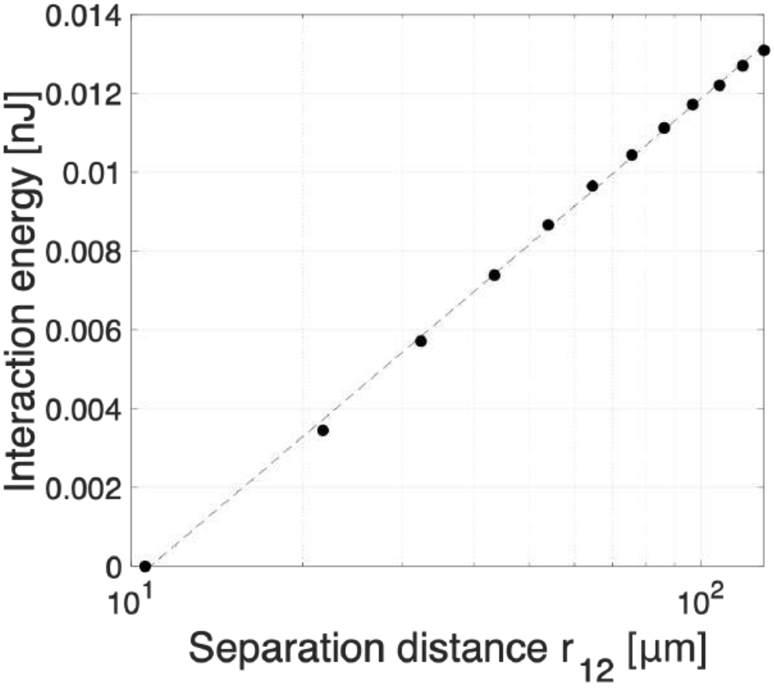

Figure 2.24 – The measurements of the interaction energy in function of the separation distance r_{12} for an aligned defects. The data are presented in the semi-log scale. The dashed line is a linear fit.

We evaluated the interaction energy in function of the mismatch angle $\delta\theta$. The results for several $\delta\theta$ and r_{12} are shown in Fig. 2.25. For each separation distance r_{12}, we rotate the -1 defect clockwise and counter clockwise, which changes the mismatch angle between the pair. A minimum of energy is found at $\delta\theta = 0$, which corresponds to the situation of an aligned pair. When increasing the mismatch $\delta\theta \neq 0$, the energy increases. We found that the latter presents a quadratic dependence on the mismatch angle in agreement with the second term in Eq. 2.15. Moreover, the logarithmic dependence of the energy in function of r_{12} remains valid even for a misaligned pair. For example, for $r_{12} = 50$, 100 and 150 μm respectively for $\delta\theta = 45°$, the energy values follow the logarithmic dependence on the separation distance.

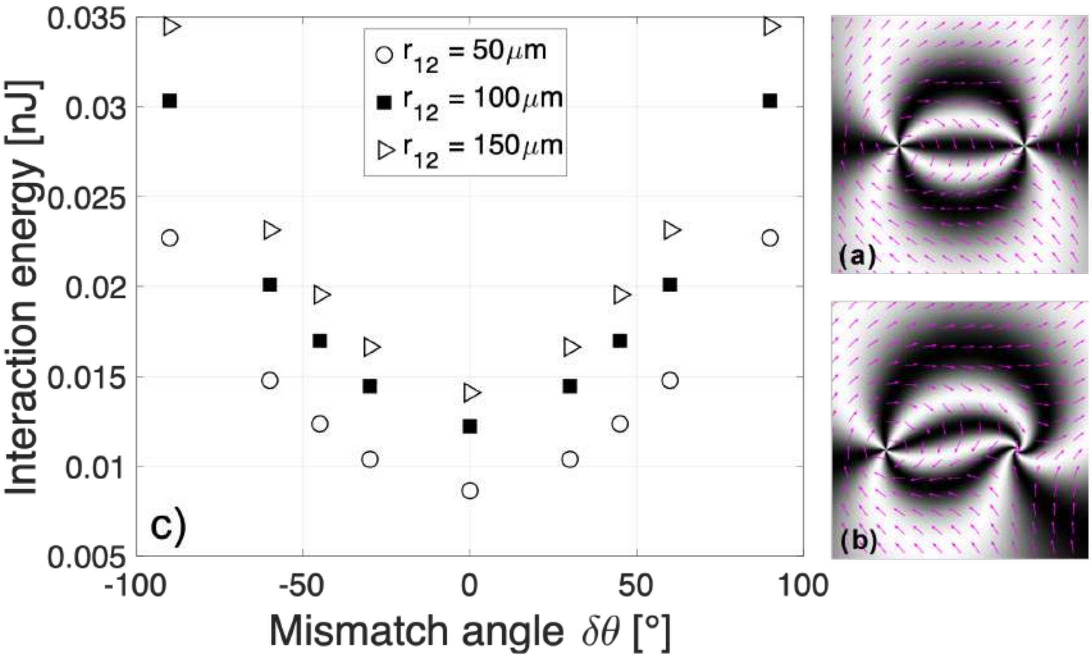

Figure 2.25 – (a) Matched defect pair with topological charges ±1. (b) Mismatched defect pair with a mismatch of $\delta\theta = 90°$. (c) The measurements of the interaction energy in function of $\delta\theta$ for three different separation distances r_{12}.

2.5.2.3 The energy dependence of the misalignment $\delta\phi$

Our recent experiments Missaoui et al. [2020] highlight the importance of the misalignment $\delta\phi$ effects on the annihilation process of the defect pairs. In this section, we check the variation of the energy as function of the misalignment angle. We consider only matched defect pairs ($\delta\theta = 0$). We change the misalignment angle $\delta\phi$ by changing the boundary conditions on the box edges.

Fig. 2.26 shows the measurements of the interaction energy as a function of randomly chosen misalignment angles. A quadratic dependence was found. The energy increases with increasing misalignment angle, i.e, increasing the elastic distortion created with respect to the homogeneous far director field. Nevertheless, the minimum of energy is found for an aligned pair $\delta\phi = 0$. The order of magnitude of the misalignment energies is greater than in the case of the mismatch energies.

In agreement with the experimental results, the matched defect pair ($\delta\theta = 0$) with zero misalignment $\delta\phi = 0$ is the most stable state with the lowest possible elastic distortion. In such situation, the -1 defect do not need to rotate and the exerted external torque is null. Thus, the pair annihilate in a straight path. This is in contrast with the misaligned and mismatched pairs, where the outer director field exerts a torque that tends to minimize the elastic distortion by rotating the pairs.

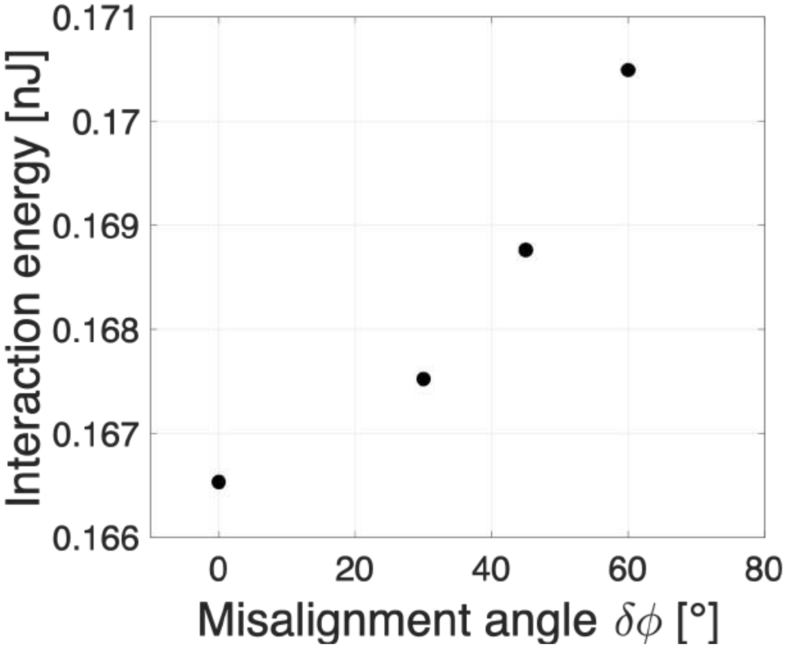

Figure 2.26 – Measurements of the interaction energy in function of $\delta\phi$. Matched defect pair is considered ($\delta\theta = 0$). For $\delta\phi = 0$, the defect pair has the lowest distorted configuration.

2.5.2.4 The correlation between misalignment $\delta\phi$ and mismatch $\delta\theta$

The experimental results (Fig. 2.16) on the annihilation of misaligned and mismatched defect pairs reveal a correlation between the mismatch and the misalignment angle as $\delta\theta \approx -\delta\phi$.

The method that can be used to numerically check the correlation between the two angles consists of: fixing the far *director* orientation at a certain angle, i.e, using solid boundary conditions at the box edges with a defined angle; then changing the mismatch angle $\delta\theta$. This has been done for misalignment angles $\delta\phi = -30°, -45°, -60°$. Fig. 4.6 shows the interaction energy in function of the mismatch angle. The minimum was found for $\delta\theta \approx -\delta\phi$. This result is consistent with the experimental investigations. The relation $\delta\theta \approx -\delta\phi$ is confirmed.

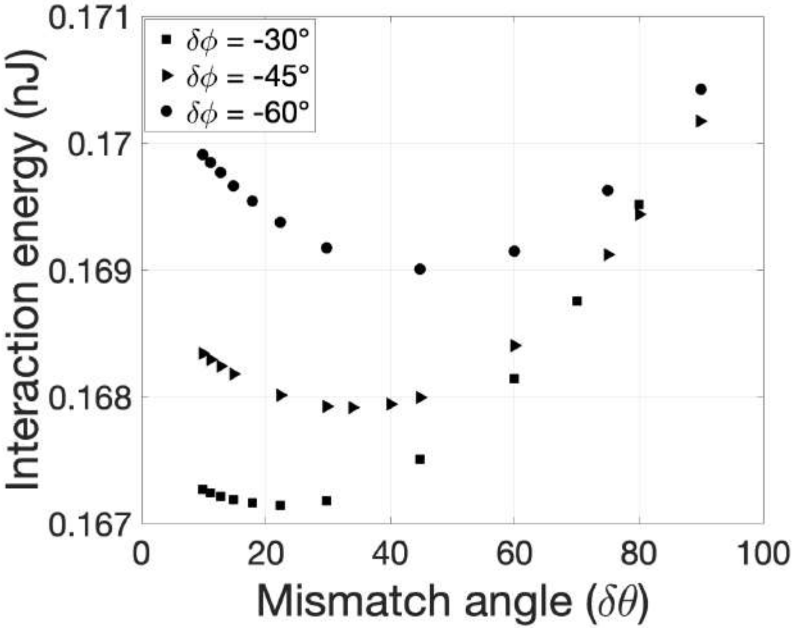

Figure 2.27 – The interaction energy calculations in function of the mismatch $\delta\theta$ for fixed misalignment $\delta\phi$. The minimum of the interaction energy is found for a mismatch angle $\delta\theta \approx -\delta\phi$.

2.5.3 Summary

To conclude, we have shown that quasi-equilibrium solutions for defect pairs with opposite topological charges ±1 in two-dimensional geometry can be reproduced via Finite Element Methods (FEM). The use of specific boundary conditions allow to control the defects phase on the one hand and the far *director* orientation on the other hand. Such a control leads to more realistic calculations as it reproduces the experimental conditions. The interaction energy can be calculated by integrating the free energy density trough the simulation geometry (see Eq. 2.13).

The classical model for defects interaction treats all disclination pairs as aligned and matched. We have shown that the mutual defects orientation has an important effects on their interaction. We performed calculations in a 2D geometry in order to check the dependency of the interaction energy according to: the separation distance r_{12}, the mismatch $\delta\theta$ and misalignment $\delta\phi$.

Our results are in good agreement with the experimental investigations. The interaction energy is found to be logarithmically dependent on the separation distance r_{12} for matched pairs ($\delta\theta = 0$) as well as for mismatched ones ($\delta\theta \neq 0$). Even though, the classical model neglects the defect orientation effects, the measurements of the interaction energy as a function of the mismatch angle has a quadratic dependency (Fig. 4.6). The mismatched pairs possess higher energy than the matched ones. This explains why, in the experiments, mismatched pairs reduce the mismatch during their way to annihilate.

We have shown in our experiments that the far *director* field orientation affects the defect dynamics. We have considered the misalignment of the pairs with respect to the far director field in our calculations. We have found that the interaction energy is a quadratically dependent function of $\delta\phi$ (Fig. 2.26). Our calculations confirm the correlation between $\delta\theta$ and $\delta\phi$ that has been found experimentally. The two parameters are not independent and the minimization of the elastic distortion take place by reducing $\delta\theta$ and $\delta\phi$ simultaneously. The model of Tang and Selinger [2017] considers K_S to be equal to K_B, similarly to our simulations. The fact that in the simulations we recover the relationship $\delta\theta = -\delta\phi$ strongly suggest that the observed disagreement with the model is finally related to the non-consideration of the *c-director* far-field in the model.

2.6 Summary

The dynamic behavior of topological defects in smectic liquid crystals, which bear striking analogies to defect structures of a wide variety of physical systems, was investigated. We have performed experiments in freely suspended *SmC* films, which behave as quasi two-dimensional polar nematics. Therefore, we have introduced a preparation technique for isolated defect pairs. The attraction and annihilation of disclination points with topological charge ±1 have been studied. Even though, the classical models remain valid for very specific case, we demonstrated that this classical description, which employs the one-constant elastic approximation and describes the defect dynamics by quasi-equilibrium states of aligned defects, fail to describe their annihilation properly because it disregards the mutual orientation of the defects and the pair's orientation with respect to the far director field.

We have demonstrated that the shape of trajectories of mutually annihilating topological defect pairs is equally influenced by their relative orientations (mismatch) and the surrounding vector field (misalignment), both being of equal importance. They are not independent of each other. We suspect that this is a common feature of topological defect pairs in many other 2D systems. During the defects approach, the misalignment $\delta\phi$ and mismatch $\delta\theta$ decay to zero, with a square root of time dependency. We have shown that even after the improvement of the classical model with new terms that take into account the mutual orientation of the defects on their dynamics Tang and Selinger [2017], the experimental results are partially in disagreement with the theoretical predictions. The expression of correlation between the two angles $\delta\phi$ and $\delta\theta$ that we have found experimentally is different from the one predicted by the new model. One assumes that in the case of mismatched and misaligned pairs, the *c-director* configurations during the approach are qualitatively similar to quasi-equilibrium states determined from the solutions of the Laplace equation Tang and Selinger [2017], but differ quantitatively. This may be caused in our films by the finite film geometry where the fixed far *c-director* cannot be disregarded.

In the second part of the chapter, we have shown that the defects pair of topological charges ±1 in a freely suspended film can be reproduced in simulation. We can change the defect properties such as their phases and the misalignment with respect to the far field. Using Finite Element Methods, we measured the interaction energy between the two defects and we have determined its dependency on the system parameters such as separation distance and the defects orientation. The fact in particular that we have recovered the experimentally observed relationship between $\delta\phi$ and $\delta\theta$, whereas I considered $K_S = K_B$ in the model, also confirms the dominating influence of the far-field *director*.

During our experimental study, we have noticed an anisotropy of the velocity of the two defects. The speed of the positive defect is enhanced up to 1.8 faster than that of the negative defect. It has been shown that the difference in defect speeds is mainly associated with the backflow effects Tóth et al. [2002]Svenšek and Zumer [2003]Blanc et al.

[2005]. It was reported that unequal elastic constants can also induce similar anisotropy but the main reason is attributed to the backflow Svenšek and Zumer [2003]. Therefore, we dedicate the next chapter to the study of the hydrodynamics of topological defects in freely suspended *SmC* films.

2.7 References

Blanc, C., Svensek, D., Zumer, S., and Nobili, M. (2005). Dynamics of nematic liquid crystal disclinations: The role of the backflow. *Physical Review Letters*, 95:097802. 66, 86

Brugués, J., Ignés-Mullol, J., Casademunt, J., and Sagués, F. (2008). Probing elastic anisotropy from defect dynamics in langmuir monolayers. *Phys. Rev. Lett.*, 100:037801. 49

Bäuerle, C., Bunkov, Y., Fisher, S., Godfrin, H., and Pickett, G. (1996). Laboratory simulation of cosmic string formation in the early universe using superfluid 3he. *Nature*, 382:332–334. 49

Chuang, I., DURRER, R., TUROK, N., and YURKE, B. (1991). Cosmology in the laboratory: Defect dynamics in liquid crystals. *Science*, 251(4999):1336–1342. 49

Dierking, I., Marshall, O., Wright, J., and Bulleid, N. (2012). Annihilation dynamics of umbilical defects in nematic liquid crystals under applied electric fields. *Phys. Rev. E*, 71:061709. 66

Guimarães, R. R., Mendes, R. S., Fernandes, P. R. G., and Mukai, H. (2013). Annihilation dynamics of stringlike topological defects in a nematic lyotropic liquid crystal. *Journal of Physics: Condensed Matter*, 25(40):404203. 49

Harth, K. and Stannarius, R. (2020). Topological point defects of liquid crystals in quasi-two-dimensional geometries. *Frontiers in Physics*, 8:112. 54, 61

Hertel, R. and Schneider, C. M. (2006). Exchange explosions: Magnetization dynamics during vortex-antivortex annihilation. *Phys. Rev. Lett.*, 97:177202. 49

Jonathan, S. (2016). Introduction to the theory of soft matter- from ideal gases to liquid crystals. *Springer International Publishing AG*. 49

Missaoui, A., Harth, K., Salamon, P., and Stannarius, R. (2020). Annihilation of point defect pairs in freely suspended liquid-crystal films. *Phys. Rev. Research*, 2:013080. 56, 59, 62, 65, 66, 68, 70, 71, 73, 82

Muševič, I., Škarabot, M., Tkalec, U., Ravnik, M., and Žumer, S. (2006). Two-dimensional nematic colloidal crystals self-assembled by topological defects. *Science*, 313(5789):954–958. 49

Muševič, I. (2019). Interactions, topology and photonic properties of liquid crystal colloids and dispersions. *The European Physical Journal Special Topics*, 227:2455–2485. 49

Oswald, P. and Pieranski, P. (2006). *Smectic and columnar liquid crystals: Concepts and physical properties illustrated by experiments*. CRC Press. 50

Polkovnikov, A., Sengupta, K., Silva, A., and Vengalattore, M. (2011). Colloquium: Nonequilibrium dynamics of closed interacting quantum systems. *Rev. Mod. Phys.*, 83:863–883. 49

Poulin, P., Stark, H., Lubensky, T. C., and Weitz, D. A. (1997). Novel colloidal interactions in anisotropic fluids. *Science*, 275(5307):1770–1773. 49

Poulin, P. and Weitz, D. A. (1998). Inverted and multiple nematic emulsions. *Phys. Rev. E*, 57:626–637. 49

Rissanen, I. and Laurson, L. (2016). Coarsening dynamics of topological defects in thin permalloy films. *Phys. Rev. B*, 94:144428. 49

Robert, R. (2003). Chapter 1 statistical hydrodynamics (onsager revisited). *Handbook of Mathematical Fluid Dynamics*, 2. 49

Rosenblatt, C. and Amer, N. M. (1980). Optical determination of smectic a layer spacing in freely suspended thin films. *Applied Physics Letters*, 36(6):432–434. 53

Ruutu, V. M. H., Eltsov, V., Gill, A. J., Kibble, T. W. B., Krusius, M., Makhlin, Y. G., Plaçais, B., Volovik, G. E., and Xu, W. (1996). Vortex formation in neutron-irradiated superfluid 3he as an analogue of cosmological defect formation. *Nature*, 382:334–336. 49

Stannarius, R. and Harth, K. (2016). Defect interactions in anisotropic two-dimensional fluids. *Phys. Rev. Lett.*, 117:157801. 56

Svenšek, D. and Zumer, S. (2003). Hydrodynamics of pair-annihilating disclinations in smc films. *Phys. Rev. Lett.*, 90:155–501. 66, 86, 87

Tang, X. and Selinger, J. V. (2017). Orientation of topological defects in 2d nematic liquid crystals. *Soft Matter*, 13:5481–5490. 59, 60, 61, 63, 69, 70, 72, 74, 76, 77, 80, 85, 86

Tang, X. and Selinger, J. V. (2020). Annihilation trajectory of defects in smectic-*c* films. *Phys. Rev. E*, 102:012702. 74

Tkalec, U., Ravnik, M., Čopar, S., Žumer, S., and Muševič, I. (2011). Reconfigurable knots and links in chiral nematic colloids. *Science*, 333(6038):62–65. 49

Tóth, G., Denniston, C., and Yeomans, J. M. (2002). Hydrodynamics of topological defects in nematic liquid crystals. *Phys. Rev. Lett.*, 88:105504. 66, 86

Vromans, A. J. and Giomi, L. (2016). Orientational properties of nematic disclinations. *Soft Matter*, 12:6490–6495. 58, 69

Wachowiak, A., Wiebe, J., Bode, M., Pietzsch, O., Morgenstern, M., and Wiesendanger, R. (2002). Direct observation of internal spin structure of magnetic vortex cores. *Science*, 298(5593):577–580. 49

Weiler, C., Neely, T., Scherer, D., Bradley, A., Davis, M., and Anderson, B. (2008). Spontaneous vortices in the formation of bose-einstein condensates. *Nature*, 455:948–51. 49

Zurek, W. (1996). Cosmological experiments in condensed matter systems. *Physics Reports*, 276(4):177 – 221. 49

Chapter 3

Hydrodynamics of Pair-Annihilating Disclinations in Freely Suspended Smectic Films

> *"I am one of those who think that science is of great beauty. A scientist in his laboratory is not only a technician: he is also a child placed in front of natural phenomena that impress him like fairy tales."*
>
> Marie Curie

Contents

3.1 Introduction

Topological defects play an important role in the macroscopic properties of materials such as mechanics and electrical conductivity. Although in some applications defects may be absolutely necessary, for example in topological networks for liquid crystal displays (LCDs) Kim and Serra [2020], in other areas, defect-free structures are necessary. The study of defect dynamics with taking into account hydrodynamic effects is very important for this purpose.

The annihilation of oppositely-charged disclinations represents an appropriate framework for hydrodynamic research. This dynamic process can be observed by optical microscopy (see chapter 2), which allows the interaction of mutual defects to be studied directly. Classical theories have been developed to describe the dynamics of topological defects Dafermos and Constantine [1970]; Kleman [1977]; Minoura et al. [1997]. It is predicted that the disclinations of opposite topological charges attract each other by a potential that scales logarithmically with the distance of separation of the defects r_{12} and an interaction force such as $1/r_{12}$. The balance between this last elastic force and the drag force (Eq. 1.21) predicts that both defects should move at the same speed given by Eq. 1.22.

In liquid crystals, topological defects move in a liquid and therefore it can be expected that the hydrodynamic flow will affect their dynamics. In our recent study detailed in Chapter 2 of the manuscript Missaoui et al. [2020], we have shown that the experimental results deviate from theoretical predictions. In thin films, defects move towards the annihilation point with different velocities according to their topological charges. In fact, such asymmetry has been previously studied by numerical calculations by Dierking et al. [2005]; Svenšek and Zumer [2003]; Tóth et al. [2002] and further commented through approximate analytic arguments by Kats et al. [2002]; Sonnet [2005]; Sonnet and Virga [2009]; Tang and Selinger [2019].

When the defect moves, the molecules close to the core are put into rotation. It has been shown that the coupling between the changing director field and the velocity field induces a hydrodynamic motion, called "backflow", which plays an important role in the defects motion. Numerical studies predict that backflow enhance the motion of positive defects and inhibits the motion of negative ones. Thus, the pairs of defects do not annihilate halfway as initially predicted by classical models.

Svenšek and Zumer [2003] have carried out numerical research on the motion of

$S = \pm 1$ defects in freely suspended *SmC* films. The authors showed that unequal Frank elastic constants can induce a similar asymmetric velocity, even when the backflow is disregarded. This result can be explained by the peculiarities of the +1 defect. Unequal elastic constants drives the positive defect to be in a state of pure splay or bend near the core, which changes its motion with the tendency to move into a region with the corresponding deformation and a velocity depending mainly on a Frank constant. The negative defect includes both types of deformation. Its speed depends on their average. This may explain why -1 defect may be less affected by the enhancement in motion.

So far, important numerical work has been carried out on the hydrodynamics of topological defects. The difference in velocity is mainly associated with the effects of backflow. It has been shown that unequal elastic constants have a smaller impact on the motion of defects Svenšek and Zumer [2003].

To the best of our knowledge, no experimental work has been reported to verify existing theories on ±1 defects hydrodynamic behavior and flow field in freely suspended *SmC* films. The aim of this chapter is to study experimentally the backflow effects on the annihilation of a ±1 topological defect pair in freely suspended *SmC* films.

3.2 Theoretical Model

3.2.1 The *SmC* hydrodynamic theory

The Ericksen–Leslie equations govern the hydrodynamics of nematic liquid crystals Leslie [1979]. They couple the flow field to the evolution of the nematic *director* $\vec{n}$. For the *SmC* liquid crystals, the hydrodynamics theory was reported by Carlsson et al. [1995]. Later, Svenšek and Zumer [2003] have simplified a numerical model for the hydrodynamics of ±1 defects in freely suspended *SmC* films. The authors reported that for the case of a *SmC* film with variations only in two dimensions and with straight smectic layers, the *SmC* theory reduces exactly to the Ericksen-Leslie theory of the nematics in 2D geometry.

It has been shown Carlsson et al. [1995]; Leslie [1979] that the director distortions induce stress. Svenšek and Zumer [2003] derived the elastic stress tensor, σ^e, in the case of *SmC* with straight layers, and no gradients in the direction of the layer normal as

$$\sigma^e_{ij} = -\frac{\partial f}{\partial(\partial_i c_k)}\partial_j c_k, \tag{3.1}$$

Where $\vec{c}$ is the smectic director. Repeated tensor indices being subject to the usual summation convention. f is the free energy density of the SmC phase (Eq. 1.8).

The viscous stress was also derived in the same simplification as Svenšek and Zumer [2003]

$$\begin{aligned}\sigma_{ij}^{v} = & \frac{1}{2}\gamma_1(N_i c_j - c_i N_j) + \frac{1}{2}\gamma_2(N_i c_j - c_i N_j) \\ & + \alpha_1 c_k c_l A_{kl} c_i c_j + \alpha_4 A_{ij} + \alpha_5 c_i A_{jk} c_k \\ & + \alpha_6 c_j A_{ik} c_k.\end{aligned} \tag{3.2}$$

The coefficients $\alpha_1, \alpha_2, ..., \alpha_6$ are called the Leslie viscosity coefficients, or simply the Leslie viscosities. $\gamma_1 = \alpha_3 - \alpha_2$ is the rotational viscosity, and $\gamma_2 = \alpha_3 + \alpha_2$. N_i is the co-rotational time flux of the director, $N_i = \dot{c}_i + W_{ij} c_j$. With $\dot{c} = \frac{\partial c}{\partial t} + (v.\nabla)c$ and the rate of vorticity tensor $W_{ij} = \frac{1}{2}(\partial_i v_j - \partial_j v_i)$. The rate of strain tensor $A_{ij} = \frac{1}{2}(\partial_i v_j + \partial_j v_i)$ Carlsson et al. [1995]; Svenšek and Zumer [2003].

The generalized elastic and viscous forces acting on the vector $\vec{c}$ are given by Svenšek and Zumer [2003]

$$\begin{aligned} h_i^e &= -(A - Cc^2)c_i + K_S \partial_i^2 c_i + (K_B - K_S)\partial_i \partial_j c_j \\ h_i^v &= -(\gamma_1 N_i + \gamma_2 A_{ij} c_j) \end{aligned} \tag{3.3}$$

Thus, the equation of motion for the *c-director* can be written as the following Svenšek and Zumer [2003]

$$h^e + h^v = 0. \tag{3.4}$$

The hydrodynamics equations can be solved numerically. An example of solution for the case of ±1 defect pairs is shown in the next section.

3.2.2 Hydrodynamics of annihilating ±1 defect pair

Svenšek and Zumer [2003] solved the coupled partial differential equations using the finite difference discretization method. They performed calculations for a pair of ±1 defects at the center of a square geometry. They set the flow velocity v to zero at the boundaries of the square and set the tilt angle to $\varphi = 30°$. Their results show that the hydrodynamic flow influences the motion of the defects. The authors reported an asymmetry in the velocity field during the ±1 defects annihilation. The velocity of the positive defect is increased by about 100% due to the backflow.

The results of Svenšek and Zumer [2003] are presented in Fig. 3.1. We first consider the trajectory (c). This one was obtained by not taking into account the backflow. In accordance with the classical model, the two defects move at the same speed and annihilate halfway between their initial position. Trajectories (a), (b) and (d) are obtained with taking into account the backflow. A significant asymmetry of the defect velocity and a modification of the annihilation time are evident compared to the non-hydrodynamic treatment (curve (c)). (Note that trajectories (e) and (f) are discussed later).

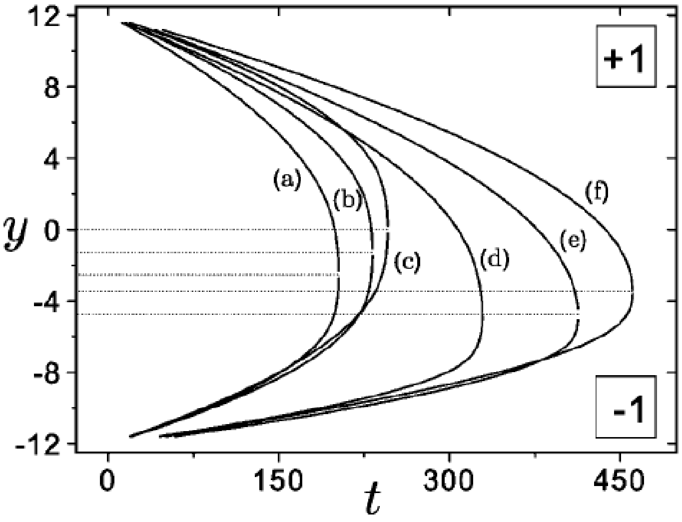

Figure 3.1 – Position of the defects vs time. The cases with one elastic constant: (a) Radial defect with S = +1: $\theta_1 = 0$ (b) Tangential S = +1: $\theta_1 = \pi/2$, (c) without flow, (d) Radial S = +1 :$\theta_1 = 0$ with the rotational viscosity γ_1 coefficient doubled. Case for $K_S \neq K_B$ (e) Radial S = +1: $\theta_1 = 0$ and $K_S/K_B = 2/3$ (f) Tangential S = +1: $\theta_1 = \pi/2$ and $K_S/K_B = -2/3$. Reprinted from Svenšek and Zumer [2003]. Copyright (2003) by The American Physical Society.

It has been shown that in the hydrodynamic equations; the two terms γ_1 and γ_2 which contain the time derivative of the order parameter $\dot{c}$ in the viscous stress tensor (Eq. 4.2), as well as the elastic stress tensor (Eq. 4.1) represent the main sources that drive the Carlsson et al. [1995] flow. Their symmetries was analyzed by Svenšek and Zumer [2003]; Tóth et al. [2002] because any term of the stress tensor, invariant with respect to the transformation $\vec{c} \rightarrow -\vec{c}$, treat both defects in the same way and do not contribute to the flow asymmetry.

Under the one-constant approximation, the elastic stress is symmetric by definition Carlsson et al. [1995]. Thus, during the defect motion the elastic stress generates a symmetric flow for both defects with respect to the rotation around the perpendicular axis. Moreover, it contributes to the reduction of the inter-defect separation r_{12} and thereby to the free energy of the system.

In the viscous stress tensor (Eq. 4.2), the term γ_1 turns out to be antisymmetric with respect to the transformation $\vec{c} \rightarrow -\vec{c}$, Svenšek and Zumer [2003]. The flow driven by γ_1 is the opposite flow for the -1 defect with respect to the flow close to the +1 defect. The efficiency of the backflow increases with the ratio of γ_1 to the isotropic viscosity α_4. The term γ_2 has no defined symmetry Svenšek and Zumer [2003]. It contains both symmetrical and antisymmetrical terms. The term γ_2 becomes relevant when the structure of the +1 defect varies from a tangential, which annihilates faster, to a radial one Svenšek and Zumer [2003].

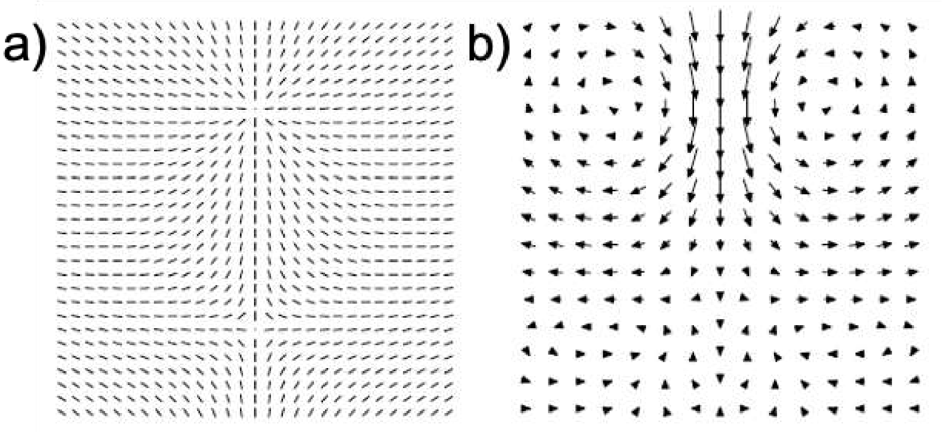

Figure 3.2 – (a) *c-director* field in radial-hyperbolic pair configuration. (b) Flow velocity field showing the strong advection in the vicinity of the +1 defect. No advective flow was observed for the case of the -1 defect. Reprinted from Svenšek and Zumer [2003]. Copyright (2003) by The American Physical Society.

To summarize, it has been shown Svenšek and Zumer [2003]; Tóth et al. [2002] that the flow created by the elastic stress accelerates the two defects symmetrically towards each other, in order to minimize the free elastic energy, thus accelerating the annihilation process. On the other hand, the flow created by the viscous term γ_1 will accelerate one of the defects and slow down the other. Therefore, for the positive defect, the flow fields of the two sources are added together. Thus, the motion of the +1 defect is accelerated. For the negative defect, the two flow field sources are destructively added together, so the contribution in this latter motion is small. This is the main reason why the positive defect always moves faster than the negative one. The flow field around the ±1 pair is shown in Fig. 3.2.

More recently, Tang and Selinger [2019] have numerically studied the motion of half disclinations in 2D nematics in a channel, by taking into account backflow effects. The channel was considered to be infinite in the x-direction but finite in the y-direction. Strong planar anchoring has been used on the top and bottom surfaces of the channel, at $y = \pm d/2$. The authors derived new equations for the velocities of the $\pm 1/2$ defect pair as following

$$\begin{aligned} v^+ &= \frac{2\pi K}{\gamma_1 d \log\frac{d}{2r_c}} \times \left[1 + \frac{\gamma_1^{1/2}}{2^{3/2}\alpha_4^{1/2}} \frac{\left(\log\frac{d}{2r_c}\right)^2 + \left(\log\frac{d}{2r_c}\right) - \frac{5}{2}}{\log\frac{d}{2r_c}} + \dots \right] \\ v^- &= \frac{2\pi K}{\gamma_1 d \log\frac{d}{2r_c}} \times \left[1 + \frac{\gamma_1^{1/2}}{2^{3/2}\alpha_4^{1/2}} \frac{\left(\log\frac{d}{2r_c}\right)^2 - 7\left(\log\frac{d}{2r_c}\right) + \frac{11}{2}}{\log\frac{d}{2r_c}} + \dots \right], \end{aligned} \tag{3.5}$$

Where K is the elastic constant and r_c is the core radius. The first term is the usual defect velocity given by the classical model (See section.1.3.1), which is identical for positive and negative defects. The new term takes into account the contributions of the viscosity parameters γ_1 and α_4. We recall that the efficiency of backflow increases with the ratio of γ_1 to the isotropic viscosity α_4 Svenšek and Zumer [2003]. The authors indicated that the new contribution is negligible in the case of an infinite flow viscosity α_4, for a material that cannot flow. However, when α_4 decreases, the defect velocity increases and becomes considerably faster for the positive defect as shown in Fig. 3.3.

The previous investigations shown in Fig. 3.1 and Fig. 3.3 are performed under the one-constant approximation ($K = K_S = K_B$) Svenšek and Zumer [2003]; Tang and Selinger [2019]. In most of the models, the asymmetric velocity of the defects is mainly attributed to the backflow effects. However, a more accurate model must incorporate the effects of elastic anisotropy. Brugués et al. [2008] have shown that unequal Frank constants induce a similar asymmetric velocity. This influences the defect drag force given in Eq. 1.21. Brugués et al. derived new equations for the drag force for the ±1 pair of defects moving with velocity v in a restricted domain of radius R as

$$\begin{aligned} F^+_{drag} &\approx \pi\gamma_1 v \ln\frac{R}{r_c} \\ F^-_{drag} &\approx \frac{1}{2} v \ln\frac{R}{r_c} \int_0^{2\pi} \left[1 + \frac{1}{\pi}\sqrt{\frac{1+\alpha\pi^2\cos(2\theta)}{1+\alpha\cos(2\theta)}} \right] d\theta, \end{aligned} \tag{3.6}$$

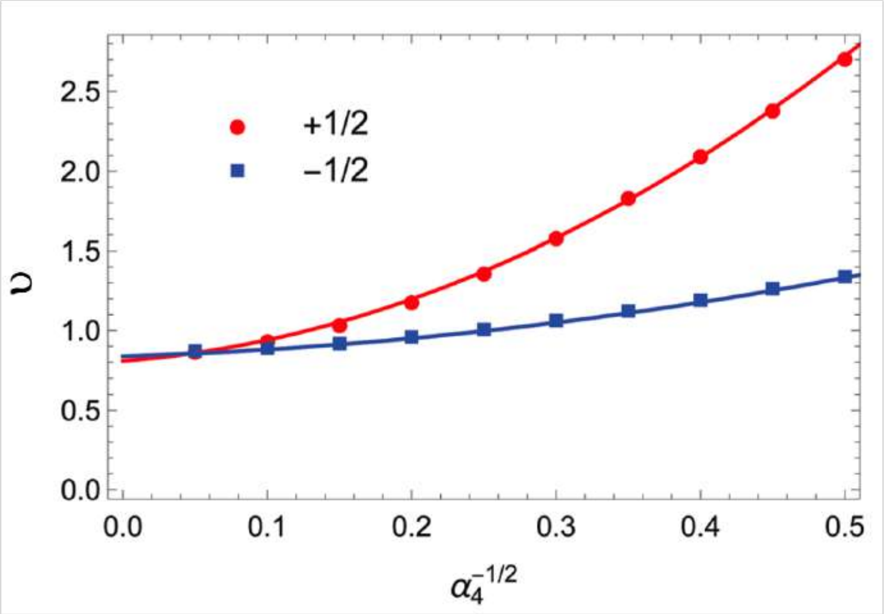

Figure 3.3 – Defects velocities as functions of the flow viscosity, α_4 for the case of 1/2 disclinations. The solid line is a quadratic fit. Reproduced from Tang and Selinger [2019] with permission from The Royal Society of Chemistry.

$\alpha = (K_S - K_B)/(K_S + K_B)$ is scaled elastic anisotropy. We notice that the drag force equation, F^{+}_{drag}, for the S = +1 defect has the usual type given by the classical model (Eq. 1.21). This is explained by the fact that the S = +1 defects are not affected by the elastic anisotropy and their symmetry can be a pure bend or splay (See section.2.3.1). It is in particular the drag force equation for defect S = -1 which must take into account the elastic anisotropy.

The effects of unequal Frank elastic constants ($K_S \neq K_B$) were reported in the numerical study of Svenšek and Zumer [2003]. An asymmetry in the velocity of the two defects was demonstrated even without taking the backflow into account. Curves (e) and (f) in Fig. 3.1 show that, considering several ratios of K_S/K_B, the positive defect moves faster than the negative one up to the annihilation point. However, the effects of unequal elastic constants are weak compared to those of backflow in freely suspended *SmC* films or 2D nematics Svenšek and Zumer [2003]; Tóth et al. [2002].

3.2.3 Summary

The velocity asymmetry of the topological defects observed in the experiments Missaoui et al. [2020] was studied theoretically Brugués et al. [2008]; Svenšek and Zumer

[2003]; Tang and Selinger [2019]; Tóth et al. [2002]. This phenomenon was mainly attributed to the effects of backflow. Unequal elastic constants can also induce such asymmetry, but with less effects than backflow Svenšek and Zumer [2003]. It has been shown that the +1 defect is subject to strong advection due to backflow (Fig. 3.2), which accelerates its movement Svenšek and Zumer [2003].

Although the theory of hydrodynamics of topological defects in *SmC* liquid crystals was introduced a few years ago, there have been no experimental attempts to verify the theoretical predictions, for example the strong advection in the vicinity of positive defects. In the following section, we present the first experiments carried out to test the effects of backflow on the annihilation of $S = \pm 1$ dislocation pairs in free suspended *SmC* liquid crystal films.

3.3 Experimental Setup

3.3.1 The liquid crystal and fluorescent dye

Experimental investigations on the flow behavior around the $S = \pm 1$ defects pair are based on a dye bleaching technique. The mixture of equal volumes 5-n-octyl-2-[4-(n-hexyloxy)phenyl]pyrimidine and 5-n-decyl-2-[4-(n-octyloxy) phenyl]pyrimidine, that exhibits a *SmC* room temperature is doped with 1 wt% of Nile Red dye, 9-diethylamino-5H-benzo[α]ph-enoxazine-5-one. The *SmC-dye* mixture is used to draw freely suspended films on a metallic holder. Defect pairs are created by piercing of the homogeneously oriented freely suspended film using a glass tip. The dynamics of the defects are observed by means of fluorescence microscopy.

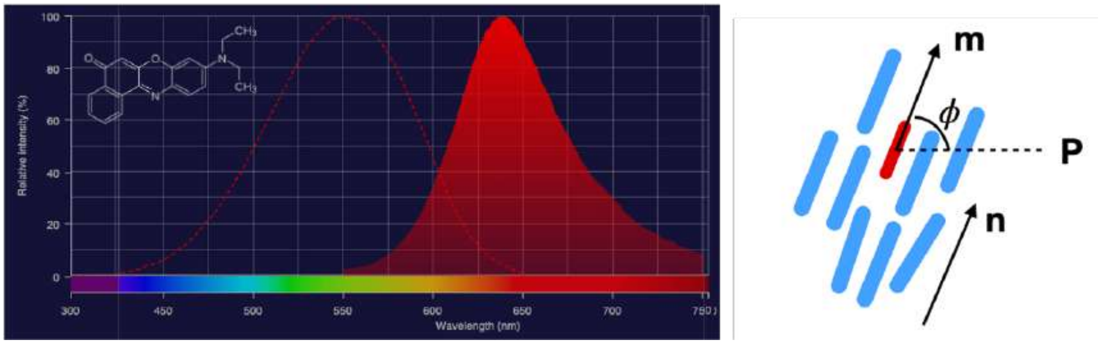

Figure 3.4 – Nile Red fluorescent spectra showing the excitation and the emission spectra. The inset shows the chemical formula. Reprinted from Thermofisher website (www.thermofisher.com).

As shown in Fig. 3.4, Nile red has a maximum excitation of about $\lambda_{\text{Exc}} = 550$ nm (green), and a maximum emission of about $\lambda_{\text{Emm}} = 638$ nm (red). The dye molecules align with the director and cause an anisotropic absorption and emission determined by their orientation (Fig. 3.4, right). The excitation is performed by linearly polarized laser light. The adsorption efficiency of the linearly polarized light is determined by the angle between the polarization direction P and the transition dipole moment m Smalyukh [2007]. The latter is given by the alignment of the director. Since the adsorption efficiency is proportional to $\cos^2(\phi)$, where ϕ is the angle between P and m, this allows mapping the director field using the intensity of the emitted fluorescence as shown in Fig. 3.5.

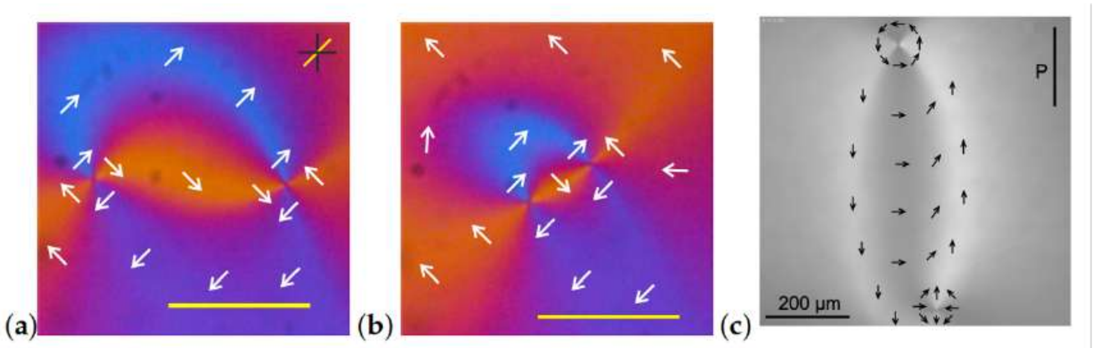

Figure 3.5 – Snapshots of two defect pairs: The +1 defect has always tangential orientation of the *c-director* near the core. The -1 defect is initially rotated respective to the partner (in mismatch) so that the director field along a straight line connecting the cores is not uniform. Image (a) was recorded 16 s before annihilation. During the mutual approach, the mismatch angle gradually reduces to zero. This state is almost reached in image (b), 3 s before annihilation. Yellow bars symbolize 50 μm. Images were recorded in polarized light with crossed polarizers (black lines) and a diagonal wave plate (slow axis: diagonal yellow line). Bluish regions characterize the *c-director* in northeast or southwest direction, while orange regions indicate a *c-director* orientation in southeast or northwest directions. In magenta regions, the *c-director* is either horizontal or vertical in the images. (c) Defects pair observed in fluorescence mode (top: +1 defect, bottom: -1 defect). The black arrows sketch the *c-director*. The polarizer orientation is indicated by a black bar. Images (a,b) are courtesy of Péter Salamon and Kirsten Harth. Reprinted from Missaoui et al. [2021].

3.3.2 The confocal microscope

A confocal microscope is an optical microscope that has the property of producing images of very shallow depth of field. By setting the focal plane of the lens at different depth levels in the sample, it is possible to create series of images from which a three-dimensional representation of the object can be obtained. The confocal microscope works with reflected light or fluorescence. In general, lasers are used as the light sources. This is called confocal laser scanning microscope (CLSM).

The fluorescence of freely suspended films made of the *SmC-dye* mixture is observed by means of Leica confocal laser scanning microscope TCS SP8. This CLSM is characterized by high sensitivity, where a photomultiplier tube detector (PMT) is used to detect wavelength in the range 580 nm-620 nm, with high performance objectives with motorized correction ring to adapt to the depth of the sample. The light sources are four laser sources with wavelengths of 405 nm, 488 nm, 552 nm and 638 nm respectively. The four lasers are used to bleach the dye molecules in the film into circular spots, hereafter referred to as ROI (region of interest). The bleached spots appear on the detector with a contrast different from that of the unbleached background film. They are then used as tracers to study the motion of the flow in the freely suspended thin films.

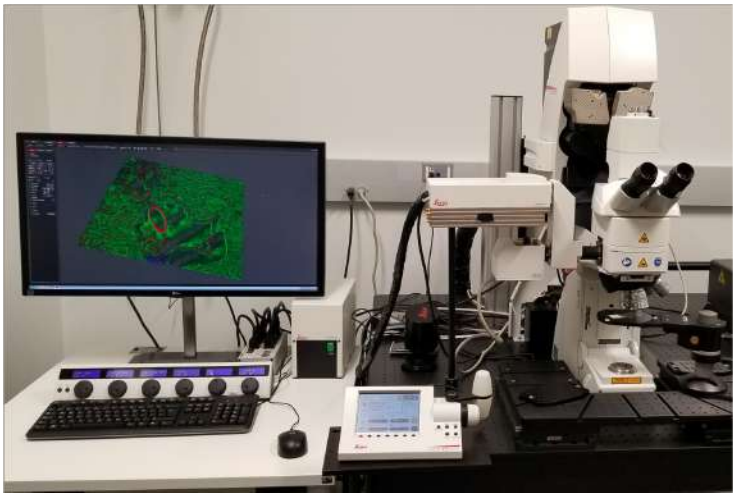

Figure 3.6 – Leica confocal microscope.

3.3.3 Dye photobleaching

Photobleaching is the loss of the fluorescence properties of a molecule. A fluorescent molecule in the excited state can either emit a photon or be in a photochemical reaction that prevents its return to an excitable state. The more a fluorescent substance is excited, the greater the proportion of photobleached molecules, until the fluorescence is extinguished.

After bleaching, the ROI in a resting film appears as a black region with circular shape, as shown in Fig. 3.7a (defect-free film). The recovery of the bleached spot starts when the illumination is suspended; see Fig. 3.7b. The intensity increases continuously and reaches the equilibrium intensity value within approximately 10 s. At the recording rate of one frame per second, we could acquire at maximum 10 frames before the ROI vanishes. Even if the recovery time of the dye would be much larger, there is a second effect that sets a time limit to the method: The diffusion of the Nile Red molecules in the smectic matrix. If one assumes that it is of the same order of magnitude as the typical self-diffusion of low molecular mass liquid crystals at room temperature, $\approx 10^{-11}$... 10^{-10} μm^{2}s^{-1}, the spot will broaden and lose contrast within several seconds. At least, the nearly isotropic diffusion of the dye has no relevant effects on the displacement of the center of the ROI that serves as our marker. The positions of the defects and the bleached ROI were tracked with an accuracy of approximately 1 μm. In addition to the displacement of the ROI spot, its shape can also change under the influence of flow divergence, providing additional information on the structure of the flow field.

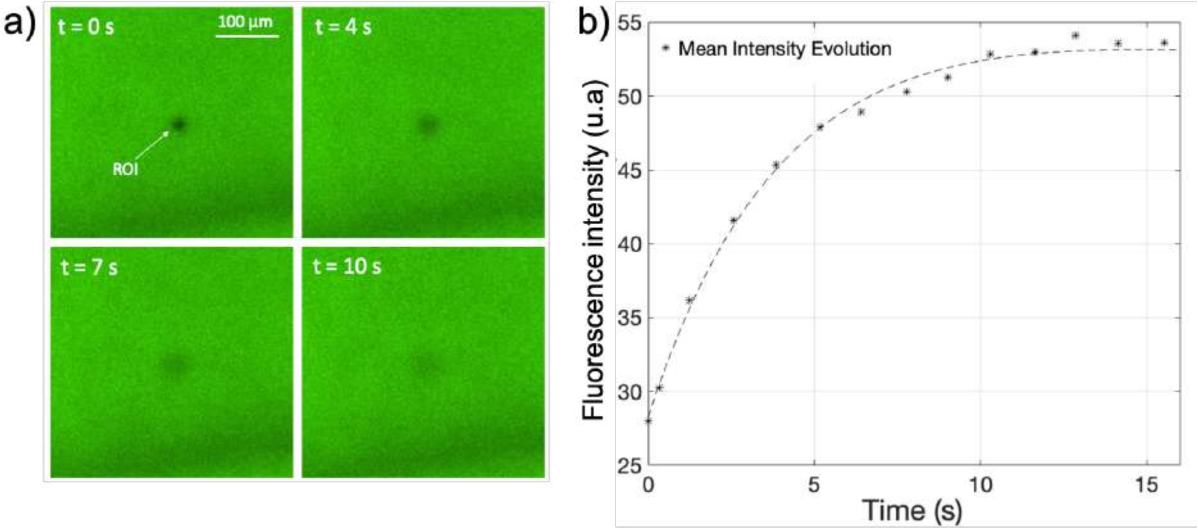

Figure 3.7 – (a) Shows fluorescence of freely suspended films and bleached ROI acquired by the fluorescence microscope. The dark spot will disappear because of the material diffusion over time. (b) The fluorescence intensity of the bleached region over time. ROI are traceable only for about 10 seconds.

In order to extract the material displacement from the bleached spot, the intensity profile was fitted by the Gaussian fit and the position of the maximum was determined for each frame. The disclination pairs are tracked from the images with an accuracy of approximately 1 μm.

3.4 Experimental results

We obtained isolated defect pairs in 29 experiments. Several regions around the positive and negative defects are bleached when the pairs are annihilating. Experimental data are extracted using Leica LAS X software. We used Matlab code to track both the defects and the bleached spots.

3.4.1 Flow behavior around the defect pairs

The annihilation dynamics strongly depends on the mutual orientation of the defects, and on the alignment of the pair respective to the far, undistorted director field Missaoui et al. [2020]; Tang and Selinger [2018]; Vromans and Giomi [2016]. In the experiment, this orientation cannot be controlled easily as discussed in the second chapter of this manuscript. In a first set of experiments, we tried to avoid the complication caused by curved trajectories. Thus we utilize the fact that the defect pairs gradually align during their mutual approach. Precisely at this stage, most of the experiments were performed.

Fig. 3.8 shows snapshots of four defect pairs together with their bleached spots. The textures of the pairs and the ROI are seen at the beginning of the recording, immediately after bleaching stopped. The defect trajectories are represented by blue (for the -1 defect) and red (for the +1 defect) curves. The time interval during which these trajectories were recorded are approximately 8 s. We have performed experiments with single and double bleached spots (Fig. 3.8a,b, respectively). The flow velocities can be estimated from the analysis of the ROI spots and are given by the arrows.

The first obvious result is that the two defects move towards the annihilation point with different velocities. As predicted by theory Svenšek and Zumer [2003], the positive defect is faster so that the annihilation does not occur halfway. Besides, the defect pairs have slightly curved trajectories, since the initial defect mismatch is not strictly zero (similar to those we examined in the second chapter of this manuscript). When flow coupling is disregarded, the models describing the defect speed Harald [1988]; Ryskin and Kremenetsky [1991] predict a velocity v for each of the defects in the film at

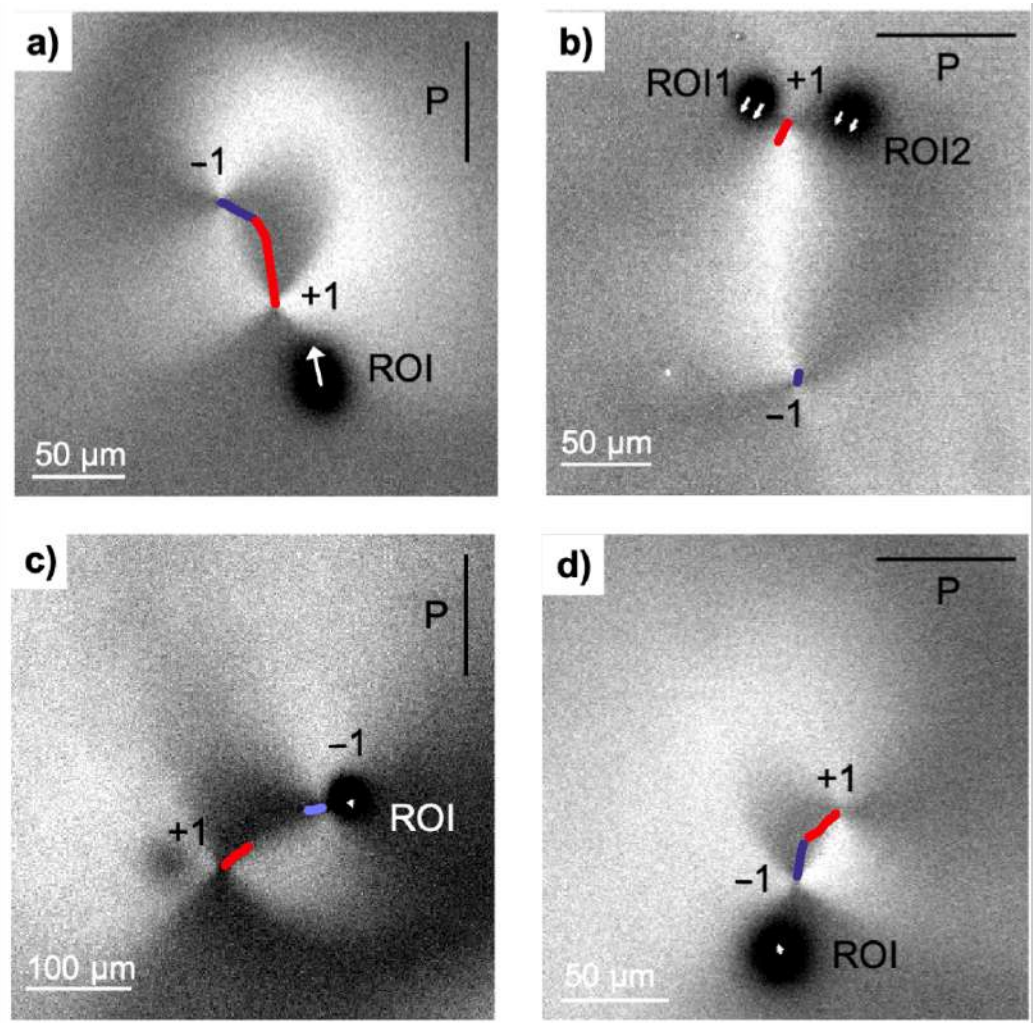

Figure 3.8 – Trajectories of the defects and the flow field in the bleached regions: The snapshots show the pairs at the beginning of the recording, immediately after bleaching stopped. The +1 defect, -1 defect, and ROI trajectories are shown in red, blue and white respectively. The motion of the ROI near the positive defect (a,b) follows the motion of the defect. The ROI near the negative defect (c,d) does not move noticeably. (a) A single ROI bleach; (b) a double ROI bleach. The trajectories of the +1 defect, of the -1 defect, and of the ROI are shown in red, blue and white, respectively. The disclinations and ROI are tracked for 8 s. The position of the excitation beam polarization is given by black lines. Reprinted from Missaoui et al. [2021].

rest

$$v_{+,-} = \pm \frac{K}{\gamma_1 \ln(3.6/E_r r_{12})}. \tag{3.7}$$

As there is no noticeable flow near the -1 defect, this equation can be used as a good reference for the dynamics of the -1 defect, and it is a reasonable approximation for the motion of the +1 counterpart relative to the moving film. Actual defect velocities can be found in the experiment from the defect positions. For that purpose, we analyzed longer trajectories without the bleaching technique. The distances of the defects from the annihilation center and their mutual distances are shown in Fig. 2.12 for a matching pair. The mutual approach occurs along a straight trajectory. In good approximation, the positions of defect i can be fitted to square-root laws $r_i = D_i\sqrt{t}$, and their distance is given by $r_{12} = D_{12}\sqrt{t}$. This corresponds to a velocity $v_{12} = D_{12}^2/(2r_{12})$. It is obvious from these equations that the observed velocities v'_+ and v'_- of the individual disclinations must relate to each other like the coefficients D_1 and D_2. The +1 defect is found to move nearly twice as fast as the -1 defect. If we assume that the reason for that difference is backflow coupling and advection, with no significant flow near the -1 defect, then it is natural to equate $\mid v_- \mid$ to $\mid v'_- \mid$ in Eq. 3.7. The difference of v'_+ and v'_- is then a signature of flow near the +1 defect.

Fig. 3.8c,d indeed show that flow is practically absent around the s = -1 disclination point. The bleached spots near the s = -1 defect remain nearly stationary. This is in accordance with the numerical model Svenšek and Zumer [2003]. Fig. 3.8a,b show that, in contrast, there is an obvious correlation between the motion of the s = +1 defect and that of the bleached spot. The spots follow the motion of the adjacent +1 defect. In the bleaching experiments, the observation time is too short to obtain the square-root law with sufficient accuracy, one rather obtains a snapshot of the dynamics in a certain phase of the defect approach. Technically, it was difficult to manually place the bleaching spot next to one of the defects just before annihilation. Thus, bleaching experiments could be performed only when the defects were still at comparably large distances from each other (e.g., Fig. 3.8b). However, a slight drift of the complete film area in the field of view cannot be avoided. It can reach values of the order of 1 μm/s. When this drift is perpendicular to the defect interconnection axis, both defect trajectories are tilted to the same side of that axis. This is evident in Fig. 3.8d. If the drift has a component in the direction of the defect interconnection axis, it may tamper the velocity ratio. This is the main error source when the defects are far apart from each

Table 3.1 – Measured flow fields in the images shown in this paper. All velocities are given in μm/s. The indices ROI+ and ROI− refer to spots near the disclinations with the respective sign. For Fig. 3.8b, the average of the velocities of both bleached spots is given. The accuracy of the velocity data is of the order of 1 μm/s. Reprinted from Missaoui et al. [2021].

Figure	v'_+	v'_-	$v_{\mathrm{ROI}+}$	$v_{\mathrm{ROI}-}$
3.8a	6.0	2.6	2.6	-
3.8b	2.6	1.7	1.2	-
3.8c	4.0	2.2	-	0.2
3.8d	4.5	3.2	-	0.5
3.9a,b	1.9	1.7	1.2	-
3.9c	1.2	1.2	-	0.3

other and their approach velocity is small. Drift can be neglected when the defects are fast, close to the annihilation point. If we consider an experimental uncertainty of the order of 1 μm/s. Table 3.1 below shows that the velocities v_{ROI} of the regions next to the +1 defect are comparable to the difference $\mid v'_+ \mid$ to $\mid v'_- \mid$.

In addition to the displacement of the ROI, the shape of the bleached spot may serve as an additional source of information. When the film material flows during the bleaching phase of about 8 s, the ROI is not a circular spot but it becomes distorted elliptically, with the long axis in the direction of the flow. One can see this effect in Fig. 3.8a. The bleached spot near to the +1 defect appears elongated in the direction of the induced backflow field. When the defects are far separated as in Fig. 3.8b, the defect motion and corresponding backflow field are small and the bleached region remains circular. The same applies for bleached spots in the vicinity of the -1 defect which is at rest (Fig. 3.8c). Again, drift of the film during bleaching as seen in Fig. 3.8c can also lead to a slight ellipticity of the bleached spot.

When the orientations of the two defects do not match, i.e., when the director field along the straight line connecting the cores is not uniform, the trajectories are curved Missaoui et al. [2020]; Tang and Selinger [2017]; Vromans and Giomi [2016]. In some cases, very large mismatch angles have been observed (Fig. 3.9). Since the +1 defect is pinned to a tangential orientation by the elastic anisotropy (see above), the director field strongly deforms to a spiral shape near the defect Eremin et al. [2006]. Then, the instant velocity and the trajectory will point side-ward, but not towards the -1 opponent.

Fig. 3.9 shows that, in such cases, the flow field next to the -1 defect is still negligibly small, while the flow field near the +1 defect points in the same direction as the defect motion. This is intuitively clear: The velocity field is evoked by the displacement of the +1 defect alone, irrespective of the location of the far -1 opponent. The quantitative measurements of the displacement velocities in the images of Fig. 3.8 and Fig. 3.9 are given in Table 3.1.

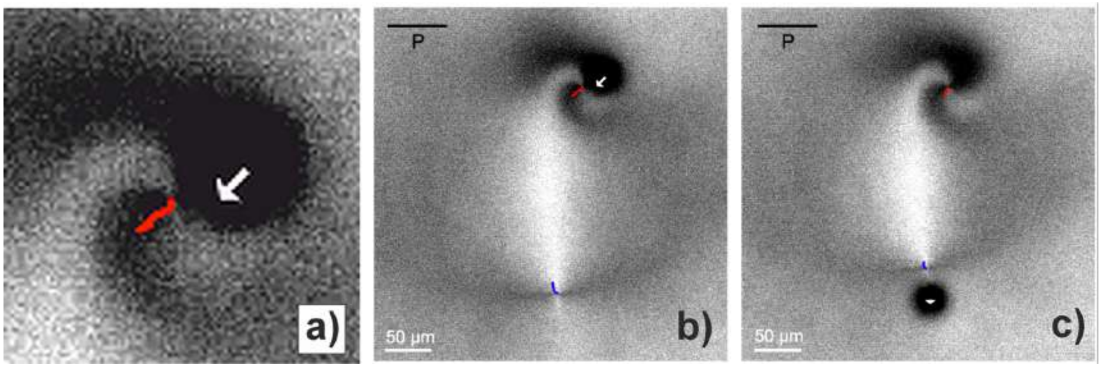

Figure 3.9 – Flow field in a strongly mismatched pair of defects (mismatch angle approximately 180°). Because of the mismatch of the orientations, the defects do not approach each other along the straight interconnection line. The images show the pair with ROI near the +1 defect (b) and the −1 defect (c). a) is a magnification of the +1 defect and ROI from image (b).

3.4.2 Hydrodynamic flow map

When different experiments are performed with different positions of the ROI, one can try to map the flow field. In principle, one can try to perform several subsequent bleaching experiments with the same pair, but this is extremely challenging. By scaling the velocities measured in different individual experiments of matching pairs, one can compose a map. This is shown in Fig. 3.10. The approach to construct this map and the symbols used is explained in the following.

First, we assume that the backflow is mainly generated by the displacement of the local disclination and that the influence of the opposite partner in the pair is irrelevant. Thus, we rotate the coordinate system in the region near the +1 defect (upper half of image Fig. 3.10a) such that the motion of the central +1 defect is downward. In an aligned pair, this would correspond to the situation shown in the numerical solution of Fig. 3.10b. Now, we have to consider that, in different experiments, the distances of the defect pairs differ; thus, the actual velocities cannot be compared. However, it is reasonable to assume that the ratio of the defect velocity and the backflow is independent of the defect distance in a pair. Thus, we scale all ROI velocities with the absolute velocity determined for the +1 defect. The initial positions of +1 defect (red circle) and the ROIs (open black circles) are indicated, and the scaled velocities are shown as black lines. For comparison, the scaled velocity of the disclination is given as a red line. In order to estimate the accuracy and reliability of the velocity data, we estimate the error by assuming a 1 μm/s drift in the film, in arbitrary directions. Of course, this drift has little effect when the disclinations are close to each other and the velocity for scaling is much larger than a potential drift (upper three ROIs in Fig. 3.10a). It has much larger effects when the defects are far from each other, the approach is slow and the approach velocity becomes comparable to the drift. We mark the estimated error due to drift by grey circles around the original ROI positions. As is seen, most of the black lines indicating the backflow reach much further than the grey uncertainty disks; thus, the analysis clearly evidences a backflow near the +1 defect that contributes roughly one half of the displacement.

A similar procedure was performed near the -1 defect. Here, the area was scaled again in units of the defect distance, the coordinates were rotated such that the -1 defect moves upward (like in the simulated matching pair in Fig. 3.10b. Velocities were scaled again, with the displacement of the +1 defect. Errors were estimated in the same way as above. The blue circle is the position of the -1 defect, the blue line its trajectory. Now, it can be seen that all black lines corresponding to the displacements of the ROIs are within the uncertainty limits of the experiment, so the observations are in agreement with the assumption of absent backflow.

When comparing the two parts of Fig. 3.10b, note that the upper and lower halves must be kept separate, since they do not belong to the same coordinate systems. All experiments were rotated as explained above, and there are no experiments that produced data in both the upper and lower parts of the image. In each experiment, bleached spots were in the vicinity of either the +1 defect or the -1 defect.

Comparison of the experimental data with the numerically predicted flow field Svenšek and Zumer [2003] (Fig. 3.10) shows good qualitative agreement. Note, however, that the backflow is not necessarily towards the opposing defect if there is a mismatch in the pair. The direction of the backflow is determined by the direction of motion of the +1 defect.

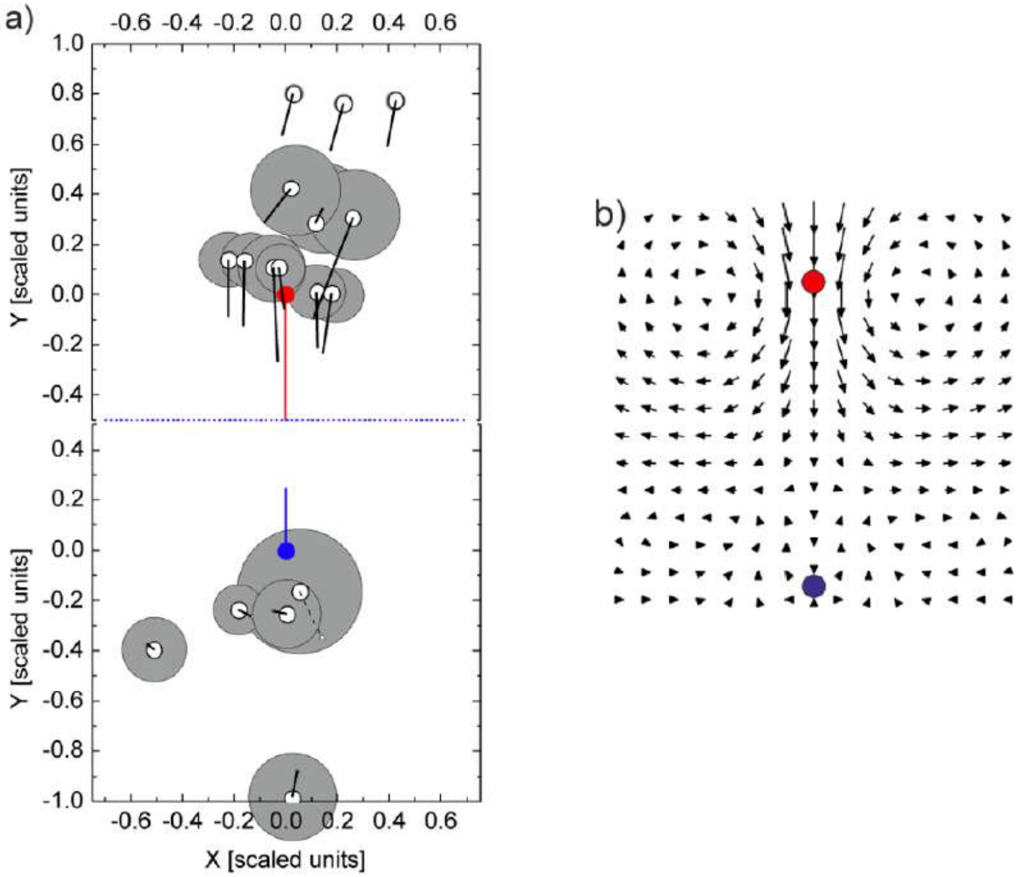

Figure 3.10 – Advective flow around disclinations in a ±1 pair. (a) Flow field determined experimentally using the fluorescence bleaching method. The velocity bars are normalized with respect to that of the $+1$ defect (see text). The motion of the $s = +1$ is accompanied by the flow in the same direction of motion. In contrast, the flow is nearly absent in the vicinity of the $s = -1$ defect. (b) Numerical flow velocity field showing the formation of the flow vortices around the $s = +1$ defect. Image (b) reproduced with permission from Svenšek and Žumer Svenšek and Zumer [2003], copyright American Physical Society. Printed from Missaoui et al. [2021].

3.5 Summary and Perspectives

We have demonstrated qualitatively and quantitatively that a topological defect of strength +1 in a *SmC* liquid crystalline freely suspended films is able to create substantial material flow when it moves in the film plane. This conclusion can be generalized, it is not exclusively the consequence of a defect pair annihilation but is a feature directly connected with the director field reorientation around the moving disclinations. We have assumed here, similar to earlier theoretical treatments of this annihilation process, that the *SmC* hydrodynamics in the 2D film geometry can be treated within the nematodynamic model of Leslie and Ericksen, by substituting the respective elastic and viscosity parameters by their appropriate equivalents for the *c-director*. Thus, the result can also be seen as a confirmation of this backflow effect in nematic cells.

Here, the focus was laid on single isolated defect pairs as the elementary process of defect pattern coarsening. There are other situations where backflow coupling of a moving defect can have essential consequences. Muzny and Clark [1992] have studied the diffusion of a single +1 defect in a freely suspended film and analyzed its Brownian motion within a model that disregards flow coupling. On the basis of the present experimental results, it is clear that backflow must be taken into consideration for an isolated +1 defect, as well. It should indeed speed up its diffusion by a factor of two. On the other hand, -1 defects in a similar film would have a slower diffusion constant, because the flow generated by this type of disclinations is considerably smaller. Another problem where the backflow should be incorporated in models is the coarsening of multi-defect patterns Muzny [1994]. However, while the flow coupling may speed up the overall coarsening process, the scaling exponent for the defect number versus time will not be affected.

The fluorescence bleaching method developed here is limited to short time scales of a few seconds, which prevents to determine accurate defect velocity data when the defects are separated more than 100 μm, but on short distances it can yield reliable quantitative data. An improved method can be developed where multiple lines in a grid are bleached instead of single spots. This would allow to get information on the complete flow field from single experiments. Moreover, the dispersion of nanometer sized glycerol-water droplets on the film surface might be also used instead of bleached micrometer sized ROI in order to check the variation of the defect/vortices distance in function of the defect separation.

3.6 References

Brugués, J., Ignés-Mullol, J., Casademunt, J., and Sagués, F. (2008). Probing elastic anisotropy from defect dynamics in langmuir monolayers. *Phys. Rev. Lett.*, 100:037801. 97, 98

Carlsson, T., Leslie, F. M., and Clark, N. A. (1995). Macroscopic theory for the flow behavior of smectic-c and smectic-c^* liquid crystals. *Phys. Rev. E*, 51:4509–4525. 93, 94, 95

Dafermos and Constantine, M. (1970). Disclinations in liquid crystals. *The Quarterly Journal of Mechanics and Applied Mathematics*, 23(2):49–64. 92

Dierking, I., Marshall, O., Wright, J., and Bulleid, N. (2005). Annihilation dynamics of umbilical defects in nematic liquid crystals under applied electric fields. *Phys. Rev. E*, 71:061709. 92

Eremin, A., Bohley, C., and Stannarius, R. (2006). Stick-slip dynamics around a topological defect in free-standing smectic films. *Phys. Rev. E*, 74:040701. 106

Harald, P. (1988). Dynamics of a disclination point in smectic-c and -$c^{/emph}$ liquid-crystal films. *Phys. Rev. A*, 37:3986–3992. 103

Kats, E., Lebedev, V., and Malinin, S. (2002). Disclination motion in liquid crystalline films. *Journal of Experimental and Theoretical Physics*, 95:714–727. 92

Kim, M. and Serra, F. (2020). Topological defect arrays in nematic liquid crystals assisted by polymeric pillar arrays: Effect of the geometry of pillars. *Crystals*, 10:314. 92

Kleman (1977). *Points, lignes, parois dans les fluides anisotropes et les solides cristallins*. Les Editions de physique. 92

Leslie, F. M. (1979). Theory of flow phenomena in liquid crystals. *Adv. Liq. Cryst*, 4:1–81. 93

Minoura, K., Kimura, Y., Ito, K., and Hayakawa, R. (1997). Dynamics of annihilation process of disclination pairs in nematic liquid crystals. *Molecular Crystals and Liq-*

uid Crystals Science and Technology. Section A. Molecular Crystals and Liquid Crystals, 302(1):345–355. 92

Missaoui, A., Harth, K., Salamon, P., and Stannarius, R. (2020). Annihilation of point defect pairs in freely suspended liquid-crystal films. *Phys. Rev. Research*, 2:013080. 92, 98, 103, 106

Missaoui, A., Lacaze, E., Eremin, A., and Stannarius, R. (2021). Observation of backflow during the anihilation of topologocal defects in freely suspended smectic films. *Crystals*, 11(4). xvi, xvii, 100, 104, 106, 109

Muzny, C. (1994). Phd thesis. 110

Muzny, D. C. and Clark, A. N. (1992). Direct observation of the brownian motion of a liquid-crystal topological defect. *Phys. Rev. Lett.*, 68:804–807. 110

Ryskin, G. and Kremenetsky, M. (1991). Drag force on a line defect moving through an otherwise undisturbed field: Disclination line in a nematic liquid crystal. *Phys. Rev. Lett.*, 67:1574–1577. 103

Smalyukh, I. I. (2007). Confocal microscopy of director structures in strongly confined and composite systems. *Molecular Crystals and Liquid Crystals*, 477(1):23/[517]–41/[535]. 100

Sonnet, A. (2005). Viscous forces on nematic defects. *Continuum Mechanics and Thermodynamics*, 17:287–295. 92

Sonnet, A. M. and Virga, E. G. (2009). Flow and reorientation in the dynamics of nematic defects. *Liquid Crystals*, 36(10-11):1185–1192. 92

Svenšek, D. and Zumer, S. (2003). Hydrodynamics of pair-annihilating disclinations in smc films. *Phys. Rev. Lett.*, 90:155–501. xvi, 92, 93, 94, 95, 96, 97, 98, 99, 103, 105, 108, 109

Tang, X. and Selinger, J. (2018). Theory of defect motion in 2d passive and active nematic liquid crystals. *Soft Matter*, 15:587–601. 103

Tang, X. and Selinger, J. V. (2017). Orientation of topological defects in 2d nematic liquid crystals. *Soft Matter*, 13:5481–5490. 106

Tang, X. and Selinger, J. V. (2019). Theory of defect motion in 2d passive and active nematic liquid crystals. *Soft Matter*, 15:587–601. 92, 97, 98, 99

Tóth, G., Denniston, C., and Yeomans, J. M. (2002). Hydrodynamics of topological defects in nematic liquid crystals. *Phys. Rev. Lett.*, 88:105504. 92, 95, 96, 98, 99

Vromans, A. J. and Giomi, L. (2016). Orientational properties of nematic disclinations. *Soft Matter*, 12:6490–6495. 103, 106

Chapter 4

Smectic Islands can Wrinkle Like Solid Sheet

> *"L'effet waouh est au rendez-vous,*
> *surtout lors de la transition entre*
> *la surpesanteur et la*
> *micropesanteur qui donne*
> *l'impression de s'envoler"*
>
> Solenn Percelay

Contents

4.1 Relaxation of Freely Floating Thin Fluid Bubbles

4.1.1 Introduction

Droplets and bubbles, have fascinated scientists, engineers and artists for a long time. Their dynamic behaviors have been studied for various purposes, for example in biology Marmottant and Hilgenfeldt [2003] Forsyth et al. [2011], environment Lee et al. [2011] and industrial context Chokkalingam et al. [2010] Chen et al. [2011].

While droplet are drops of liquid surrounded by an external fluid (See Fig. 4.1a), bubbles are spheres of gas that can be surrounded by a liquid, for example a CO_2 bubble in an aqueous medium, or separated from another gas by a liquid membrane (See Fig. 4.1b). A simple and well-known example of a bubble is the colorful soap bubble, which fascinate grown-up humans often just as much as children. They are made of a layer of water encapsulated between two layers of soap molecules (the membranes). The evolution of their shape in order to minimize the surface energy, provide nature's solution to mathematical minimization problems. A number of studies investigated the relaxation dynamics of soap films from a strongly distorted initial state to the final spherical one Harth [2016]; Kornek et al. [2010]. The special properties of soap films, such as their mass, make the bubble dynamics unique. Depending on the film thickness and bubble size, the mass of the film and its redistribution can affect the relaxation dynamics. Relaxing soap bubbles exhibit damped oscillations of large initial amplitudes as they begin to relax from highly deformed shapes. Their dynamics was found to be driven by surface tension and inertia of the air and the soap films Harth [2016].

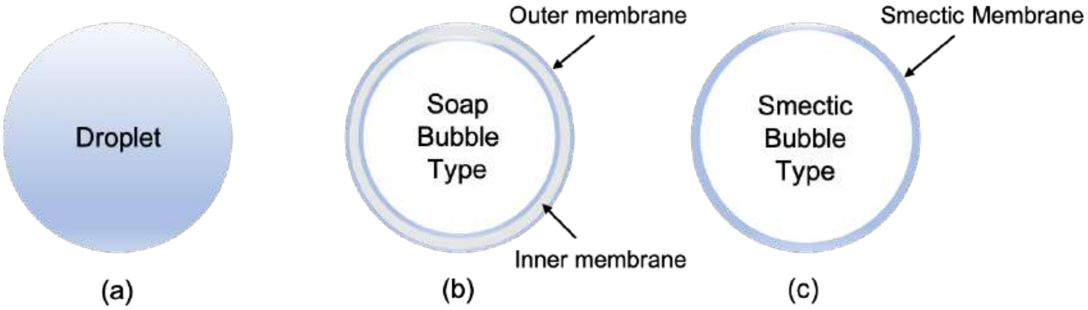

Figure 4.1 – (a) Small drop of liquid. (b) Soap bubble type formed by two membranes. (c) Smectic bubble type formed by an inner fluid isolated by another one by the smectic membrane.

Whereas the dynamics of soap bubbles is mostly driven by surface tension Harth [2016]; Kornek et al. [2010]; May et al. [2012], in another extreme scenario, droplet and bubble dynamics can be purely driven by elastic properties. A well known example corresponds to a water droplet enclosed by a thin layer of polymers Knoche et al. [2013]; Paulsen et al. [2015]. When the elastic membrane covering the drop of water is deformed, the dynamics of the droplet will be determined by the polymer elastic properties. It has been shown that "wrinkling" patterns are frequently observed due to the deformation of the elastic sheet covering the interface (See Fig. 4.2). The wrinkles are in general aligned parallel to the applied stress Cerda and Mahadevan [2003].

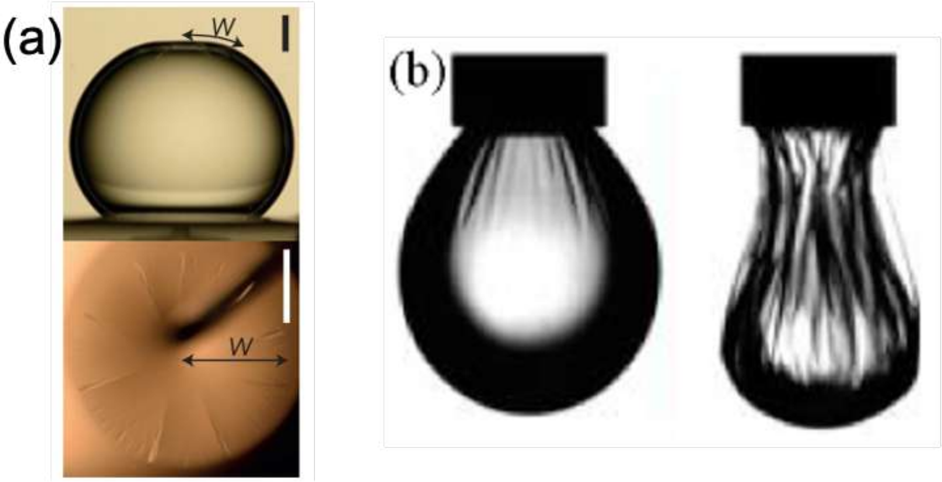

Figure 4.2 – (a) Side and top views of a circular polystyrene sheet wrapping a water drop. The polymer sheet is decorated with wrinkles and crumples. Scale bar, 1 mm. Reproduced by permission from Springer Nature (Paulsen et al. [2015]), Copyright (2015). (b) Wrinkling of a thin elastic capsule enclosing a pending drop. The images show the relaxed membrane and a state where some fluid was retracted. Width of the nozzle ≈1.6 mm. Reprinted with permission from (Knoche et al. [2013]). Copyright (2010) American Chemical Society.

4.1.2 Relaxation of *SmC* bubbles

It has been believed for a long time that freely suspended smectic films can only be stretched on a frame where they are connected by the intermediate of the meniscus, e.g., rectangular films shown in the second chapter of this manuscript. However, experiments by Müller and Stannarius [2006] reported the formation of freely floating smectic bubbles by the collapse of a "catenoid-shaped" film.

Freely floating smectic bubbles are systems that lie between the extreme systems of pure elasticity and those of pure surface tension driven dynamics. Smectic bubbles are the equivalent of freely suspended films with neither sample holder, nor meniscus. Their dynamics is governed by the smectic inner fluid (Fig. 4.1c), which is always composed of an integer number of smectic layers. Fig. 4.3 shows the relaxation dynamics of a *SmC* bubble of equilibrium radius $a \approx 0.57$ cm May et al. [2012]. During the oscillation phase, the bubble alternates complex relaxation shapes before reaching the final equilibrium spherical shape. Quantitatively, the dynamics of smectic bubbles is unusual and different from that of the soap bubbles May et al. [2012]. For the example shown in Fig. 4.3, the authors reported that, at the end of the oscillations, the smectic bubble achieves a spherical shape, associated with a reduction of the film surface of about 30%. This requires on average an increase in the number of layers of the same rate. However, the smectic membrane possesses an integer number of layers, and changes of the layer thickness are countered by elastic moduli on the order of $10^4 ... 10^8$ Pa Oswald and Pieranski [2006]. Thus, islands (excess smectic layers) surrounded by dislocation lines must be formed and must grow to achieve the required increase in film thickness, which is a slow process compared to the time scale of the bubble oscillations. This can limit the rate of surface area reduction and slow down the oscillations. Thus, the bubbles become strongly deformed and oscillate forming complex shapes.

May et al. [2014] have shown that the slowing process is mainly caused by the structure of the smectic film. For the same bubble size, smectic films in their experiments are at least 30 times thinner than soap ones. Thus, the mass of the smectic film is totally negligible compared to that of the enclosed air. Therefore, as long as a decrease of the bubble surface area is necessary to reach the spherical shape, the relaxation process will be governed by the time constant related to growth of the smectic islands.

4.1.3 Dynamics of islands in freely floating bubbles

In general, a compression of the smectic film is always coupled to a flow and thus to a redistribution of the film material. Therefore, islands are formed to accommodate the excess smectic material generated during the reduction of the surface area of the smectic films. They act as a reservoir of material similar to the meniscus in frame-supported films. Their dynamics is characterized by two major stages: first nucleation and then growth. They are expected to grow as long as the in-flow exists. However, they are delimited by lines of dislocation. Thus, their growth is expected to be governed by the

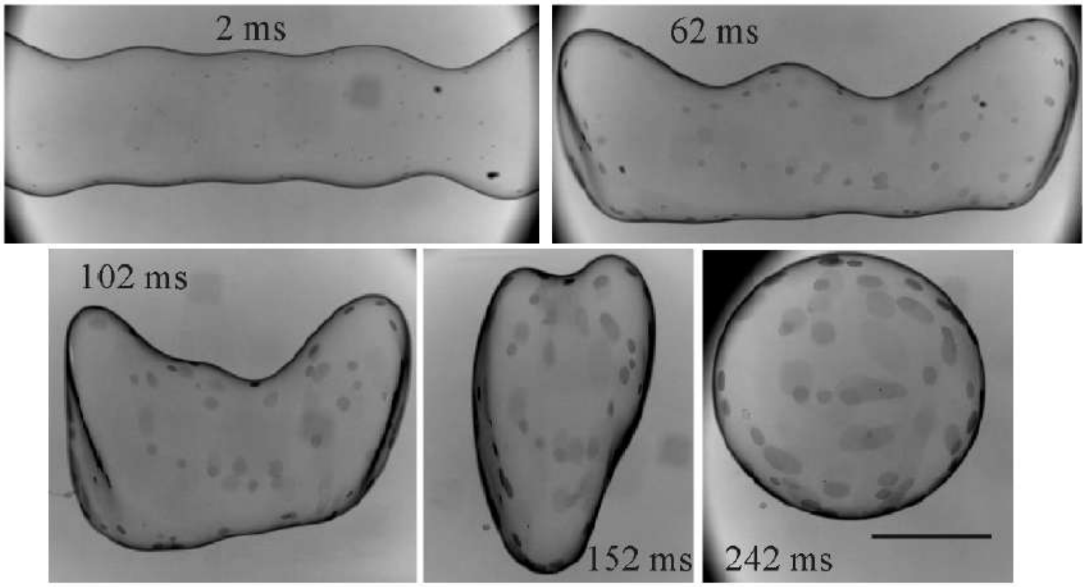

Figure 4.3 – Relaxation of a smectic bubble with equilibrium radius a ≈ 0.57 *cm*. Darker spots on the surface are growing islands of different heights and diameters. The time after pinch-off is indicated on the images. Scale bar 5 mm. Adapted from *Dynamics of freely floating smectic bubbles* by May et al., EPL 100 16003 (2012), website iopscience.iop.org/epl.

properties of the dislocations dynamics (See section.1.2.3 and section.1.3.3).

Oswald et al. [2003] have studied the dynamics of smectic islands in *SmA* frame-supported films. The authors have shown that the islands grow with a radius that increases linearly with time (Fig. 4.4). The linear growth is systematically for all the measured islands. It has been shown that only the growth rate of the linear dependence changes as a function of the difference in thickness between the film and the islands on the one hand and as a function of the pressure difference, ΔP, between the film and the meniscus on the other hand. Such a result is consistent with the theoretical model which predicts a constant velocity of dislocations after nucleation with a rate being dependent on the thickness of the islands as well as on the pressure difference between the film and the meniscus (See section.1.2.3 and section.1.3.3).

May et al. [2012] and Dähmlow et al. [2018] have studied the growth of islands during the relaxation of freely floating *SmC* bubbles (Fig. 4.5). The authors have shown that the growth of the area of individual islands is quadratic as a function of time, which is consistent with a linear dependence of the radius as a function of time. This result was systematic for all the islands studied during these works. It has been shown that only the growth rate varies from one island to another according to the difference of

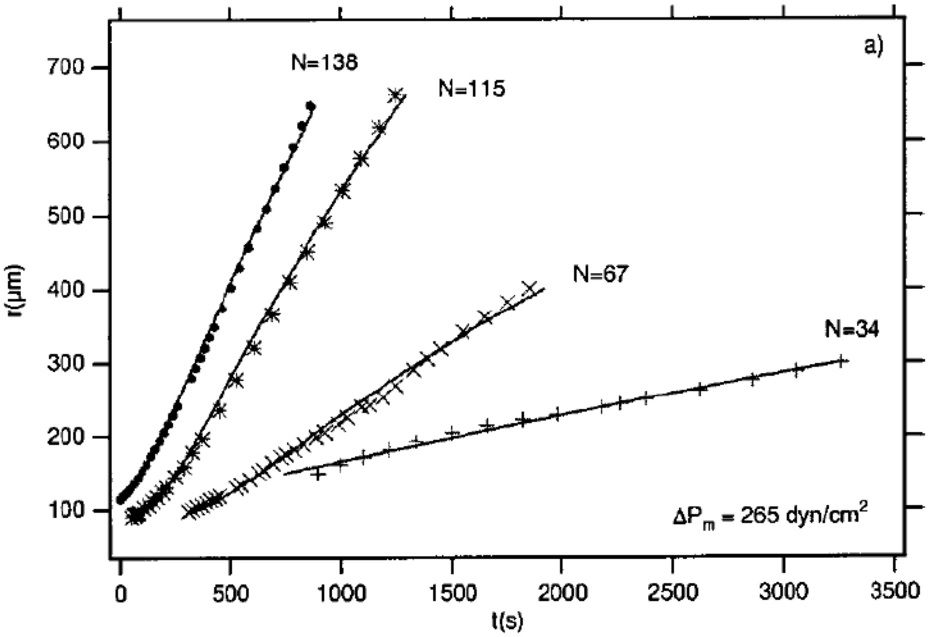

Figure 4.4 – Radius growth of smectic islands in freely suspended *SmA* films of thickness *N*. Reprinted from Oswald et al. [2003]. Copyright (2003) by The American Physical Society.

thickness between the islands and the film. Thicker islands have been found to grow more slowly than thinner ones. However, the time of islands nucleation has not been studied because of the limited spacial resolution and also due to the fact that islands are nucleated before the start of the recording. The results of the islands growth during these studies remain consistent with the theoretical model that predicts a constant velocity of dislocations even in the absence of meniscus.

May et al. [2014] and Harth et al. [2019] studied the relaxation dynamics of freely floating *SmC* bubbles. The authors reported an alternative scenario of stress relaxation, where the smectic film reacts to the lateral compression with an extrusion of "bulges" at the centers of islands (See Fig. 4.6). This particular sort of island dynamics is unusual and has never been observed in freely suspended frame-supported films. The authors attributed the behavior of the islands to the strong compression applied by the bubbles during relaxation to the spherical shape. However, the detailed mechanism of their formation was not fully understood.

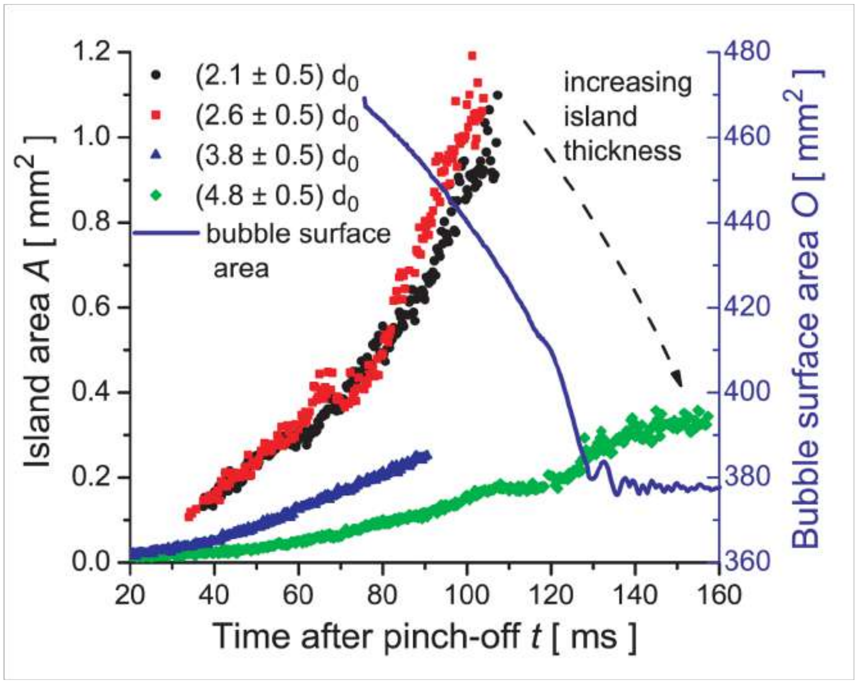

Figure 4.5 – Typical growth of the area of islands in a bubble with a = 0.5 cm. The island thicknesses shown in the legend have been obtained from the transmitted light intensities, relative to the background film. Thick islands have the tendency to grow slower than thinner ones. The surface area of the bubble is shown by the blue curve. Adapted from *Dynamics of freely floating smectic bubbles* by May et al., EPL 100 16003 (2012), website iopscience.iop.org/epl.

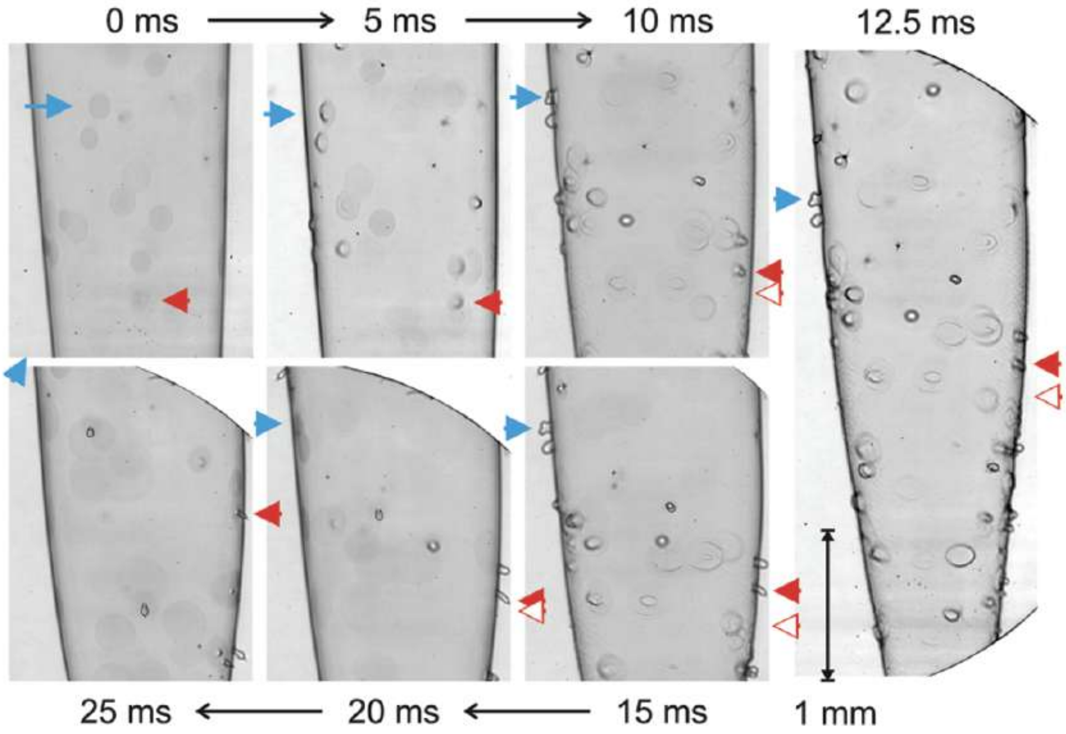

Figure 4.6 – Formation of bulges during the compression of the bubble. Islands and bulges of larger film thicknesses are seen as darker spots on the bubble. Republished with permission of ROYAL SOCIETY OF CHEMISTRY, from Dynamic wrinkling of freely floating smectic films, Harth et al. [2019]. 2019, 15, 6769; permission conveyed through Copyright Clearance Center, Inc.

4.1.4 Summary

The meniscus has been found to play a crucial role in the dynamics of dislocations surrounding smectic islands. It directly effects their growth or shrinkage. Only few studies have investigated the dynamics of smectic islands in meniscus-free systems; the freely floating bubbles Dähmlow et al. [2018]; May et al. [2012, 2014]. In these geometries, the islands surface are were found to grow following the quadratic dependence predicted by the theoretical model. However, in some cases, an extrusion of "bulges" at the center of the islands has been observed during the relaxation of the bubbles. This phenomenon has not been explained and the details of its formation remain unexplained.

On the other hand, the relaxation dynamics of the freely floating *SmC* bubbles was found to be affected by the dynamics of the dislocation loops surrounding the islands. This can significantly limit the surface area reduction and cause bubbles to oscillate towards complex shapes. Although the dynamics of smectic islands is considered to play an essential role in the bubble relaxation process, they have so far received little attention Dähmlow et al. [2018]; Harth et al. [2019]; May et al. [2012, 2014]. The detailed study of the mechanism of their formation and the description of the quantitative relationships between island size, line tensions and external compressive forces remain unexplored. I will therefore present in the following an experimental study of the behavior of islands during relaxation of the smectic bubble. But first, I discuss the new characteristics of freely floating smectic bubbles recently reported by Harth [2016]; Harth et al. [2019]; the wrinkling of smectic films.

4.2 Wrinkling of Thin Fluid Films

4.2.1 Introduction

In general, wrinkles in soft matter systems can be divided into two major types; They can be static or dynamic. Examples of static structures are wrinkles on human skin or an aged apple that shrunk in volume due to loss of the water while the skin roughly keeps its area. These are quasi-static responses to the stress balances. Usually, such undulations represent stable or metastable energy minima.

In the case of liquid crystals, spontaneous periodic surface undulations of the meniscus of freely suspended *SmC* films have been reported Harth et al. [2011]; Harth and

Stannarius [2009]; Loudet et al. [2011]. In fact, these static instabilities may be the consequences of the disclinations present in the menisci structure. Furthermore, static layers undulations can be induced mechanically in smectic liquid crystal films confined to thin sandwich cells with fixed boundary conditions, e.g, the classical Helfrich–Hurault instability in *SmA* Bevilacqua and Napoli [2005]. They occur in thin cells under dilation strain when the cell thickness is increased by external forces. The layer undulations are energetically preferred over an increase of the smectic layer spacing. The elastic energy required for the change of the layer thickness is much larger than the elastic energy of the director distortions initiated by the layer's bend.

Besides the quasi-static structures that represent conservative equilibrium static patterns with minimal energy, dynamic structures may also occur. In contrast to the static ones, their spontaneous formation is a transient dynamic process. They have been observed for example in soap films with immobile surfactants Petit et al. [2015] and in extremely thin soap films McEntee and Mysels [1969]. Interesting effects are reported during the rupture of the films: Sudden cracks appear around a growing hole in the film and the retraction of the soap membrane slows down. Moreover, it has been also shown that collapsing bubbles of very viscous liquids generate wrinkles under the action of the gravity force Silveira et al. [2000]. When a viscous drop forms a thin film spread out in a crater created when impacting a liquid pool, such films can wrinkle transiently Li et al. [2017]. This phenomenon is reminiscent of elastic sheets under external stress. It has been shown that visco-elastic fluid filaments can also exhibit dynamic buckling upon compression Merrer et al. [2012] Salili et al. [2016]. As extreme cases, one may consider deformations of lipid, cell membranes and vesicles, whose dynamics at short time scales is dominated by the bending rigidity instead of surface tension Jahnig [1996]. When such membranes undergo strong compression, wrinkles and extrusion of tubuli can be observed Kantsler et al. [2007] Staykova et al. [2011] Wang et al. [2011] Liu et al. [2016]. However, these structures are transient, the relevant parameter is the relaxation time scale of the film or filament compared to that of the externally applied stresses.

In the next section, I present recent studies about dynamic wrinkles in freely floating smectic liquid crystal bubbles Harth et al. [2019]. I review the formation of regular film undulations, consequences of the local in-plane compression applied on the smectic film Dähmlow et al. [2018] Harth et al. [2019].

4.2.2 Wrinkling of smectic freely floating films

Recently, Harth et al. [2019] have investigated the dynamics of freely floating *SmC* bubbles when they undergo local in-plane compression under the action of an external forcing. The authors reported that these membranes can dynamically wrinkle and bulge out of plane. As shown in Fig. 4.7, they form regular undulation instabilities during their relaxation process. This phenomenon is described with a model for a transient dynamic buckling instability Harth et al. [2019]. The growth rates of unstable undulation modes determine the wavelength selection. Short wavelength modes are suppressed by the elastic forces related to deformations of the smectic layers, while long wavelengths grow slowly because they require the redistribution of the outer fluid over greater distances. The authors have identified the converging flow of the surrounding air as an external driving force that locally compresses the bubble surface area. This study showed that smectic film can form similar structures as polymer sheets under sufficient compression stress (Fig. 4.2). This phenomenon is specific to smectic materials and cannot occur in conventional low-viscosity soap films because they can instantly change their thickness and film surface under lateral compression.

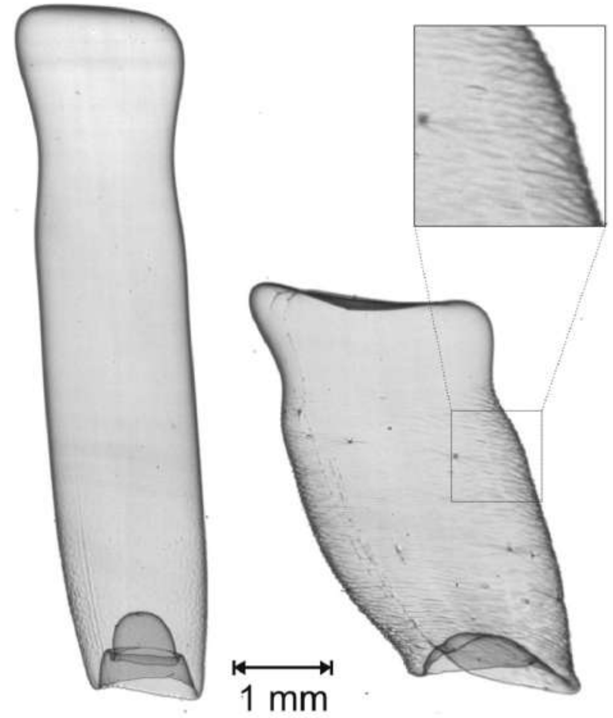

Figure 4.7 – Freely floating smectic bubble with homogeneous film thickness of 50 nm that is axially compressed by air flow. Thereby, it develops a wrinkled structure normal to the compression direction. The right hand image was recorded 50 ms after the left one. The bubble was produced under normal gravity. Republished with permission of ROYAL SOCIETY OF CHEMISTRY, from Dynamic wrinkling of freely floating smectic films, Harth et al. [2019]. 2019, 15, 6769; permission conveyed through Copyright Clearance Center, Inc.

4.3 Experimental Setup

In this section, I describe the method that allows to create smectic satellite bubbles. I also describe the experimental setup used to visualize these latter in micro-gravity conditions.

4.3.1 The liquid crystal

We report observations on freely floating *SmC* bubbles made of the same LC as the one used in chapters 2, 3 and Harth [2016]; Harth et al. [2019]; May et al. [2012, 2014]. This is a mixture of equal amounts of 5-n- octyle-2-[4-(n-hexyloxy)phenyl]pyrimidine and 5-n-decyl-2-[4-(n-octyloxy) phenyl] pyrimidine synthesized by SYNTHON Chemicals. The room temperature SmC phase is followed upon heating by SmA phase (T_{CA} = 52°C) and a nematic phase (T_{AN} = 68°C) before the isotropic phase is reached (T_{NI} = 72°C). The mixture has a surface tension of 22.45 mN/m at room temperature May et al. [2012].

4.3.2 Catenoids, pinch-off and formation of smectic bubbles

Freely floating bubbles are created by the collapse of a catenoid-shaped *SmC* film. First, a small amount of about 1 mg of the smectic material is introduced between two coaxial circular metallic rings with an inner radius R_{ring}. Second, the rings are brought into contact. Third, they are subsequently slowly separated from each other, so that a catenoid shaped smectic film is formed in-between (See Fig. 4.8). The film is vulnerable to rupture during this initial phase and can be destroyed by external perturbations, e.g., vibrations imposed on the setup during the parabolic flights. When reaching a larger separation distance between the two rings, the films are in general stable. The displacement of the two metal rings of the catenoid is controlled by a LabView computer software because manual manipulation was not possible under the experimental conditions.

The equilibrium surface of the catenoid-shaped smectic film spanned between two open concentric rings can be determined via minimization of the surface area of constant mean curvature. The minimal surface for a separation D between the rings is given by Salvert [1881]

$$r(z) = r_{\text{m}} \cosh(\frac{z}{r_{\text{m}}}), \tag{4.1}$$

where r_m is the waist radius and z is the axial coordinate. The catenoid holders (the metallic rings) are at positions $z = \pm D/2$, if we consider the origin of the coordinate system in the mirror plane of the catenoid whose normal coincides with the z-direction. In experiments, we seek solutions for a given holder radius $R_\mathrm{ring} = r(\pm D/2)$ and separation D. In order to satisfy these boundary conditions, it is necessary that

$$r_\mathrm{m} = \frac{R_\mathrm{ring}}{\cosh(D/(2r_\mathrm{m}))}. \tag{4.2}$$

Above the critical separation between the rings, $D_\mathrm{crit} \approx 1.3254 R_\mathrm{ring}$, the catenoid solution as the minimal surface is not defined any longer Chen and Steen [1997]. As a consequence, the catenoid collapses as soon as the critical distance is exceeded. In the following, this step will be called the catenoid collapse. Mainly because of its inertia, some of the air inside the catenoid is trapped between the two pinch-off points, thus an elongated bubble is formed Robinson and Steen [2001].

Smectic catenoid's stability and vibration modes have been investigated previously by Ben Amar et al. [1998]. Moreover, Müller and Stannarius [2006] studied the collapse of smectic catenoids of thickness 200 nm. The authors have used 8CB, which exhibits a *SmA* phase at room temperature. The film thickness was determined using optical interference patterns in parallel transmitted monochromatic light under the assumption of axial symmetry. The authors have shown that the film thickness remains constant until very shortly time before the catenoid collapse. This result confirms that the change in material volume in the catenoid film during its elongation is compensated by the inflow into the meniscus at the rings. In order to produce the *SmC* freely floating bubbles during our study, our set-up is inspired by the one developed by Müller and Stannarius [2006].

After pinch-off, the bubble oscillates for a few dozen milliseconds. Accurate investigations of such processes require a specific observation setup. In the next section, I describe the experimental system that we have used for such a purpose.

4.3.3 The observation setup

The observation system used during our studies is an improved version of the one previously developed by Torsten Trittel for previous parabolic flights. The improvements are made with the help of Christoph Klopp and Torsten Trittel (OvGU-Magdeburg).

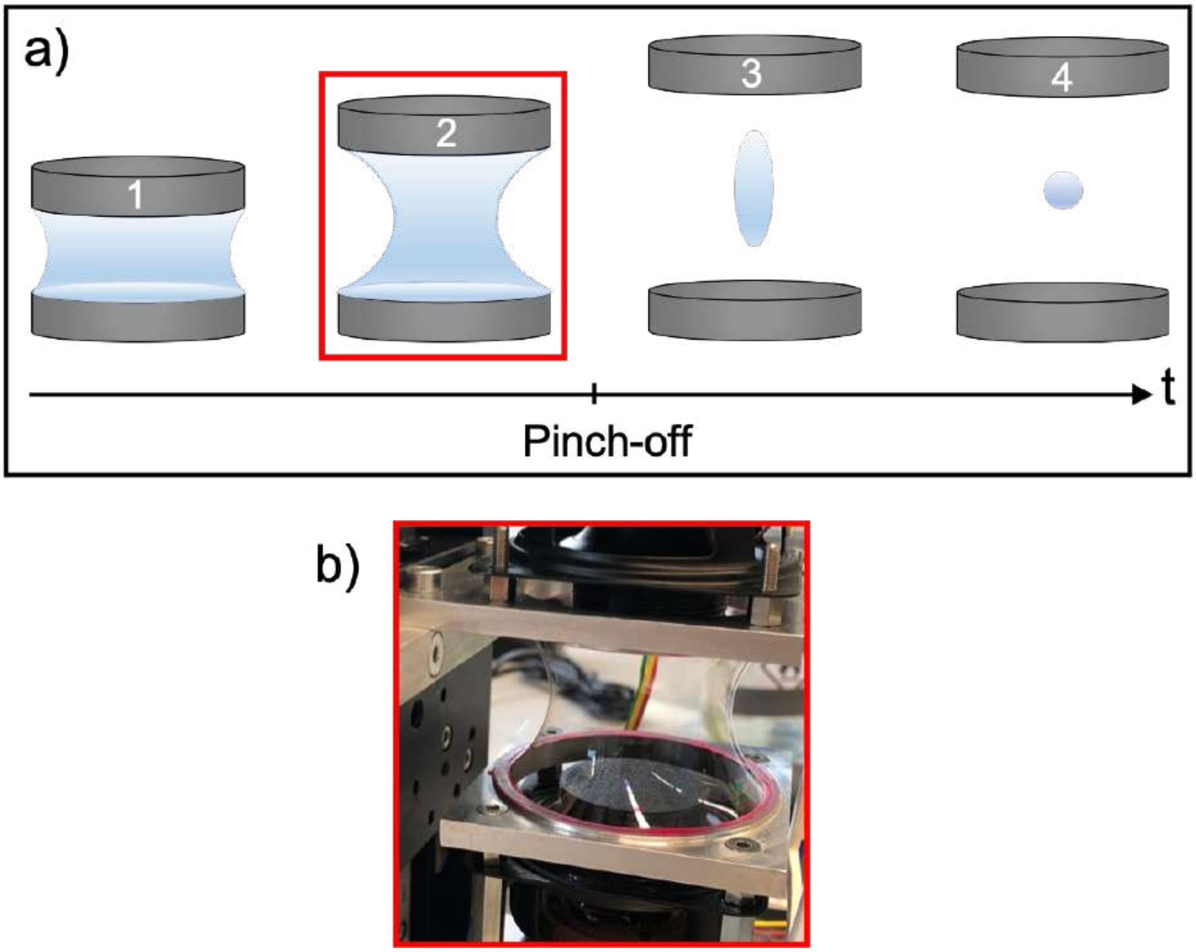

Figure 4.8 – (a) The stages of bubble formation. The pinch-off occurs between steps two and three. Later, the bubble oscillates (between steps three and four) until it reaches the spherical shape. (b) Side view of the bubble generator setup. The stepper motor moves the upper ring up and down (opening and closing of the catenoid). Two loudspeakers have been placed on the top and bottom of the metal rings.

The smectic catenoid is illuminated by either white or monochromatic parallel light using a white and blue LED of wavelength 450 nm from the back. The displacement of the two metal rings of the catenoid is controlled by a LabView computer software because manual manipulation was not possible under the experimental conditions. The collapse process takes place within less than a few milliseconds, thus we have used a high speed camera (Phantom VEO 710) equipped with a commercial Canon lens (See Fig. 4.9). The typical recording speed is 7500 fps with a spatial resolution of approximately 1μm/pixel. It is focused on the side of the bubble facing the camera (front side) with high magnification to ensure that details of the island dynamics can be acquired. However, it is not possible to observe the global shape of the bubble and the details of the surface dynamics with sufficient resolution on the same camera image. Thus, a GoPro camera at a recording speed of 120 fps is implemented at 90° with respect to the Phantom camera in order to acquire the global view of the bubble during the oscillation (Fig. 4.9). Two loudspeakers are implemented and controlled by a waveform generator synchronized with the high-speed camera in order to generate acoustic waves with a frequency of 50 Hz, a phase of 180° and a duration of 1 s from the moment of pinch-off.

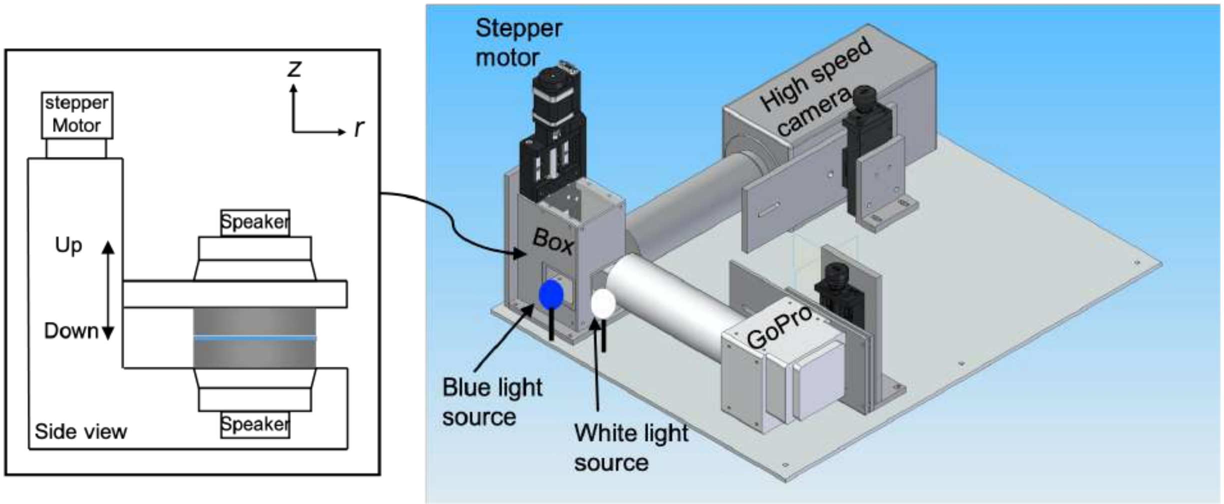

Figure 4.9 – (Right) The observation setup, showing the high speed and GoPro cameras. The catenoid setup is enclosed inside a closed metallic box with glass windows in order to minimize external disturbances such as airflow. Monochromatic blue light source is implemented in front of the high speed camera. White light source is implemented in front of the GoPro. The bubbles are observed in transmitted light. Note that the sketch of the GoPro camera is an approximation. The image on the right is a sketch of the experimental setup designed on SolideEdge by Christoph Klopp. (Left) side view of the catenoid setup.

After pinch-off, the bubbles oscillate for a few tens of milliseconds, before reaching a spherical shape of equilibrium. It is in this time interval that the dynamics of the smectic islands must be observed. However, under normal gravity conditions, the initial shape of the bubble just after pinching-off is asymmetric. It usually pinches at the upper end first, which influences the oscillatory behavior. In addition, since they are freely floating bubbles, it is difficult to keep them in focus; they move from the focal plane and even leave the observation window of the optical microscope rather fast. Hence, it is very difficult to study island dynamics in earth gravity experiments.

For this purpose, most of the experiments are performed in micro-gravity conditions during the VP148 parabolic flights campaign of CNES at NOVESPACE (Bordeaux, France) in October 2019. This campaign was carried out together with Torsten Trittel and Christoph Klopp from the University of Magdeburg. It represents the continuation of a series of previous parabolic flight experiments devoted to smectic bubbles by the Magdeburg group.

During the parabolic flight campaign, more than 70 videos of oscillating bubbles have been recorded. The data have been evaluated using a MATLAB routine that allows to determine the island characteristics; positions, shape, radius, topology.

4.4 Smectic bubble produced by catenoid collapse

In the present study, we are interested in the dynamics of smectic islands under the effects of the changes in the shape of the smectic bubble shape a non-equilibrium form to the final spherical shape. In the next sections, I start by a brief discussion concerning the bubbles produced by the catenoid collapses. Then, I discuss the results concerning generation of islands. Later, I show results about the dynamics of the smectic islands under an applied external stress.

4.4.1 Oscillation and Wrinkling of *SmC* bubbles

As we have shown in section 4.3.2, above the critical distance D_{crit}, the catenoid collapses and a satellite bubble is created at the center (Fig. 4.8). Fig. 4.10 shows image sequences of the rupture of a catenoid-shaped film and the formation of a satellite bubble that oscillates for a few dozen milliseconds until it reaches the stable spherical shape. For such bubbles, the typical relaxation process goes through different stages

Harth et al. [2019]; May et al. [2012, 2014]; First, a minimum neck radius is formed in the vertical mirror plane of the catenoid. Second, the catenoid-shaped film collapses and the satellite bubble forms in the center. Third, the bubble has an initial elongated shape and it oscillates between prolate and oblate shapes while keeping a constant volume of material and reducing the global surface. Finally, the spherical shape is reached. It is the most stable shape that minimizes the system energy.

The equilibrium average radius of the bubbles is about $a \approx 2.3$ mm. The exact bubble radius in individual experiments slightly depends on the film thickness, local temperature and other parameters. However, the film thickness can be controlled to some extent by the ring's separation velocity May et al. [2012]. Faster expansion typically yields thinner films similar to the case of rectangular freely suspended smectic films.

The smectic bubbles produced by the collapse of catenoid films can have diverse complex shapes during the oscillation process. This can be explained on the one hand by the particular properties of the structure of the smectic films, its thickness and homogeneity (See section.4.1.2) and on the other hand by the different ways that smectic bubbles pinch-off. The asymmetric collapse of thick and non-homogeneous catenoid films have a crucial effect on the bubble shapes during relaxation Harth [2016].

Additionally, there are often two oscillating films that adhere at the rings after the pinch-off. Their oscillations cause motion in the air surrounding the bubble, which may represent additional forces that can affect the relaxation dynamics of the bubble Harth et al. [2019]; May et al. [2014]. Alternatively, we can induce deformations of the bubbles via acoustic waves generated with two loudspeakers implemented on the rings (See Fig. 4.8). Then, one has the advantage to control the excitation amplitudes, phases and frequencies. However, as soon as the spherical shape is reached, neither the oscillating remnant films nor the loudspeakers implemented in our setup are able to excite the bubbles and induce noticeable shape changes.

As a result of these dynamic disturbances, holder film oscillations or acoustic waves, bubbles that are far from the equilibrium spherical shape may undergo specific local compression of the film area. Fig. 4.11 shows the formation of undulations on a smectic bubble with a preferential orientation perpendicular to the contraction direction similar to the results reported previously by Harth et al. [2019]. Such dynamical transient patterns are observed when the bubble undergoes fast geometrical shape transformations that may induce a strong enough local compression. When the compression stress

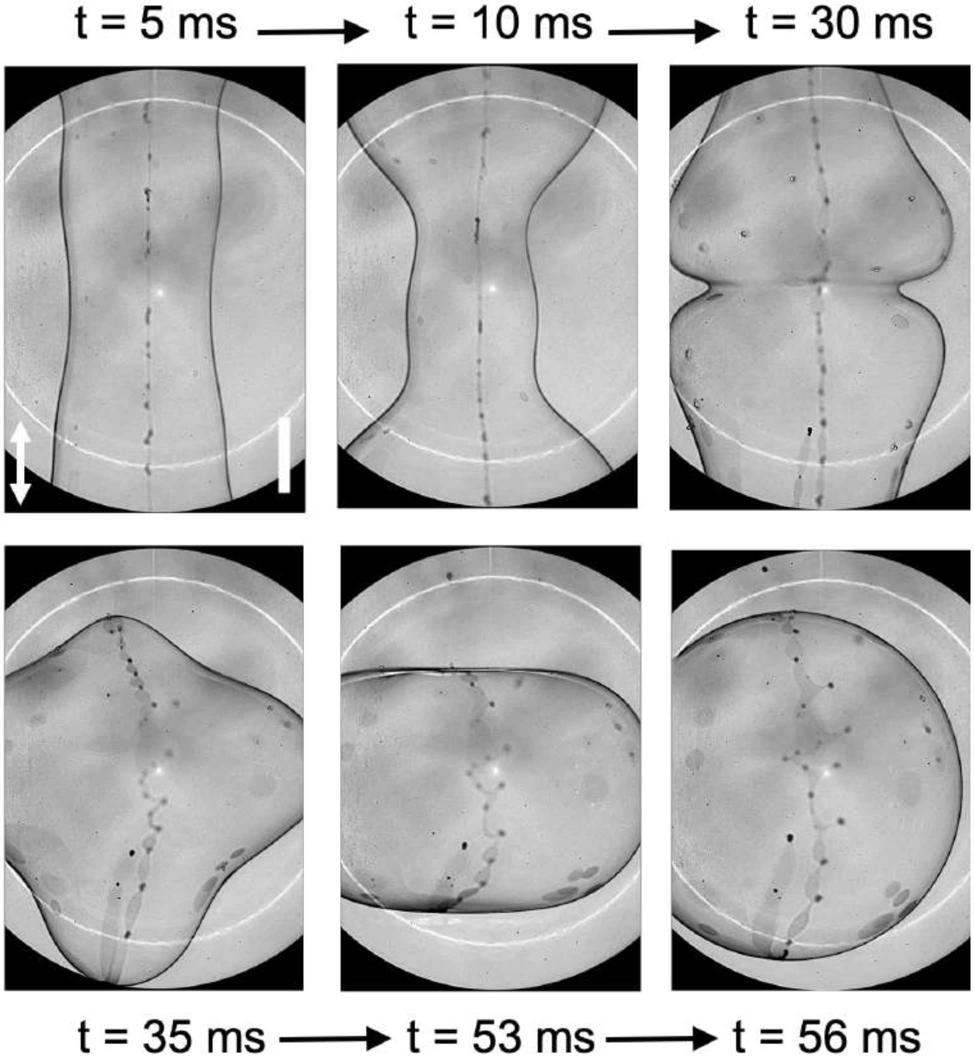

Figure 4.10 – Relaxation of a smectic bubble of equilibrium radius $a \approx 2.3$ mm, created by the collapse of a catenoid-shaped film. After pinch-off (t = 0 ms), the bubble has an elongated shape. It will then relax to acquire the stable spherical shape, after about 56 ms. The bubble is excited with oscillating films remaining on the catenoid rings and without loudspeakers. The white bar represents 1 mm. The axis of symmetry of the catenoid is indicated by the white arrow.

ceases, the wrinkling region is stretched and the undulations disappear. This wrinkling phenomenon only happens when there is an external forcing. Without this forcing, the coupled fluid mechanics of film and air control the stresses and in a simple relaxation without undulations Harth [2016]; Harth et al. [2019].

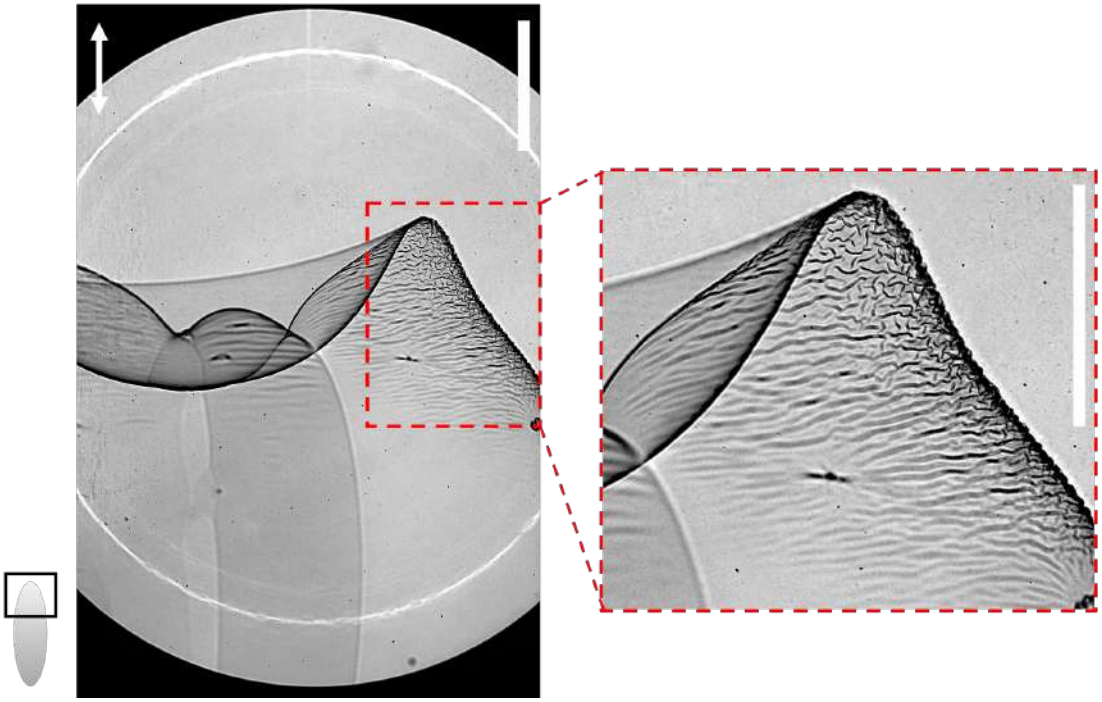

Figure 4.11 – Formation of wrinkles in a freely floating smectic bubble. The latter is compressed axially by the air flow generated around it by the residual films in the rings. The wrinkles are normal to the direction of compression. The equilibrium radius of the bubble is estimated by the two cameras to : $a \approx 5$ mm. The black square on the sketch of the bubble in the left image indicates the field of view of the camera. The white bars represent 1 mm. The axis of symmetry of the catenoid is indicated by the white arrow. The bubble is excited with oscillating films remaining on the catenoid rings and without loudspeakers

4.4.2 Island generation

The thickness reduction of a smectic liquid crystal film is always coupled with flow and thus redistribution of the film material. A local increase of the thickness of a smectic film necessarily induces the generation and/or growth of islands (See Fig. 4.12) May et al. [2012]. In addition to the reduction of the surface area at constant volume that can generate the islands, other effects can also induce a reorganization of the smectic layers. The airflow generated around the bubbles by the two oscillating films remaining at the level of the metal rings creates an advection flow in the smectic material which forces the film to reorganize locally Harth et al. [2019]. In fact, such a flow can be divergent. A positive divergence can lead to thinning of the film, such as the creation of holes or even rupture of the film. A negative divergence compresses the film, so that the latter reacts by forming islands. However, the islands nucleate in general from sites of the film that contain impurities or seeds Oswald and Pieranski [2006]. Thus, their formation is directly limited by the presence of seeds/impurities in the film. Therefore, it may not be possible to nucleate more islands if there are no impurities, even a negative divergent flow cannot induce island formation in this case. This is consistent with our experimental observations, where the islands are nucleated either already during the formation of the catenoid film or just before the pinch-off. We did not observe the nucleation of new islands during bubble oscillations, only the growth of the existent islands.

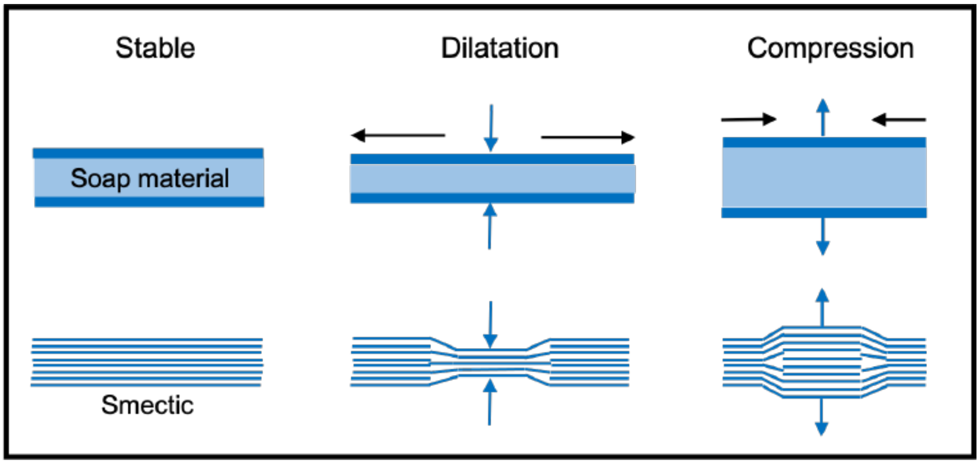

Figure 4.12 – Reaction of soap (top) and smectic (bottom) films to dilatation and compression forces. The force direction is indicated by the black arrows while the film reaction is along the blow arrows. Soap film react to external perturbation by instantaneous thickness change, while smectic membrane react by building islands or holes. Figure reproduced from May [2012].

Fig. 4.13 shows randomly distributed circular islands on a freely floating *SmC* bubble. They are excess smectic layers in a thinner background film. They are surrounded by dislocation lines that provide a line tension which shapes them circularly in equilibrium. Geometrically, these islands are equivalent to two-dimensional droplets in a two-dimensional fluid. In general, one cannot see the dislocation loops directly in the reflective microscope, as their size is well below the resolution limit. What we see is the boundary between regions of different thickness, which are in general of different optical reflectivity, identified thus by different transmitted intensity.

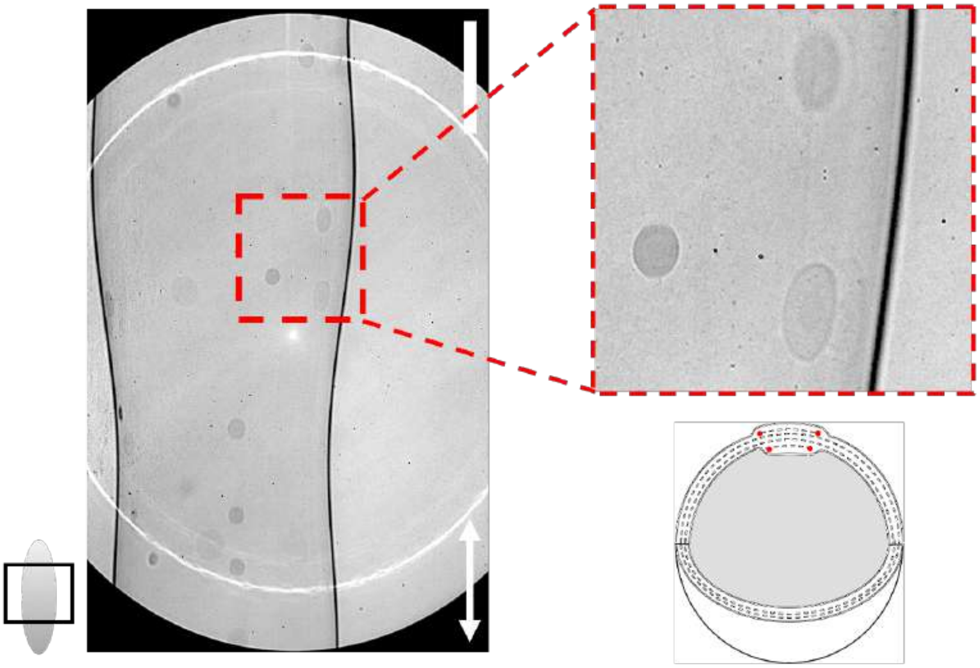

Figure 4.13 – Islands formed in freely floating bubble. Regions of larger film thickness are seen as dark spots on the bubble. The equilibrium radius of the bubble is estimated by the two cameras to : $a \approx 2.7$ mm. The sketch shows a section cut of an island bounded by a lines of dislocations (in red). The black square on the sketch of the bubble in the left image indicates the field of view of the camera. The white bar represents 1 mm. The axis of symmetry of the catenoid is indicated by the white arrow. The bubble is excited with oscillating films remaining on the catenoid rings.

4.5 Dynamics of Smectic Islands During Bubble Relaxation

4.5.1 Island growth in freely floating *SmC* bubbles

Fig. 4.14 shows snapshots of the relaxation process of a smectic bubble of equilibrium radius $a \approx 2.7$ mm. The data are extracted from a video recorded at 7500 fps in transmitted monochromatic light. The pinch-off time is approximated from the shape of the bubble in the videos of the Phantom and GoPro cameras after the synchronization of the two recording times. The axis of symmetry of the catenoid lies in the vertical direction of Fig. 4.14.

The islands were already formed before the pinch-off. This can be explained by the fact that catenoid-shaped smectic films reduce their surface area just before pinching May [2012]. In Fig. 4.14, islands are identified by the dark spots. Their brightness is directly related to the local film thickness Stannarius and Cramer [1998]. In our system, we were not able to measure the exact values of the islands thickness because of the white light reflected from the light source used for the GoPro camera observations. However, we can estimate the thickness of the islands from the previous work by May et al. [2012, 2014], where the authors have used monochromatic light for thickness measurements. For bubbles of the same size as those we have studied and made of the same *SmC* material, the bubbles film have a thickness of about 20 nm. On the other hand, the islands are found to have a few extra layers compared to the background film. Thus, considering the thickness of one smectic layer for our *SmC* material, $d \approx 3$ nm, the islands can have thicknesses close to that of the background film.

We measured an average of 30 to 40 islands formed on each bubble. They can interact with each other and in some cases, the islands can even merge. Despite the importance of the coalescence phenomenon, it will not be analyzed during this work Shuravin et al. [2019]. We have chosen islands that are sufficiently isolated from neighboring ones to avoid any coalescence during the analysis of dynamics. In addition, depending on their position and orientation on the bubble's surface respective to the optical axis of the camera's lens, any island that lies in a plane forming an angle other than 90° to the optic axis, are deformed due to the perspective view. Therefore, for the measurements of the dynamics, we have considered the long axis of the elongated island as the radius r (see Fig. 4.15). The shape of the islands in equilibrium is circular.

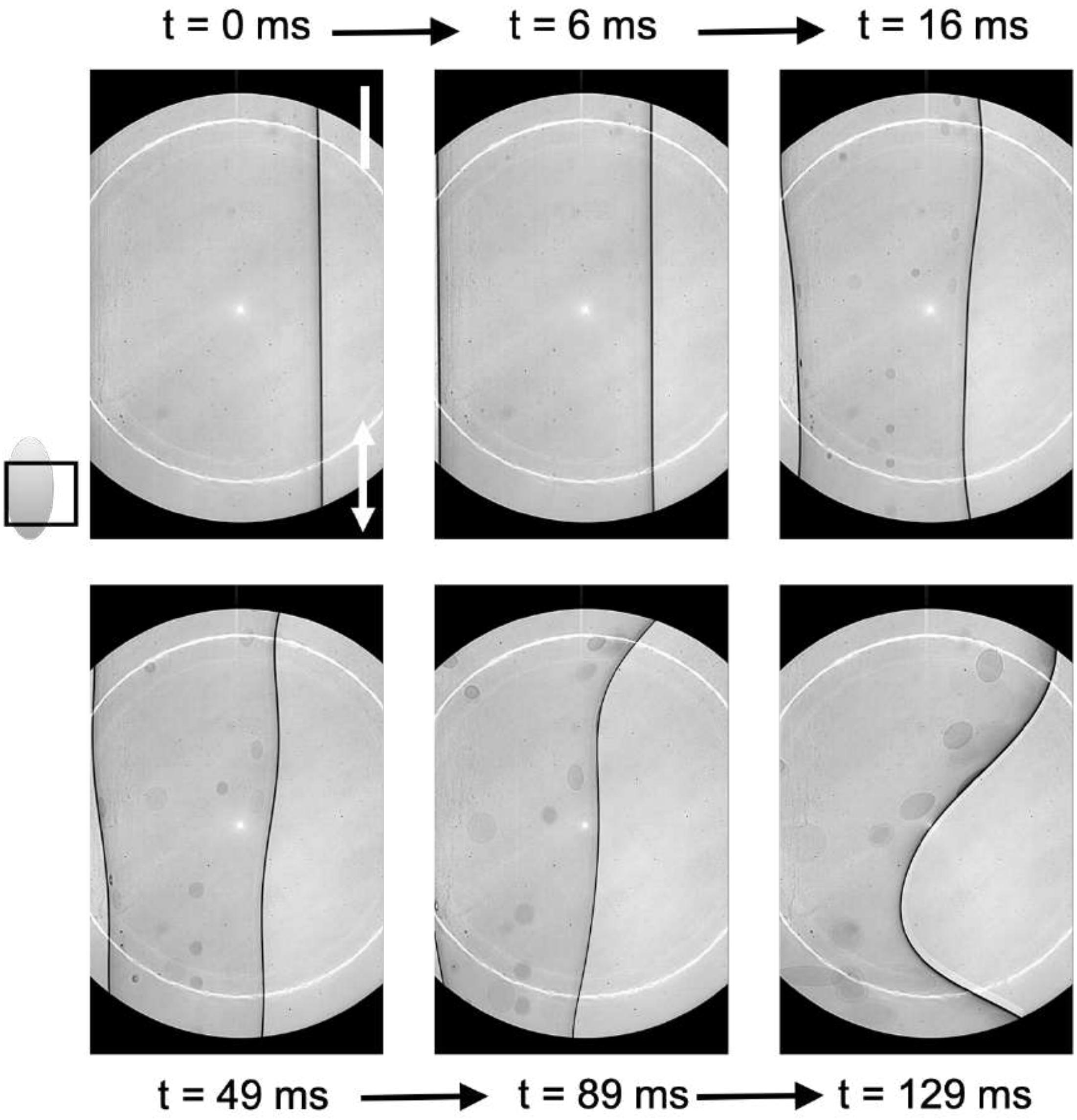

Figure 4.14 – Relaxation dynamics of a freely floating smectic bubble. The dark spots on the film are growing islands of different thicknesses and diameters. t = 0 ms is the pinch-off time. The equilibrium radius of the bubble is approximated by the two cameras to : $a \approx 2.7$ mm. The black square on the sketch of the bubble in the left image indicates the field of view of the camera. The white bar represents 1 mm. The axis of symmetry of the catenoid is indicated by the white arrow. The bubble is excited with oscillating films remaining on the catenoid rings.

However, when the oscillations of the bubble are faster than the relaxation of the island shape, the islands can be temporarily stretched into elongated shapes. We have chosen to study islands which remain mostly circular and are not stretched.

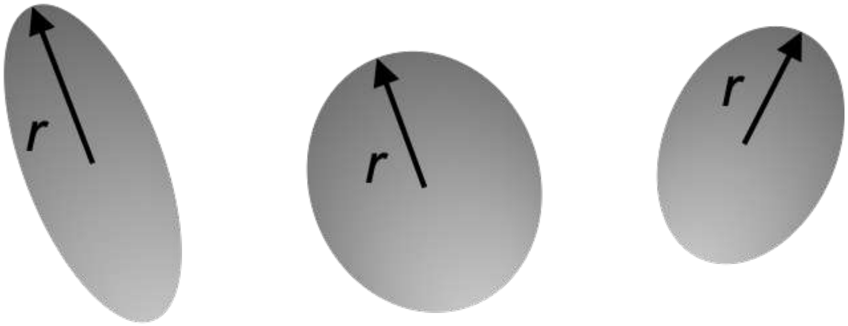

Figure 4.15 – Sketch of examples of islands deformed due to the perspective view. For dynamic measurements, the radius, r, is considered as the long axis of the elongated island.

I have evaluated the dynamics of about 80 smectic islands from 70 bubbles. Fig. 4.16 shows the growth rates of the surface area of three randomly chosen islands taken with a similar size and from two different bubbles. The results show the existence of two different regimes. A first regime corresponds to the surface area of the island increasing approximately quadratically as a function of time. This regime has previously been reported by Dähmlow et al. [2018]; May et al. [2012, 2014]. It is only observed during the oscillation phase of the bubble. As soon as the contractions of the bubble cease and the spherical shape is reached, the second regime is observed, where the surface area of the island remains approximately constant. It is expected that during the second regime, further island dynamics, e.g., coalescence, may take place but on the time scale of minutes or hours Clark et al. [2017]; Shuravin et al. [2019].

A close look at Fig. 4.16 reveals a difference in the rate of growth in the surface area of the islands. Such a result can be explained by the difference in thickness of the islands. The thicker islands, which appear darker, tend to grow more slowly (black and red curves) than the thinner islands (blue curve) as the bubble size decreases. Such a result is consistent with those reported by May et al. [2014]; Oswald et al. [2003].

Strange behavior of some islands

In the routine of measuring the evolution of the surface area of the islands, we have noticed that in 25 plots out of 80, the curves display a strange behavior. This phe-

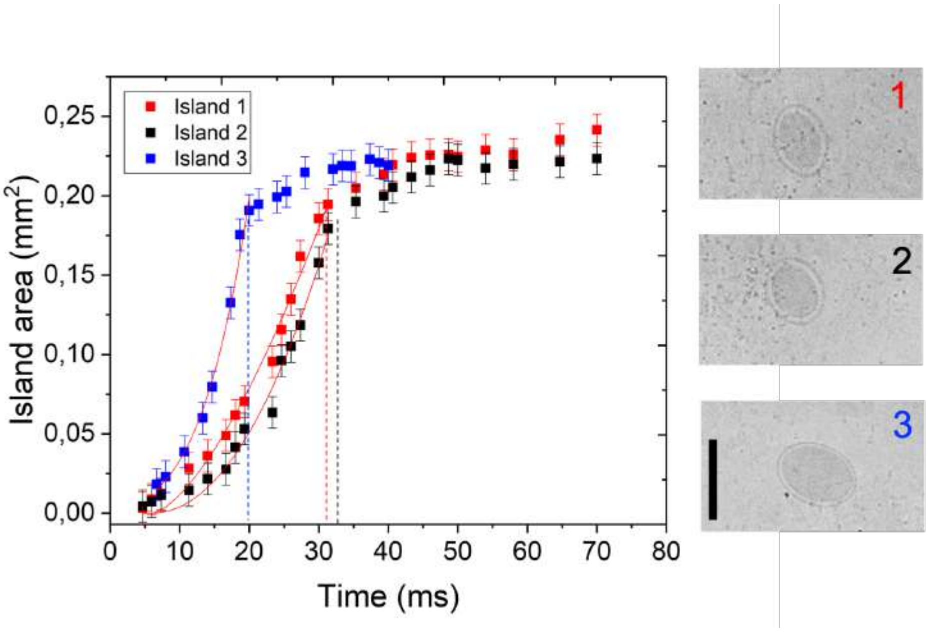

Figure 4.16 – Growth of the surface area of the islands as a function of time. The dotted line separates the two different island dynamics regimes. A quadratic growth is specific to the oscillation regime, while a constant surface area characterizes the second dynamic regime. The difference in growth rate in the first regime can be attributed to the difference in thickness of the islands. The right images, show the three measured islands. The island number 3 is the thinnest (brightest) and number 2 is the thickest (darkest); see text for explanation. The black bar represents 200 μm

nomenon is shown in Fig. 4.17. After pinch-off, the island area, which is the projection of the surface area of the island in the film plan, starts to grow with the usual quadratic dependence on time. Suddenly, the radius of the island decreases rapidly and we observe a decrease in the island area (see the dashed squares in Fig. 4.17). After a short time, the island area starts to grow again reaching back the initial quadratically increasing curve. Then, it continues to grow until the bubble reaches the spherical shape and until the second regime is reached. Fig. 4.17b shows the same behavior as Fig. 4.17a but with two drops. This feature has been observed in 3 cases of islands out of 25.

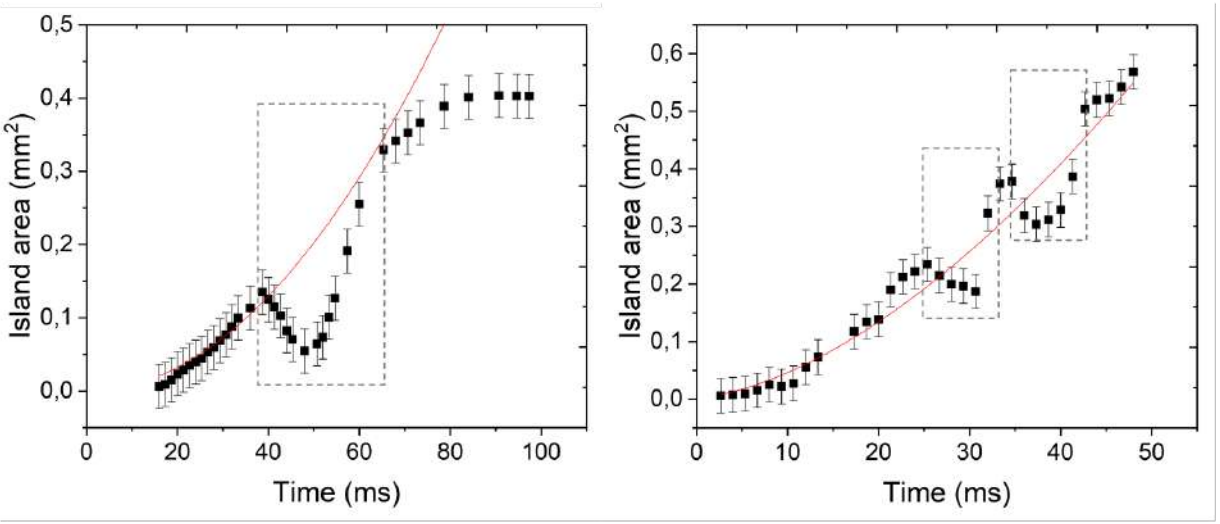

Figure 4.17 – Growth of the island area as a function of time. The brutal drops are indicated by the black dotted squares. The solid red line is a quadratic fit. See text for more explanation.

Where did this strange drop come from? Harth et al. [2019] have reported that smectic bubbles can bulge out of the plane when they undergo strong and fast in-plane compression. They showed that the bulge sites are exactly at the positions of the islands. Thus, one may associate the observed drop in the curve of the island area in function of time with such a phenomenon. In the following section, I focus on this specific behavior of the islands.

4.5.2 Wrinkling of smectic islands

4.5.2.1 Ring-shaped wrinkles

Fig. 4.18a shows the optical image sequences of a typical island during the appearance of the strange phenomenon; we do not identify any bulge but instead: circular wrinkles are observed within the island. In Fig. 4.18b, we show the optical microscopy intensity profile measured along a line drawn across the island (see red dashed line in Fig. 4.18a). The wrinkles are characterized by a selection of a wavelength λ. For this exemplary island, the wavelength is $\lambda \approx 40 \pm 5$ μm at t = 72 ms, which is of the same order of magnitude as that measured for wrinkles in bubbles, $\lambda \approx 20$ μm, by Harth et al. [2019].

We show in Fig. 4.18c the space-time plot of this island. The intensity profile of the wrinkles along the red line is shown in function of time in Fig. 4.18a. Note that the dark lines parallel to the radial-coordinate axis at about t = 70 ms, are artifacts due to the background film. We deduce from the figure that the wrinkles regularly form at the inside first, then new wrinkles appear at the outside during the time as shown by the dark and bright lines parallel to the time axis being formed gradually. This process is achieved with a simultaneous small reduction of the wavelength, λ, of approximately 15% between t = 49 ms and t = 72 ms. This result is consistent with that reported by Harth et al. [2019], where the wavelength of the wrinkles that appear in the bubble film decreases during the compression phase and subsequent increase during the expansion phase. Unfortunately, on the other islands displaying concentric wrinkles, we never had an optical quality good enough to confirm this result.

The wrinkles develop on a time scale of a few milliseconds, much faster than the time scale for the generation or expansion of new islands. However, after a certain period of time, the wrinkle patterns gradually disappear on the outer side first, and the effective area of the island in the film plane increases again to reach back the first rate of growth (Fig. 4.17) and keeps growing until the bubble reaches the spherical shape. The fact that once the wrinkles have disappeared, the evolution of the radius of the islands back again on the same curve as before the wrinkles appeared (See Fig. 4.17), demonstrates that the surface area of the islands continues to grow even during the formation of the wrinkles. This can be achieved by increasing the amplitude of existing wrinkles and by the formation of new undulations, which may reduce the wavelength. This is qualitatively consistent with the amplitude measurement of optical intensity in Fig. 4.18b. Between t = 49 ms and t = 72 ms, the intensity amplitude is almost doubled indicating that the amplitude of the wrinkles increased.

Even though the energy required to deform the smectic film is larger for a thick film than for a thin film Harth et al. [2019], it seems contradictory that islands, which

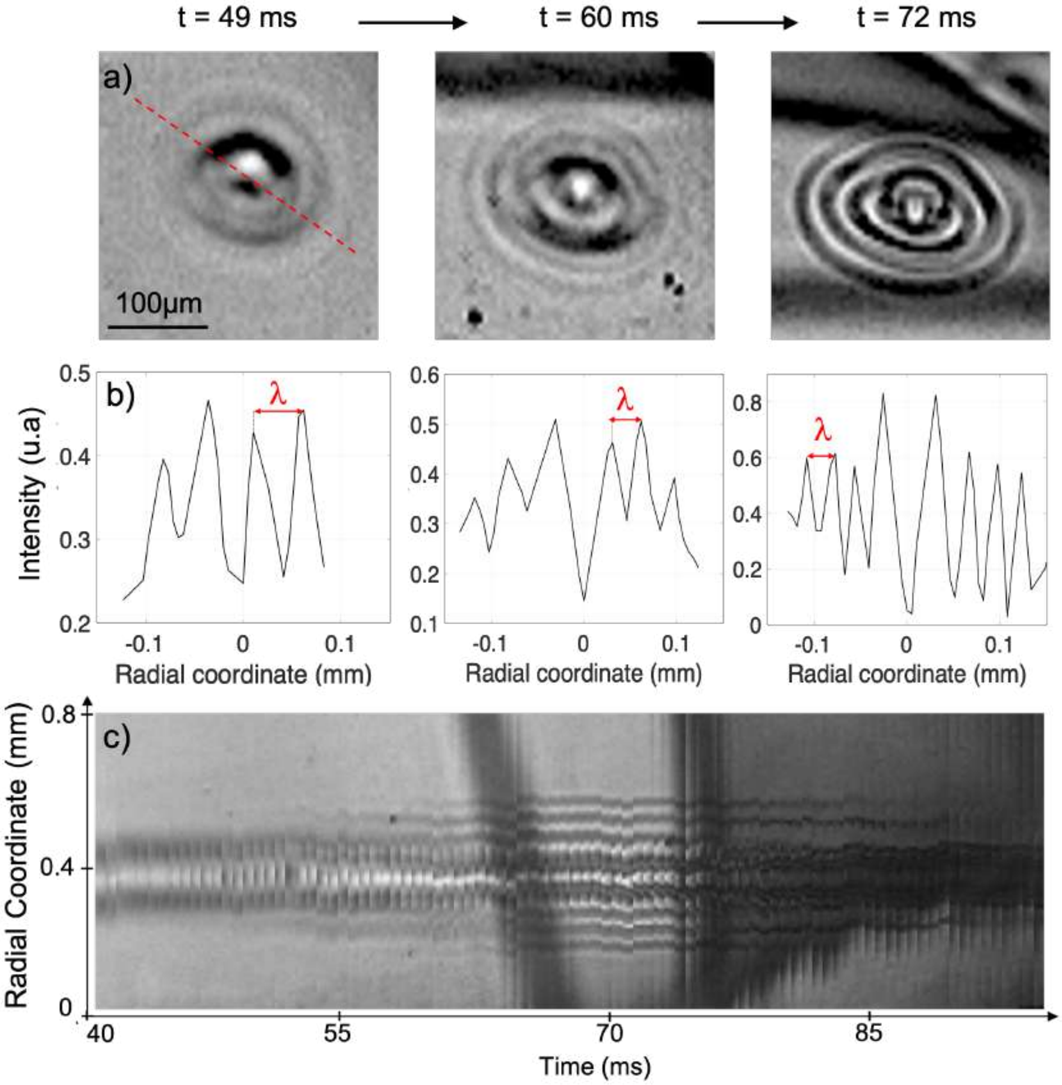

Figure 4.18 – (a) Formation of typical ring-shaped wrinkles within the island surface. (b) Wrinkle intensity profile plot along the red line as a function of time. (c) Space-time plot showing the dynamics behavior of wrinkles over time. The wrinkles regularly form at the inside first, then new wrinkles appear at the outside as a function of time as shown by the dark and bright lines parallel to the time-axis being formed gradually. The bubble is excited with oscillating films remaining on the catenoid rings.

are thicker regions, deform before the background film. We study in the following a possible origin of this observation.

4.5.2.2 External perturbations

What can induce the appearance of such wrinkles within the islands? The fact that wrinkle patterns appear with a certain delay and not just after pinch-off may be related to some additional brutal stress that the island may undergo during their growth. The additional stress may be due to the fact that after pinch-off, smectic bubbles undergo at several occasions a strong and fast external perturbation. For example, the airflow created around the bubble by the two remaining films on the catenoid rings or the two loudspeakers can create an additional lateral compression. This leads to a local shrinkage of the bubble which can induce wrinkle generation in bubbles already discussed in the section 4.4.1 Harth et al. [2019] and could also induce a wrinkling of islands. Another source of perturbations may be associated with the complex shapes that a smectic bubble can acquire during the oscillations regime. Fig. 4.19 shows the region where the island studied in Fig. 4.18 is observed. When these complex regions appear, they can create local compression in the film that in this case not only induces wrinkles in the island shown by the black arrow but also an array of the bubble entirely covered by wrinkles (See the circle in Fig. 4.19).

Fig. 4.20 shows an example of section of a bubble randomly speckled with islands. In order to estimate the local compression applied to this section, I mark the vertical positions of two randomly chosen island, at $t = 14$ ms, by an upper and a lower solid blue arrows. In the following images, I track the instant positions of the two selected islands, which is shown by the upper and the lower open blue arrows. The solid arrows point to the initial position of the islands at $t = 14$ ms. Thus, from the difference between the open and solid arrows, we can measure the local axial contraction of the bubble section. We found that between $t = 14$ ms and $t = 37$ ms, this section contracts by about 35%, with a shrinkage rate of about 1.5% per millisecond. When the axial contraction reaches about 10% ($t \approx 24$ ms), some islands in the displayed region react to the lateral compression in a different way than normal growth or wrinkles generation. They extrude bulges in their centers. The bulge consists of a nucleus that appears and grows at the center of the island and that has been evidenced previously by Harth [2016]; Harth et al. [2019]; May et al. [2012] (See section.4.2.2). It has been shown that

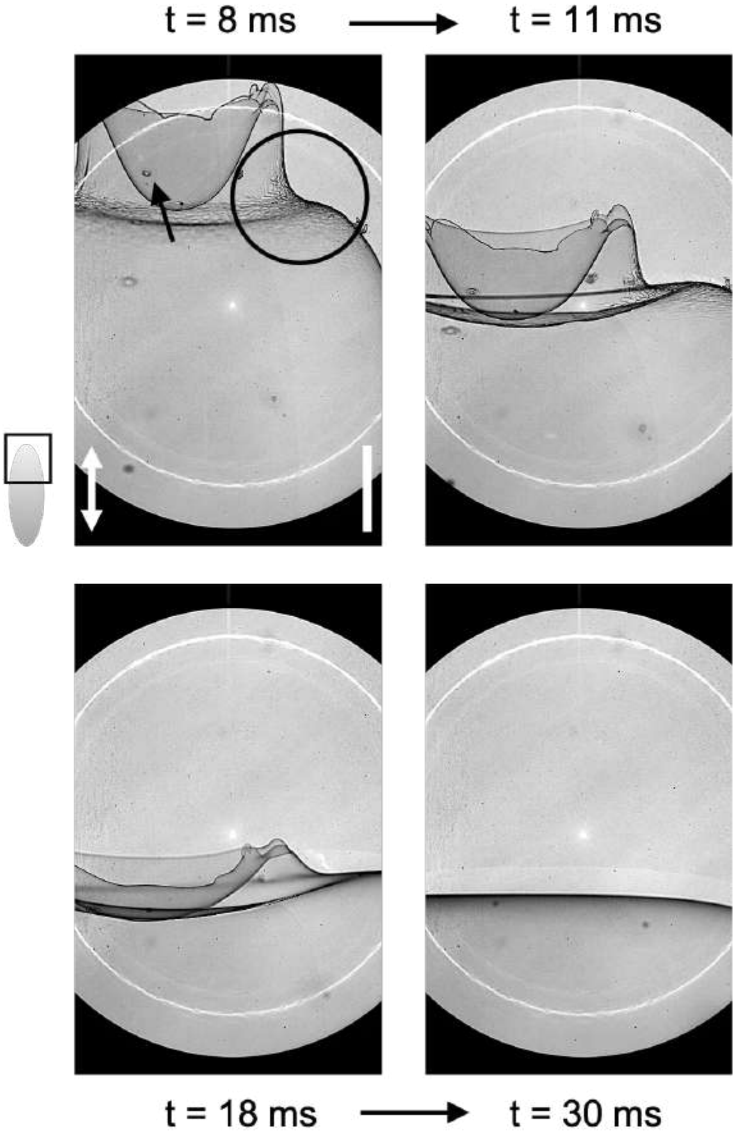

Figure 4.19 – Complex shape acquired by the *SmC* freely floating bubble during the oscillation regime. Bubble wrinkles are formed close to the deformed region of the film (shown by the black circle). The island studied in Fig. 4.18 is shown by the black arrow. The black square on the sketch of the bubble in the left image indicates the field of view of the camera. The white bar represents 1 mm. The axis of symmetry of the catenoid is indicated by the white arrow. The bubble is excited with oscillating films remaining on the catenoid rings.

the characteristic lateral extensions of the bulges depend on the size of the islands. The diameters of the bulges are of the same order as the diameters of the islands. They occur on a time scale of a few milliseconds, much faster than the formation of new islands. As long as the section of the bubble contracts, the bulges develop and can form tubules that may even separate from the film (See the black arrow at t = 37 ms in Fig. 4.20). However, when the compressed section stretches again, the bulges disappear and the islands become flat again.

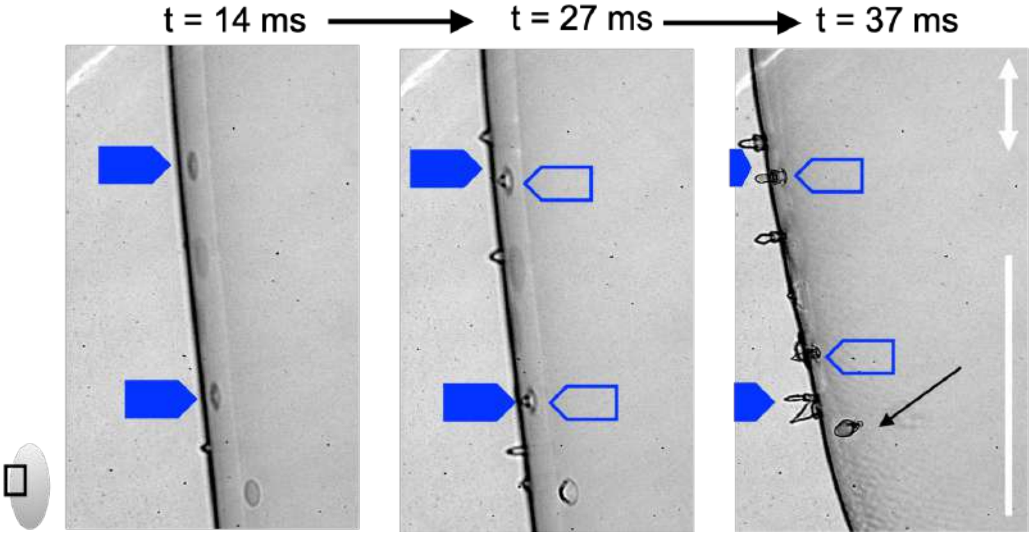

Figure 4.20 – Formation of bulges at the islands during the oscillation of a bubble. The blue arrows are used to determine the local compression (see the text for explanation). The black arrow in the image at t = 37 ms, shows the formation of a tubule. The black square on the sketch of the bubble in the left image indicates the field of view of the camera. The white bar represents 1 mm. The axis of symmetry of the catenoid is indicated by the white arrow. The bubble is excited with oscillating films remaining on the catenoid rings.

When the external compressive stress is too fast to be compensated by the growth of the surface area of the island alone, the island may react by generating wrinkles and bulges. They are formed in order to compensate the compressive stress while keeping the same rate of growth of the island surface area. The wrinkles allow for the smectic film within the island to be drawn towards each other in three-dimensional space, i.e. to reduce the effective surface area of the bubble locally. Thus, their presence shows that under fast and strong compressive stress, the smectic films behave like membranes with zero surface tension. Such phenomena cannot be observed in low-viscosity conventional fluid films, such as soap bubbles, because those bubbles can almost instantaneously change their thickness or reduce their surface when exposed to strong and fast compression.

4.5.2.3 Wrinkling bubble model

Harth et al. [2019] have developed a model to describe the wrinkle structures observed in freely floating bubbles and to estimate the value of the selected wavelength. The model has been developed for *SmA* films but was applied to *SmC* bubbles. The external disturbances were mainly associated with the complex airflow that causes local compression of the bubble film. The model, for simplicity, is one-dimensional, but it captures the main features of the structure qualitatively. The authors considered a rectangular film with a fixed width B and initial length $L_0 = L(t = 0\ s)$ (See Fig. 4.21). The wrinkle wavelength is λ and the amplitude is a. The film area is considered compressed by opposing forces $\vec{F}_s$ along z and -z. Thus, the film reacts by forming N wrinkles with an initial wavelength $\lambda_0 = L_0/N$ and amplitude *a(t)*. The authors approximated the small deformations of the film in the x direction by the harmonic ansatz $X(z) = a \sin qz$, with $q = 2\pi/\lambda$ (See Fig. 4.21). The initial wave number is $q_0 = 2\pi N/L_0$. As the model treats the initial wavelength selection process, the authors approximated the wavelength to be fixed during the wavelength selection and $q \approx q_0$. The temporal variation in the experiments does not exceed $\approx 10\%$. For the description of the wavelength selection process, at least one mechanism that inhibits the formation of short-wavelength undulations and another that inhibits the tail at long wavelength have to be defined Harth et al. [2019].

The compressive force per unit of width of the undulated film is given by $f_s = F_s/B$. This force perform a mechanical work on the film during the compression as: $W_s(t) = f_s B(L_0 - L(t))$. Using the relation $L_0 = \int_0^L \sqrt{1 + (\mathrm{d}X/\mathrm{d}z)^2}\mathrm{d}z$, L_0 can be expressed as a function of L as the following: $L_0 \approx (1 + a^2q^2/4)L$. Thus, W_s can be written as

$$W_s = \frac{f_s BL}{4} a^2 q^2 \tag{4.3}$$

This term contributes to a preference for short wavelength modes.

The presence of the wrinkles bends the smectic membrane. This bend is related to a free energy density contribution of the form

$$\mathrm{w}_b = \frac{1}{2} K(X'')^2 \tag{4.4}$$

K here is considered as the bending elasticity of the smectic layers. It mostly contains contribution from the splay deformation of the director $\vec{n}(z)$. Harth et al. [2019]

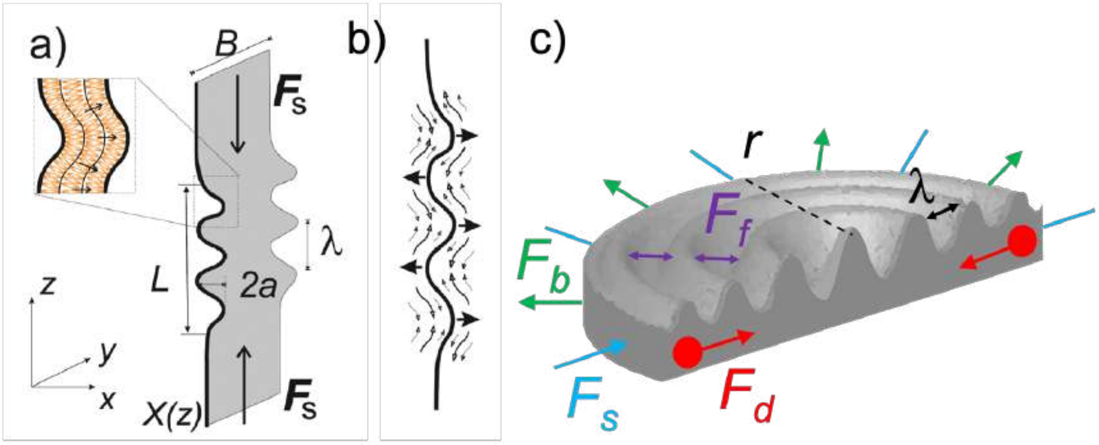

Figure 4.21 – (a) Rectangular compressed film geometry. The left sketch shows the details of the film layer structure and the molecular arrangement. The arrows indicate the local director $\vec{n}$ orientation. (b) Characteristics of the air flow on both sides of the film (small arrows) induced by the formation of wrinkles (big arrows). Republished with permission of ROYAL SOCIETY OF CHEMISTRY, from Dynamic wrinkling of freely floating smectic films, Harth et al. [2019]. 2019, 15, 6769; permission conveyed through Copyright Clearance Center, Inc. (c) 3D sketch of a wrinkling circular island showing the applied forces. The red circles indicate the dislocation lines surrounding the island. λ is the wrinkles characteristic wavelength.

reported that only the splay deformation dominates the smectic layer bending elasticity, other contributions can be neglected Fujii et al. [2011]; Santangelo and Kamien [2005]. In the case of small deformations, the spatial derivative of the director $\vec{n} \approx (1, 0, X') = (1, 0, -aq\cos qz)$, is linearly coupled to layer undulation in the *SmA* phase as

$$(\nabla \vec{n}) = \frac{\mathrm{d}n_z}{\mathrm{d}z} = -\frac{\mathrm{d}^2 X}{\mathrm{d}z^2}. \tag{4.5}$$

Thus,

$$\mathrm{w}_b \approx \mathrm{w}_{elastic} = \frac{1}{2} k_s (\nabla \vec{n})^2 = \frac{k_s}{2} a^2 q^4 \sin^2 qz. \tag{4.6}$$

The corresponding mechanical work can be obtained by integrating w_b over the wrinkled region, with the average $\overline{\sin^2 qr} = \overline{\cos^2 qr} = 1/2$ as

$$W_b = \frac{k_s LBh}{4} a^2 q^4. \tag{4.7}$$

h is the smectic film thickness. The authors reported that this model is correct only for *SmA* films because the elastic deformations are more complicated for the *SmC* bubble. This is why this simplified model is dedicated to the qualitative description of the instability mechanism.

On the other hand, the rate of wrinkle growth needs to be connected to the airflow, as described in Fig. 4.21b, from the crests to the valleys of the undulation, and consequently to the pressure profile along the film, $p(z) = p_0 \sin qz$. Harth et al. [2019] have used the following damping mechanism, already used for the description of wrinkles of elastic sheets on a layer of a viscous fluid by Kodio et al. [2017], in order to qualitatively relate the pressure gradients ($p'(z)$) in the film plane with the airflow along the film (z direction), j_z, as the following

$$j_z = -Cp'(z). \tag{4.8}$$

C is a geometric constant that describes the complex flow processes that redistribute the air along the wrinkling film on both sides. Harth et al. [2019] assumed that C is wavelength independent. The film deformation changes according to

$$\dot{X} = \frac{\mathrm{d}j_z}{\mathrm{d}z} = -Cp''(z). \tag{4.9}$$

Eq. 4.9 leads to the relation between the growth of the deformation amplitude and the pressure amplitude as Harth et al. [2019]

$$\dot{a} = Cq^2 p_0, \;\; p = \dot{a}C^{-1}q^{-2}\sin qz. \tag{4.10}$$

The dissipated energy in the process is Harth et al. [2019]

$$W_f = \int_0^L p\mathrm{d}V = B\int_0^L pX\mathrm{d}z. \tag{4.11}$$

The authors have shown that the film locally performs the work $p\mathrm{d}V$ associated with the air pushed aside which is assumed to be dissipated by the displacement of air near the film during the growth of the undulation amplitude. Therefore,

$$W_f = B\int_0^L C^{-1}q^{-2}\sin^2(qz)a\dot{a}\mathrm{d}z = \frac{BL}{2Cq^2}a\dot{a}. \tag{4.12}$$

The balance between the works, $W_s = W_f + W_b$, yields the following dispersion relation

$$\dot{a} = (f_s q^4 - k_s h q^6)\frac{C}{2}a, \tag{4.13}$$

which describes exponential growth of an unstable mode band between q=0 and $q_c = \sqrt{f_s/(k_s h)}$ Harth et al. [2019]. This implies that wrinkles with short wavelength are suppressed by the bending elasticity of the smectic layers and those with large wavelength grow slowly. Hence, for an intermediate wavelength, an optimum growth rate exists allowing for a specific wavelength selection. The fastest growing mode is calculated to be

$$q_{max} = \sqrt{\frac{2f_s}{3k_s h}}. \tag{4.14}$$

with the maximum growth rate

$$s_{max} = \frac{2C}{27}\frac{f_s^3}{k_s^2 h^2}. \tag{4.15}$$

The wave number q_{max} (Eq. 4.14) depends on the elastic constant and the film thickness. It decreases when increasing h and k_s for a given compressive force f_s. The compressive force is thus the essential ingredient for the formation of the undulation in the film. It needs to exceed a critical value set by h and k_s in order to form an unstable mode band with sufficiently quick growth rates Harth et al. [2019]. The authors reported that for a wavelength of 20 μm, the model leads to f_s of the order of 3 nN m^{-1} ($k_s = 10$ pN and h = 20 nm).

4.5.2.4 Wrinkling island model

The model developed by Harth et al. [2019] treats the experimental case where wrinkles appear in the bubble-forming film considered with a constant surface (Fig. 4.21). Thus, we try to adapt this model to circular islands, where the line tension of the surrounding dislocations must be taken into account. The surface area of the island is considered to be compressed by external compressive forces, $\vec{F}_s$, considered as dispersed along the island perimeter. The corresponding mechanical work, W_s, in the radial configuration of the wrinkling island is therefore: $W_s = f_s 2\pi r(r_0 - r)$, with f_s the force per unit of length and r_0 the initial island radius. Proceeding as the previous model, the response of the film is formation of wrinkles with initial wavelength λ_0 and amplitude *a(t)*. The initial wave number is $q_0 = 2\pi/\lambda_0$. We approximate the wavelength, λ, to be fixed during the wavelength selection process, and $q \approx q_0$. The temporal variation in the experiments is indeed only about 15%.

In the case of an undulated island, the small deformations of the film in the radial direction are different from those considered by Harth et al. [2019]. The presence of a small ridge in the center of the island, shown in Fig. 4.18, does not allow perfectly to describe the radial deformation by the Ansatz harmonic function. The use of another set of Ansatz functions such as the Bessel function could be a consistent description. However, for a first simplified model, we approximate the radial deformation of the undulated island by $h(r) = a\cos qr$, with $q = 2\pi/\lambda$, which may be correct for small enough undulations. The surface area of the island in the absence of wrinkles is: $A = \pi r_0^2$. In the presence of wrinkles, the surface area can be obtained in the cylindrical coordinate system as $A = 2\pi \int_0^r \sqrt{1 + h'^2}\, \rho \, \mathrm{d}\rho \approx \pi r^2(1 + \frac{a^2q^2}{4})$. Thus, we obtain $r_0 \approx r\sqrt{1 + \frac{a^2q^2}{4}} \approx r(1 + \frac{a^2q^2}{8})$, for small enough undulations. Therefore, the mechanical work performed by the compressive force, W_s, can be written as

$$W_s = f_s \frac{\pi r^2}{4} a^2 q^2. \tag{4.16}$$

The bending of smectic membranes induced by the wrinkles leads to an elastic free energy density contribution of the form Harth et al. [2019]

$$\mathrm{w}_b \approx \mathrm{w}_{elastic} = \frac{k_s}{2} a^2 q^4 cos^2 qr. \tag{4.17}$$

The mechanical work associated with the bend of the smectic layer can be derived similarly to the previous model Harth et al. [2019], with the average $\overline{\cos^2 qr} = 1/2$, as

$$W_b = \frac{k_s \pi r^2 h}{4} a^2 q^4. \tag{4.18}$$

On the other hand, the relationship between the growth rate of the undulation, the airflow and the pressure profile in the case of wrinkling islands could differ from that of rectangular films. The inhomogeneities of the amplitude of the wrinkles, especially when approaching the center where the small ridge is formed, could induce a distribution of the airflow not homogeneous across the wrinkles in contrast with the case in rectangular films. Since we are interested primarily in the qualitative description of the instability mechanism and to compare the order of magnitudes of the different parameters, this effect is considered of secondary importance. Therefore, the performed mechanical work, W_f, in the radial geometry of the island is assumed to be

$$W_f = \frac{\pi r^2}{2Cq^2} a\dot{a}. \tag{4.19}$$

If we now want to take into account the line tension created by the dislocation lines around the islands, we can notice that the line tension, γ, plays a role similar to f_s with a positive work when the island perimeter decreases. The performed mechanical work can be written as: $W_d = \gamma 2\pi(r - r_0)$, therefore

$$W_d = \gamma \frac{\pi r}{4} a^2 q^2. \tag{4.20}$$

The balance between the works, $W_s + W_d = W_b + W_f$, leads to the following dispersion relation

$$\dot{a} = \left[(f_s + (\gamma/r_c))q^2 - k_s h q^4\right] \frac{C}{2} q^2 a = \left[(f_s + (\gamma/r_c))q^4 - k_s h q^6\right] \frac{C}{2} a. \tag{4.21}$$

Since we are interested in a qualitative description of the instability mechanism, the radius r is approximated to be set to a constant value $r_c \approx 10^{-4}$ m. Eq. 4.21 describes an exponential growth of an unstable mode band between q=0 and $q_c = \sqrt{(f_s + (\gamma/r_c))/(k_s h)}$. The fastest growing mode is calculated to be

$$q_{max} = \sqrt{\frac{2(f_s + (\gamma/r_c))}{3k_s h}} \tag{4.22}$$

with the maximum growth rate

$$s_{max} = \frac{2C}{27} \frac{(f_s + (\gamma/r_c))^3}{k_s^2 h^2} \tag{4.23}$$

We have obtained a wavelength of 40 μm. If we consider that the wrinkling island shown in Fig. 4.18 has only two extra layers compared to the background film, we find that $(f_s + (\gamma/r_c))$ of the order of 2 nN m^{-1}.

This result is consistent with the observation that wrinkles are favored by the effect of line tensions and are formed in islands without inducing wrinkles in the bubble because f_s is smaller than 3 nN m^{-1}. However f_s is not negligible with respect to γ/r_c otherwise wrinkles would be observed in all islands even without external perturbations. This leads to a value for γ not larger than 2.10^{-13} N. In the literature there are very few measurements of dislocation line tensions. It has been measured by Géminard et al. [1998] for *SmA* 8CB, to be proportional to the Burgers vector and to a line tension T of the order of 10^{-11} N. This value is significantly larger than the one found here which may be related at least partly to the *SmC* nature of the material. For example it has been shown recently that the internal structure of *SmC* edge dislocations could be significantly different than the one of *SmA* Zhang et al. [2015].

4.5.2.5 Influence of island size

Fig. 4.22 shows a typical image sequence of a contracting section of a relaxing bubble which is randomly speckled with islands. The islands were either already present in the catenoid or formed during the pinch-off. In order to visualize the contraction of the bubble along the axis of the catenoid (axial contraction), we mark two random islands located in the direction parallel to the axis of symmetry of the catenoid by the solid green arrows. Then we follow their instantaneous position, indicated in the following images by the open green arrows, during the contraction of the bubble with respect to the initial positions (solid green arrows). The total axial contraction of the bubble in the displayed region amounts to ≈ 9%.

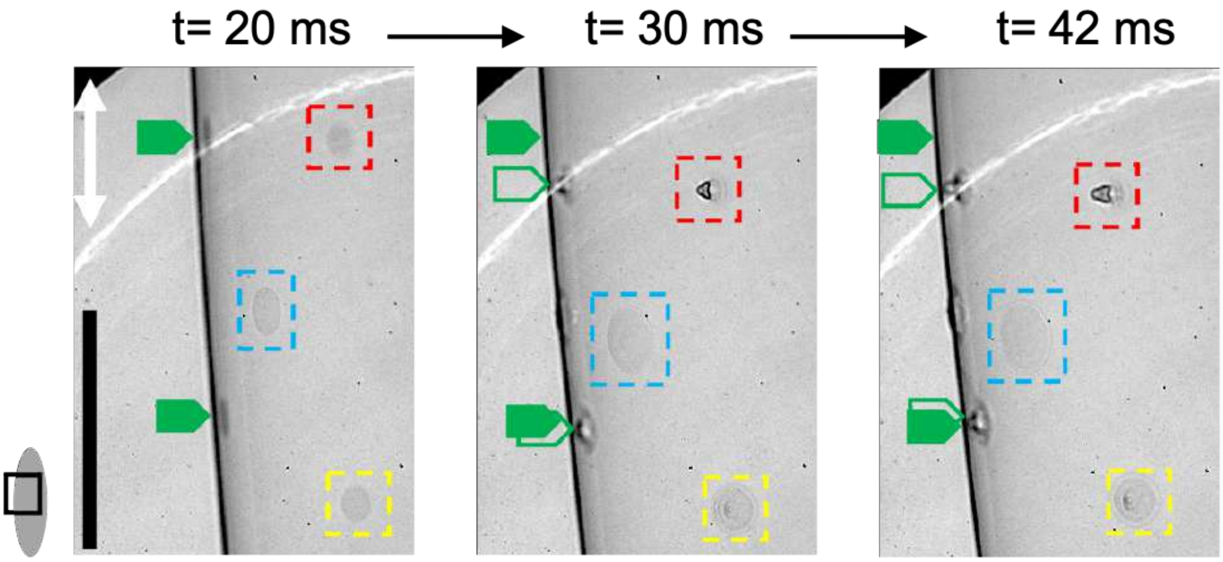

Figure 4.22 – Formation of a bulge at the center of the island shown by the red square. The island shown by the yellow square generates circular wrinkles. The island shown by the blue square seems not affected by the lateral compression and it grows normally. The solid and open green arrows indicate the lateral compression over time. t = 0 ms is the pinch-off time. The axis of symmetry of the catenoid is indicated by the white arrow. The bubble is excited with oscillating films remaining on the catenoid rings. The black bar indicates 1 mm.

The region shown in Fig. 4.22 is interesting because we evidence three different phenomena in parallel. The large island shown by the blue square grows without developing any wrinkles. On the other hand, the island shown by the yellow square is affected by the compression and generates ring-shaped wrinkles similar to the pattern observed in Fig. 4.18 (particularly visible at t = 30 ms). The small island, shown by the red square reacts to the compression by a formation of a bulge at the center.

The medium-sized island shown by the yellow square undergoes a stress large enough to induce wrinkles in the island. From pinch-off and up to $t = 30$ ms, this island grows normally without forming any deformation to reach a radius of about 90 μm. From $t = 30$ ms, wrinkles appear. At this time an abrupt external stress may be applied to the islands leading to a formation of wrinkles with a selection of wavelength.

We consider the various islands to be of equivalent thickness according to their similar contrast on the images. We understand from the observation that no wrinkles are observed in the large island surrounded by a blue square. This island continuously grows but does not display any wrinkle. The compressive force, f_s, can be considered similar to the one for the intermediate island surrounded by a yellow square, which is very close. However γ/r_c is smaller for the larger island since r_c is larger. As a result, $(f_s + \gamma/r_c)$ is not large enough to induce wrinkles if r_c is larger than 90μm, the radius of the large island. f_s being too small to induce wrinkles in the large island, consistently we may expect no wrinkle in the bubble around as observed.

The third and smallest island shown by the red square undergoes the highest stress compared to the two previous islands, because the term γ/r_c becomes important in this small island. The compressive stress added to the line tension exerts a large stress. As a consequence, the island has the tendency to also wrinkle like the intermediate island. However, it may not be possible to accommodate formation of wrinkles because the size of the island is smaller or of the same order of magnitude as the characteristic wavelength of the wrinkles λ. This suggests that for islands with a radius of the order of λ or smaller, the formation of wrinkles cannot be accommodated within the islands. Thus, instead the island bulges out of the film plane. Indeed a bulge is observed in the small island at the same time where wrinkles are observed in the intermediate one, so when the external abrupt stress starts. Sometimes the bulges transform into tubule that can even pinch-off from the film. This can finally induce another type of wrinkle pattern, which I discuss in the next section.

It is now clear that the line tension of the dislocations around the islands plays a crucial role to select the wavelength of the wrinkles observed in the islands.

4.5.2.6 Star-shape wrinkles

When a small island cannot react to compressive stress by generating circular wrinkles, this island bulges out of the plane of the film and tubule can form as shown in Fig.

4.22. However, the formation of thin bulge or tubule in the center of the island may provide a different type of stress which induces radially aligned wrinkles. Fig. 4.23 shows a typical example of star-shaped wrinkles, where radial indentations are formed within the island surface. This situation was observed only in two islands during our study. The effect induced by the extrusions of the island's tubule is similar to that induced by an AFM tip pressing the surface of a graphene sheet Lee et al. [2008]. This type of wrinkle morphology has also been observed in bubbles Harth [2016]. It forms when the bubble film is stretched in a direction other than the overall relaxation direction of the bubble (Fig. 4.24).

For both types of wrinkle patterns; ring and star-shaped, it is reasonable to assume that the surface area of the island follows the quadratic dependence in function of time even when wrinkles are formed. Only the extension of the island in the film plane (projection on the film plane) is reduced. The wrinkles allow for the smectic layered material to be drawn towards each other in three-dimensional space. Similar to wrinkles observed in freely floating smectic bubbles (See section.4.4.1), island wrinkles are transient dynamic instabilities. They disappear as soon as the local compressive stress ceases.

In summary, we can see now that smectic islands react to external stress in unexpected ways. Our experiments revealed two types of dynamic wrinkles; ring and star-shaped patterns. The type of wrinkle depends on the distribution of stress. As we will see in the following section, the topology of the observed wrinkles is similar to that of a solid sheet subjected to unilateral compression.

4.5.3 Smectic islands can wrinkle like solid sheets?

In a recent study by Zhao et al. [2011], a shape-memory polymer was covered with a thin gold layer. The authors have described different wrinkle morphologies upon temperature changes as a consequence of thermal expansion mismatches between the gold and polymer layers. Fig. 4.25 shows in the upper row two images of the polymer/gold film stack after shape recovery of the polymer material. In the left image, the polymer was treated such that it forms a protrusion after thermal recovery, and a radial ray-like pattern is formed. In the right image, the gold film wrinkles in a circular target-like pattern. The wave length selection of the target pattern in the polymer film is governed by the ratio of elastic moduli of mutually connected layers. On the other

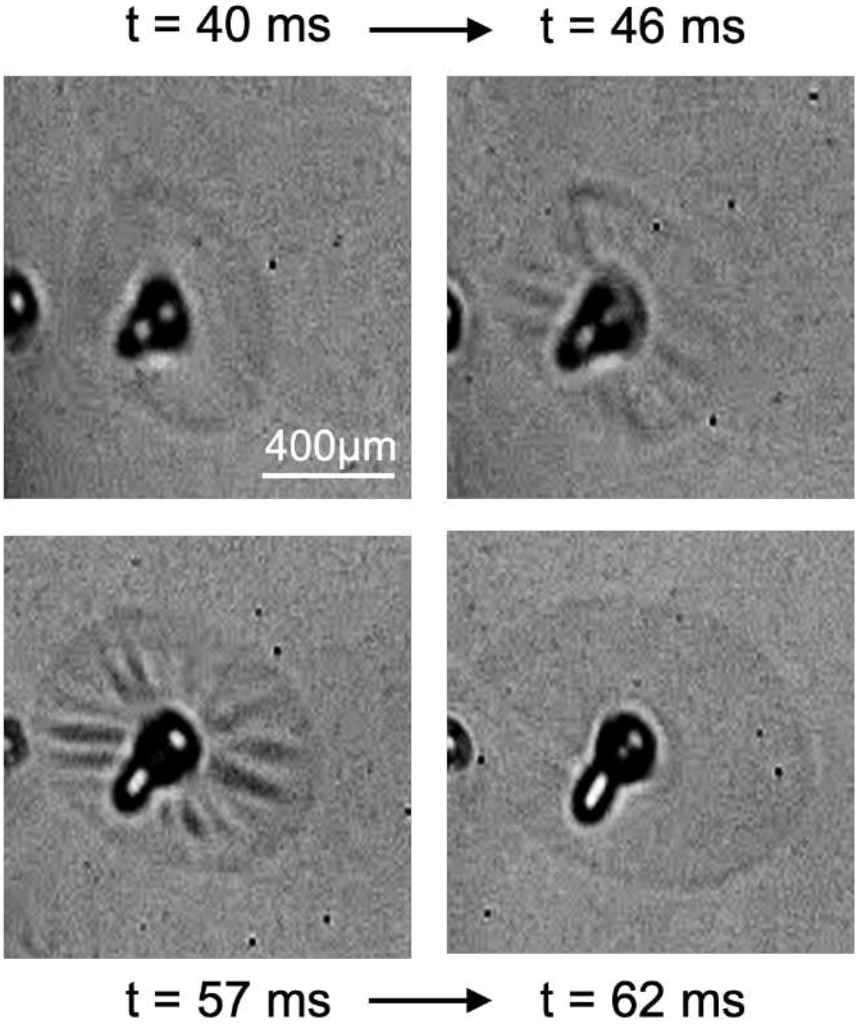

Figure 4.23 – Formation of a tubule in the center of an island. The detachments of such a tubule creates a stress that causes the island to wrinkle as shown at t = 57 ms. Note that t = 0 ms is the pinch time. When the disturbance induced by the tubule ceases, the wrinkles disappear as observed at t = 62 ms and the island continues to grow until the spherical shape of the bubble is reached. The bubble is excited with oscillating films remaining on the catenoid rings.

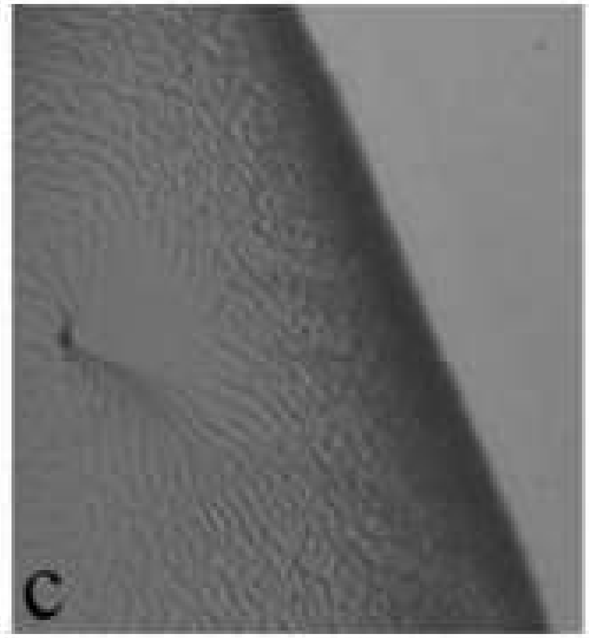

Figure 4.24 – Formation of radial-shaped wrinkles in *SmC* bubbles. Image reprinted with permission of K. Harth Harth [2016].

hand, the star-like radial wrinkles can be attributed to a compromise of stretching and bending of an out-of-plane indented membrane. Similar patterns have been described, e. g., in solid polymer films floating on water surfaces Huang et al. [2007] Holmes and Crosby [2010] Vella et al. [2015].

The patterns shown in Fig. 4.25 are very similar to the *SmC* wrinkles observed in our bubbles (Fig. 4.25c and Fig. 4.25d), and similar explanations may be sought. These structures are related to the same compression processes, but their nature is quite different. The key difference with respect to previously described patterns in uniformly thick smectic films, common to all patterns shown in Fig. 4.25, is that the circular island geometry poses specific boundary conditions to the patterns that define the pattern morphologies. However, the main difference between smectic island and gold or polymer is related with the mechanism driving the wrinkles which monitors the typical distances at play. However, more investigations remain required now to deeply understand the phenomenon, in particular the development of more quantitative models.

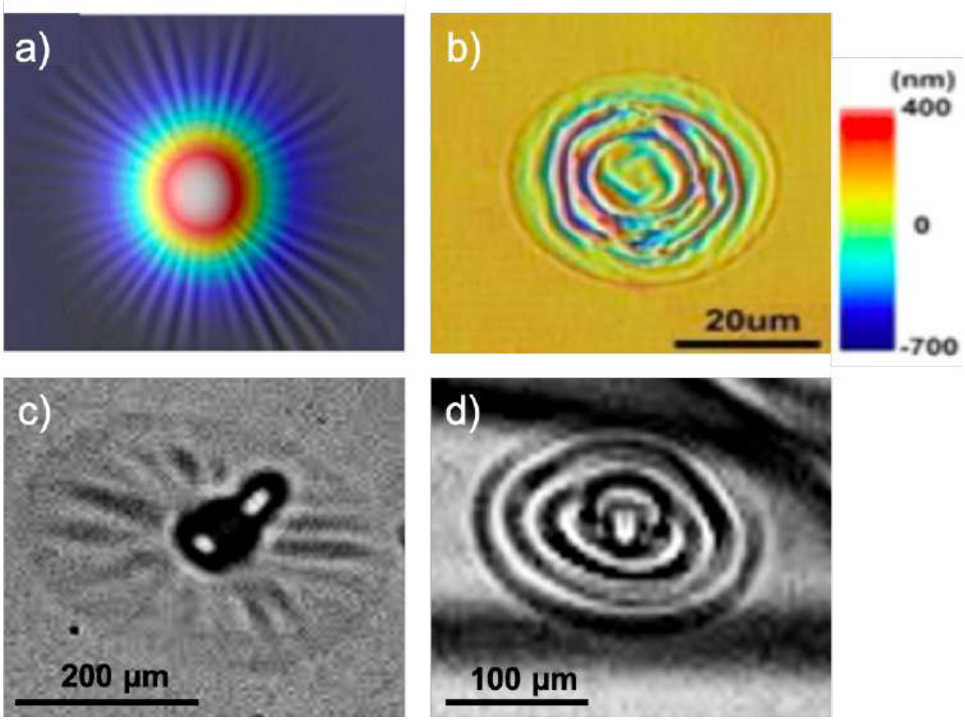

Figure 4.25 – (a) and (b) : Images of gold coated shape memory polymers after shape recovery of a locally indented sample. Left: Radial pattern above a protrusion of the shape-recovered polymer, right: Ring pattern above a pre-indented area. Image reproduced from Zhao et al. [2011] with permission of IOP Publishing, Ltd. (c) and (d) : Star and ring shaped wrinkle patterns observed in smectic islands.

4.6 Summary

Our investigation on the dynamics of the islands formed in *SmC* freely floating bubbles have been performed by means of high-speed camera, under zero-gravity conditions. We have recovered the already demonstrated quadratic growth of the islands, but that appears to be followed by a second regime where further islands dynamics, for example coalescence, may take place at time scale of minutes or hours. We have shown that smectic islands in freely floating bubbles can form dynamical wrinkles with two types of patterns when they undergo in-plane compression: ring and star shaped wrinkles with a selection of wavelength λ of the order of some tenths of micrometers. The formation of these wrinkles is a consequence of the abrupt compression applied on the islands. We have associated this abrupt change to external disturbances that can take place due to two main sources: (1) The airflow around the bubble generated by the oscillating films remaining on the two catenoid rings or the loudspeakers, which locally compresses the smectic film. (2) The complex deformed areas that the bubble acquires during the relaxation dynamics, which can also create local compression of the film.

The model previously developed to describe the structure of wrinkles in bubbles has been adapted for the case of circular island deformation. This new model explains the fact that islands, which are thicker regions, deform before the background film, highlighting the importance of the line tension of the dislocations that surround the islands. The line tension is added to the compression force applied to the island during bubble relaxation to provide enough stress allowing to form the wrinkles, these wrinkles being not observed in the background film next to the island, where the compression force without the line tension may not be enough to form the wrinkles in the film.

The adapted model also explains the experimental observations, related to the size of the islands. The contribution of line tension decreases with the radius of the island and, when added to the compression force, it does not provide enough stress to form the wrinkles in large islands. This is in contrast with smaller islands, where the contribution of line tension becomes important and provides enough stress to form circular wrinkles with a λ wavelength selection. However, when the size of the islands becomes of the order of λ or smaller, the formation of circular wrinkles can no longer be accommodated and the island bulges out of the film plane.

The formation of bulge in the center of the islands causes another type of stress different from that applied by the compression force and line tension on flat islands. This new type of stress induces the formation of another wrinkles pattern: radial-shaped wrinkles.

We were then able to conclude that smectic islands can behave as solid sheets under sufficient compression stress. The wrinkle patterns in smectic islands are structurally equivalent to, for example, thin gold films on a polymer substrate with incompatible coefficients of thermal expansion under temperature changes. This phenomenon cannot occur in conventional low-viscosity soap films because they can instantly change their thickness and film surface under lateral compression.

4.7 References

Ben Amar, M., Silva, P., Limodin, N., Langlois, A., Brazovskaia, M., Even, C., Chikina, I., and Pieranski, P. (1998). Stability and vibrations of catenoid-shaped smectic films. *Physics of Condensed Matter*, 3:197–202. 128

Bevilacqua, G. and Napoli, G. (2005). Reexamination of the helfrich-hurault effect in smectic-*a* liquid crystals. *Phys. Rev. E*, 72:041708. 124

Cerda, E. and Mahadevan, L. (2003). Geometry and physics of wrinkling. *Phys. Rev. Lett.*, 90:074302. 117

Chen, H., Zhao, Y., Li, J., Guo, M., Wan, J., Weitz, D. A., and Stone, H. A. (2011). Reactions in double emulsions by flow-controlled coalescence of encapsulated drops. *Lab Chip*, 11:2312–2315. 116

Chen, Y.-J. and Steen, P. H. (1997). Dynamics of inviscid capillary breakup: collapse and pinchoff of a film bridge. *Journal of Fluid Mechanics*, 341:245–267. 128

Chokkalingam, V., Weidenhof, B., Krämer, M., Maier, W. F., Herminghaus, S., and Seemann, R. (2010). Optimized droplet-based microfluidics scheme for sol–gel reactions. *Lab Chip*, 10:1700–1705. 116

Clark, N. A., Eremin, A., Glaser, M. A., Hall, N., Harth, K., Klopp, C., Maclennan, J. E., Park, C. S., Stannarius, R., Tin, P., Thurmes, W. N., and Trittel, T. (2017). Realization of hydrodynamic experiments on quasi-2d liquid crystal films in microgravity. *Advances in Space Research*, 60(3):737–751. 139

Dähmlow, P., Trittel, T., May, K., Harth, K., and Stannarius, R. (2018). Surface reduction of freely floating smectic bubbles. *Liquid Crystals*, 45(7):993–1003. 119, 123, 124, 139

Forsyth, A. M., Wan, J., Owrutsky, P. D., Abkarian, M., and Stone, H. A. (2011). Multiscale approach to link red blood cell dynamics, shear viscosity, and atp release. *Proceedings of the National Academy of Sciences*, 108(27):10986–10991. 116

Fujii, S., Komura, S., Ishii, Y., and Lu, C.-Y. D. (2011). Elasticity of smectic liquid crystals with focal conic domains. *Journal of Physics: Condensed Matter*, 23(23):235105. 148

Géminard, J.-C., Laroche, C., and Oswald, P. (1998). Edge dislocation in a vertical smectic-*a* film: Line tension versus film thickness and burgers vector. *Phys. Rev. E*, 58:5923–5925. 152

Harth, K. (2016). *Episodes of the life and death of thin fluid membranes - patterns and dynamics at the cross-over from two to three dimensions*. PhD thesis, Otto-von-Guericke-Universität Magdeburg. 116, 117, 123, 127, 132, 134, 144, 155, 157

Harth, K., Schulz, B., Bahr, C., and Stannarius, R. (2011). Atomic force microscopy of menisci of free-standing smectic films. *Soft Matter*, 7:7103–7111. 123

Harth, K. and Stannarius, R. (2009). Corona patterns around inclusions in freely suspended smectic films. *The European physical journal. E, Soft Matter*, 28:265–72. 123

Harth, K., Trittel, T., May, K., and Stannarius, R. (2019). Dynamic wrinkling of freely floating smectic films. *Soft Matter*, 15:6769–6778. 120, 122, 123, 124, 125, 126, 127, 132, 134, 135, 141, 142, 144, 147, 148, 149, 150, 151

Holmes, D. P. and Crosby, A. J. (2010). Draping films: A wrinkle to fold transition. *Phys. Rev. Lett.*, 105:038303. 157

Huang, J., Juszkiewicz, M., de Jeu, W. H., Cerda, E., Emrick, T., Menon, N., and Russell, T. P. (2007). Capillary wrinkling of floating thin polymer films. *Science*, 317(5838):650–653. 157

Jahnig, F. (1996). What is the surface tension of a lipid bilayer membrane? *Biophys. J.*, 3:1348–1349. 124

Kantsler, V., Segre, E., and Steinberg, V. (2007). Vesicle dynamics in time-dependent elongation flow: Wrinkling instability. *Phys. Rev. Lett.*, 99:178102. 124

Knoche, S., Vella, D., Aumaitre, E., Degen, P., Rehage, H., Cicuta, P., and Kierfeld, J. (2013). Elastometry of deflated capsules: Elastic moduli from shape and wrinkle analysis. *Langmuir : The ACS Journal of Surfaces and Colloids*, 29:12463–12471. 117

Kodio, O., Griffiths, I. M., and Vella, D. (2017). Lubricated wrinkles: Imposed constraints affect the dynamics of wrinkle coarsening. *Phys. Rev. Fluids*, 2:014202. 149

Kornek, U., Müller, F., Harth, K., Hahn, A., Ganesan, S., Tobiska, L., and Stannarius, R. (2010). Oscillations of soap bubbles. *New Journal of Physics*, 12(7):073031. 116, 117

Lee, C., Wei, X., Kysar, J. W., and Hone, J. (2008). Measurement of the elastic properties and intrinsic strength of monolayer graphene. *Science*, 321(5887):385–388. 155

Lee, J., Weon, B. M., Park, S., Je, J., Fezzaa, K., and Lee, W.-K. (2011). Size limits the formation of liquid jets during bubble bursting. *Nature Communications*, 2:367. 116

Li, E. Q., Beilharz, D., and Thoroddsen, S. T. (2017). Vortex-induced buckling of a viscous drop impacting a pool. *Phys. Rev. Fluids*, 2:073602. 124

Liu, K., Hamilton, C., Allard, J., Lowengrub, J., and Li, S. (2016). Wrinkling dynamics of fluctuating vesicles in time-dependent viscous flow. *Soft Matter*, 12:5663–5675. 124

Loudet, J. C., Dolganov, P. V., Patrício, P., Saadaoui, H., and Cluzeau, P. (2011). Undulation instabilities in the meniscus of smectic membranes. *Phys. Rev. Lett.*, 106:117802. 124

Marmottant, P. and Hilgenfeldt, S. (2003). Marmottant p, hilgenfeldt scontrolled vesicle deformation and lysis by single oscillating bubbles. *Nature*, 423:153–6. 116

May, K. (2012). Oszillationen dunner flussiger freistehender film. *Diplomarbeit, Universitat Magdeburg, Institut fur Experimentelle Physik*. 135, 137

May, K., Harth, K., Trittel, T., and Stannarius, R. (2012). Dynamics of freely floating smectic bubbles. *EPL Europhysics Letters*, 100(1):16003. 117, 118, 119, 123, 127, 132, 134, 137, 139, 144

May, K., Harth, K., Trittel, T., and Stannarius, R. (2014). Freely floating smectic films. *Chem Phys Chem*, 15(7):1508–1518. 118, 120, 123, 127, 132, 137, 139

McEntee, W. R. and Mysels, K. J. (1969). Bursting of soap films. an experimental study. *The Journal of Physical Chemistry*, 73(9):3018–3028. 124

Merrer, M. L., Quere, D., and Clanet, C. (2012). Measurement of the proton-air cross section with the pierre auger observatory. *Phys. Rev. Lett.*, 109:062002. 124

Müller, F. and Stannarius, R. (2006). Collapse of catenoid-shaped smectic films. *Europhys. Lett.*, 3:1102. 117, 128

Oswald, P., Picano, F., and Caillier, F. (2003). Dislocation loop dynamics in freestanding smectic films: The role of the disjoining pressure and of the finite permeability of the meniscus. *Phys. Rev. E*, 68:061701. 119, 120, 139

Oswald, P. and Pieranski, P. (2006). *Smectic and columnar liquid crystals: Concepts and physical properties illustrated by experiments*. 118, 135

Paulsen, J., Démery, V., Santangelo, C., Russell, T., Davidovitch, B., and Menon, N. (2015). Optimal wrapping of liquid droplets with ultrathin sheets. *Nature Materials*, 14:1206–1209. 117

Petit, P., Le Merrer, M., and Biance, A.-L. (2015). Holes and cracks in rigid foam films. *Journal of Fluid Mechanics*, 774:R3. 124

Robinson, N. D. and Steen, P. H. (2001). Observations of singularity formation during the capillary collapse and bubble pinch-off of a soap film bridge. *Journal of Colloid and Interface Science*, 241(2):448 – 458. 128

Salili, S. M., Ostapenko, T., Kress, O., Bailey, C., Weissflog, W., Harth, K., Eremin, A., Stannarius, R., and Jakli, A. (2016). Rupture and recoil of bent-core liquid crystal filaments. *Soft Matter*, 12:4725–4730. 124

Salvert, F. (1881). Mémoire sur la théorie de la courbure des surfaces. *F. Hayez*, page 477–510. 127

Santangelo, C. D. and Kamien, R. D. (2005). Curvature and topology in smectic-a liquid crystals. *Proceedings of the Royal Society A: Mathematical, Physical and Engineering Sciences*, 461(2061):2911–2921. 148

Shuravin, N. S., Dolganov, P. V., and Dolganov, V. K. (2019). Coalescence of viscous two-dimensional smectic islands. *Phys. Rev. E*, 99:062702. 137, 139

Silveira, R. d., Chaieb, S., and Mahadevan, L. (2000). Rippling instability of a collapsing bubble. *Science*, 287(5457):1468–1471. 124

Stannarius, R. and Cramer, C. (1998). Self-supporting bubbles of thermotropic smectic liquid crystals. *Europhysics Letters*, 42(1):43–48. 137

Staykova, M., Holmes, D. P., Read, C., and Stone, H. A. (2011). Mechanics of surface area regulation in cells examined with confined lipid membranes. *Proceedings of the National Academy of Sciences*, 108(22):9084–9088. 124

Vella, D., Huang, J., Menon, N., Russell, T. P., and Davidovitch, B. (2015). Indentation of ultrathin elastic films and the emergence of asymptotic isometry. *Phys. Rev. Lett.*, 114:014301. 157

Wang, L., Castro, C. E., and Boyce, M. C. (2011). Growth strain-induced wrinkled membrane morphology of white blood cells. *Soft Matter*, 7:11319–11324. 124

Zhang, C., Grubb, A. M., Seed, A. J., Sampson, P., Jákli, A., and Lavrentovich, O. D. (2015). Nanostructure of edge dislocations in a smectic-C^* liquid crystal. *Phys. Rev. Lett.*, 115:087801. 152

Zhao, Y., Huang, W. M., and Fu, Y. Q. (2011). Formation of micro/nano-scale wrinkling patterns atop shape memory polymers. *Journal of Micromechanics and Microengineering*, 21(6):067007. 155, 158

Chapter 5

General summary and perspectives

During the thesis, we have explored a small part of the rich field of the dynamics of topological defects in liquid crystals. The specificity of freely suspended smectic films over LC cells makes them particularly suitable for defects dynamics experiments. Homogeneous films can be prepared with thicknesses down to some nanometers. If they are kept away from external disturbances, they can remain solid for a long time up to several months. The large aspect ratios between the thickness and the surface area on the one hand, and the intern *SmC* structure on the other hand make them ideal two-dimensional systems for the dynamical study of topological defects. We went through several geometries of freely suspended smectic films, frame-supported flat films and freely floating bubbles, in order to study the dynamics of defects of different types: dislocations and disclinations.

In the second Chapter, we considered rectangular frame-supported freely suspended *SmC* flat films. We prepared films with thicknesses of the order of 1 μm and a width of about 5 mm. In the course of our investigations, we performed a study of the dynamics of isolated and well-controlled ± 1 defect pairs in freely suspended *SmC* films. The defect pairs have been created with a new technique which allows to control their numbers as well as their spatial positions in the film. We have focused on a detailed analysis of the mutual attraction and annihilation of the ± 1 defect pairs. Our experimental results show that the classical model that describes the motion of defect pairs using a quasi-equilibrium configuration partially fail to describe the annihilation process of ± 1 defects. Most pairs annihilate along a curved and non-linear trajectory not predicted by the classical model. We argue that this disagreement is due to the properties of the defects themselves which have been disregarded by the classical model. The orientation of the defects must be taken into account to describe their mutual interaction and annihilation, a parameter that has not been considered in the classical model. We have shown that the defects simultaneously change their phases as well as their spatial positions during the annihilation, which induces the curved trajectories, a result that is consistent with a recent model that underlines the importance of defect orientations. However, we have shown that the far *c-director* field which has been ignored in the recent model affects directly the defect dynamics. It exerts a torque that tends to align the pair in a direction corresponding to the minimum elastic distortion. The correlation function between the defects phase mismatch, $\delta\theta$, and the misalignment of the pair with respect to the far director field, $\delta\phi$, has been determined experimentally. We have shown that both parameters are not independent of each other. We suspect that this is a common feature of topological defect pairs in many other 2D systems. The classical model remains valid for the special case of aligned, matching pairs. For misaligned and mismatched pairs the experimental data reveal the limitations of the defect interaction models in liquid crystals.

We have found that the experimental results are in agreement with the simulations, which are based on the one-constant approximation, regarding the correlation between $\delta\theta$ and $\delta\phi$. This suggests that the anisotropy of the elastic constants ($K_S \neq K_B$) does not play a major role, but it is essentially the far *c-director* that plays a crucial role in the dynamics of ± 1 topological defects. A short-term perspective would be to carry out similar experiments on the dynamics of ±1 topological defects in freely suspended films using other *SmC* materials that have different values of elastic constants. This could allow to confirm the non-crucial role of the elastic anisotropy.

A long-term perspective is the study of the dynamics of topological defects in *SmC* freely suspended films with topological charges other than $S = \pm 1$. These studies could present a frame that would serve to develop generalized theoretical models for the dynamics of topological defects in liquid crystals. Such problems are of direct interest for cosmology-related topological defects, where it is essential to acquire knowledge about the dynamics of cosmologically relevant defects, such as cosmic string evolution.

The following Chapter 3, is devoted to the study of the observed velocity asymmetry of the defects during the annihilation process. We found that the +1 defect moves up to twice as fast as the -1 during the annihilation. This phenomenon has been observed previously in nematic cells. It was associated with the effects of the backflow on the motion of defects according to their topological charges. Using a technique based on dye bleaching, we have studied the behaviors of the flow field around the defect pairs during their mutual attraction in freely suspended *SmC* films. By tracking bleached ROIs, we have found that the motion of the +1 defect is accompanied by a flow of material in the same direction and with comparable velocity. This contrasts with the -1 defect around which no material flow has been observed. The observations reveal the existence of weak flow advection around the positive defect that we have linked to the predictions of a numerical study that predicts the existence of flow vortices around the latter defect.

Our experimental investigations on the backflow features are in agreement with the numerical study that used the one-constant approximation $K_S = K_B$, whereas this condition is not fulfilled in our study where $K_S = 2.2\ K_B$. This suggests that the backflow is the main mechanism behind the observed velocity asymmetry. However, the experimental results show that the expected distance between the vortices and the defect is larger than that predicted by the numerical study. Regarding the difference in time scales between experiments and simulations, it is possible that the elastic anisotropy plays a significant role at the early stage of the annihilation process being possibly responsible for the larger distance defect/vortices than expected.

Further more investigations could be performed. For example, the same dye bleaching technique can be used to bleach ROI further away from defects in order to highlight the flow vortices predicted by the numerical study. A long-term perspective of this work would consist in the dispersion of nanometer sized droplets, e.g. glycerol-water droplets, on the film surface for the tracking of their motion during the defects annihilation process. This could allow to highlight the variation of the defect/vortices distance in function of the defects separation distance.

The last chapter is devoted to the dynamics of smectic islands in freely floating *SmC* bubbles studied in micro-gravity conditions during parabolic flight campaigns organized by the National Center for Space Studies (CNES). We used the catenoid film collapse as a method to prepare freely floating smectic bubbles. Smectic islands were found to nucleate at the surface of the bubble, either before or during the pinch-off. They grow during the relaxation of the deformed bubble following a quadratic dependency. When the bubble is relaxed and reaches the spherical shape, the islands stop growing and only further dynamics related to islands coalescence is expected.

We have revealed the consequence of the impossibility of rapid adjustments of the surface area when islands undergo abrupt local compression. Two types of dynamical wrinkle patterns are observed within the islands: star and ring shaped wrinkles with a clear selection of wavelength λ. Ring-shaped wrinkles consist of deformation of the island surface into circular undulations. We have found that the characteristic wavelength is of the order of some tenths of micrometers, a value that is of the same order of magnitude as that determined by previous work on bubble wrinkles. Star-shaped wrinkles are formed when a tubule exists in the center of the island which induces the formation of radial wrinkles. We have found that the surface area of the islands continues to grow even during the existence of wrinkles. As soon as the local compression ceases, the wrinkles disappear and the islands continue to grow with the initial dependency determined before the wrinkles appearance.

We have found that these wrinkles are mainly caused by the abrupt stress applied on the islands. We related the applied compression forces to external disturbances that can occur during bubble oscillations, such as the surrounding airflow, which can be generated by the remaining films on the catenoid rings or by the loudspeakers. This airflow can create an abrupt local compression of the bubble. The second source of external disturbances are the complex deformed shapes that the bubble adopts during relaxation, which can also create abrupt local compression of the bubble film. These external disturbances can create an abrupt compressive forces that induce the formation of wrinkles within the islands.

We have developed a preliminary model, based on the model developed for the case of wrinkles formed in bubbles, to describe the structure of ring-shaped wrinkles formed within the islands with considering on the one hand the radial distribution of forces in such geometry and on the other hand the line tension of the dislocations. The characteristic wavelength of the wrinkles, λ, is expected to depend on the properties of the island such as its thickness, the elastic constant k_s of the material, the compressive force as well as the dislocations line tension.

The adapted model explains the experimental observations, where islands react differently according to their size. In medium sized islands, the contribution of line tension becomes important and provides enough stress together with the compressive force to form circular wrinkles with a λ wavelength selection while no wrinkles are formed around in the bubble. This highlights the crucial role of the line tension related to the presence of dislocations that favors wrinkle formation. However, the effect of line tension is expected to decrease with the island size and this is indeed observed. On the other hand, when the size of the islands becomes of the order of λ or smaller, the formation of circular wrinkles can no longer be accommodated and the island bulges out of the film plane, which can induce the second type of wrinkles pattern: radial wrinkles.

We finally arrive to the conclusion that smectic islands behave like solid sheets under sufficiently high and fast compression stress. The dynamical wrinkle patterns are analogue to that observed in gold or plastique sheet. This phenomenon is not observed in conventional low-viscosity fluid films because they can instantly change their thickness and reduce their surface area under lateral compression.

A short-term perspective of this work would be to develop a more advanced model than the preliminary model we have developed. Such an advanced model must take into account the detailed structure of the circular wrinkles such as the existence of the ridge in the center of the island as well as the non-homogeneous distribution of the airflow within the wrinkles and it has to consider the variation of island radius during wrinkle. These studies could help to understand in details the mechanisms that induce the formation of wrinkles in smectic islands. This could then possibly be extended for the study of the mechanisms of wrinkle formation in other systems such as gold and polymer sheets.

Relaxation dynamics of smectic bubbles and islands is an exciting field which needs more investigation for a better understanding of the physical properties. They hold an immense potential for new exciting results in order to investigate the role of the material parameters. In particular, the use of another *SmC* material could present a start for such investigation. During a second campaign of parabolic flights in October 2020, we carried out experiments on freely floating bubbles made of another type of *SmC* material. The set-up was improved during the year 2020 in order to also add fluorescent nanoparticles to the suspended bubbles with the right concentration that does not induce aggregation. Since a number of studies have shown that nanoparticles in smectic films will be trapped by the dislocation lines and can influence the line tension of the latter Coursault et al. [2012]; Do et al. [2020], it is expected that the dynamics of the smectic islands in the freely floating bubble will be different than that without the nanoparticles. We now need to analyze the dynamics of islands in presence of nanoparticles already collected in this last 2020 campaign.

In parallel, I have set up a system that allows to study the dynamics of islands in the presence of nanoparticles in rectangular freely suspended films in the laboratory. Such a system allows to inject nanoparticles into the films in a well-controlled manner unlike conventional techniques which are based on mixing the LC with the nanoparticles, resulting in their aggregation and trapping in the meniscus. This technique may allow an extension to various other topics. For example we could inject nanoparticles in freely suspended bubbles in micro-gravity in order to compare the dynamics of nanoparticles attracted by the dislocations and in the presence/absence of the meniscus. This could be done for nanoparticle concentrations larger than the right concentration inducing aggregation. I show in the Fig.5.1 one of the first results obtained with this technique where rod-shaped fluorescent nanoparticles are trapped in the dislocation lines surrounding the islands. The nanoparticles seem to be concentrated in the dislocation lines where they reproduce the linear shape. The line tension of the dislocation lines is modified due to the presence of these nanoparticles. Such a study can also provide information on the properties of the topological defects themselves, in particular their size, structure and energy of the core, which remain unknown Rahimi et al. [2017].

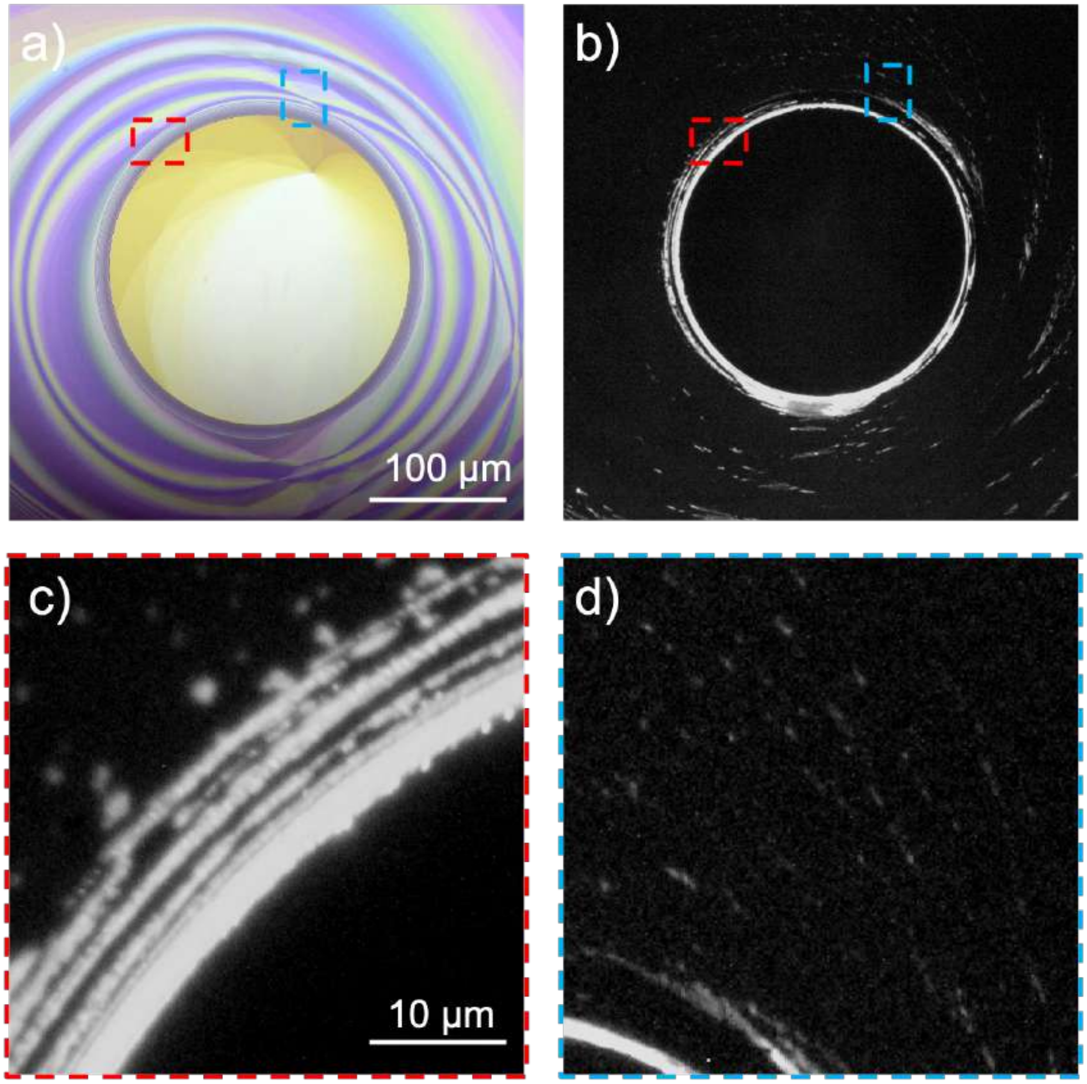

Figure 5.1 – (a) Optical microscope image revealing of smectic island in freely suspended smectic film. The interference colors reveal the thickness change. (b) Fluorescence image of nanoparticles emission of $\lambda = 500$ nm. Nanoparticles are trapped in the dislocation line around the island. They form an a concentrated structure. (c) cut-off from along the red dashed square in (b) showing the high complex organization pattern of nanoparticles in the dislocations region around the island. (d) Nanoparticles trapped in adjacent dislocation lines.

5.1 References

Coursault, D., Grand, J., Zappone, B., Ayeb, H., Lévi, G., Félidj, N., and Lacaze, E. (2012). Linear self-assembly of nanoparticles within liquid crystal defect arrays. *Advanced Materials*, 24(11):1461–1465. 171

Do, S.-P., Missaoui, A., Coati, A., Resta, A., Goubet, N., Royer, S., Guida, G., Briand, E., Lhuillier, E., Garreau, Y., Babonneau, D., Goldmann, M., Constantin, D., Croset, B., Gallas, B., and Lacaze, E. (2020). Interactions between topological defects and nanoparticles. *Frontiers in Physics*, 7:234. 171

Rahimi, M., Ramezani-Dakhel, H., Zhang, R., Ramirez-Hernandez, A., Abbott, N., and de Pablo, J. (2017). Segregation of liquid crystal mixtures in topological defects. *Nature Communications*, 8:15064. 171